Internal Structure and Optical Appearance of Circumstellar Dust Shells around Cool Carbon Giants

vorgelegt von

Dipl.–Phys. Jan Martin Winters
aus Stuttgart

Vom Fachbereich 04 (Physik)
der Technischen Universität Berlin
zur Erlangung des akademischen Grades

Doktor der Naturwissenschaften (Dr. rer. nat.)

genehmigte Dissertation

Berlin 1994

D 83

Promotionsausschuß:

Vorsitzender:	Prof. Dr. H. Niedrig
Berichter:	Prof. Dr. E. Sedlmayr
	Priv.–Doz. Dr. J. P. Kaufmann

Tag der mündlichen Prüfung: 24. 3. 1994

Fürs erste darf nicht angenommen werden, daß die Erkenntnis der Himmelserscheinungen, mögen sie in größerem Zusammenhange oder selbstständig für sich besprochen werden, ein anderes Ziel verfolgt als die Beruhigtheit und feste Zuversicht, wie das ja auch bei allen anderen Dingen der Fall ist.

Epikur, 341–270 v. Chr.

Zusammenfassung

Kühle Riesensterne späten Typs repräsentieren wichtige Stadien in der Entwicklung von Sternen mittlerer und geringer Masse. Diese Objekte sind im allgemeinen von ausgedehnten zirkumstellaren Staubhüllen (ZSH) umgeben, die zu beträchtlichen Massenverlusten führen.

In der vorliegenden Arbeit werden detaillierte physikalische Modelle solcher staubbildenden zirkumstellaren Hüllen um späte, kohlenstoffreiche Riesen präsentiert. Diese Modelle enthalten eine konsistente Behandlung von Hydrodynamik, Thermodynamik, Chemie, Staubbildung und –wachstum und des Strahlungstransportproblems. Sowohl die komplette Atmosphärenstruktur, als auch ihr Erscheinungsbild im infraroten Spektralbereich ergeben sich als Resultat der Rechnung.

Diese Arbeit ist in zwei wesentliche Teile gegliedert.

Im ersten Teil wird eine selbstkonsistente Lösung für das stationäre, sphärisch symmetrische Problem eines staubgetriebenen Windes vorgestellt. Die resultierende Hüllenstruktur sowie auch die Massenverlustrate sind vollständig durch die vier fundamentalen stellaren Parameter stellare Masse $M_\star$, stellare Leuchtkraft $L_\star$, Photosphärentemperatur $T_\star$ sowie die Elementhäufigkeiten $\epsilon_{\rm i}$ festgelegt. Die Resultate zeigen, daß in einem stationären staubgetriebenen Wind die übliche Annahme kleiner Teilchen zur Berechnung der Transportkoeffizienten der Staubkomponente nicht gerechtfertigt ist. Insbesondere in den inneren Hüllenbereichen wird die auf die Staubkörner wirkende Strahlungskraft erheblich durch das Vorhandensein großer Teilchen reduziert. Die Abhängigkeit der Modelle von den stellaren Parametern wird diskutiert, und die resultierenden Spektren werden im Rahmen von Infrarot Zweifarbdiagrammen mit den Beobachtungen verglichen. Eine Anwendung dieser Modellrechnungen auf das bekannte Infrarot–Objekt IRC +10216 ergibt die beste Übereinstimmung mit der beobachteten Energieverteilung und den interferometrischen Daten (gemessen während des Lichtmaximums) für die stellaren Parameter $M_\star = 0.7 M_\odot$, $L_\star = 2.4 \cdot 10^4 L_\odot$, $T_\star = 2010{\rm K}$ und ein Verhältnis von Kohlenstoff zu Sauerstoff $\epsilon_{\rm C}/\epsilon_{\rm O} = 1.40$, was zu einer Massenverlustrate von $\dot{M} = 8 \cdot 10^{-5} M_\odot {\rm yr}^{-1}$ führt. Aus diesem Modell wird eine Entfernung zu IRC +10216 von $d = 170{\rm pc}$ abgeleitet. Die gesamte in der ZSH enthaltene Masse liefert eine anfängliche Hauptreihenmasse für IRC +10216 von $M_{\rm ZAMS} \geq 1.3 M_\odot$.

Im zweiten Teil werden die Ergebnisse detaillierter, frequenz– und winkelabhängiger Strahlungstransportrechnungen präsentiert, welche auf zeitabhängigen Modellen

für pulsierende Atmosphären von kohlenstoffreichen langperiodisch veränderlichen Sternen (LPVs) basieren. Diese Modelle sind durch die vier stellaren Parameter und zwei zusätzliche Größen festgelegt, welche die innere Pulsation des Sterns beschreiben. In diesen Rechnungen werden die Transportkoeffizienten für den Grenzfall kleiner Teilchen im Sinne der Mie Theorie beschrieben, was im Falle der pulsierenden Atmosphären gerechtfertigt ist. Aufgrund der periodischen Bildung von Staubschalen ergibt sich eine inhomogene radiale Staubverteilung, welche die optische Erscheinung dieser Modelle entscheidend beeinflußt. Es wird gezeigt, daß die synthetischen Lichtkurven intermediäre Maxima und überlagerte Perioden aufweisen, wie sie ähnlich auch in den beobachteten Lichtkurven realer LPVs vorhanden sind. Die Spektren der dynamischen Modelle werden im Rahmen eines Nah–Infrarot Zweifarbdiagrammes mit Beobachtungen verglichen. Es zeigt sich, daß für eine physikalisch konsistente Modellierung der Nah–Infrarot Spektren die Pulsationseffekte berücksichtigt werden müssen. Die diskrete, schalenartige Staubverteilung verursacht darüberhinaus signifikante Strukturen in den Oberflächenhelligkeitsprofilen sowie in den synthetischen Kontrastverläufen, die in qualitativer Übereinstimmung mit den entsprechenden Beobachtungen sind.

Die diskrete Struktur der ZSH liefert erstmalig eine Erklärung sowohl für die signifikanten Charakteristika in den beobachteten Lichtkurven von kohlenstoffreichen LPVs als auch für die kleinskaligen Strukturen, die in beobachteten räumlichen Spektren und in den Intensitätsprofilen vorhanden sind.

Abstract

Cool late–type giant stars represent important stages in the evolution of low and intermediate mass stars. These objects generally are surrounded by extended circumstellar dust shells accompanied by considerable mass loss.

In this thesis, detailed physical models of the dust forming circumstellar shells around late–type carbon–rich giants are presented. These models include a consistent treatment of hydrodynamics, thermodynamics, chemistry, dust formation and growth and of the radiative transfer problem. The complete atmospheric structure as well as the infrared appearance of the models is a result of the calculations.

This work is divided into two major parts.

In the first part, a selfconsistent solution of the stationary, spherical symmetric dust driven wind problem is presented. The resulting shell structure and the mass loss rate are completely determined by the four fundamental stellar parameters stellar mass $M_\star$, stellar luminosity $L_\star$, stellar temperature $T_\star$ and the element abundances $\epsilon_{\rm i}$. The results imply, that in a stationary dust driven wind the common assumption of the small particle approximation for calculating the transport coefficients of the dust component is not justified. In particular in the inner shell region, the radiative force acting on the grains is essentially reduced by the presence of large particles. The dependence of the models on the stellar parameters is discussed and the resulting spectra are compared to the observations in the frame of infrared two colour diagrams. Application of these model calculations to the prominent infrared object IRC +10216 yields best agreement with the observed energy distribution and the interferometric data obtained at light maximum for the stellar parameters $M_\star = 0.7 M_\odot$, $L_\star = 2.4 \cdot 10^4 L_\odot$, $T_\star = 2010$K and a carbon to oxygen ratio of $\epsilon_{\rm C}/\epsilon_{\rm O} = 1.40$, which yields a mass loss rate of $\dot{M} = 8 \cdot 10^{-5} M_\odot {\rm yr}^{-1}$. From this model a distance to IRC +10216 of $d = 170$pc is deduced. The total mass contained in the circumstellar dust shell implies an initial main sequence mass of $M_{\rm ZAMS} \geq 1.3 M_\odot$ for IRC +10216.

In the second part, the results of detailed frequency and angle–dependent radiative transfer calculations are presented, which are based on time–dependent models for the pulsating atmospheres around carbon–rich Long–period variable stars (LPVs). These models are specified by the four fundamental stellar parameters and two additional quantities, which describe the interior pulsation of the star. In these calculations, the transport coefficients of the dust component are described in the

small particle limit of Mie theory, which is justified in the case of a pulsating atmosphere. Due to the periodic formation of dust layers, an inhomogeneous radial dust distribution is produced, which decisively influences the optical appearance of the models. It is shown that the synthetic lightcurves exhibit intermediate maxima and secondary periods, which similarly occur in the observed lightcurves of real LPVs. The spectra of the dynamic models are compared with observations in the frame of a near infrared two colour diagram. For a physically consistent modelling of the near infrared spectra, it turns out to be necessary to take the effects of the stellar pulsation into account. The discrete shell–like distribution of dust also causes significant structures in the surface brightness profiles and in the synthetic visibility functions, which are in qualitative agreement with the respective observations.

The discrete structure of the circumstellar dust shell for the first time provides an explanation for both, the significant characteristics present in the observed lightcurves of carbon–rich LPVs as well as for the small–scale structures present in the observed spatial spectra and in the brightness profiles.

Contents

List of Figures

List of Tables

Sonne, Mond und Sterne sind feurige Steine, die die Umdrehung des Äthers mitmachen [...] Die Sonne übertrifft den Peloponnes an Größe. Der Mond hat kein eigenes Licht, sondern er erhält es von der Sonne.

Anaxagoras, ca. 500 – 425 v. Chr.

Chapter 1

Introduction

Almost the only source of direct information we have about the stars emanates from their radiation which, on reaching our planet is accessible to our receivers. This fact implies, that every knowledge we are at all able to gain about a particular celestial object ultimately has to be derived from the analysis of its light and from the interpretation of the extracted information by the use of comprehensive physical models. Since we cannot impose any conditions on the astronomical objects (a fact, that just defines the difference between "experiment" and "observation"), these models necessarily have to be rather sophisticated. They have to account for both, the physical processes leading to the internal structure relevant for the appearance of the object and also for the complex interplay among the different processes involved.

Only on the reliable basis of a model, which involves solely the *external* parameters characterizing the object under consideration (e.g. the fundamental stellar parameters) it is possible to really check the theoretical results against the observed facts. This kind of comparison enables the derivation of constraints (e.g. on the input physics) or reveals basic shortcomings of the theoretical approach, thereby allowing the further improvement of the physical models. Ultimately, the goal of such modelling must be a *selfconsistent* description of the complete physical system (e.g. the whole star), providing us with the only tool to thoroughly understand the detailed physical nature of these objects. The requirement of selfconsistency means that the system has to be described by basic physical principles, i.e. without introducing simplifying assumptions regarding the physical subsystems and/or without even neglecting important couplings among the individual subsystems. An a priori neglect of specific interactions and/or the introduction of simplifying assumptions might lead to doubtful results, since the systems under consideration are typically strongly nonlinear.

At the present time, a quantitative reliable selfconsistent modelling of any complete cosmic object unfortunately is still severely hampered by the often only poorly known input data (e.g. nuclear or chemical reaction rates, molecular opacities, collisional excitation cross sections, ...) or by poorly understood physical mechanisms (e.g. convection or other dissipative processes), or simply by limitations within computing facilities. In most cases, therefore, we are still far from this kind of complete description and, thus, we are a long way from a physically consistent quantitative interpretation of the huge variety of observed facts obtained from astronomical sources.

Although several physical details are to a certain extent still unclear, during the last decades it has become possible to construct consistent models at least for some isolated regions of a star by adopting specific assumptions with regard to the general properties of the system (e.g. its geometry or its temporal behaviour) or by a more or less reasonably simplified description of some of the physical processes involved (e.g. adopting an equilibrium description instead of treating the appropriate rate equations). By the successful application of current physical models, developed on earth, to the stellar objects, we have obtained a coherent general picture of their present status, their evolution and their interaction with their environment.

The work presented in this thesis is concerned with detailed selfconsistent models of the internal structure of circumstellar dust shells (CDS) around cool carbon–rich giant stars, and in particular with the directly observable properties resulting from these models. In order to get an impression about the nature and the evolutionary status of these systems, the next section gives a brief description of the present knowledge on the evolution of low– and intermediate–mass stars. This summary is based on [Shu *et al.* 1987], [Boothroyd and Sackmann 1988b, Boothroyd and Sackmann 1988c], [Kippenhahn and Weigert 1990], and on the reviews of [Weidemann and Schönberner 1990] and [Iben 1991].

1.1 Evolution of low–mass and intermediate–mass stars

Stars are born from the collapse of dense cores formed in cold, dark interstellar clouds.

These self–gravitating objects consist of molecular gas and small solid particles, somewhat vividly also called dust grains.

While collapsing, the central density in the cloud core increases and, when the inner region becomes optically thick, the core is heated by the release of gravitational energy. Once the free fall of the central region is stopped due to the increasing pressure, the central core attains a quasi–hydrostatic equilibrium state. This *protostar* is still surrounded by the freely inward falling envelope material, which finally is stopped on impact at the surface of the core. The kinetic energy is largely converted into radiation and provides most of the object's luminosity. Probably a slowly rotating disk forms around the protostar, composed of gas and, as time proceeds, also composed of an increasing amount of dust. Perhaps a planetary system will emerge from this disk ...

In any case, the protostar further contracts and is heated by gravitational energy release. Gradually, the envelope material becomes depleted by accretion onto the "stellar" surface and probably also by an energetic bipolar stellar wind, which blows the gas away.

When the central temperature T_c of the protostar exceeds a value of about $8 \cdot 10^6$K, nuclear hydrogen burning starts: a new star is born.

This temperature, necessary for the ignition of hydrogen, is reached by stars having initial masses $M_i \geq 0.08 M_\odot$ (the symbol "$\odot$" denotes the solar values). The net result of this process is the fusion of four ^{1}H nuclei to one ^{4}He nucleus. Depending on the temperature, two different burning processes are possible: For central temperatures less than $1.5 \cdot 10^7$K, (corresponding to an initial stellar mass of $M_i < 1.5 M_\odot$), the energy production predominantly proceeds via the *pp* chain, while for higher central temperatures energy release via the CNO cycle prevails. Since in the latter case the heavy elements carbon, nitrogen and oxygen act as catalysts for the helium production, these have to be already present in the star–forming interstellar cloud. The existence of two separate temperature regimes is caused by the very different temperature dependences of the rates of energy release in both processes. For the *pp* chain, the energy production is roughly proportional to T^5, whereas the energy generation rate of the CNO cycle is approximately proportional to T^{18}.

Irrespective of the energy production mechanism, the phase of quiet central hydrogen burning is by far the longest living phase in the life of every star. As most stars are found in this evolutionary stage, it is called the *main–sequence phase*.

After central hydrogen exhaustion, the helium core rapidly contracts and is again heated by gravitational energy release, while hydrogen continues to burn in a thin shell surrounding the inactive helium core. During this phase the star moves to the right in the *Hertzsprung–Russell diagram* (HRD), approaching the *red giant branch* (RGB).

From this point onwards, the further fate of a star depends on its initial mass. However, the precise values of the masses, which segregate the stars into the so called high–mass stars, intermediate–mass stars, and low–mass stars are at present rather uncertain, mainly due to the insufficient theory of convection. Therefore, the masses quoted below should be considered as rough estimates only.

High–mass stars (i.e. those with $M_i > 8 M_\odot$) ignite core–helium burning before they can reach the RGB and successively run through core He, C, O and Si burning phases, which ultimately leads to the production of ^{56}Fe, the strongest bound nucleus. At this stage the star is no longer able to produce energy by nuclear fusion and, therefore, cannot resist the gravitational forces any longer. Ultimate core contraction now sets in and, as the core mass exceeds the Chandrasekhar limit of $1.4 M_\odot$, the star will end its life in a violent explosion as a Type II supernova, leaving a neutron star or even a black hole as the central object of its expanding remnant envelope.

Intermediate–mass stars (i.e. $2M_\odot \leq M_\mathrm{i} \leq 8M_\odot$), when approaching the RGB are characterized by a rapidly inward extending convective envelope. The base of this convective zone finally reaches down into layers where products of the CNO cycle (He and N) have been enriched by the hydrogen burning shell. These newly formed elements are now being mixed upwards to the surface layers. This process of convectively mixing nuclearly processed material into the outer layers of the star is called the *first dredge–up*, leading to an enrichment of the surface layers essentially in ^{14}N. The star now evolves upwards on the RGB i.e. its luminosity increases at a nearly constant surface temperature of $T_\star \approx 4000$K, typically from $\log(L/L_\odot) = 2.8$ to $\log(L/L_\odot) = 3.1$ and, simultaneously, also its radius swells, typically up to $R_\star \approx 300R_\odot$. During this phase the central He core is further contracting, being heated by gravitational energy release. When a central temperature of $T_\mathrm{c} \approx 10^8$K is reached (the central density at this instant typically is $\rho_\mathrm{c} \approx 10^4\mathrm{gcm}^{-3}$) helium burning is ignited in the central region under *non–degenerate* conditions, producing ^{12}C via the *triple alpha* (3α) reaction. Successive α capture by the newly produced ^{12}C simultaneously leads to the formation essentially of ^{16}O and ^{20}Ne. The onset of core helium burning under non electron–degenerated conditions demarcates the intermediate–mass stars from low–mass stars. After helium ignition the star first moves down the RGB and then turns to higher surface temperatures and higher luminosities in the HRD. During this phase, hydrogen burning continues in a thin shell, providing $\approx$ 80% of the star's surface luminosity and causing the hydrogen–exhausted core to grow, whilst the matter within the core is still being converted into carbon and oxygen. This core helium burning phase only lasts for about 25% of the hydrogen burning main–sequence phase. As the helium content in the central region declines below a critical value, core–burning stops but He continues to burn in a thick shell, which works its way outwards and thereby narrows. The helium exhausted core again contracts and heats while the hydrogen rich envelope expands and cools, thereby extinguishing the H burning shell source. In the HRD the star again evolves towards the giant branch and again the base of the convective envelope reaches layers, enriched with nuclearly processed material. This time the convective envelope crosses the H–He interface and moves into a layer, where hydrogen has been completely converted into helium and most of the original carbon and oxygen has been converted into nitrogen. By this mechanism, called the *second dredge–up*, fresh helium and nitrogen is mixed upwards into the outer layers. Due to the He burning shell, the base of the convective envelope is being heated up and H burning is reignited within a second shell located on top of the He shell source. Simultaneously the carbon–oxygen core becomes compacted ($\rho_\mathrm{c} \approx 10^6\mathrm{gcm}^{-3}$) at a temperature of $T_\mathrm{c} \approx 2 \cdot 10^8$K and electron degeneracy sets in. The core has now actually become a hot white dwarf, in the HRD the star has reached the *asymptotic giant branch* (AGB), where alternate H and He shell burning (see below) will set in. From now on, the intermediate–mass star behaves very similar to a low–mass star.

Low–mass stars (i.e. $0.08M_\odot \leq M_\mathrm{i} \leq 2M_\odot$), in contrast to the intermediate–mass stars, do develop an electron–degenerate helium core (which is also surrounded by a hydrogen burning shell) after leaving the main–sequence. The onset of degeneracy is due to the higher central densities ($\rho_\mathrm{c} > 10^2 \mathrm{gcm}^{-3}$) achieved in low–mass stars already during the main–sequence phase. The star ascends the red giant branch, first without igniting core helium burning until it reaches a luminosity of typically $\log(L/L_\odot) = 3.4$ (note that the luminosity at the beginning of the RGB phase for a low–mass star is only a few $L_\odot$). At the base of the RGB, the temperature of the helium core reaches a minimum value close to the temperature of the surrounding hydrogen burning shell. This temperature decrease is caused by electron conduction transporting the energy effectively out of the central region. At this stage the first dredge–up also occurs in low–mass stars. Due to helium deposition from the hydrogen burning shell, the core mass increases, the core shrinks, and its temperature increases, as does the temperature of the hydrogen burning shell. The outer layers of the star expand, causing an increase in surface luminosity while the core further contracts and is heated by gravitational energy release. At a temperature of $T_\mathrm{c} \approx 10^8$K (the core now has reached a mass of $M_\mathrm{c} \approx 0.45M_\odot$ and a density $\rho_\mathrm{c} \approx 10^6 \mathrm{gcm}^{-3}$) helium is ignited in the highly electron degenerate central region. Thus, the temperature rises, which in turn steeply increases the rate of energy production (roughly proportional to T^{30} for the 3α process), which again increases the temperature. This thermal runaway is called the *core helium flash*. Since in the degenerate gas the pressure depends only in $2nd$. order on the temperature, the core cannot react by expansion as the temperature increases until degeneracy is removed (typically at a few 10^8K). Now the core expands at constant mass (thereby extinguishing the hydrogen burning shell) and cools down to values of $T_\mathrm{c} \approx 10^8$K, where the next phase of quiescent helium burning starts. In the HRD the star has moved downwards along the RGB and now settles at a luminosity of $L_\star \approx 100L_\odot$. Up to this point the post main–sequence phase of the low–mass star took about 30% of its time spent on the main–sequence. During the following phase of core helium burning (which only lasts for a few percent of the main–sequence lifetime), the central He supply becomes gradually exhausted and an electron degenerate carbon–oxygen core develops, surrounded by a helium burning shell and a hydrogen rich envelope.

After central helium exhaustion, the star climbs up the *early asymptotic giant branch* (E–AGB). During this phase, the surface luminosity increases up to some $10^4 L_\odot$ (caused by the growing core–mass due to the deposition of nuclearly processed material from the helium burning shell) at an almost constant surface temperature (typically $T_\star \leq 3000$K), and the stellar radius strongly increases while the He shell source narrows. Eventually hydrogen burning is reignited in a second shell located closely above the rather thin helium shell. At this stage, the hydrogen shell supplies $\approx 80\%$ to the total luminosity.

The low–mass star now has adopted a structure very similar to its intermediate–mass relative and both will further evolve in a very similar way. Thus: **All stars with initial masses between $\approx 0.1M_\odot \leq M_\mathrm{i} \leq 8M_\odot$ will reach the AGB.**

Due to its small geometrical extension, the helium shell becomes thermally unstable, since an expansion of the shell proceeds isobaric and, thus, would lead to an *increase* of the shell temperature. This instability gives rise to the so called *helium shell flashes* (or *thermal pulses* (TP)), which occur under non–degenerate conditions. A slight increase in T causes a steep increase in the release of nuclear energy due to the extreme temperature sensitivity of the 3α process. But now the shell reacts by an expansion, which further increases the temperature and, in turn, the rate of energy production. Within a few years, the temperature rises to values as high as $3 \cdot 10^8$K and the luminosity produced in the helium shell reaches a sharp peak value of the order of several $10^5 L_\odot$, while the helium shell is still expanding. Most of the energy produced however, is used up in the expansion of the outer layers of the envelope on top of the He shell and the changes in surface luminosity are only minor. This expansion of the outer region considerably reduces the temperature in the H burning shell, which finally is practically extinguished. When reaching the luminosity peak, the He shell is widely geometrically extended and, therefore, is no longer thermally unstable. Subsequently, the whole region contracts again, the H shell is reactivated and after some $10^3 - 10^4$yr the pre–flash structure is almost reached again and the flash cycle will be repeated nearly periodically during the star's subsequent evolution. Starting with the first thermal pulse, the star is located on the TP–AGB. Theoretically, this thermal pulsing phase could continue until the core mass exceeds the critical value ($\approx 1.1 M_\odot$) for core–carbon ignition, but in practice this limit is never reached due to **considerable mass loss during the AGB phase** (see Sect. 1.2). Mass loss limits the number of thermal pulses and prevents the star from the catastrophe of becoming a supernova.

A second important mechanism at work during the shell–flash phase is the *third dredge–up* process. During the TP–AGB phase, two convective zones are present. The first (inner) convective zone is located within the inter–shell region and mixes processed material from the helium shell upwards close to the hydrogen burning shell. The second (outer) convective region extends from the stellar surface down to and, during a flash maximum, even beyond the hydrogen–burning shell. By this mechanism newly processed material is distributed over the whole outer envelope up to the stellar surface after each thermal pulse. Therefore, the outer layers now become enriched mainly in carbon, but also in a variety of neutron–rich isotopes (the so called s–process elements; e.g. technetium), which are successively built up in the helium–burning shell by neutron capture and subsequent β^- decay of ^{56}Fe and its progeny. **This third dredge–up mechanism is supposed to be responsible for the formation of the carbon–rich AGB stars (late–type carbon–stars).**

After the star has lost most of its envelope mass, mainly due to a massive stellar wind, the core rapidly evolves at nearly constant luminosity to higher surface temperatures and moves to the left in the HRD until at $T_\star \approx 3 \cdot 10^4$K the surrounding shell, consisting of the material ejected during the AGB phase, becomes ionized. The object can now be observed as a *planetary nebula* (PN). Its central star (the former C–O core of the AGB star) typically has a mass of $0.6 M_\odot$ and is still sur-

rounded by a thin, nuclear active shell, which is responsible for its high luminosity. Finally, after reaching a maximum surface temperature of $\approx 10^5$K, nuclear burning ceases as the fuel supply is used up. The star has died.
Its corpse ultimately cools down and ends as a *white dwarf*.

The preceding overview of stellar evolution, though state of the art, nevertheless should be considered a qualitative picture rather than quantitative knowledge. Several ingredients needed for a stellar evolution calculation are at present only poorly known. One of the shortcomings in all such calculations is that a rigorous theory of convection is still lacking. Most calculations performed so far rely on the classical mixing–length theory, and many of the numerical results obtained, depend on the values chosen for the mixing–length parameter. A second severe problem is the treatment of mass loss during the AGB evolution. In most calculations only a parameterized fit formula is used in order to describe the high mass loss rates, which are needed to match the observed white dwarf masses for the remnant cores of AGB evolution. Usually the so called Reimers formula ([Reimers 1975])

$$\dot{M} = -\eta \, (4 \cdot 10^{-13}) \, \frac{L_\star R_\star}{M_\star} \; M_\odot \mathrm{yr}^{-1} \tag{1.1}$$

is used ($L_\star$, $R_\star$, $M_\star$ in solar units). This formula gives a fit to the observed mass loss rates of **RGB** stars if a value for the parameter $\eta = 0.4$ is used. For realistic values of the stellar parameters appropriate for **AGB** stars, mass loss rates of up to a maximum $\dot{M} \approx 10^{-6} M_\odot$ can be described by Eq. (1.1). As the observed characteristics of planetary nebulae require mass loss rates larger than of $10^{-5} M_\odot \mathrm{yr}^{-1}$ during the AGB phase, [Renzini 1981] introduced the term *superwind* to describe these high mass loss rates. In order to account for the superwind mass loss in evolutionary calculations, the Reimers parameter η is ad hoc switched to different values needed during different evolutionary stages with the constraint, that the final core masses after termination of the AGB phase match the observed masses of white dwarfs (e.g. [Schönberner 1983], [Boothroyd and Sackmann 1988b]). Up to now, no consistent treatment of the mass loss process has been used in evolutionary calculations.

Based on a selfconsistent solution of the stationary dust driven wind problem, a fit formula has been published by [Dominik *et al.* 1990], which describes the dependence of the mass loss rate on the basic stellar parameters for carbon–rich AGB stars. This formula is capable of explaining the observed high mass loss rates without introducing artificial fit parameters. Intentions are to incorporate this description into evolutionary calculations during the late AGB phases ([Wagenhuber and Weiss 1994]).

Concluding this section, a few major results regarding evolutionary aspects relevant for this thesis are summarized:

- Stars with initial masses between $\approx 0.1 M_\odot$ and $\approx 8 M_\odot$ run through the AGB phase. According to the initial mass function of [Miller and Scalo 1979], these are $\approx 50\%$ (by mass) of all stars formed in our galaxy. (Stars formed since the formation of our galaxy with initial masses $0.08M_\odot \leq M_\mathrm{i} \leq 1M_\odot$ are still located on the main–sequence.)

- During the TP–AGB phase the surface layers become enriched with carbon and with a variety of neutron rich s–process elements.

- Substantial mass loss occurs during stellar evolution. As the remnant cores after termination of the AGB phase have typical white dwarf masses of the order of $0.6M_\odot$ (cf. [Weidemann and Koester 1983]), low– and intermediate–mass stars have to get rid of $40\% - 90\%$ of their initial mass. Thus, an appreciable fraction of the (partly nuclearly processed) stellar material is returned to the interstellar medium.

1.2 Phenomenology of AGB stars

According to their evolutionary status, AGB stars are characterized by low surface temperatures ($T_\star \leq 3000$K), high luminosities ($L_\star \approx 10^4 L_\odot$) and by a peculiar (i.e. non solar) chemical composition. From the first two properties, one recognises, that these stars must also have very large radii. This further implies, that the atmospheres of these objects have rather large density scale heights ($H_\rho = |\partial \ln \rho / \partial r|^{-1}$) and, thus, are largely geometrically extended. The atmospheres of these giant stars, due to the low temperatures and simultaneously high densities, provide favourable thermodynamic conditions for the formation of complex molecules. The spectra obtained from these objects are thus crowded by millions of molecular lines, arising e.g. from the diatomic species CO, C_2, CN, CH, TiO, SiO, ZrO but also from polyatomic molecules such as H_2O, HCN, C_2H_2 …(cf. [Olofsson 1988] and [Gustafsson 1989]).

According to the photospheric abundance ratio of carbon to oxygen, the stars can be classified as M–stars (C/O< 1), S–stars (C/O ≈ 1) and C–stars (C/O> 1). Owing to its large bond energy of 11.1eV, the CO molecule already forms at rather high temperatures in the stellar photosphere and therefore blocks the respective less abundant element. The CO molecule thus plays a key role for the molecular composition of the atmospheric gas (even under non–equilibrium conditions, cf. [Beck *et al.* 1992]). Consequently, the spectra of M–stars are dominated by the lines of oxygen bearing molecules e.g. the metal oxides SiO and TiO, and H_2O, whereas in C–star atmospheres the carbon bearing molecules like CH, C_2, C_2H_2 and HCN prevail.

As the solar (and also the mean interstellar) abundance ratio is C/O< 0.5, at least the S and C–stars must have been enriched with carbon during their evolution. This carbon enrichment can be achieved essentially by two mechanisms: i) through mass transfer from a companion star in a close binary system, and ii) via the third dredge–up mechanism, which is considered here.

That stars have actually experienced the third dredge–up and, thus, are in fact AGB objects, can be deduced from the presence of s–process elements in their photospheres. The most convincing indicator for recent mixing is provided by the detection of technetium lines in their spectra. In particular, 75% of the C–stars show Tc in their spectra. As mainly ^{99}Tc, which has a half–life of only $t_{1/2} = 2.13 \cdot 10^5$yr, is produced by the s–process, (the longest lived isotope ^{98}Tc has a half–life of $t_{1/2} = 4.2 \cdot 10^6$yr, e.g. CRC Handbook) the presence of Tc clearly indicates very recent production of this element. Technetium has in fact been found in several stars (e.g. [Peery 1971], [Little *et al.* 1987]), which are thus clearly revealed as AGB objects. Additionally, a simultaneous increase of the C/O ratio and of the abundance of s–process elements has been found for a sample consisting of 279 M, S and C–stars, thus indicating an evolutionary sequence starting from oxygen–rich giants via S–stars towards the luminous C–stars ([Little *et al.* 1987]).

A common feature of AGB stars is the presence of expanding circumstellar dust shells (CDS), which are accompanied by considerable mass loss.

Already [Adams and MacCormack 1935] found a systematic displacement essentially of the sodium D lines and of the Ca H and K lines relative to the stellar velocity in the spectra of 7 nearby M–type giants. They interpreted their results in terms of circumstellar gas envelopes, which expand with a velocity of the order of $5\,\mathrm{kms}^{-1}$. From a detailed spectral analysis of the M–giant component of the system α Her [Deutsch 1956] demonstrated, that this system is surrounded by a common envelope, expanding at a velocity of $10\,\mathrm{kms}^{-1}$. He further concluded, that this envelope has been ejected by the M–star, leading to a mass loss rate for this star of the order of $10^{-7} M_\odot \mathrm{yr}^{-1}$ and that such mass loss rates should be a common phenomenon for all M–giants and supergiants. (For comparison: the solar wind carries a mass loss of $\approx 10^{-14} M_\odot \mathrm{yr}^{-1}$.)

Further observations in the infrared spectral region revealed a continuous excess emission and also broad emission features around 10μm in M–type giants ([Woolf and Ney 1969] and [Gillett *et al.* 1971]) and a feature around 11μm in the spectra of C–type giants ([Treffers and Cohen 1974]). These features could not be attributed to chromospheric emission and were thus concluded to be of circumstellar origin ([Woolf and Ney 1969]).

The formation of the features can be explained as a result of the interaction of photons with the vibrational modes of certain active molecular groups contained in solid particles (dust grains). The identification of the features implies the presence of silicate compounds (e.g. Mg_2SiO_4 or Al_2SiO_5) in the shells of M-stars ([Gilman 1969] and [Gillett *et al.* 1971]) and of carbon compounds (e.g. amorphous or graphitic carbon (which produce the featureless continuum) and SiC) in the shells of C-stars ([Gilman 1969] and [Treffers and Cohen 1974]).

From the observed colour excess at 11μm, [Gehrz and Woolf 1971] derived mass loss rates in the range from $\approx 10^{-7}$ to $\approx 10^{-5} M_\odot \mathrm{yr}^{-1}$ for more than 50 late–type giant stars and additionally proposed that radiation pressure on dust grains is driving these winds.

Very detailed information is obtained by high resolution observations in the radio spectral range. The observed widths of the molecular rotation lines (mainly of CO) indicate expansion velocities of the circumstellar shells in the range from 8 to 40 kms^{-1} (e.g. [Knapp *et al.* 1982]). By calculating theoretical profiles of the CO J=1–0 and J=2–1 rotation lines, [Knapp and Morris 1985] derived mass loss rates for 50 late–type M and C–stars in the range from $\sim 10^{-7}$ up to some 10^{-4}M$_\odot$yr^{-1}. Similar values for the mass loss rates are further obtained from submillimeter observations (e.g. [Sopka *et al.* 1985]) and, in the case of oxygen rich stars, from fitting the 10μ silicate feature ([Schutte and Tielens 1989]).

In the far infrared (FIR) spectral region, which is not accessible by earth bound telescopes, a vast amount of information was obtained by the **I**nfra**R**ed **A**stronomical **S**atellite (IRAS), launched in 1983. During this mission, nearly 158000 stellar objects were observed at 12, 25, 60 and 100μm. Signs of extended circumstellar emission were found for $\approx 50\%$ of these objects, which confirms that the presence of CDS around these objects is a quite common phenomenon for all late–type stars.

Since the photospheric temperatures $T_\star \geq 2000$K are too high for solid particles to exist, the dust grains must form in the expanding circumstellar shells. As a natural consequence of the observed correlation between infrared excess (probing the amount of dust) and the mass loss rate (e.g. [Veen and Rugers 1989]) it seems likely, that the formation of dust plays a decisive role for the generation of the mass outflow. However, most of the dusty AGB objects are also known to be pulsating variable stars (long–period variables (LPVs)) (e.g. [Jura 1986b] and [Habing 1990]) having typical periods between 100d and 1000d (cf. [Beyer 1965]). The radial pulsations of these stars generate strong shock waves, which propagate through the atmosphere and the circumstellar shell. Thus, the situation becomes rather complex, as the dissipation of shock wave energy and momentum also might contribute to the mass loss mechanism (cf. Sect. 1.3).

In any case, the mass loss rates occuring during AGB evolution are so high, that they have a significant impact on the evolution of the central star (e.g. [Weidemann and Schönberner 1990], [Schönberner 1990] and [Vassiliadis and Wood 1993]).

The main implications derived from the observations of AGB stars can be summarized as follows:

- Highly evolved intermediate–mass and low–mass stars generally are surrounded by expanding circumstellar dust shells.

- These dust shells are characterized by low expansion velocities (5 kms^{-1} $\leq v_\infty < 40$ kms^{-1}) and high mass loss rates ($\approx 10^{-7} M_\odot$yr^{-1} $\leq \dot{M} \leq 10^{-4} M_\odot$yr^{-1}).

- The material lost during the AGB phase, enriched with nuclear processed material, complex molecules, and solid dust particles is recycled to the interstellar medium. AGB stars, therefore, are important sources of freshly processed matter and, consequently, play a key role for the chemical evolution of the interstellar medium. 87% of the total dust mass returned to the interstellar medium, according to [Gehrz 1989], is produced by stars evolving along the AGB.

1.3 Mass loss mechanisms for cool giant stars

From the observed facts it is clear, that heavy mass loss, connected with the formation of dust, occurs during the late evolutionary phases of low– and intermediate–mass stars.

In contrast to the fast massive winds of hot luminous stars, which are driven by radiation pressure on ultraviolet (UV) lines of abundant atomic ions (e.g. [Castor *et al.* 1975], [Pauldrach *et al.* 1986]), no generally accepted mechanism exists for driving the cool massive winds of low gravity stars. Depending on the evolutionary status of the object, different mechanisms might be involved, but in most cases a selfconsistent description of the mechanisms, which could account for both, the observed high mass loss rates and the low terminal velocities, is still lacking (cf. the reviews by [Holzer and MacGregor 1985], [Gail 1990] and [Lafon and Berruyer 1991]).

The mechanisms currently being discussed in the literature essentially comprise: i) the dissipation of energy and momentum of different kinds of waves which may propagate through the atmosphere; ii) radiation pressure on dust (or molecules), and iii) the combined effect of these mechanisms, i.e. levitation of the atmosphere by wave dissipation and effective acceleration of the material by radiation pressure on dust grains. These mechanisms are described below in more detail:

i) Wave driving

Small amplitude waves may be induced by the turbulent motion of sub–photospheric mass elements, which occurs in the outer convective zone of the star. In the presence of magnetic fields, two kinds of waves: (compressive) acoustic waves and (noncompressive) Alfvén waves may result.

Undamped **Alfvén waves** (i.e. no heating of the atmosphere by energy dissipation) are able to extend the atmosphere and to lift the material out of the stellar gravitational field. However, most of the energy flux is transferred to the gas in the outer, supersonic region of the wind. Therefore, undamped Alfvén waves are able to produce high mass loss rates, but the resulting terminal wind velocities are much too high in comparison to what is actually observed (cf. [Holzer and MacGregor 1985]). If the Alvfén waves are damped over a characteristic length of about one stellar radius, most of the wave energy is transformed to thermal energy of the gas, and is radiated away. By this mechanism, the terminal velocities can be considerably reduced. This, however, involves the introduction of a damping length parameter. Since the calculated terminal wind velocities are very sensitive to the adopted value of the damping length, its values are confined to a rather small range in order to produce the observed velocities. It is however unclear, which physical mechanism could lead to such a fine–tuning of the damping length. Additionally, these calculations result in extended warm atmospheres ([Holzer *et al.* 1983]), which are not observed for AGB stars.

Driving the winds by **acoustic waves** has been investigated e.g. by [Pijpers and Hearn 1989] and [Pijpers and Habing 1989]. They consider the effects of small amplitude sound waves (represented by the divergence of a pressure tensor) on isothermal atmospheres (i.e. $T = T_\star \approx 3000$K throughout the atmosphere). They also need to prescribe the damping length as a parameter but are able to obtain values for the mass loss rate and the terminal velocity, which are in agreement with the respective observations. Generally, these winds accelerate slowly over a long distance (see [Hearn 1990]) with the transition from subsonic to supersonic motion occuring outside of $10R_\star$. However, dust forms much closer to the photosphere (e.g. [Danchi *et al.* 1990], [Danchi *et al.* 1994]). The additional action of radiation pressure on dust would then not only lead to higher terminal velocities but also to considerably higher mass loss rates and, thus, would completely dominate the wind structure (see ii)). Wind generation by sound waves, therefore, seems unlikely to be a primary mechanism in dusty AGB stars.

Since most AGB stars with high mass loss rates are also known to be long–period variables, it seems natural to consider the effects of **shock waves** in propelling the wind. Shock waves alone as a driving mechanism for late–type stellar outflows have been explored e.g. by [Wood 1979]. In these calculations, the shocks were treated in the isothermal limit case as well as in the adiabatic limit case. In the isothermal case, no continuous outflow is produced, and only a small amount of material is occasionally ejected. The mass loss rates produced by these models are of the order of $10^{-12}M_\odot\mathrm{yr}^{-1}$. Pure isothermal shocks thus are incapable of accounting for the observed much higher values. In the adiabatic models, continuous winds with low terminal velocities develop, but the mass loss rates ($\dot{M} \approx 10^{-2}M_\odot\mathrm{yr}^{-1}$) associated with these winds are by at least two orders of magnitude too high as compared to the observed values. Wood's calculations were considerably improved by [Bowen 1988], who considered a time–dependent post–shock relaxation of the gas by means of a parameterized cooling function. This approach results in rather low outflow velocities (at $20R_\star$ the velocities are actually smaller than the escape velocity) and rather small mass loss rates ($\dot{M} \approx 10^{-9}M_\odot\mathrm{yr}^{-1}$). A further result is the formation of a kind of chromosphere, i.e. an extended region between $3R_\star$ and $10R_\star$ with an enhanced gas temperature of $T^{\mathrm{g}} \approx 8000$K. From these results it is obvious, that shock waves alone cannot be responsible for the observed winds of AGB stars. However, already [Wood 1979] introduced a parameterized step function in order to account for radiation pressure on dust in a very schematic way. This additional ingredient produced a considerable increase in the mass loss rate and a nearly unchanged terminal velocity. This schematic approach was also considered by [Bowen 1988], who found, that the combined effect of shock wave dissipation and radiation pressure on dust is in fact able to drive the observed massive, low velocity winds (cf. iii)).

ii) Radiation pressure

AGB stars are characterized by high luminosities. Therefore, radiative acceleration seems to be a good candidate for driving their outflows. A prerequisite for this mechanism of course is an effective momentum coupling between the radiation field and the atmospheric material. In hot stars, which emit an appreciable fraction of their radiation in the form of energetic photons in the UV regime of the spectrum, this coupling is provided by absorption of radiative momentum in strong UV lines of highly ionized atoms (e.g. C IV, O V, N VI, cf. [Pauldrach and Puls 1990] and [Puls and Pauldrach 1990]). Due to the Doppler shift of the outwards accelerated gas elements, photon momentum from a rather broad spectral region is accessible to each of these lines. Cool stars, however, emit their radiation mainly in the less energetic infrared spectral region. In this case the coupling may be provided either by broad molecular absorption bands or by continuous absorption of dust.

The effects of **radiation pressure on molecules** has been investigated e.g. by [Gustafsson and Plez 1992] for M–stars and by [Jørgensen and Johnson 1992] for M and C–stars. The results indicate, that the absorption of photon momentum by molecules may significantly levitate the atmosphere for both types of stars, but this mechanism alone does not suffice to drive a massive wind. The relevant molecules were identified to be H_2O in the case of M–stars and HCN, C_2H_2 and C_3 in the case of carbon stars. Although radiation pressure on molecules alone cannot account for the outflow, this mechanism nevertheless, may play an important role for wind generation as it considerably reduces the effective gravitational acceleration in the atmosphere (and, thus, the force needed to lift the material out of the gravitational field). Furthermore, it induces high densities at low temperatures which favour effective dust condensation.

The suggestion, that **radiation pressure on dust grains** alone might be sufficient for driving the outflow ([Wickramasinghe *et al.* 1966]) has been supported by both, empirical and theoretical evidence. If radiation pressure on dust grains causes the outflow, then the momentum flux of the radiation field should be related to the momentum flux of the outflowing material. Observations indicate, that in many dust–forming shells the ratio between the momentum flux of the material and the momentum flux of the radiation field is of the order of unity ([Jura 1986a]) and proportional to the UV optical depth of the dust component in the circumstellar shell ([Knapp 1986]). This result confirms, that radiation pressure on dust grains at least accelerates the wind to its terminal velocity. On the theoretical side, detailed calculations of the hydrodynamic structure of stationary circumstellar dust shells have been performed by several authors (e.g. [Salpeter 1974]; [Lucy 1976]; [Menietti and Fix 1978]; [Tielens 1983]; [Berruyer and Frisch 1983]; [Kozasa *et al.* 1984]; [Gail and Sedlmayr 1985]; [Gail and Sedlmayr 1987b]). Each of these works emphasizes different aspects of dust forming winds. The common conclusion is, that radiation pressure on dust alone is in fact capable of driving an outflow exhibiting the observed high mass loss rates and low terminal velocities. This mechanism requires a minimum mass loss rate of the star, which implies a minimum luminosity (cf. [Gail and Sedlmayr 1987c] and [Dominik *et al.* 1990]). Therefore, dust driven winds are only possible during the late phases of AGB evolution. The selfconsistent approach of [Gail and Sedlmayr 1987b] is a breakthrough in the modelling of stationary dust driven winds. This paper shows that the solution of the wind problem is completely determined by the specification of the four fundamental stellar parameters: *stellar mass* $M_\star$, *stellar luminosity* $L_\star$ *stellar temperature* $T_\star$ and initial element abundances $\epsilon_{\rm i}$. The complete structure of the circumstellar shell, in particular the mass loss rate is a result of the selfconsistent calculation.

iii) Shock waves and radiation pressure on dust

The observations indicate, that most dust enshrouded AGB stars are LPVs or Miras [Jura 1986b], [Habing 1990]. Therefore, a two–step mechanism has been proposed as being responsible for the mass loss of LPVs ([Jones *et al.* 1981]): i) levitation of the atmosphere by dissipation of shock waves, and ii) subsequent acceleration of the material by radiation pressure on dust grains.
In order to explain the observed mass loss rates ($\dot{M} \geq 10^{-7} M_\odot {\rm yr}^{-1}$) of AGB stars, [Wood 1979] has introduced a parameterized expression to account for the effects of dust acceleration. This approach has been improved by [Bowen 1988] with regard to the hydrodynamic calculations. However, in both cases the process of dust formation has not been considered in detail and, thus, important couplings between the dust complex and the atmospheric structure have not been taken into account. A major improvement has been achieved by the work of [Fleischer *et al.* 1991], [Fleischer *et al.* 1992] and [Fleischer 1994]. In these calculations, the coupled system describing time–dependent hydrodynamics, thermodynamics, chemistry, and dust formation, growth and

evaporation is solved simultaneously. The detailed treatment of the dust complex and of the interaction between dust and the atmospheric structure leads to surprising new dynamic effects, which decisively influence both the resulting shell structure (cf. [Fleischer 1994]), as well as the optical appearance of these models (cf. [Winters *et al.* 1993] and Chap. 5 of this thesis).

1.4 Aim and structure of this work

It is the aim of this work to provide a reliable basis for the quantitative interpretation of the observations obtained from mass loosing AGB objects by means of selfconsistent physical models.

Two approaches are presented, which both focus on the **atmospheres** of dust enshrouded AGB stars. The first approach is devoted to the description of stationary, purely dust driven winds, the second comprises a time–dependent description of the dynamic effects caused by the radial pulsations of LPV stars.

In order to specify a particular model, only the fundamental parameters of the central star – stellar mass $M_\star$, stellar luminosity $L_\star$, stellar temperature $T_\star$ and the element composition ϵ_i – are prescribed. In the time–dependent description, two additional parameters are necessary to account for the interior pulsation of the star.

Both types of calculation include a realistic description of the coupling among the dust component and the hydrodynamic and thermodynamic structure of the shell and thus provide for the first time realistic infrared spectra of the dust shell models. As the structure of the models is completely determined by the fundamental stellar parameters, the comparison between the calculated spectra and observed spectra of individual objects allows the determination of the stellar parameters of these objects. Since the luminosity is a physical parameter in the calculations, which decisively influences the model structure, and is not only a scaling factor, the distance to the objects can also be derived from comparing the fluxes of calculated and observed spectra. From the resulting brightness distributions, the spatial structure of the models is also comparable to the corresponding observations, which allows a further test of the theoretical models.

The main objective of this comparison between theory and observations is to obtain a thorough understanding of both, the individual objects and the general properties of the important class of AGB stars. This task can only be achieved in terms of a comprehensive and reliable theoretical description of the complete system under consideration.

This aim shall be approached by the work presented in this thesis, which is organized in the following way:

Chapter 2 gives an overview of the physical problem that describes a dust forming circumstellar shell. The ingredients necessary for a consistent modelling of such systems are summarized and their mutual interrelations are considered.

Chapter 3 comprises the basic equations constituting the coupled system, which needs to be solved. Special emphasis is placed on the description of the thermodynamic complex, i.e. on the determination of the transport coefficients and the solution of the radiative transfer problem. In the last section of this chapter, the range of parameter values appropriate for the description of AGB stars is addressed.

Chapter 4 deals with selfconsistent models of stationary dust driven winds. The internal structure of one typical model is discussed in detail. The parameters of this "standard" model have been chosen to emphasize the effects of dust formation, rather than to describe a real object. Based on this calculation, the dependence of internal structure and optical appearance of the dust shell on the basic parameters is discussed. Following this explorative investigation, a comparison between theory and observation is presented in the frame of infrared two colour diagrams. This comparison demonstrates, that stationary, spherically symmetric models of dust driven winds are appropriate to describe the characteristic far infrared (FIR) appearance of the CDS around C-rich AGB stars. Especially from the near infrared (NIR) flux ratios, specific conclusions on the stationary modelling approach are drawn. Finally, a model for IRC +10216, the prototype of extreme carbon stars, is discussed. This chapter ends with a summary of the conclusions regarding the stationary modelling approach.

Chapter 5 is concerned with directly observable implications resulting from the time–dependent description of dust forming atmospheres around LPVs. After a short description of the radial structure of the CDS (investigated in detail by [Fleischer 1994]), the synthetic lightcurves of three different models are presented. A comparison with respective observations reveals, that some hitherto not well understood features, which are present in the observed lightcurves can well be explained by the model calculation in terms of periodic dust formation. As a first step towards a spectral modelling, the temporal variation of the NIR flux ratios is discussed in the following section. Subsequently, calculated radial brightness distributions and visibilities are presented and compared to the corresponding observations. It turns out, that the dynamic behaviour of the dust component leads to a rippled or even step–like structure of both, the radial intensity profiles and the synthetic visibility functions. Very similar structures are present in observed brightness distributions and visibilities, which again can be interpreted as an effect of periodic dust formation.

Chapter 6 summarizes the main conclusions of this thesis and highlights some aspects for future investigation, directly arising from the basis provided by the work presented herein.

The

Appendix contains some remarks on the problems regarding the determination of the stellar temperature and the stellar radius of a star, which is surrounded by an extended circumstellar shell.

Nichts ereignet sich von selbst, sondern alles geschieht aus einem sinnvollen Grund und unter dem Druck der Notwendigkeit.

Leukippos, ca. 450 v. Chr.

Chapter 2

The problem of a dust forming stellar atmosphere

Already the modelling of a classical (dust free, hydrostatic and plane–parallel) stellar atmosphere involves the simultaneous solution of a coupled equation system, which describes the hydrodynamic, thermodynamic, and chemical structure to which the atmosphere adjusts. The additional consideration of the formation of solid particles in a star's atmosphere implies a considerable further increase in the complexity of the problem to be solved:

First of all, a physical description of the phase transition from the gas phase to the solid state is required for those chemical species, which possess a stable solid phase under the circumstellar conditions. Once solid particles have formed in the circumstellar environment, they cause immense repercussions on the structure of the dust forming atmosphere itself. Thus, the occurrence of dust in the system leads to a strong, nonlinear coupling among the different physical subsystems and, therefore, decisively influences the local and global structure of the circumstellar shell.

The physical problem of a dust forming atmosphere surrounding a late–type star is depicted in Fig. 2.1. It consists of the coupled system of hydrodynamics, thermodynamics, chemistry and dust formation and growth.

Favoured by the decreasing temperature, an increasingly complex chemistry develops with increasing distance from the star, leading from the atomic ions present in the innermost regions of the photosphere, via the first (most stable) diatomic molecules, up to rather large polyatomic aggregates present in the outer shell region. The solution of the chemical equations (which, in principle, also include the equations for the internal level–population and the ionisation ratios) yields the particle densities of all species considered and, in particular, the concentrations of the dust forming atoms and molecules. The densities of the chemical species, together with the respective extinction and absorption cross sections, determine the transport coefficients $\chi_\nu^{\rm g}$ (extinction coefficient) and $\kappa_\nu^{\rm g}$ (absorption coefficient) of the *gas* phase, which govern the transport of radiation through the molecular gas.

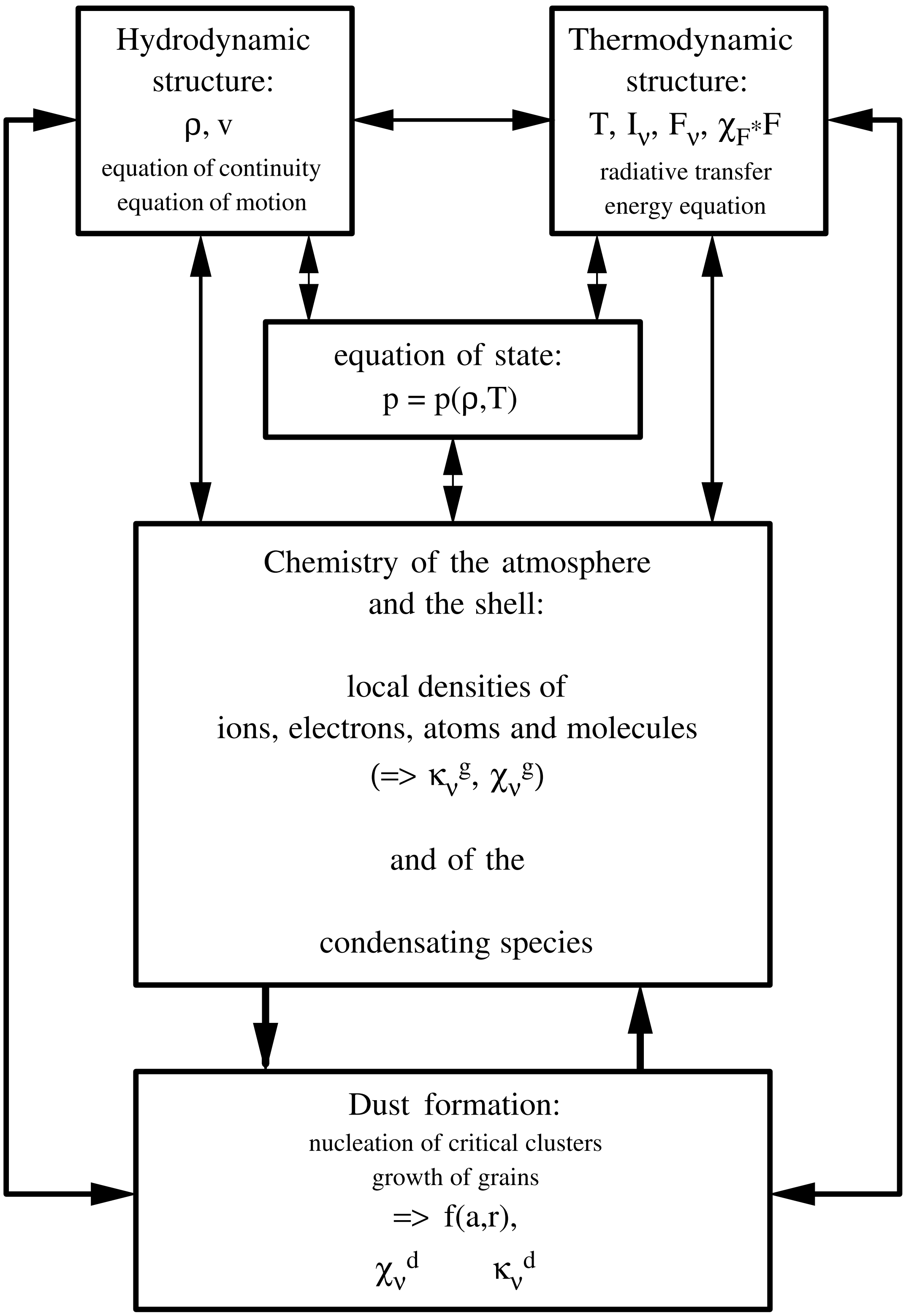

Figure 2.1: The physical problem of a dust forming stellar atmosphere (adopted with changes from [Sedlmayr and Winters 1991])

The condensating species, i.e. those molecules, which possess a stable solid phase under the local circumstellar conditions, will form clusters of critical size, which subsequently grow to macroscopic solid particles (dust grains). By consumption of the condensating molecules, the process of dust formation and growth couples back to the chemical structure of the gas phase. Moreover, the dust grains may adsorb atoms or molecules from the gas and thereby could act as catalysts for chemical surface reactions, which would not occur in the gas phase (e.g. the formation of H_2, which needs a three–body collision).

A detailed calculation of the process of dust formation and growth provides the chemical composition as well as the size distribution function $f(a, r)$ of the dust particles at every site throughout the atmosphere. Both, chemical composition and size distribution determine the extinction and absorption coefficients χ_ν^{d} and κ_ν^{d} of the *dust* component. Due to the huge cross section of macroscopic particles for absorption and scattering especially of short wavelength photons, the dust grains effectively interact with the radiation field. Since the dust opacity is by orders of magnitude larger than the opacity of the gas, dust, once it is present, controls the hydrodynamic structure as well as the energy balance of the atmosphere:

- By absorbing and scattering the short wavelength photons of the stellar radiation field, the dust grains gain the photon momentum, which subsequently is effectively transferred to the ambient gas by collisional coupling of the grains to the molecules. Therefore, the dust component strongly couples to the hydrodynamic equations by causing a considerable radiative acceleration of the atmospheric material.

- By thermalizing the energy of the absorbed short wavelength photons within their internal degrees of freedom, the dust grains transfer the photon energy to infrared radiation, which can escape from the circumstellar shell. Therefore, the dust grains effectively cool the system and, thus, couple to the thermodynamic equations. This process, furthermore, causes the infrared excess which is characteristic for the spectra of these objects. Due to their large opacity, the dust grains decouple thermodynamically from the gas and adopt an internal lattice temperature, which differs from the kinetic temperature of the gas. If the grains absorb photons with an efficiency proportional to some positive power of the photon energy (this is the case e.g. for carbon grains), the lattice temperature will be higher than the corresponding blackbody temperature. This internal heating of the grains is known as the *greenhouse effect.*

The thermodynamic structure of the system is determined by the transport of the stellar radiation through the dust shell. A detailed treatment of the radiative transfer problem yields the intensity distribution $I_\nu(r, \mu)$ of the radiation field throughout the atmosphere and, of course, the observable spectrum F_ν of the dust shell. The energy transfer processes between radiation field and matter, together with the constraint of conservation of the total energy, determine the resulting temperature stratification $T(r)$ of the circumstellar shell. The temperature, in turn, strongly couples back to the effectivity of grain formation, since the nucleation rate is an extremely steep function of T. The radiation intensity, via possible photo–reactions, also acts back on the chemical structure of the shell. Apart from this, the collision rates between the reacting species depend on their kinetic temperature.

The total local force density exerted on the atmospheric material by the radiation field is given by the frequency integral over the product of the local radiative flux and the extinction coefficient of the material. In those atmospheric regions, where dust is present, this term dominates in the equation of motion. Thus, the problem of radiative transfer is strongly coupled to the hydrodynamic equations.

From the equation of mass conservation and the equation of motion, the hydrodynamic structure (i.e. the density and velocity stratification) of the circumstellar shell is determined. The resulting hydrodynamic and thermodynamic structure in turn provide the conditions, under which the molecular composition of the gas is established and, therefore, determine the densities of the nucleating species. Additionally, the velocity field directly controls dust growth by limiting the time available for the grains to grow under favourable conditions.

By consumption of the dust-forming species, dilution of the surrounding gas by generating an outflow, and by thermal heating, the dust changes its surroundings and, thus, regulates the conditions of its own formation. The process of dust formation in a circumstellar environment, therefore, is an extremely fine-tuned self-regulating process.

The consistent solution of this problem is completely determined if four fundamental stellar parameters (e.g. *stellar mass* M_*, *stellar luminosity* L_*, *stellar temperature* T_*, and the initial *element abundances* ϵ_i) are specified.

In the case of a pulsating object (Mira or LPV), as long as only the stellar photosphere and the circumstellar shell are considered, two additional parameters have to be introduced to account for the star's interior pulsation. These are the pulsation period P and the velocity amplitude Δu_P at the base of the photosphere (cf. Sects. 3.6 and 5.2).

For an extended circumstellar shell, which may be optically thick, it is still an ambiguous problem to define a meaningful stellar temperature (cf. [Baschek *et al.* 1991]). In the stationary case, however, the solution of the equation of mass conservation requires the prescription of the mass loss rate $\dot{M}$ as an integration constant. From this physical situation, it is natural to consider the *mass loss rate* as a fundamental parameter instead of the stellar temperature. In this case, the stellar temperature (and the stellar radius) can be obtained from the result of the model calculation (cf. Appendix A).

For the time–dependent models of LPV atmospheres, which are discussed in Chap. 5, the stellar temperature is considered as a model parameter. In these models, the (in principle time–dependent) mass loss rate is a result of the model calculation.

Die Kontrolle durch das Experiment ist natürlich die triviale Voraussetzung für die Richtigkeit einer Theorie. Aber man kann ja nie alles nachprüfen. Daher interessiert mich das, was Sie über die Einfachheit gesagt haben, noch mehr. Aber ich würde nie behaupten wollen, daß ich wirklich verstanden hätte, was es mit der Einfachheit der Naturgesetze auf sich hat.

Albert Einstein, zitiert nach Werner Heisenberg: Der Teil und das Ganze

Chapter 3

Basic equations

The selfconsistent modelling of a dust forming circumstellar envelope requires the simultaneous solution of the coupled system of basic equations sketched in Fig. 2.1. In order to arrive at a numerically manageable equation system, we assume **spherical symmetry** of the central star and its circumstellar envelope. This assumption seems to be observationally justified at least for the outer regions of the circumstellar shells around AGB stars, but may become questionable in the very inner shell regions (e.g. [Cohen 1990]). As in these inner regions, due to the relatively high temperatures close to the star, mainly short wavelength radiation is involved, possible asymmetries manifest itself in the near infrared spectral region, influencing the observed energy distribution as well as the spatial brightness distribution (cf. [Efstathiou and Rowan-Robinson 1990] and [McCarthy *et al.* 1980], [Ridgway and Keady 1988]).

In principle, there exist two different types of aspherical structures, which are caused by two basically different physical mechanisms. The first type is the more or less symmetric elliptical or disc–like structure, which is observed mainly for stars at the very end of their AGB evolution. Several mechanisms could be responsible for causing this kind of deviation from spherical symmetry, e.g rotation of the central star, magnetic fields, the companion in a binary system, ..., which all would lead to a flattened or even disc–like structure of the circumstellar shell and could also cause a bipolar geometry of the outflows, as is observed during the transition of the progenitor star to the planetary nebula stage (e.g. [Habing *et al.* 1989] and [Balick 1989]). However, no consistent treatment of such an asymmetric system is at hand by now. A few attempts have been made to model the observed near infrared characteristics of non spherically symmetric shells, which are based on parameterized axisymmetric models (e.g. [Lefèvre *et al.* 1983], [Efstathiou and Rowan-Robinson 1990]). These calculations however, do not include a reliable treatment of the involved physical mechanisms and, therefore, do not allow a real quantitative interpretation of these observations. On the other hand, based on a simple analytical model, [Jura 1983b] demonstrates, that important global quantities (such as the derived mass loss rate or the dissociation radii of the molecules) are not much affected by the assumption of an aspherical outflow as compared to a spherical model.

A quite different reason for producing an inhomogeneous shell structure in the case of a dusty outflow is provided by the process of dust formation itself: As the nucleation rate is an extremely steep function of the temperature, even modest temperature fluctuations can cause sudden dust formation within a well confined spatial region. This would lead to a clumpy (or cloudy) dust distribution, again especially in the inner parts of the shell, as is observed in some objects (e.g. [Olofsson *et al.* 1992]). The overall shell structure of these objects, as mapped in the CO rotation lines, however, seems to be spherically symmetric to a high degree (cf. [Olofsson *et al.* 1992]). This conclusion also holds for the majority of the oxygen rich OH/IR stars, which were found from observations of the 1612 MHz OH maser line to give the overall impression of spherical symmetry ([Habing *et al.* 1989]).

3.1 Hydrodynamics

The density and velocity structure of the circumstellar outflow are determined by the principal physical laws of **mass conservation** and **momentum conservation**, respectively. Throughout this work a *compressible ideal fluid*, i.e. a nonviscous, nonconducting gas is considered. For the hydrodynamics of this gas, we adopt a continuum description of the actual multicomponent system consisting of a variety of gaseous chemical species and of macroscopic solid particles. We assume complete momentum coupling between the dust grains and the surrounding gas molecules.
The assumption of complete momentum coupling between gas and dust component is always justified in the regime of substantial mass loss ($\dot{M} \geq 10^{-8} M_{\odot}\mathrm{yr}^{-1}$), which is considered in this work. In a thorough investigation [Krüger *et al.* 1994] show, that in this case the dust grains always move with their (size–dependent) equilibrium drift velocity (which is of the order of the isothermal sound speed) relative to the gas. Thus, although the grains are not position coupled to the gas, they are in fact completely momentum coupled to the gas.
With the assumption of spherical symmetry, and neglecting the (small) equilibrium drift velocity of the grains, the law of mass conservation provides the equation of continuity

$$\frac{\partial \rho}{\partial t} + \frac{1}{r^2}\frac{\partial}{\partial r}\left(r^2 \rho v\right) = 0\,, \tag{3.1}$$

where ρ is the total mass density, t is the time, r the radial coordinate, and v is the flow velocity.
For stationary situations, which are considered in Chapter 4, the time derivative in Eq. (3.1) vanishes, and the equation of continuity can readily be integrated to yield

$$4\pi r^2 \rho v = \dot{M} \tag{3.2}$$

where the mass loss rate $\dot{M}$ has to be specified as integration constant. In Chap. 4, the mass loss rate is considered as one of the fundamental model parameters.

From the law of momentum conservation, the equation of motion in spherical symmetry is given by

$$\frac{\partial v}{\partial t} + v\frac{\partial v}{\partial r} = \frac{1}{\rho}f - \frac{1}{\rho}\frac{\partial p}{\partial r}\,. \tag{3.3}$$

In Eq. (3.3), f denotes the sum of the *external* forces acting on a volume element and p is the (internal) gas pressure.
In the work presented here we are concerned with circumstellar outflows, which are accelerated by radiation pressure on dust grains. Therefore, the external forces considered here are the inward directed gravitation force of the central star and the outward directed radiation force, which yields

$$\frac{\partial v}{\partial t} + v\frac{\partial v}{\partial r} = \frac{1}{\rho}\left(-\rho\frac{GM_r}{r^2} + \frac{4\pi}{c}\int_0^\infty \chi_\nu H_\nu d\nu\right) - \frac{1}{\rho}\frac{\partial p}{\partial r}\ , \tag{3.4}$$

where G is the gravitation constant and c the speed of light.
The gravitational acceleration of a mass element located at radial position r is due to the mass M_r enclosed by the spherical surface of radius r:

$$M_r = \int_0^r 4\pi r'^2 \rho(r')dr' = M_\star + \int_{R_\star}^r 4\pi r'^2\rho(r')dr'\,. \tag{3.5}$$

The current mass of the star $M_\star$ has to be prescribed as a model parameter.
The radiation force $f_{\rm rad}$ is proportional to the frequency integrated product of the total monochromatic extinction coefficient χ_ν of the material (cf. Sects. 3.2.1 and 3.2.3) and the monochromatic Eddington flux H_ν of the radiation field (cf. Sect. 3.2.4):

$$f_{\rm rad} = \frac{4\pi}{c}\int_0^\infty \chi_\nu H_\nu d\nu = \frac{4\pi}{c}\chi_H H\ , \tag{3.6}$$

where the flux–mean extinction coefficient χ_H is defined by

$$\chi_H = \frac{\int_0^\infty \chi_\nu H_\nu d\nu}{\int_0^\infty H_\nu d\nu} = \frac{\int_0^\infty \chi_\nu H_\nu d\nu}{H}\ . \tag{3.7}$$

Usually, the radiative acceleration is expressed in units of the local gravitational deceleration

$$\alpha = \frac{r^2}{GM_r}\frac{4\pi}{c}\frac{\chi_H}{\rho}H\ , \tag{3.8}$$

and the equation of motion is given by

$$\frac{\partial v}{\partial t} + v\frac{\partial v}{\partial r} = -\frac{GM_r}{r^2}(1-\alpha) - \frac{1}{\rho}\frac{\partial p}{\partial r}\ . \tag{3.9}$$

Conservation of the radiation energy in case of a spherical atmosphere implies

$$H = \frac{L_\star}{16\pi^2 r^2} \quad . \tag{3.10}$$

In this situation of *radiative equilibrium*, Eq. (3.8) reduces to

$$\alpha = \frac{\chi_H}{\rho} \frac{L_\star}{4\pi c G M_r} \quad , \tag{3.11}$$

In order to fix the energy flux which is transported through the atmosphere, the stellar luminosity $L_\star$ has to be prescribed as a model parameter.

In the case of a **stationary wind** (where the time derivative vanishes) it is useful to introduce the isothermal sound velocity

$$c_T^2 = \frac{p}{\rho} \tag{3.12}$$

and to rewrite Eq. (3.9) in the form of the so called *wind equation* (Eq. (3.2) is used to eliminate ρ)

$$\left(\frac{v^2 - c_T^2}{v}\right) \frac{\partial v}{\partial r} = -\frac{GM_r}{r^2}(1-\alpha) + \frac{2c_T^2}{r} - \frac{\partial c_T^2}{\partial r} \tag{3.13}$$

which reveals the existence of a critical point of the differential equation at $r = r_c$ which is fixed by the condition $v(r_c) = c_T(r_c)$. This point is henceforth called the sonic point. For a dust driven wind, the velocity of sound as well as its radial variation are small compared to the first term on the r.h.s. of Eq. (3.13). Therefore, the radiative acceleration at the sonic point has to be large enough in order to yield

$$\alpha \approx 1 \tag{3.14}$$

at the sonic point, i.e. to be able to drive the wind.

3.2 Thermodynamics

Regarding the thermodynamic structure of the dust envelope, a multi–component system consisting of molecular gas and solid dust particles is considered. The molecules, thermodynamically treated as one component, are assumed to be thermal emitters, characterized by the local gas–kinetic temperature $T^{\rm g}(r)$. The dust grains are assumed to be spherical particles obeying the local size distribution $f(a,r)$ where a denotes the grain radius. Each grain is assumed to be a thermal emitter, radiating according to its (size–dependent) internal lattice temperature $T^{\rm d}(a,r)$.

3.2.1 Transport coefficients of the grains

The transport coefficients of the dust grains contained in the size interval $(a, a+da)$ are defined by

$$\begin{aligned} \chi_\nu^{\mathrm{d}}(a,r)da &= \pi a^2 Q^{\mathrm{ext}}(\nu,a) f(a,r)da && (3.15)\\ \kappa_\nu^{\mathrm{sca,d}}(a,r)da &= \pi a^2 Q^{\mathrm{sca}}(\nu,a) f(a,r)da && (3.16)\\ \kappa_\nu^{\mathrm{abs,d}}(a,r)da &= \chi_\nu^{\mathrm{d}}(a,r)da - \kappa_\nu^{\mathrm{sca,d}}(a,r)da && (3.17) \end{aligned}$$

where $\chi_\nu^{\mathrm{d}}(a,r)da$ denotes the extinction coefficient, $\kappa_\nu^{\mathrm{sca,d}}(a,r)da$ the scattering coefficient and $\kappa_\nu^{\mathrm{abs,d}}(a,r)da$ the absorption coefficient of dust grains having radii in the interval $(a, a+da)$. In writing Eq. (3.16) we assume isotropic, conservative (often also called coherent) scattering of radiation by the dust grains. The extinction and scattering efficiencies $Q^{\mathrm{ext}}(\nu,a)$ and $Q^{\mathrm{sca}}(\nu,a)$ of a grain of radius a are calculated from Mie theory assuming homogeneous spherical particles with given complex refractive index of the grain material (cf. Sect. 3.2.2).
As the grains are assumed to be thermal emitters, the radiation energy emitted by dust grains in the size interval $(a, a+da)$ is determined by

$$\epsilon_\nu^{\mathrm{d}}(a,r)da = \pi a^2 Q^{\mathrm{abs}}(\nu,a) B_\nu(T^{\mathrm{d}}(a,r)) f(a,r)da \qquad (3.18)$$

where B_ν is the Kirchhoff–Planck function. The absorption efficiency $Q^{\mathrm{abs}}(\nu,a)$ follows from

$$Q^{\mathrm{abs}}(\nu,a) = Q^{\mathrm{ext}}(\nu,a) - Q^{\mathrm{sca}}(\nu,a) \qquad (3.19)$$

(cf. [Bohren and Huffman 1983]).

In order to apply Mie theory, the above equations (3.15) ...(3.18) have to be restricted to macroscopic particles, i.e. to grain sizes $a > a_\ell$, where a_ℓ is a lower limit size of the grains. The value of a_ℓ is chosen in the order of $10^{-3}\mu$m which corresponds to a minimum number of $\approx 10^2 \ldots 10^3$ atoms contained in the smallest dust grains. The required transport coefficients of an ensemble of particles consisting of the same material follow from the respective efficiencies by integrating the contributions of the individual size intervals over the range $a_\ell \leq a < \infty$:

$$\begin{aligned} \chi_\nu^{\mathrm{d}}(r) &= \int_{a_\ell}^{\infty} \chi_\nu^{\mathrm{d}}(a,r)da && (3.20)\\ \kappa_\nu^{\mathrm{sca,d}}(r) &= \int_{a_\ell}^{\infty} \kappa_\nu^{\mathrm{sca,d}}(a,r)da && (3.21)\\ \kappa_\nu^{\mathrm{abs,d}}(r) &= \int_{a_\ell}^{\infty} \kappa_\nu^{\mathrm{abs,d}}(a,r)da && (3.22)\\ \epsilon_\nu^{\mathrm{d}}(r) &= \int_{a_\ell}^{\infty} \epsilon_\nu^{\mathrm{d}}(a,r)da \ . && (3.23) \end{aligned}$$

If several grain components are present their individual contributions have to be added up to the total extinction and scattering coefficient.

Since the size distribution function of the particles is a result of the process of dust formation and growth, which depends sensitively on the hydrodynamic and thermodynamic conditions in the dust forming medium, the determination of $f(a,r)$ itself requires the knowledge of the local transport coefficients. Therefore, the realistic calculation of the extinction properties of the grains involves the simultaneous solution of the complete set of equations describing the physical conditions in the dust forming medium (cf. Sect. 2).

In order to avoid this difficult problem, up to now only some approximate expressions of the dust extinction properties have been discussed in the literature. The most common assumption is that of a unique particle radius a_u (i.e. $f(a)da \rightarrow n^d \delta(a-a_u)$ with n^d being the (prescribed) particle density of the dust grains and $\delta(x)$ is the Dirac function). At large wavelengths ($\lambda \gg 2\pi a$) the *small particle limit* of Mie theory yields:

$$Q^{\rm ext}_{\rm small}(\lambda, x) = -4x{\rm Im}\left\{\frac{m(\lambda)^2-1}{m(\lambda)^2+2}\right\} \tag{3.24}$$

$$Q^{\rm sca}_{\rm small}(\lambda, x) = \frac{8}{3}x^4{\rm Re}\left\{\frac{m(\lambda)^2-1}{m(\lambda)^2+2}\right\}^2 ,\ x = \frac{2\pi a}{\lambda} \ll 1 \tag{3.25}$$

while at short wavelengths the *large particle limit* holds:

$$Q^{\rm ext}_{\rm large}(\lambda, x) \rightarrow 2 \tag{3.26}$$

$$Q^{\rm sca}_{\rm large}(\lambda, x) \rightarrow 1,\ x = \frac{2\pi a}{\lambda} \gg 1\ . \tag{3.27}$$

In most previous work on radiative transfer in dust shells either the small particle limit is used over the whole wavelength region (e.g. [Lucy 1976]; [Rose 1987]), or the two limiting cases are fitted together at some fixed value of x (for example $x = 1/2$, see [Rowan-Robinson 1980], [Rowan-Robinson and Harris 1983]. The efficiencies resulting from this "fitting" procedure are then used for radiative transfer calculations in a parameterized model of the CDS. The influence of the "fitting" procedure on the spectral appearance of the dust shells can be seen from the model spectra presented in [Rowan-Robinson and Harris 1983]. Since they assume a constant particle radius of $a_u = 0.1\mu$m, the wavelength at which x equals $1/2$ is fixed to a value $\lambda \approx 1.3\mu$m. At this wavelength the wavelength-dependence of $Q(\lambda)$ switches from a $1/\lambda$-law to a constant value with respect to λ. In the spectra this "switch over" in $Q(\lambda)$ results in a pronounced non-monotonic course of the emergent flux at approximately 1.3μm. An improved treatment of grain extinction is presented by [Martin and Rogers 1987], who also prescribe a unique particle radius and the particle density structure, but perform detailed Mie-calculations for the wavelength dependence of the efficiencies including explicitly the effects of the wavelength dependence of the complex refractive index. This approach results in a satisfactory fit to the observed spectrum of IRC+10216.

The aim of all these radiative transfer calculations is to fix the set of parameters used to describe the shell structure by modelling the observed energy distributions of several individual sources. Typically, these models are characterized by the effective temperature $T_{\rm eff}$ and the bolometric flux $L_\star/R_\star^2$ of the central star, the dust condensation temperature T_c, a power law dust density structure $n^{\rm d} = n_0 x^{-\beta}$, an optical depth τ and the geometrical extension $r_{\rm max}/r_c$ of the dust shell. The physical mechanisms, which produce the dust shells are not considered in these calculations.

Another approach to investigate the structure of circumstellar dust shells is followed in a series of papers by our group. In these calculations the dust complex is treated in detail by applying the moment method ([Gail *et al.* 1984]; [Gail and Sedlmayr 1988]; [Gauger *et al.* 1990]). Selfconsistent models of circumstellar dust shells have been calculated ([Gail and Sedlmayr 1987b]; [Fleischer *et al.* 1992]) by solving the coupled set of equations describing chemistry, hydrodynamics, radiative transfer and dust formation and growth. In these models, the radiative transfer problem is treated in the grey Eddington approximation for spherical symmetry ([Lucy 1971], [Lucy 1976]). The transport coefficients of the dust component which enter into the equation of motion and the energy equation, are calculated from the small particle limit of Mie theory. This approach does not provide the optical appearance of the dust shells, but it avoids the ad–hoc prescription of a parameterized dust shell structure.

From the radial profile of the mean grain radius, which is provided by the moment equations, it was already clear from the results of [Gail and Sedlmayr 1987b], that at least in the innermost region of a stationary dust envelope the particles are rather large and, therefore, the assumption of small particles is not valid in a dust driven wind model. [Dominik *et al.* 1989] present a method, which allows for the calculation of the grain size distribution function at every site throughout the dust shell once the model equations are solved. The size distribution functions discussed in their paper are the result of model calculations, where the coupling between dust component and hydrodynamic and thermodynamic structure is treated in the small particle limit. However, large particles are in fact present in a stationary dust driven wind (especially in the innermost region where dust formation starts) and, thus, the assumption of small particles is not justified (cf. Sect. 4.4.2).

3.2.2 Optical properties of the grains

The extinction and scattering efficiencies ($Q^{\rm ext}(\lambda, a)$ and $Q^{\rm sca}(\lambda, a)$) at wavelength λ of spherical particles having radius a are provided by Mie theory if the complex refractive index $m(\lambda)$ of the grain material is given (eg. [Bohren and Huffman 1983]).

For the calculation of the transport coefficients of the dust component we, therefore, need to know the wavelength–dependent complex refractive index of the grains formed in the stellar wind. In this work we consider pure carbon grains, i.e. we do not attempt to model the dust features present in the spectra of C-stars (e.g. SiC, [Treffers and Cohen 1974] or metal oxides, e.g. MgS, [Goebel and Moseley 1985]).

The optical constants of the grains however, do not only depend on the dust material but also on the microscopic structure of the particles. In case of an ordered (crystalline) structure one finds a $1/\lambda^2$ - dependence of the FIR extinction, while a disordered (amorphous) structure exhibits a $1/\lambda$ - dependence (e.g. [Wirsich 1987]). In the case of carbon dust, both structures, *amorphous carbon* and crystalline *graphite* are possible.

The actual structure of the grains formed in the wind is not known a priori. Recent spectral modelling (e.g. [Jura 1983a], [Jura 1986a]; [Sopka *et al.* 1985]; [Martin and Rogers 1987]; [Rose 1987]; [LeBertre 1987]; [Griffin 1990]; [Orofino *et al.* 1990]) implies the presence of amorphous grains rather than graphite in the circumstellar shells around C-stars. This is consistent with physical considerations, predicting the formation of inhomogeneous grains with crystalline cores surrounded by amorphous mantles ([Gail and Sedlmayr 1984]), as only the mantles interact with the radiation field.

In the case of amorphous grains there exist several sets of data in the literature which are obtained from laboratory measurements. However, the exact structure of the grains produced in the laboratory and, therefore, the values of the extinction efficiency depend rather sensitively on the experimental details (cf. [Bussoletti *et al.* 1987]; [Maron 1990]).

For the calculations presented in this work, the optical properties tabulated in [Maron 1990], which describe amorphous carbon grains, have been adopted.

3.2.3 Transport coefficients of the gas

Whereas the transport coefficients of the dust grains are treated in some detail in this thesis, the gas opacity is represented only by its Rosseland–mean absorption coefficient. Thus, light scattering by the molecules is neglected and the frequency dependence of the gas opacity is not explicitly taken into account.

The total extinction coefficient χ_ν resulting from the gas and the dust component together

$$\chi_\nu(r) = \chi_\nu^{\mathrm{g}}(r) + \chi_\nu^{\mathrm{d}}(r) = \kappa_\nu^{\mathrm{abs,g}}(r) + \kappa_\nu^{\mathrm{sca,g}}(r) + \chi_\nu^{\mathrm{d}}(r) \tag{3.28}$$

is replaced by

$$\chi_\nu(r) = \kappa_{\mathrm{R}}^{\mathrm{abs,g}}(r) + \chi_\nu^{\mathrm{d}}(r) \tag{3.29}$$

in the present calculations. $\kappa_{\mathrm{R}}^{\mathrm{abs,g}}$ is the Rosseland–mean absorption coefficient of the gas.

3.2.4 Radiative transfer

In this section the equations and the iterative scheme used in the present work for the solution of the radiative transfer problem in a two component medium are summarized. Basically, we solve the second order form of the radiative transfer equations in radial and tangential direction as discussed in [Mihalas and Hummer 1974] but with some alterations concerning the source function, outer boundary conditions and the iterative scheme.

In its general form, the radiative transfer equation is given by

$$\frac{1}{c}\frac{\partial I_\nu(\mathbf{r},\mathbf{n},t)}{\partial t} + \frac{\partial I_\nu(\mathbf{r},\mathbf{n},t)}{\partial s} = \eta_\nu(\mathbf{r},\mathbf{n},t) - \chi_\nu(\mathbf{r},\mathbf{n},t) I_\nu(\mathbf{r},\mathbf{n},t) \ . \tag{3.30}$$

$I_\nu(\mathbf{r},\mathbf{n},t)$ is the monochromatic specific intensity of radiation within the frequency interval $(\nu, \nu + d\nu)$ at position $\mathbf{r}$ in direction $\mathbf{n}$ and η_ν is the emissivity within the frequency interval $(\nu, \nu + d\nu)$, respectively.

The time derivative in Eq. (3.30) becomes important, if the transport coefficients vary on a timescale comparable to (or even shorter than) the time needed for the photons to cross the region where these changes occur. Thus, the time derivative has to be maintained if e.g.

$$\frac{|\Delta r|}{c} \geq \frac{\chi}{|\dot{\chi}|} \ . \tag{3.31}$$

The pulsating atmospheres discussed in Chap. 5, where a nonstationary treatment of radiative transfer might become important, are characterized by the sudden formation of discrete dust layers. Typically, the formation of a new dust layer takes about 10% of the pulsation period (which is of the order of 1yr). Within this time interval, the extinction coefficient typically varies between $\approx 10^{-15}\mathrm{cm}^{-1}$ and $\approx 10^{-13}\mathrm{cm}^{-1}$, which gives a timescale of

$$\frac{\chi}{|\dot{\chi}|} \approx 2.6 \cdot 10^4 \mathrm{s} \ . \tag{3.32}$$

The spatial region, within which these changes occur is typically of the order of one stellar radius, i.e. some 10^{13}cm. Thus, the light travel time through this region is

$$\frac{|\Delta r|}{c} \approx 10^3 \mathrm{s} \ . \tag{3.33}$$

Since this is short compared to the time during which relevant changes occur in the transport coefficients, the **stationary transfer equation** is considered throughout the present work.

In the case of spherical symmetry, the path differential ds is expressed in terms of a displacement of the radial coordinate dr and a change of the angle θ between the direction of photon propagation $\mathbf{n}$ and the radial direction $\mathbf{r}$. As only $\sin\theta$ and $\cos\theta$ are involved in this transformation, it is convenient to define a new angle variable $\mu := \cos\theta$.

Assuming a two component material (molecular gas and solid dust particles) which absorbs and scatters isotropically, the stationary, spherically symmetric radiative transfer equation is given by:

$$
\begin{aligned}
\mu \frac{\partial I_\nu(\mu, r)}{\partial r} + \frac{1-\mu^2}{r} \frac{\partial I_\nu(\mu, r)}{\partial \mu} &= \\
&- (\kappa_\nu^{\mathrm{abs,g}} + \kappa_\nu^{\mathrm{abs,d}} + \kappa_\nu^{\mathrm{sca,g}} + \kappa_\nu^{\mathrm{sca,d}}) I_\nu(\mu, r) \\
&+ (\kappa_\nu^{\mathrm{sca,g}} + \kappa_\nu^{\mathrm{sca,d}}) J_\nu(r) \\
&+ \kappa_\nu^{\mathrm{abs,g}} B_\nu(T^{\mathrm{g}}(r)) + \epsilon_\nu^{\mathrm{d}}(r)
\end{aligned}
\tag{3.34}
$$

The superscripts g and d refer to the gas and the dust component, respectively and $J_\nu(r)$ is the monochromatic mean intensity (see below).

The so called Eddington moments of the specific monochromatic intensity are defined by:

$$M_\nu^i := \frac{1}{2} \int_{-1}^{1} \mu^i I_\nu \, d\mu \quad . \tag{3.35}$$

Usually, the *zeroth*, *first* and *second* moment are denoted by J_ν (monochromatic mean intensity), H_ν (monochromatic Eddington flux) and K_ν (monochromatic Eddington pressure), respectively. These moments are connected with the physical quantities

monochromatic energy density of the radiation field

$$E_\nu = \frac{4\pi}{c} J_\nu \tag{3.36}$$

monochromatic energy flux

$$F_\nu = 4\pi H_\nu \tag{3.37}$$

and

monochromatic radiation pressure

$$P_\nu = \frac{4\pi}{c} K_\nu \quad . \tag{3.38}$$

3.2.4.1 Solution of the radiative transfer equation

Even in the simple case of local thermal equilibrium (LTE) (where the transport coefficients are determined solely by the local conditions), the scattering term in Eq. (3.34) introduces a nonlocal coupling of the specific intensity to the state of the material at (in principle) any other point in the atmosphere. The scattering of photons makes the transport equation Eq. (3.34) to a partial *integro* differential equation. For its solution, an iterative scheme, which involves the angular moments of the radiative transfer equation is applied.

Moment equations With the definitions of the total extinction coefficient χ_ν (cf. Eq. 3.28),
the monochromatic source function

$$S_\nu = \frac{1}{\chi_\nu}\left\{\left(\kappa_\nu^{\rm sca,g} + \kappa_\nu^{\rm sca,d}\right) J_\nu + \kappa_\nu^{\rm abs,g} B_\nu(T^{\rm g}) + \epsilon_\nu^{\rm d}\right\} \quad , \tag{3.39}$$

the variable Eddington factor

$$f_\nu(r) = \frac{K_\nu(r)}{J_\nu(r)} = \frac{\int_{-1}^{1} \mu^2 I_\nu(\mu, r) d\mu}{\int_{-1}^{1} I_\nu(\mu, r) d\mu} \quad , \tag{3.40}$$

the sphericality function

$$\ln(r^2 q_\nu) = \int_{r_c}^{r} \frac{3f_\nu - 1}{r' f_\nu} dr' + \ln(r_c^2), \tag{3.41}$$

$$(r_c : \text{radius at the inner boundary}) \tag{3.42}$$

and the depth scale

$$dX_\nu = -q_\nu \chi_\nu dr \quad , \tag{3.43}$$

the first two moment equations of Eq. (3.34) (with respect to μ) are combined to (cf. [Mihalas and Hummer 1974]):

$$\frac{\partial^2}{\partial X_\nu^2}(f_\nu q_\nu r^2 J_\nu) = \frac{r^2}{q_\nu}(J_\nu - S_\nu). \tag{3.44}$$

The Eddington flux H_ν is given by

$$\frac{\partial}{\partial X_\nu}(f_\nu q_\nu r^2 J_\nu) = r^2 H_\nu \quad . \tag{3.45}$$

Boundary conditions In order to allow for the inclusion of an external radiation field at the outer boundary $r = r_{\rm max}$, we introduce the quantity g_ν^+, defined by:

$$g_\nu^+ = \frac{H_\nu^+(r_{max})}{J_\nu^+(r_{max})} = \frac{\int_0^1 \mu I_\nu(+\mu, r_{max}) d\mu}{\int_0^1 I_\nu(+\mu, r_{max}) d\mu}. \tag{3.46}$$

With the decompositions

$$\begin{aligned} H_\nu(r) &= H_\nu^+(r) - H_\nu^-(r) \\ &= \frac{1}{2}\int_0^1 \mu I_\nu(+\mu, r) d\mu - \frac{1}{2}\int_0^1 \mu I_\nu(-\mu, r) d\mu \end{aligned} \tag{3.47}$$

and

$$\begin{aligned} J_\nu(r) &= J_\nu^+(r) + J_\nu^-(r) \\ &= \frac{1}{2}\int_0^1 I_\nu(+\mu, r) d\mu + \frac{1}{2}\int_0^1 I_\nu(-\mu, r) d\mu \quad , \end{aligned} \tag{3.48}$$

the outer boundary condition of Eq. (3.44) is determined by

$$\begin{aligned}\frac{\partial}{\partial X_\nu}(f_\nu q_\nu r^2 J_\nu)|_{r_{max}} &= r_{max}^2[g_\nu^+ \\ &\quad \left(J_\nu(r_{max}) - J_\nu^-(r_{max})\right) \\ &- H_\nu^-(r_{max})] \ , \qquad (3.49)\end{aligned}$$

where the first two moments of the prescribed outer radiation field occur explicitly.

At the inner boundary $r = r_c$ we apply the diffusion approximation in a form which ensures that the correct total flux is transported through the innermost radius shell

$$\frac{\partial}{\partial X_\nu}(f_\nu q_\nu r^2 J_\nu)|_{r_c} = \frac{r_c^2}{\chi_\nu}\frac{\partial B_\nu}{\partial T}\frac{H_c}{\int_0^\infty \frac{1}{\chi_\nu}\frac{\partial B_\nu}{\partial T} d\nu} \ . \qquad (3.50)$$

The flux transported through the inner boundary is given by

$$H_c = \frac{L_*}{16\pi^2 r_c^2} \qquad (3.51)$$

The solution of Eqs. (3.44), (3.49) and (3.50) requires knowledge of the Eddington factor $f_\nu(r)$ and of the boundary factor g_ν^+. These values are computed from the formal solution of the radiative transfer equation in (p, z)-coordinates (cf. [Mihalas and Hummer 1974]).

Ray equations Along each ray with constant impact parameter p (These are the characteristic paths of the partial differential equation Eq. (3.34)), we solve the second order differential equation (S_ν assumed to be given)

$$\frac{\partial^2 j_\nu}{\partial \tau_\nu^2}|_{p=\text{const}} = (j_\nu - S_\nu)|_{p=\text{const}} \ , \qquad (3.52)$$

where the intensity–like variable j_ν is defined by

$$j_\nu = \frac{1}{2}(I_\nu^+ + I_\nu^-) \qquad (3.53)$$

and the tangential optical depth τ_ν results from the differential equation

$$d\tau_\nu = -\chi_\nu dz, \ \tau(z \to \infty) = 0. \qquad (3.54)$$

The half–range intensities I_ν^+ and I_ν^- describe the radiation propagating in the direction of $+z$ and $-z$, respectively.

Boundary conditions At the outer boundary we have

$$\frac{\partial j_\nu}{\partial \tau_\nu}|_{z=z_{max}} = j_\nu - I_\nu^-|_{z=z_{max}} \tag{3.55}$$

where I_ν^- is the prescribed specific intensity of the external radiation field.

The inner boundary condition for the ray equations is provided either by

$$\frac{\partial j_\nu}{\partial \tau_\nu}|_{z=0} = 0 \tag{3.56}$$

if $z = 0$ ($p \geq r_c$)

or by

$$\frac{\partial j_\nu}{\partial \tau_\nu}|_{z=z_{min}} = \mu \frac{3}{\chi_\nu} \frac{\partial B_\nu}{\partial T} \frac{H_c}{\int_0^\infty \frac{1}{\chi_\nu} \frac{\partial B_\nu}{\partial T} d\nu}|_{z=z_{min}} \tag{3.57}$$

if $z = z_{min} \neq 0$ ($p < r_c$).

Iterative solution Once $j_\nu(p,z)$ is known from the solution of Eq. (3.52), $I_\nu(+\mu, r_{max})$ is given by

$$\begin{aligned} I_\nu(+\mu, r_{max}) &= I_\nu^+(\mu(p, z_{max}), r_{max}) \\ &= 2j_\nu(p, z_{max}) - I_\nu^-(\mu, r_{max}) \ . \end{aligned} \tag{3.58}$$

The values of $f_\nu(r)$ and g_ν^+, required for solving the moment equations are computed from Eq. (3.40) and Eq. (3.46), respectively with the intensities resulting from the ray equations inserted.

In order to calculate the radiation field, an iteration is performed between the second order moment equation (3.44) (S_ν from Eq. (3.39) inserted) and the set of ray equations (3.52) (together with the appropriate boundary conditions). The iteration is stopped once J_ν has converged. Subsequently, the flux is computed from Eq. (3.45). The iteration is started with $f_\nu(r) \equiv \frac{1}{3}$ and $g_\nu^+ \equiv \frac{1}{2}$.

3.2.5 Temperature stratification

For calculating the temperature structure of the dust envelope, we consider energy transport by radiation only. Due to the low densities (less than $10^{-10}\mathrm{g\,cm^{-3}}$), convective energy transport is inefficient and, thus, is neglected in the circumstellar shell. In the work presented here, we do not consider any energy release in the atmosphere due to dissipation of waves (the LPV models, presented in Chap. 5 are calculated in the isothermal limit case, i.e. instantaneous cooling of the postshock gas is assumed). Thus, the energy exchange can only occur by radiative gain and loss processes and by collisions between particles, which are characterized by different temperatures. For calculating the gas temperature only the Rosseland–mean absorption coefficients of the gas phase have been available. Thus, the gas phase is thermodynamically treated as one component, described by a single LTE temperature. Grain–grain collisions can be neglected due to the low particle density of the dust grains ($n^{\rm d} < 1{\rm cm}^{-3}$). Grain–gas collisions do not affect the temperature of the grain (cf. Appendix D in [Gauger *et al.* 1990]) but could be important for the gas temperature. However, the net energy gain or loss of the gas by this process critically depends on the coupling of the gas to the radiation field. As this coupling cannot be correctly described by the Rosseland–mean opacities, we do not consider this process here. (For a detailed discussion of this point see [Krüger *et al.* 1994].) Therefore, the energy gain and loss processes considered here are absorption and thermal emission of radiation by the gas in grey approximation and frequency–dependent absorption and thermal emission by the dust grains. Hence, we assume radiative equilibrium for the gas component and the dust grains separately. Under this assumption the gas temperature is fixed by

$$\int_0^\infty \kappa_\nu^{\rm abs,g}(r)\,(B_\nu(T^{\rm g}) - J_\nu(r)) = 0 \tag{3.59}$$

i.e.

$$T^{\rm g}(r) = \left[\frac{\pi}{\sigma}\frac{\kappa_{\rm J}^{\rm g}(r)}{\kappa_{\rm P}^{\rm g}(r)} J(r)\right]^{1/4} \tag{3.60}$$

where

$$\kappa_J^{\rm g} = \frac{\int_0^\infty \kappa_\nu^{\rm abs,g} J_\nu d\nu}{\int_0^\infty J_\nu d\nu} = \frac{\int_0^\infty \kappa_\nu^{\rm abs,g} J_\nu d\nu}{J} \tag{3.61}$$

denotes the absorption–mean and

$$\kappa_P^{\rm g} = \frac{\int_0^\infty \kappa_\nu^{\rm abs,g} B_\nu(T^{\rm g}) d\nu}{\int_0^\infty B_\nu(T^{\rm g}) d\nu} = \frac{\int_0^\infty \kappa_\nu^{\rm abs,g} B_\nu(T^{\rm g}) d\nu}{B(T^{\rm g})} \tag{3.62}$$

the Planck-mean absorption coefficient of the gas, respectively, J is the frequency integrated mean intensity of the radiation field and σ the Stefan–Boltzmann constant. With the present approximate treatment of the gas opacity, which means that

$$\kappa_{\rm J}^{\rm abs,g}(r) = \kappa_{\rm P}^{\rm abs,g}(r) = \kappa_{\rm R}^{\rm abs,g}(r)\ , \tag{3.63}$$

Eq. (3.60) reduces to

$$T^{\rm g}(r) = \left[\frac{\pi}{\sigma} J(r)\right]^{1/4}\ . \tag{3.64}$$

Assuming radiative equilibrium for each grain size a

$$\int_0^\infty Q_\nu^{\rm abs,d}(a)\left(B_\nu(T^{\rm d}(a,r)) - J_\nu(r)\right) = 0\ , \tag{3.65}$$

the temperature of the grains is given by

$$T^{\mathrm{d}}(a,r) = \left[\frac{\pi}{\sigma}\frac{Q_{\mathrm{J}}^{\mathrm{abs}}(a)}{Q_{\mathrm{P}}^{\mathrm{abs}}(a)}J(r)\right]^{1/4} \quad . \tag{3.66}$$

$Q_{\mathrm{J}}^{\mathrm{abs}}(a)$ and $Q_{\mathrm{P}}^{\mathrm{abs}}(a)$ are the absorption-mean and Planck-mean values of the absorption efficiency of the dust particles, respectively. In case of a size independent dust temperature, Eq. (3.66) transforms to

$$T^{\mathrm{d}}(r) = \left[\frac{\pi}{\sigma}\frac{\kappa_{\mathrm{J}}^{\mathrm{abs,d}}(r)}{\kappa_{\mathrm{P}}^{\mathrm{abs,d}}(r)}J(r)\right]^{1/4} \quad . \tag{3.67}$$

For the numerical determination of the temperature stratification the Unsöld–Lucy procedure, modified for spherical geometry is applied.

3.2.5.1 Temperature correction procedure

As the temperature determination is a nonlinear problem, an iterative procedure is applied. Starting from a first guess of the temperature structure, an improved stratification results from

$$T^{\mathrm{g,d}} = \left(T'^{\mathrm{g,d}^4} + \frac{\pi}{\sigma}\Delta B^{\mathrm{g,d}}\right)^{1/4} \tag{3.68}$$

In Eq. (3.68) and in the following, ($'$) denotes the current values of the respective quantities. $\Delta B^{\mathrm{g,d}}$ is given by

$$\begin{aligned}
\Delta B^{\mathrm{g,d}} &= B(T^{\mathrm{g,d}}) - B(T'^{\mathrm{g,d}}) \\
&= \frac{1}{fqr^2}\frac{\kappa_J^{\mathrm{g,d}}}{\kappa_B^{\mathrm{g,d}}} \cdot \\
&\quad \left[\int_0^{\tau_H} qr^2\Delta H dt + f(0)q(0)r^2(0)\Delta J(0)\right] \\
&+ \frac{\kappa_J^{\mathrm{g,d}}}{\kappa_B^{\mathrm{g,d}}}J' - B'^{\mathrm{g,d}}
\end{aligned} \tag{3.69}$$

where B, J, H, f and q denote the frequency integrated values and $\kappa_J^{\mathrm{g,d}}$, $\kappa_B^{\mathrm{g,d}}$ are the absorption-mean and Planck-mean values of the appropriate absorption coefficient, respectively. τ_H is the flux-mean optical depth measured inward in radial direction. In Eq. (3.69), the flux deviation is calculated from

$$\Delta H = H - H' = \frac{L_*}{16\pi^2 r^2} - H' \tag{3.70}$$

and $\Delta J(0)$ is determined by the assumption

$$\frac{\Delta J(0)}{J'(0)} = \frac{\Delta H(0)}{H'(0)} \quad . \tag{3.71}$$

A similar method for the temperature correction is described in [Wolfire and Cassinelli 1986] who calculate the temperature structure of different grain sizes in accretion flows onto massive protostars.

For the dynamic calculations of Chap. 5, the transport coefficients of the dust grains are described by the small particle limit of Mie theory in grey approximation. In this case, also the dust temperature is given by Eq. (3.64). In these models, the mean intensity J is calculated from a two–stream approximation for the spherical case ([Lucy 1971], [Lucy 1976]), i.e. no temperature correction is performed.

3.3 Equation of state

The gas pressure is determined from the equation of state which in the diluted gas of the circumstellar envelope is given by the ideal gas law

$$p = \frac{\rho}{\mu m_\mathrm{H}} k T^\mathrm{g} \quad . \tag{3.72}$$

The mean molecular weight μ is calculated from the dominant gaseous species H, $\mathrm{H_2}$ and He (k = Boltzmann constant and m_H = mass of a hydrogen atom)

$$\mu = \frac{n_\mathrm{H} + 2n_\mathrm{H_2} + 4n_\mathrm{He}}{n_\mathrm{H} + n_\mathrm{H_2} + n_\mathrm{He}} \quad . \tag{3.73}$$

The dust particles can safely be neglected in the equation of state, as their particle density is typically ten orders of magnitude smaller than the particle density of the gas.

3.4 Chemistry

In general, the chemical structure of a reacting gas is described by a system of rate equations, which represents the time evolution of the particle density n_i of each chemical species i. For the special case of spherical symmetry this system can be written as:

$$\frac{\partial n_i}{\partial t} + \frac{1}{r^2}\frac{\partial}{\partial r}(r^2 n_i v) = Q_i \,; \quad i = 1, \ldots, N \quad , \tag{3.74}$$

where N denotes the number of species considered. The source term Q_i is the net rate for the production of species i, including all gain and loss processes due to kinetic and photo processes.

The molecular composition of the gas is important for two aspects of the model calculation:

i) The chemical structure determines the gas opacity. In this work the opacity of the gas is described by the Rosseland-mean absorption coefficient, interpolated from tables given in the p-T plane. These opacity tables follow from chemical equilibrium calculations for C-rich compositions containing 95 species ([Scholz and Tsuji 1984]).

ii) The concentrations of the species which contribute to dust formation and growth have to be known. In a carbon–rich element mixture, these are essentially C, C_2, C_2H, C_2H_2, and C_3H, the densities of which are calculated from a reduced equilibrium chemistry including only 7 species (cf. [Dominik *et al.* 1990]).

In the special case of *chemical equilibrium*, the set of continuity equations Eq. (3.74) is replaced by the *law of mass action*, which provides the concentrations of each species i for the local values of kinetic temperature T and gas pressure p. Defining the partial pressure p_i of species i by

$$p_i = n_i kT \quad , \tag{3.75}$$

the law of mass action yields

$$p_i = \exp\left\{\frac{\Delta G_i}{kT}\right\} \prod_{j=1}^{J} p_j^{(\nu_{i,j})} \quad . \tag{3.76}$$

Here j denotes the elements, ΔG_i is the change of free energy for the formation of species i from the constituent atoms, and $\nu_{i,j}$ is the number of atoms of the element j contained in species i. This system is completed by the conservation of the particle number of atoms j, which can be expressed as

$$p_j = \epsilon_j \, n_{<\mathrm{H}>} \, kT = \sum_i \nu_{i,j} \, p_i \quad . \tag{3.77}$$

The assumption of chemical equilibrium is justified in all situations where the expansion velocity is small and ionizing photons (e.g. from a chromosphere or the interstellar radiation field) are absent ([Beck *et al.* 1992]). The observations indicate, that dust forming cool giants, which are considered in this thesis, generally do not possess chromospheres ([Jura 1986b]). Furthermore, interstellar UV photons cannot penetrate into the inner region of the dust shell ([Mamon *et al.* 1988]) and, thus, do not reach the region where the grains are formed. Photo–reactions, therefore, can be neglected in the dust formation region.

In a stationary dust driven wind the velocity field is only produced by radiation pressure on dust. In the region where effective dust formation and growth takes place, the velocity is small. Hence, dilution effects on the chemical time scales, which would cause deviations from the kinetic equilibrium, are negligible in the inner region of the shell and thus do not affect the concentrations of the dust forming species.

In case of the dynamic models presented in Chap. 5, the concentrations of the dust forming species in fact may be affected by departures from kinetic equilibrium. The adoption of chemical equilibrium also in these models, nevertheless, provides at least a reasonable first approximation for investigating the basic physical interactions among dust formation, hydrodynamics and radiation field.

For a quantitative interpretation of molecular lines, however, chemical non-equilibrium has to be considered in order to obtain reliable results e.g. for the column densities of these molecular species. In the present work molecular lines are not considered in detail. Therefore, the concentrations of the chemical species are calculated from the assumption of **chemical equilibrium** in the gas phase.
The initial element composition of the gas is in all cases assumed to be solar ([Allen 1973]) with the exception of the carbon abundance $\epsilon_{\rm C}$, which is considered as a parameter in order to account for a C-rich mixture.

3.5 Grain nucleation and growth

The condensation of solid particles out of the gaseous phase can be conceived as a two–step process:

- the formation of *critical* molecular clusters which, under the local thermodynamic conditions, are stable against dissociation and, thus, preferentially grow by addition of further molecules of the dust forming chemical species

and

- the growth of these clusters to macroscopic particles which, in a circumstellar environment, strongly interact with the stellar radiation field and, thus, become observable.

In the work presented here, the condensation of carbon grains is described by classical nucleation theory extended to heteromolecular, homogeneous growth of these particles ([Gail *et al.* 1984], [Gail and Sedlmayr 1988]). Starting from the master equation for the grain size distribution function $f(a,t)$, they derive an equation system that describes the time evolution of moments K_i of the grain size distribution function. As long as the dust grains remain small compared to the relevant wavelength of the stellar radiation field (typically $\lambda > 1\mu$m for the objects under consideration), the knowledge of the moments suffices to describe both, the dust component itself (number density of dust particles, mean particle radius, amount of condensed material, ...) as well as its interaction with the radiation field. Thus, if the transport coefficients of the dust component are accurately described by the *small particle limit* of Mie theory (i.e. if $2\pi a/\lambda \ll 1$) the moment method yields the complete information about the dust component necessary for the construction of consistent dust shell models (cf. [Gail and Sedlmayr 1987b]).

With the definition of the (i^{th}) moment K_i of the distribution function (assuming three–dimensional spherical dust particles)

$$a_0^i K_i = \int_{a_\ell}^{\infty} a^i f(a,t)\,da \tag{3.78}$$

the moment equations are given by

$$\frac{\partial K_0}{\partial t} + \frac{1}{r^2}\frac{\partial}{\partial r}(r^2 v K_0) = J_\star \tag{3.79}$$

$$\frac{\partial K_i}{\partial t} + \frac{1}{r^2}\frac{\partial}{\partial r}(r^2 v K_i) = \left(\frac{a_\ell}{a_0}\right)^i J_\star + \frac{i}{3}\frac{1}{\tau}K_{i-1} \quad , \quad i = 1, 2, 3, \ldots \tag{3.80}$$

where $J_\star$ is the rate of formation of critical clusters per unit volume and $1/\tau$ is the net time scale of particle growth. In the present work the nucleation rate is calculated according to the equations given in [Gail *et al.* 1984]. The growth time scale includes heteromolecular particle growth ([Gail and Sedlmayr 1988]) and, in case of the LPV models presented in Chap. 5 also the effects of thermal evaporation of the dust grains described by the formalism of ([Gauger *et al.* 1990]).

This treatment of the dust complex is appropriate to describe the formation of homogeneous grains, e.g. of amorphous carbon clusters in a C–rich element mixture. As the observations seem to be compatible with the emergence of the amorphous component, this description of the dust formation process should be justified at least for the spectral modelling of the dust shell. Classical nucleation theory, however, cannot describe the formation of large polyaromatic molecules which also might emerge from a circumstellar environment ([Keller and Sedlmayr 1983]; [Keller 1987]; [Cherchneff *et al.* 1992]; [Sedlmayr 1994]). Unfortunately, no quantitative description of the chemical pathway leading from rather simple molecules (e.g. C_2H_2) via aromatic rings (PAHs: polyaromatic hydrocarbon molecules) to macroscopic dust particles is at hand by now ([Sedlmayr 1994]). Therefore, at the present state the calculations are based on the concepts of classical nucleation theory.

For the reliable determination of the transport coefficients of the dust grains the local grain–size distribution function is required (cf. Eqs. (3.15) ...(3.17)). Since the distribution function is a result of the grain formation and growth process, which in turn depends critically on the hydrodynamic and thermodynamic conditions in the dust forming medium, which again are essentially determined by the local transport coefficients, the determination of $f(a,r)$ represents a highly nonlinear regulation problem. Thus, any reliable calculation of the dust extinction requires the simultaneous solution of the complete set of the basic equations describing the physical conditions in the dust forming medium (cf. Fig. 2.1). [Dominik *et al.* 1989] have developed a method which for dust forming circumstellar shells allows the calculation of the local size distribution function by an integration along the flow–characteristic once the model equations are solved. This method has been extended by [Gauger *et al.* 1990] for the application to nonstationary situations like Mira and LPV dust envelopes. We apply this method for calculating the particle size distribution function.

3.6 The range of parameters

For the stationary calculations presented in Chap. 4, the stellar mass $M_\star$, stellar luminosity $L_\star$, and the mass loss rate $\dot{M}$ have been chosen as basic parameters. For the calculation of the dust complex also the carbon abundance ϵ_C has to be specified in order to account for a carbon–rich mixture. All other elements are assumed to have solar abundances.

- **stellar mass** $M_\star$: The total mass M_tot of a star surrounded by a circumstellar shell is the sum of the mass of the central star $M_\star$ (i.e. the mass contained inside the photosphere) and the mass contained in the circumstellar shell M_CS. In this thesis cool C-giants are considered, which according to their evolution are believed to be AGB objects (e.g. [Jura 1991]). As these objects probably evolve into planetary nebulae with central star masses of $M_\star \geq 0.55 M_\odot$ ([Schönberner 1983]), the minimum value of $M_\star$ should be $0.55 M_\odot$. The total mass M_tot, on the other hand, cannot exceed the initial mass M_ZAMS of the progenitor star when it was located at the main sequence. According to [Barnbaum *et al.* 1991], the initial mass of carbon-rich AGB-stars may be as large as $4M_\odot$. The mass of a carbon-rich AGB-star, therefore, is approximately confined to the range $0.55M_\odot \leq M_\star < 4M_\odot$. Since purely dust driven winds are possible only during the final AGB phases, the objects under consideration already have lost a considerable fraction of their initial mass during their evolution to the top of the AGB. For this reason, the models presented here refer to the lower region of the possible mass range: $0.6M_\odot \leq M_\star \leq 1M_\odot$.

- **stellar luminosity** $L_\star$: Due to considerable uncertainties in the distance determination, the luminosities of AGB-stars are not known very accurately from the observations. Current estimates for the luminosities of these stars range from $2 \cdot 10^3 L_\odot$ to $5 \cdot 10^4 L_\odot$ (cf. [Veen and Rugers 1989] and references therein). In the case of a purely dust driven wind a minimum Eddington–luminosity is required for driving the outflow (cf. [Gail and Sedlmayr 1987a] and [Dominik *et al.* 1990]). For the range of stellar masses considered here, the required minimum luminosities are $L_\star \geq 2 \cdot 10^4 L_\odot$. Thus, the stationary models are calculated for $2 \cdot 10^4 L_\odot \leq L_\star \leq 5 \cdot 10^4 L_\odot$, whereas for the dynamic models luminosities between $1 \cdot 10^4 L_\odot$ and $3 \cdot 10^4 L_\odot$ are adopted.

- **mass loss rate** $\dot{M}$: The observations indicate that the mass loss rates for dust forming AGB stars range from $\approx 10^{-7} M_\odot \mathrm{yr}^{-1}$ to $10^{-4} M_\odot \mathrm{yr}^{-1}$ (cf. [Knapp and Morris 1985]). Accordingly, the adopted values for the mass loss rates of our models cover the range from $10^{-6} M_\odot \mathrm{yr}^{-1}$ to $10^{-4} M_\odot \mathrm{yr}^{-1}$.

- **carbon abundance** ϵ_C: In order to describe a carbon-rich element mixture values of $\epsilon_\mathrm{C}/\epsilon_\mathrm{O} > 1$ are chosen. Essentially three investigations exist in the literature, which are concerned with the determination of the C/O ratio in the photospheres of carbon-rich AGB-stars. [Lambert *et al.* 1986] determine rather low values of the C/O–ratio of $1 \leq \epsilon_C/\epsilon_O \leq 1.6$ where most of their objects have $\epsilon_C/\epsilon_O < 1.2$. [Gow 1977] on the other hand finds considerably higher values of $1 \leq \epsilon_C/\epsilon_O \leq 10$ with most of the objects from his sample having $1.3 \leq \epsilon_C/\epsilon_O \leq 4$. Finally, [Frantsman and Eglitis 1988] derive a mean value of $\langle \epsilon_C/\epsilon_O \rangle = 1.7$ from their analysis. As our model calculations indicate an almost linear correlation between the carbon to oxygen ratio and the terminal velocity of the wind ([Dominik *et al.* 1990]; [Fleischer *et al.* 1992]; [Fleischer 1994]; Sect. 4.5 of this thesis), high C/O ratios lead to terminal velocities, which are much higher than observed and thus are excluded from our calculations. The models presented here are calculated for $1.2 \leq \epsilon_C/\epsilon_O \leq 2$.

For the time–dependent models presented in Chap. 5 it is not possible to simply integrate the equation of continuity (Eq. (3.1)) by fixing the mass loss rate as an integration constant. In these models the classical set of parameters is chosen, i.e. the stellar temperature is considered as fundamental parameter instead of the mass loss rate. In the time–dependent models we do not perform a detailed radiative transfer calculation in order to obtain the temperature structure in these models, but rely on the Lucy approximation ([Lucy 1971], [Lucy 1976]) for fixing the temperature and, thus, the dynamic structure of the atmosphere. In this case, the solution of the equation system is subject to the consistency condition that the resulting temperature profile has to match the stellar temperature $T_\star$ at the location of the stellar radius $R_\star$ (which is fixed by the Stefan–Boltzmann law).
In addition, a temporal boundary condition has to be prescribed in order to simulate the pulsation of the central star. The usual method, which is also applied here, is the prescription of a sinusoidal temporal variation of the velocity at the inner boundary of the atmosphere characterized by a *period* P and a *velocity amplitude* Δu_P.

- **stellar temperature** $T_\star$: The effective temperatures of carbon giants, as derived by different methods typically range from $\approx$ 2400K to 3200K (e.g. [Tsuji 1981]), the values obtained by the different methods are in good agreement with each other. The models presented in Chap. 5 are calculated for stellar temperatures from the lower part of the observed range (2450K $\leq T_\star \leq$ 2600K).

- **pulsation period** P: The periods of Miras and LPVs (as derived from the observed lightcurves) range from $\approx$ 80d to $\approx$ 1000d. The carbon–rich objects (about 10% of all known LPVs) mostly have periods longer than $\approx$ 300d with a maximum by number at $P \approx$ 400d (cf. [Beyer 1965]). Recent observations (e.g. [LeBertre 1992]) show, that there exist C–rich LPVs with periods up to at least 750d. The models presented in Chap. 5 cover the interval 370 d $\leq P \leq$ 650 d.

- **velocity amplitude** Δu_P: The velocity amplitude at the inner boundary cannot be directly determined from observations. However, detailed model calculations indicate, that the resulting shell structure is almost independent of Δu_P as long as a lower limit value of typically $1\,\mathrm{kms}^{-1}$ is exceeded and as long as the amplitude remains smaller than an upper limit in the order of $10\,\mathrm{kms}^{-1}$ (cf. [Fleischer 1994]). The values adopted for the models presented in Chap. 5 are taken from the interval $2\,\mathrm{kms}^{-1} \leq \Delta u_P \leq 6\,\mathrm{kms}^{-1}$.

Freilich: der Glaube allein tut's nicht, er kann, wie die Geschichte einer jeden Wissenschaft lehrt, leicht auch einmal in die Irre führen und in Beschränktheit und Fanatismus ausarten. Um ein zuverlässiger Führer zu bleiben, muß er beständig an der Hand der Denkgesetze und der Erfahrung nachgeprüft werden, und dazu verhilft in letzter Linie nur gewissenhafte, oft mühsame und entsagungsvolle Einzelarbeit. [...] Gerade in solchem harten Ringen reift und läutert sich die Weltanschauung. Nur wer diesen Prozeß an seinem eigenen Leibe durchgekostet hat, wird dessen Sinn und Bedeutung voll zu würdigen wissen.

Max Planck

Chapter 4

Models of stationary dust driven winds

4.1 Introduction

Selfconsistent models of stationary dust driven winds around carbon–rich giant stars are presented.

In these models, *radiation pressure on dust grains* is the dominant force, which lifts the material out of the star's gravitational field and accelerates the wind to its terminal outflow velocity. In this case, the complete momentum of the material is gained from the radiation field, the coupling between matter and radiation being provided by the opacity of dust grains, which form in the circumstellar shell. As a consequence, the area of efficient dust formation in a dust driven wind always coincides with the region, where the wind develops and, thus, with the location of the sonic point. Due to the self–regulated interaction between dust formation and hydrodynamics (cf. Chap. 2), a dust driven wind represents a very stable mass loss mechanism. Therefore, the internal shell structure produced by a dust driven wind (velocity profile, temperature stratification, location and extension of the dust formation zone, ...) is almost independent of the precise values of the fundamental stellar parameters. Important observable quantities, as the terminal wind velocity, or the spectral energy distribution of the dust shell however, depend on the numerical values of the stellar parameters.

An inherent property of the stationary approach to describe a dust driven wind is of course, that the temporal evolution towards the wind solution cannot be considered. Thus, the models presented here demonstrate, that pure dust driving suffices to **maintain** an outflow. More mathematically speaking, the existence of these models means, that there exist physical solutions of the coupled system of the stationary differential equations within a certain range of the model parameters. The onset of the wind may proceed as follows: If somewhere in a hydrostatic atmosphere the conditions necessary for dust formation are met (i.e. low temperatures ($T \approx 1400$K) in a region with sufficiently high densities ($\rho \approx 10^{-14}\mathrm{gcm}^{-3}$)), dust will condense and, thereby, will provide the opacity necessary to couple the radiation momentum to the gas. The onset of dust formation, therefore, requires low effective temperatures and low surface gravities of the central star. If the star further provides a sufficiently high luminosity (i.e. sufficient momentum of the radiation field), the material in the condensation zone is effectively accelerated outwards. As no vacuum can be left behind, gas from the inner regions starts to flow into the condensation zone and continuously provides the necessary supply of condensable material. Therefore, once effective dust formation sets in, an outflow is generated, which maintains itself. This mechanism for starting a stable dust driven wind is recovered by the time–dependent calculations of [Fleischer 1994], who starts with an initially hydrostatic atmosphere and calculates the temporal evolution of the wind by solving the time–dependent model equations.

The investigation described in this chapter is an extension of the approach of [Gail and Sedlmayr 1987b], who constructed the first selfconsistent model of stationary dust driven winds. In their work, the resulting atmospheric structure is completely determined by the fundamental stellar parameters $M_\star$, $L_\star$, $T_\star$ and the element abundances ϵ_i. Despite their selfconsistency, the models presented in [Gail and Sedlmayr 1987b] suffer from severe restrictions:

- the radiative transfer is treated in a semi-analytical approximation ([Lucy 1971], [Lucy 1976]),
- the coupling among radiation field and hydrodynamic and thermodynamic structure of the shell is described in the small particle limit for the transport coefficients of the dust component,
- the transport coefficients of the gas and the dust are replaced by frequency integrated mean values,
- the temperature structure is calculated from the total opacity of gas and dust together, considered as a single component.

In the case of optically thick dust shells the Lucy approximation is not valid, which may lead to an incorrect determination of the radiation field and, therefore, of the temperature structure. The grey approximation does, of course, not provide the synthetic spectra of the dust shell models and, therefore, does not allow a comparison to observed spectra.

It is the aim of the work discussed in this chapter, to eliminate these shortcomings in order to arrive at a more realistic description which allows a reliable quantitative comparison to the observations. For this purpose it is necessary

- to solve the angle and frequency–dependent radiative transfer problem,

- to calculate realistic frequency–dependent transport coefficients by means of the size distribution function of the dust grains,

- to treat gas and dust as separate phases for calculating their individual temperature structures.

Due to the selfconsistent treatment, the model parameters are closely connected via the model equations and, thus, any other set of independent parameters, e.g. $M_\star$, $L_\star$, and mass loss rate $\dot{M}$ can be chosen. In this case the stellar temperature $T_\star$ is a result of the calculation. In the stationary approach it is convenient to select this set of model parameters, which avoids the ambiguous definition of a stellar temperature (cf. [Baschek *et al.* 1991]) and additionally can be advantageous for a more direct comparison to the observable quantities.

The improved models discussed here, yield a more realistic description of the coupling between the dust component and the hydrodynamic and thermodynamic structure of the shell and in particular provide for the first time realistic infrared spectra of the dust shell models.

After a summary of the assumptions made for the present calculations (Sect. 4.2) and a short description of the iteration scheme applied for calculating a stationary dust driven wind (Sect. 4.3), in Sect. 4.4 we present the typical structure of a 'standard' dust driven wind model, characterized by the parameters: stellar mass $M_\star = 0.7 M_\odot$, stellar luminosity $L_\star = 3 \cdot 10^4 L_\odot$, carbon–to–oxygen ratio $\epsilon_C/\epsilon_O = 1.40$ and mass loss rate $\dot{M} = 1 \cdot 10^{-4} M_\odot \mathrm{yr}^{-1}$. Based on this model, an exemplary discussion of the sensitivity of the resulting spectra, terminal velocities and stellar temperatures against variations of the model parameters is given in Sect. 4.5. This discussion is followed by a comparison of the resulting shell spectra of a grid of model calculations with photometric observations of C–rich AGB star shells (Sect. 4.6). Finally, a detailed model for the carbon rich AGB star IRC +10216 is presented in Sect. 4.8. This chapter ends with some conclusions concerning the stationary modelling approach.

4.2 Assumptions

Throughout this chapter, stationary purely dust driven winds are considered. This assumption excludes any effects of pulsation of the star such as levitation and heating of the atmosphere by dissipation of wave momentum and -energy. The forces considered in the equation of motion are the gradients of thermal- and radiation pressure and the gravitation force. Complete momentum coupling between gas molecules and dust grains is assumed. Thus, the grain–gas mixture is hydrodynamically treated as one component. (For a thorough discussion of a two–component treatment of hydrodynamics and energy balance in the case of a stationary dust driven wind see [Krüger *et al.* 1994].) Concerning the thermodynamic structure, a multicomponent description is adopted, which provides separate temperatures for the gas component and the different grain sizes.

4.3 Iterative solution of the problem

A consistent model of the dust shell is calculated by means of iteration between the equations describing the hydrodynamic and chemical (including dust) structure of the shell and the equations describing the radiative transfer, energy balance and radiation pressure on the dust grains. The whole iteration cycle is sketched in Fig. 4.1. The initial model for this iteration is computed essentially from the equation system discussed in [Dominik *et al.* 1990], which includes some slight modifications compared to the equations given in [Gail and Sedlmayr 1987b]. In this first model, the temperature structure of the dust shell is computed from the grey Eddington approximation for the spherical case ([Lucy 1971], [Lucy 1976]). The consistency requirement $T(R_*) = T_*$ yields a value for the stellar radius of the initial model which is further referred to as R_0. The problem of defining the stellar radius of the converged model is considered in Appendix A. The flux-mean extinction coefficient of the gas–grain mixture is replaced by the Rosseland-mean absorption coefficient of the mixture. For the construction of the first model the radiation pressure is calculated from the large particle approximation in the inner part of the dust shell and from the small particle approximation in the outer region (with an appropriate interpolation between this two limiting cases, cf. Sect. 4.4.2). This procedure turned out to be necessary in order to achieve convergence of the iteration. In the following iteration steps, the exact size distribution function of the dust particles is taken into account and the dust extinction is computed from Mie theory for arbitrary particle sizes.

The initial model provides a first guess of the complete atmospheric structure, including the size distribution function of the dust particles. From this radial stratification the dust opacity is calculated, and the radiative transfer problem is solved. By calculating the flux mean extinction coefficient, an improved stratification of the radiative acceleration is obtained. If it deviates from the previous guess, the atmospheric structure is recalculated with suitably improved values for the radiative acceleration and with the current temperature structure (both remain unchanged during the Newton–Raphson iteration within the “atmospheric structure block”).

This inner cycle is repeated until α (i.e. the radiative acceleration in units of the local gravitational deceleration) has converged. Then a check for flux-constancy is performed and, if necessary, an improved temperature stratification is determined, which is subsequently used for recalculating the atmospheric structure.

Radiative acceleration as well as the temperature stratification are updated by applying automatically adjusted damping factors to the corrections which ensure numerical stability of the iterative process. A typical model takes some 200 iteration cycles until both, radiative acceleration and temperature structure have converged.

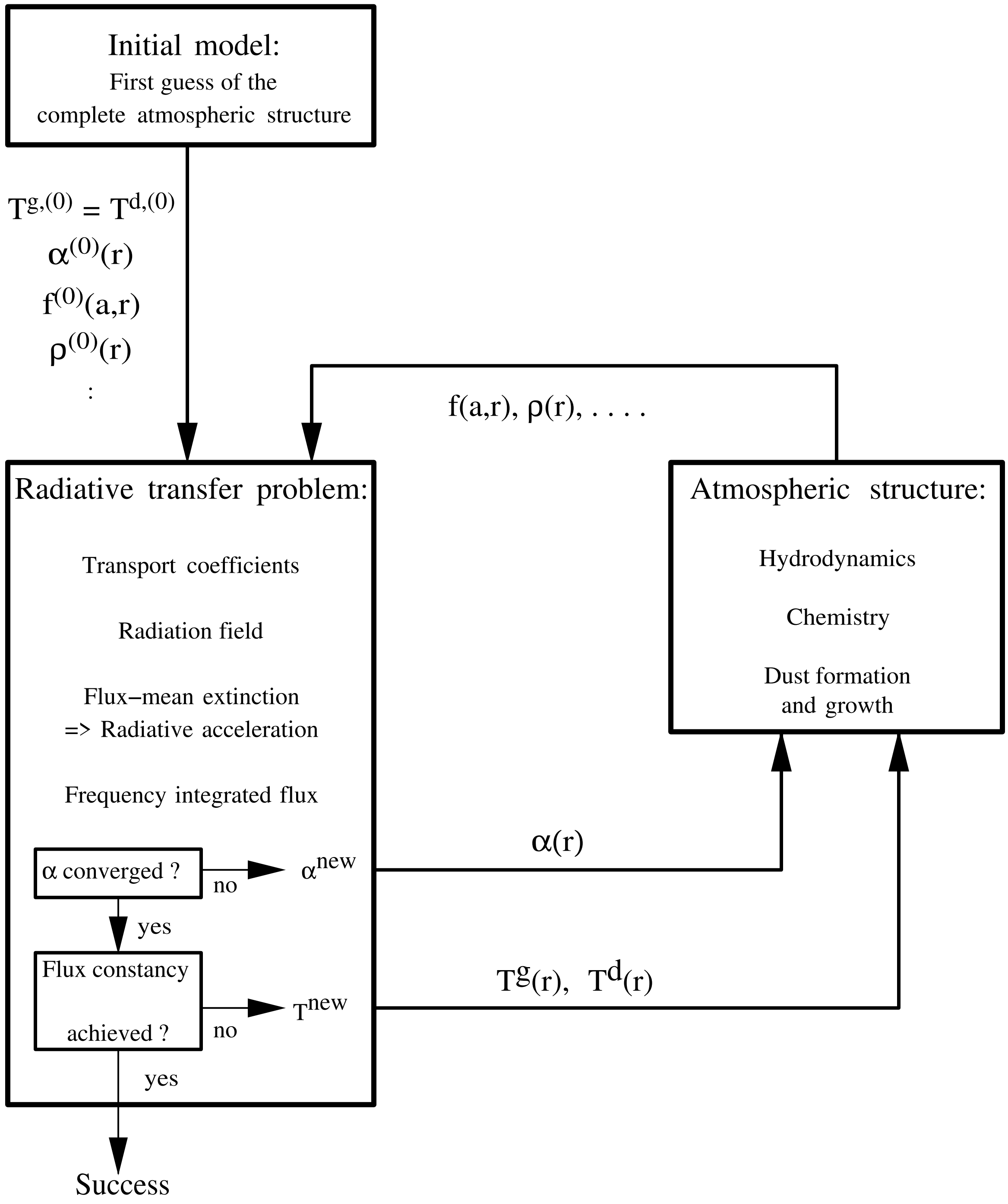

Figure 4.1: Sketch of the global iterative scheme

4.4 A typical dust driven wind model

4.4.1 Radial structure

For the discussion of the typical shell structure produced by a stationary dust driven wind, a model fixed by the parameters given in Tab. 4.1 is chosen.

The dust grains are assumed to consist of amorphous carbon, described by the optical properties tabulated in [Maron 1990].
Henceforth, this model is called the *standard model*.

Table 4.1: Stellar parameters of the standard dust driven wind model

stellar mass	$M_\star$	$0.7M_\odot$
stellar luminosity	$L_\star$	$3 \cdot 10^4 L_\odot$
carbon abundance	ϵ_C/ϵ_O	1.40
mass loss rate	$\dot{M}$	$1 \cdot 10^{-4} M_\odot \mathrm{yr}^{-1}$

The radial shell structure of the standard model is displayed in Fig. 4.2.
The formation of carbon grains starts around $2.0R_0$, i.e. relatively close to the stellar surface where the temperature is 1400K and the density is $1.3 \cdot 10^{-13}\mathrm{gcm}^{-3}$. As can be seen from the radial course of the nucleation rate J_* (upper diagram of Fig. 4.2), *effective grain condensation* takes place within a very narrow spatial region, extending from $\approx 2.0R_0$ to $\approx 3.9R_0$. The nucleation rate is sharply peaked at $2.8R_0$, with a maximum number of $3.4 \cdot 10^{-11}$ particles formed per second and cubic centimeter.

Accordingly, the number of dust grains per H–atom $n^{\mathrm{d}}/n_{<\mathrm{H}>}$ steeply increases within this spatial region. The final number of dust particles is already reached at $3.4R_0$, where the number of dust grains per H–atom is $5 \cdot 10^{-13}$.
The process of *grain growth*, though also concentrated in the inner region of the dust shell, extends over a much broader radial interval. From the degree of condensation f_c (cf. upper middle diagram of Fig. 4.2) it can be seen, that already in the very inner region of the dust shell ($r \approx 2R_0$) a measurable amount ($\approx 2\%$) of the condensable carbon is contained in dust grains. However, as the particle density of grains is only $4 \cdot 10^{-19}$ per H–atom in this region, these particles have to be extremely large. The degree of condensation then steeply increases due to massive dust formation and subsequent growth of these newly formed particles. At $5R_0$ the degree of condensation has already reached a value of 31% but the particles continue to grow until at $r = 40R_0$ the final degree of condensation of 42% is reached.
In the lower middle diagram of Fig. 4.2 the dynamic effect of dust formation is shown. The radiative acceleration of the atmospheric material increases steeply in the dust formation zone as can be seen from the course of the acceleration factor α.

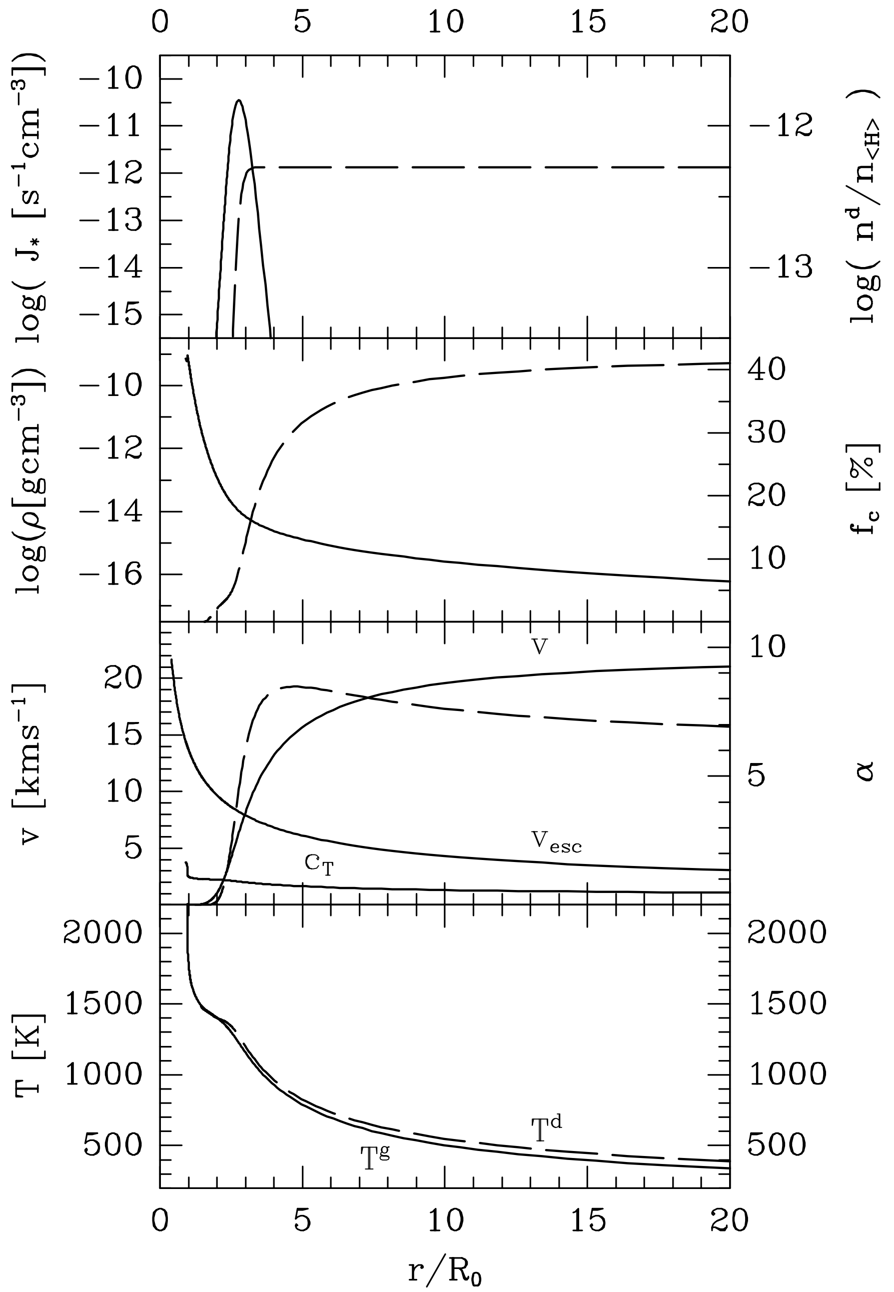

Figure 4.2: Radial structure of the standard dust shell model (cf. Tab. 4.1).
Upper diagram: logarithm of the nucleation rate J_* (solid line) and logarithm of the number of dust grains per H–atom $n^{\rm d}/n_{<\rm H>}$ (dashed line);
upper middle diagram: logarithm of the gas density ρ (solid line) and degree of condensation $f_{\rm c}$ (dashed line);
lower middle diagram: hydrodynamic velocity v, local escape velocity $v_{\rm esc}$ and velocity of sound c_T (solid lines), and radiative acceleration in units of the local gravitational deceleration α (dashed line);
lower diagram: gas temperature $T^{\rm g}$ (solid line) and size–independent dust temperature $T^{\rm d}$ (dashed line).

Initiated by the radiation pressure on dust, a velocity field develops, which exceeds the velocity of sound at $r = r_c = 2.2R_0$ and surmounts the local escape velocity at $r = 3.0R_0$. The expansion velocity further increases until the terminal wind velocity of $v_\infty = 22.2\,\mathrm{km s^{-1}}$ is reached at $r \approx 50R_0$.
Due to the blocking mainly of the short wavelength stellar radiation field by the dust grains, a backwarming of the material located inside the dust shell occurs. This backwarming effect can be seen from the temperature profile within the dust formation zone (lower diagram of Fig. 4.2). The energy balance between heating of the grains (by absorption of the short wavelength stellar photons) and radiative cooling (by thermal infrared emission) results in a grain temperature, which differs from the (grey) gas temperature. In the case of amorphous carbon grains, whose absorption efficiency is roughly proportional to the photon frequency, the grain temperature *exceeds* the gas temperature, i.e. the carbon grains exhibit a *greenhouse* effect. In this standard model, the size–independent dust temperature T^{d} (cf. Eq. (3.67)) exceeds the gas temperature T^{g} by ≈ 55K.

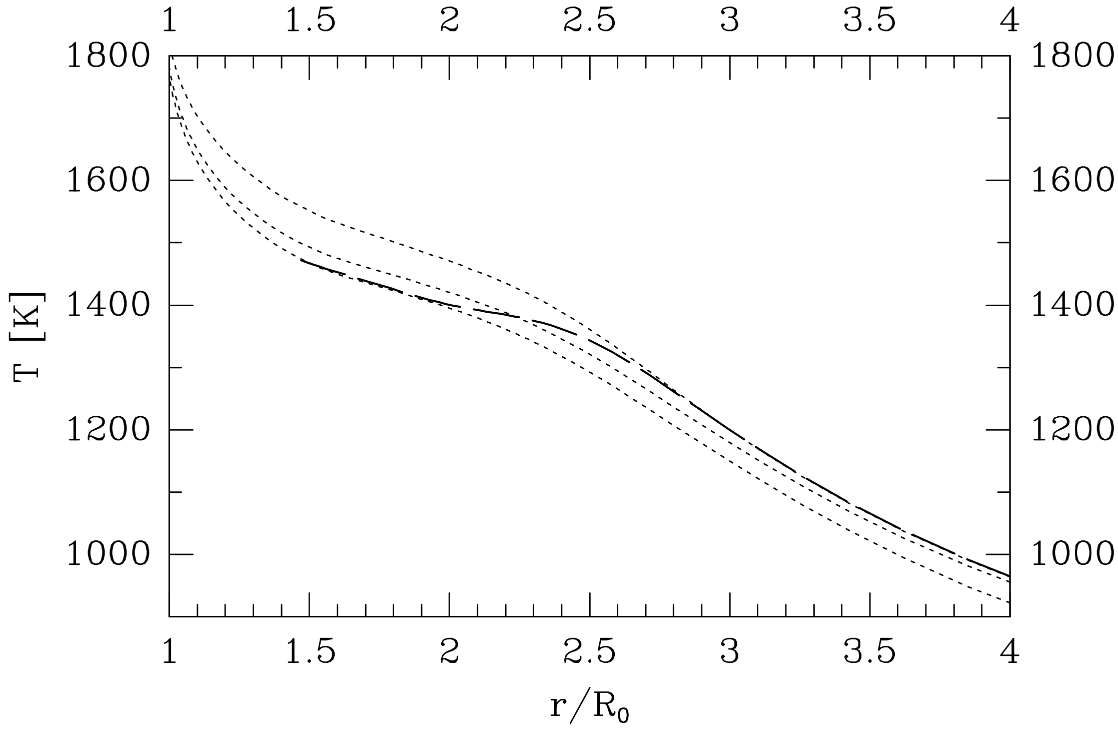

Figure 4.3: Temperature structure for different grain sizes in the region around the sonic point. Upper dotted curve: particle radius $a = 0.01\mu$m, middle dotted curve $a = 1\mu$m, lower dotted curve $a = 10\mu$m, dashed curve: size–independent dust temperature

Figure 4.3 displays the temperature structure for different grain sizes in the region of effective dust formation. The size–independent dust temperature (dashed curve, computed from Eq. (3.67)) approaches the temperature of a small particle ($a = 0.01\mu$m, upper dotted curve) within a narrow transition region around the sonic point between $2R_0$ and $\approx 2.5R_0$. The temperature of a large particle ($a = 10\mu$m, lower dotted curve), which is the grey temperature (since $Q(\nu)$ = const. for large particles), is also shown in Fig. 4.3. The intermediate case ($a = 1\mu$m) is indicated by the middle dotted curve. This particle is large compared to the typical wavelength of the *stellar* radiation field (the maximum of $J_\nu(R_0)$ is reached at 2.5μm) but, concerning the temperature, becomes a small particle at distances $r > 4R_0$ (the maximum of $J_\nu(r > 4R_0)$ is reached at $\lambda > 4.7\mu$m). Thus, the small particle approximation is appropriate for calculating the temperature of the dust component *outside* the sonic point.

4.4.2 Grain extinction

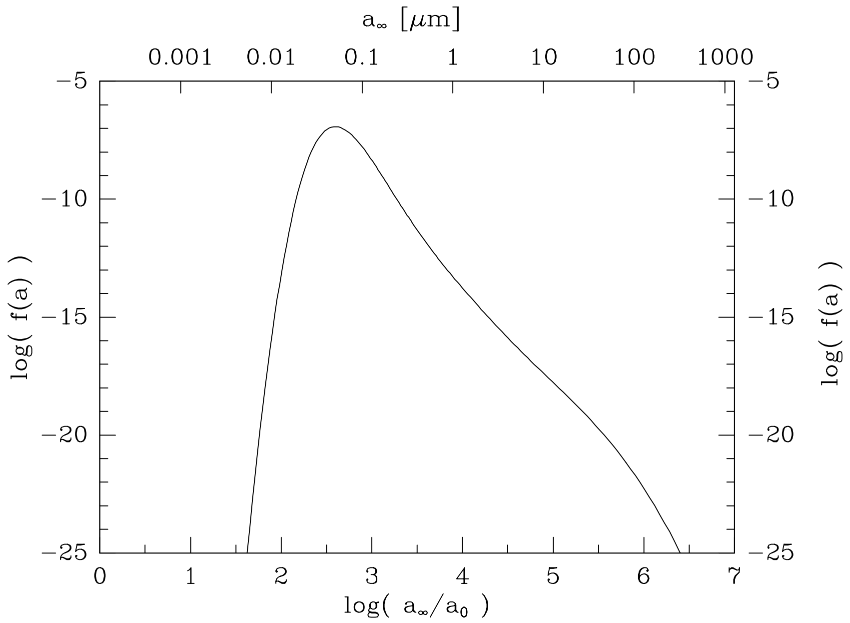

Figure 4.4: Grain–size distribution function produced by the standard model

The particle size distribution function produced in a stationary dust driven wind is a power–law spectrum over a large interval of particle sizes: $f(a) \approx a^{-5}$ for $0.05\mu m < a < 100\mu m$ ([Dominik *et al.* 1989]; [Dominik 1992]). Thus, in particular in the inner region of the dust shell there exists a relevant number of particles, which are large compared to the typical wavelength λ of the stellar radiation field. Therefore, the usual assumption of the small particle limit ($2\pi a \ll \lambda$) for calculating the transport coefficients of the dust grains is not justified in the stationary situation.

Fig. 4.4 shows the grain size distribution function $f(a)$ produced by the standard model on a double logarithmic scale. The abscissa gives the particle size a_∞

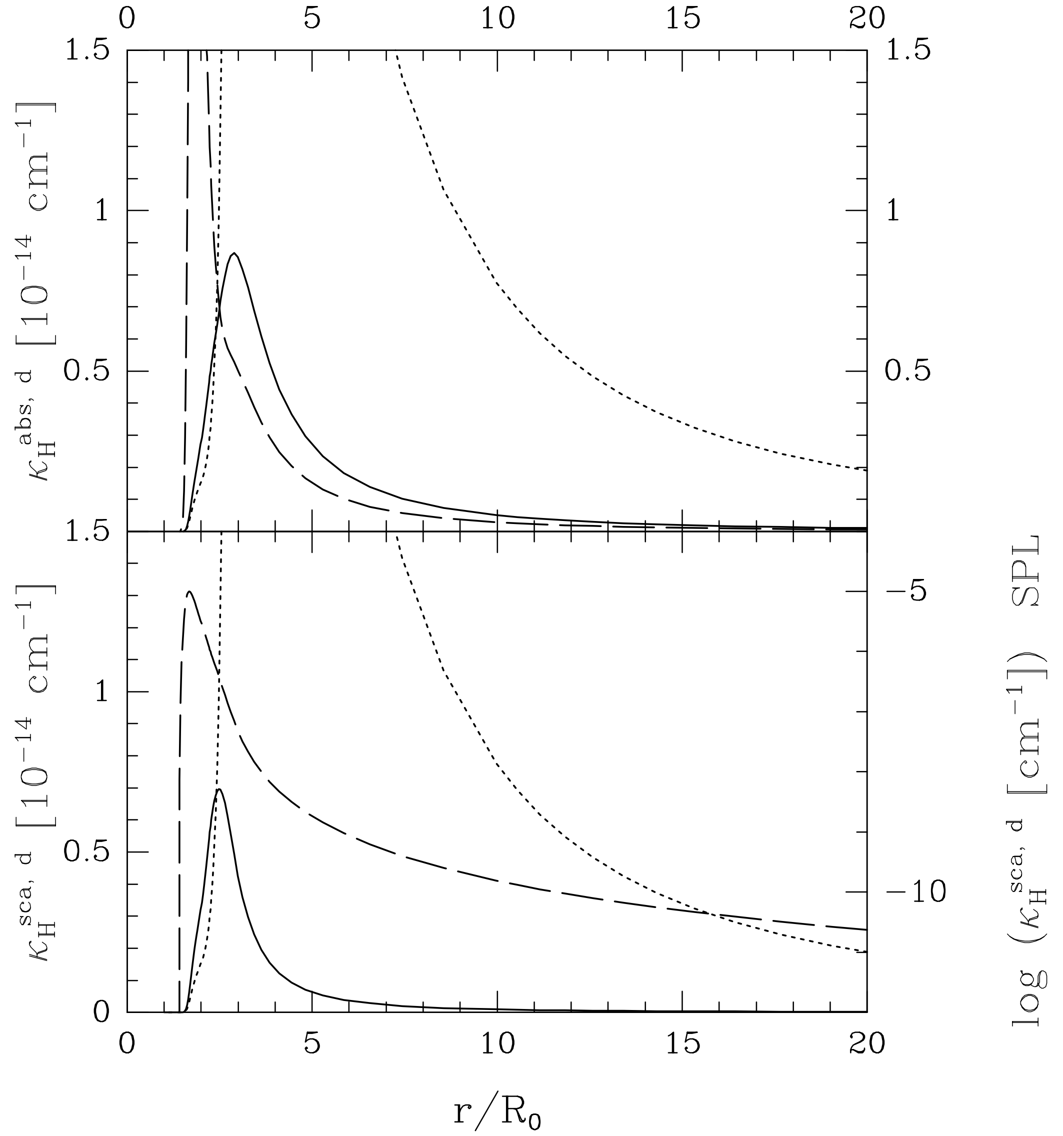

Figure 4.5: Radial variation of the flux-mean absorption coefficient (upper diagram) and flux-mean scattering coefficient (lower diagram) of the dust component. The solid lines represent the values obtained from the size distribution function; the dotted lines refer to the large particle limit and the dashed lines show the small particle limit. In the lower diagram, the values of $\kappa_{\rm H}^{\rm sca}$ in the small particle limit (dashed line) are given by the ordinate at the r.h.s. on a logarithmic scale.

of the dust grains in the outer shell region, where the process of dust formation and growth has ceased. (At the lower abszissa, a_0 denotes the hypothetical radius of a monomer contained in a grain which is $1.28 \cdot 10^{-8}$cm for amorphous carbon.) The largest particles have been formed in the inner shell region, while the small particles emerge from the region outside the sonic point (cf. [Dominik *et al.* 1989]).

The fact, that the grain size distribution function produced by a dust driven wind essentially displays a power–law dependence on the particle radius, is an immediate consequence of the self regulation mechanism. The power–law dependence can only be achieved if dust formation and wind acceleration occur within the same spatial region of the shell (cf. [Dominik 1992]). In cases, where the wind is driven by some different mechanism (e.g. dissipation of wave momentum), i.e. in cases where dust formation is *not* responsible for the wind generation, the resulting grain size distribution functions are no longer power–law spectra but Gaussian–like distributions (cf. [Dominik 1992] and [Fleischer 1994]). On the other hand, the emergence of power law distribution functions seems to be a general feature of any self–regulated phenomena as is discussed e.g. in [Bak *et al.* 1988], who investigate the topic of *self–organized criticality*.

In order to demonstrate the errors introduced by the small particle approximation (Eqs. (3.25) and (3.25)) in the case of a stationary dust driven wind, in Fig. 4.5 the resulting flux-mean values of the absorption and scattering coefficient of the dust component, defined by

$$\kappa_H^{\mathrm{abs,d}} = \frac{\int_0^\infty \kappa_\nu^{\mathrm{abs,d}} \, H_\nu \, d\nu}{\int_0^\infty H_\nu \, d\nu} \tag{4.1}$$

$$\kappa_H^{\mathrm{sca,d}} = \frac{\int_0^\infty \kappa_\nu^{\mathrm{sca,d}} \, H_\nu \, d\nu}{\int_0^\infty H_\nu \, d\nu} \tag{4.2}$$

are compared with the results obtained from Eqs. (3.21) and (3.22) using the size distribution function.

It can be seen from the upper diagram in Fig. 4.5 that in the outer parts of the dust shell ($r > 10R_0$) the small particle limit (dashed curve) yields a reasonable approximation of the absorption coefficient. In the innermost part of the shell, on the other hand, the absorption coefficient is well represented by the large particle limit ($2\pi a \gg \lambda$, dotted curve). Due to the relatively high gas density and the low expansion velocity in the region inside the sonic point ($r = r_\mathrm{c} \simeq 2.2R_0$), the newly formed dust grains grow under excellent conditions. This leads to the formation of large particles, which dominate in the inner region of the dust shell. The existence of these large particles is a specific result of the considered *stationary* wind: A gas element moves very slowly outwards in the region around the sonic point and, therefore, the dust particles contained in the element have much time to grow under favourable thermodynamic conditions.

From the lower diagram of Fig. 4.5 it can be seen, that in the innermost region the scattering coefficient is also closely approximated by the large particle limit. At no site in the atmosphere, however, scattering can be described in the small particle limit. Note, that the corresponding values of the small particle limit are given at the r.h.s. ordinate on a logarithmic scale. The values obtained for the scattering coefficient assuming the small particle limit deviate by orders of magnitude from the true values. This enormous effect is caused by the factor $(2\pi a/\lambda)^4$ in the expression for the small particle scattering efficiency where, in contradiction to the basic assumption, $2\pi a/\lambda$ is not small compared to unity in the relevant range of particle radii a and wavelengths λ.

Therefore, at least in cases where scattering is not negligible, it is necessary to calculate the transport coefficients from the exact expressions Eqs. (3.21) and (3.22) in order to obtain physically consistent results both for the radiative acceleration and the scattering optical depth and, thus, for the hydrodynamic structure of the wind and the emergent spectrum of the dust shell, respectively.

The main implication of the existence of large particles especially in the inner part of the dust shell is a considerable increase of the stellar luminosity required to accelerate the dust driven wind: A necessary condition for dust driving is that the radiative acceleration of the material has to reach sufficiently high values inside the sonic point in order to surmount the stellar gravitational deceleration. Since particles large compared to the photon wavelength absorb radiation only proportional to their surface area (instead of proportional to the volume in the case of particles small compared to the wavelength) a correspondingly increased luminosity $L_\star$ is required to surmount the Eddington limit $L_{\rm Edd}$ for a dust driven wind:

$$L_\star > L_{\rm Edd} = \alpha_{\rm crit}\, 4\pi c G M_\star (\frac{\rho}{\chi_{\rm H}}) \ . \tag{4.3}$$

At the sonic point $\alpha_{\rm crit}$ is typically of the order of 0.7.

4.4.3 Angular structure of the radiation field

In Fig. 4.6 the radial profile of the condensate density is sketched for a dust driven wind (not to scale) together with several lines of sight originating from an arbitrary position P located in the outer shell region. The different lines of sight denote

1: the radial direction ($\mu = \cos\theta = 1$),

2: ray tangent to the stellar surface R_0 ($\mu = \mu_\star$),

3: ray tangent to the inner edge of the dust shell ($\mu = \mu_{\rm s}$),

4: ray tangent to the radius of maximum condensate density ($\mu = \mu_{\max(K_3)}$, the 3rd moment of the grain size distribution function K_3 is the number of condensed monomers per cubic centimeter), and

5: ray perpendicular to the radial direction ($\mu = 0$).

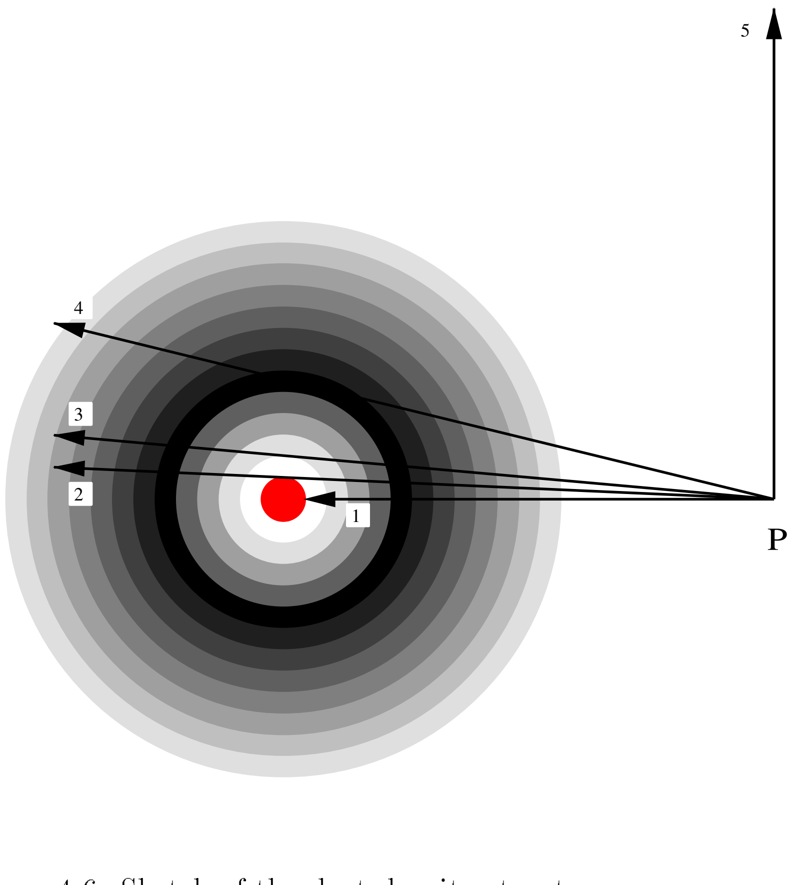

Figure 4.6: Sketch of the dust density structure

The angular variation of the specific monochromatic intensity $I_\nu(\mu)$ at different locations of P is shown in Fig. 4.7. The intensity received from the half range $[1 \geq \mu \geq 0]$ is denoted by I^+ in Fig. 4.7, while the intensity received from $[0 \geq \mu \geq -1]$ is labelled by I^-, which in Fig. 4.7 means $I(-\mu)$.

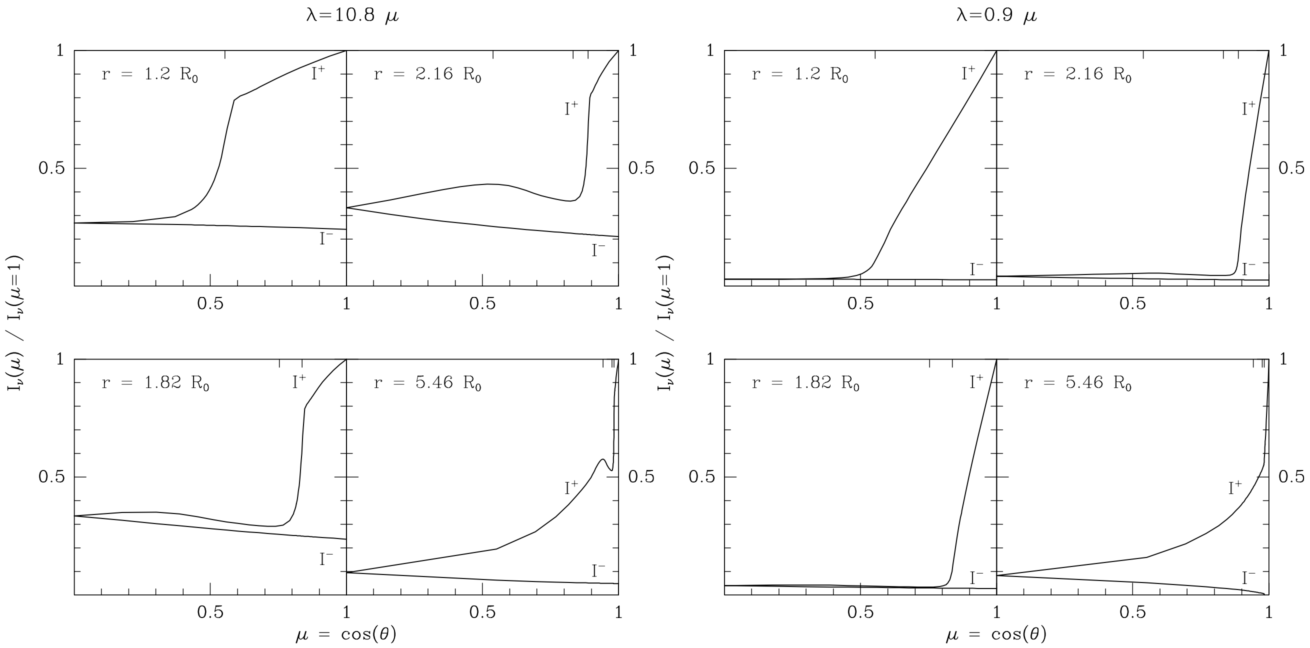

Figure 4.7: Angular variation of the specific intensity at different locations inside the dust shell for two different wavelengths

Each of the diagrams displays $I_\nu(\mu)$ in units of $I_\nu(\mu = 1)$ for a frequency corresponding to $\lambda = 10.8\mu$m (left part of Fig. 4.7) and $\lambda = 0.9\mu$m (right part of Fig. 4.7), respectively.

The reference position of P is located at

upper left diagrams: the inner edge of the dust shell $r = r_\mathrm{s}$ $(= 1.2R_0)$,

lower left diagrams: at the radius, where the maximum condensate density is reached $r = r_{\mathrm{max}(K_3)}$ $(= 1.82R_0)$,

upper right diagrams: at the distance, where the condensate density has decreased to half its maximum value $(r = 2.16R_0)$, and

lower right diagrams: at the distance, where the condensate density has decreased to 1/10 of its maximum value $(r = 5.46R_0)$.

The ticks plotted at the upper abszissa of each diagram denote the angle-cosine, under which (from right to left) the stellar photosphere, the inner edge of the dust shell, and the radius of maximum condensate density is seen from the respective location of P.

At a given distance from the star, the angular variation of the specific intensity is strongly determined by the radial stratification of the dust component inside the fixed location of P.

At long wavelengths, a pronounced second maximum (besides the intensity peak seen in direction to the center of the star) appears in the direction of maximum column density of dust along the line of sight, i.e. around the line of sight tangent to the shell $r = r_{\max(K_3)}$. At these long wavelengths, thermal dust emission leads to a bright rim around the central star with a maximum brightness of more than 50% of the central intensity peak.

At 0.9μm thermal dust emission is of course rather weak. Secondly, due to the large absorption coefficient at short wavelengths, the geometrical distance at which an optical depth $\tau_\nu = 1$ is reached, is rather small. As a result, the radiation field is essentially determined by the central source, and no secondary brightness maximum occurs. Instead, the radiation of the central star becomes 'smeared out' around the radial direction for large distances of P from the center of the star. This effect is due to effective scattering of light by the dust grains at short wavelengths (cf. lower right diagram at 0.9μm).

The non–monotonic structure of the dust density is also evident from the radial course of the Eddington factors, which are displayed for different wavelengths in Fig. 4.8 (next page). With increasing distance from the photosphere, the radiation field first becomes increasingly peaked in the radial direction, which is simply due to the geometrical dilution of the solid angle subtended by the stellar disk. Thus, the Eddington factors reach a local maximum, the value of which depends on the wavelength (cf. also Fig. 4.7). In the inner region of the dust shell, the Eddington factors decrease, which indicates a successive 'isotropization' of the radiation field. This effect is caused by thermal dust emission (at longer wavelengths) and by dust scattering (at short wavelengths). The radius at which the minimum value of f_ν is reached, as well as the minimum value itself again depend on the wavelength. At long wavelengths, the radiation field is less strongly peaked in radial direction (due to effective dust emission at large λ), and the minimum value of f_ν is already reached closer to the star, i.e. the radiation field at long wavelengths is almost isotropic in the very inner region of the dust shell.

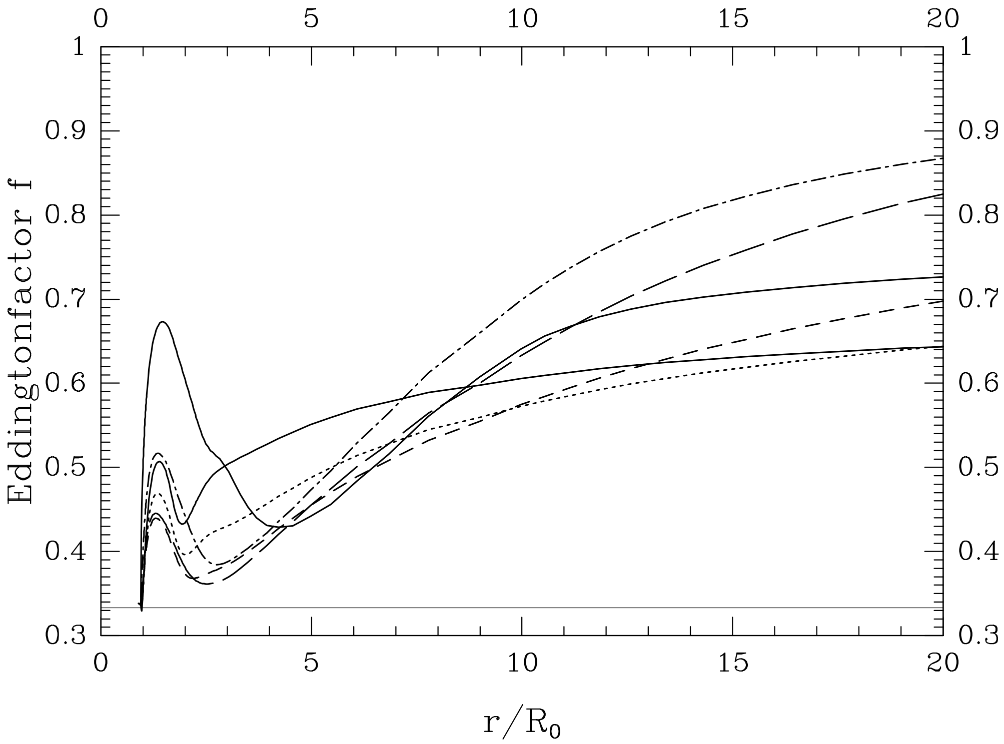

Figure 4.8: Radial variation of the Eddington factor at different wavelengths. (Upper) solid line: $\lambda = 0.90\mu$m, dash–dotted line: $\lambda = 2.1\mu$m, long–dashed line: $\lambda = 4.7\mu$m, short–dashed line: $\lambda = 10.8\mu$m, dotted line: $\lambda = 25\mu$m, (lower) solid line: $\lambda = 57\mu$m.

4.4.4 Optical depths

The monochromatic optical depth of the dust shell (measured inward in radial direction) is given in Fig. 4.9 as a function of frequency.

The optical depth produced by gas absorption is independent on wavelength ($\tau^{\mathrm{g}} = 0.105$), which is due to our description of the gas extinction by the Rosseland–mean absorption coefficient (cf. Sect. 3.2.3). Thus, the frequency variation of τ_ν is caused by the dust opacity alone. At wavelengths $\lambda \leq 250\mu$m, the total optical depth (gas and dust, measured down to the photospheric radius R_0, solid line) is dominated by dust extinction (dotted line). Due to the steep wavelength dependence of the dust *scattering* coefficient, the scattering optical depth (dashed line) becomes increasingly important for increasing frequency until at very short wavelengths ($\lambda < 0.7\mu$m) it contributes the dominant fraction to the total optical depth. The wavelength, for which the stellar photosphere ($r = R_0$) is located at an optical depth of $\tau_\nu = 1$ is $\lambda = 15.6\mu$m. At shorter wavelengths, therefore, the emergent intensity contains direct information almost only from the dust shell. The radius, at which τ_ν equals unity is given as function of frequency by the dash–dotted curve in Fig. 4.9 (the values of the

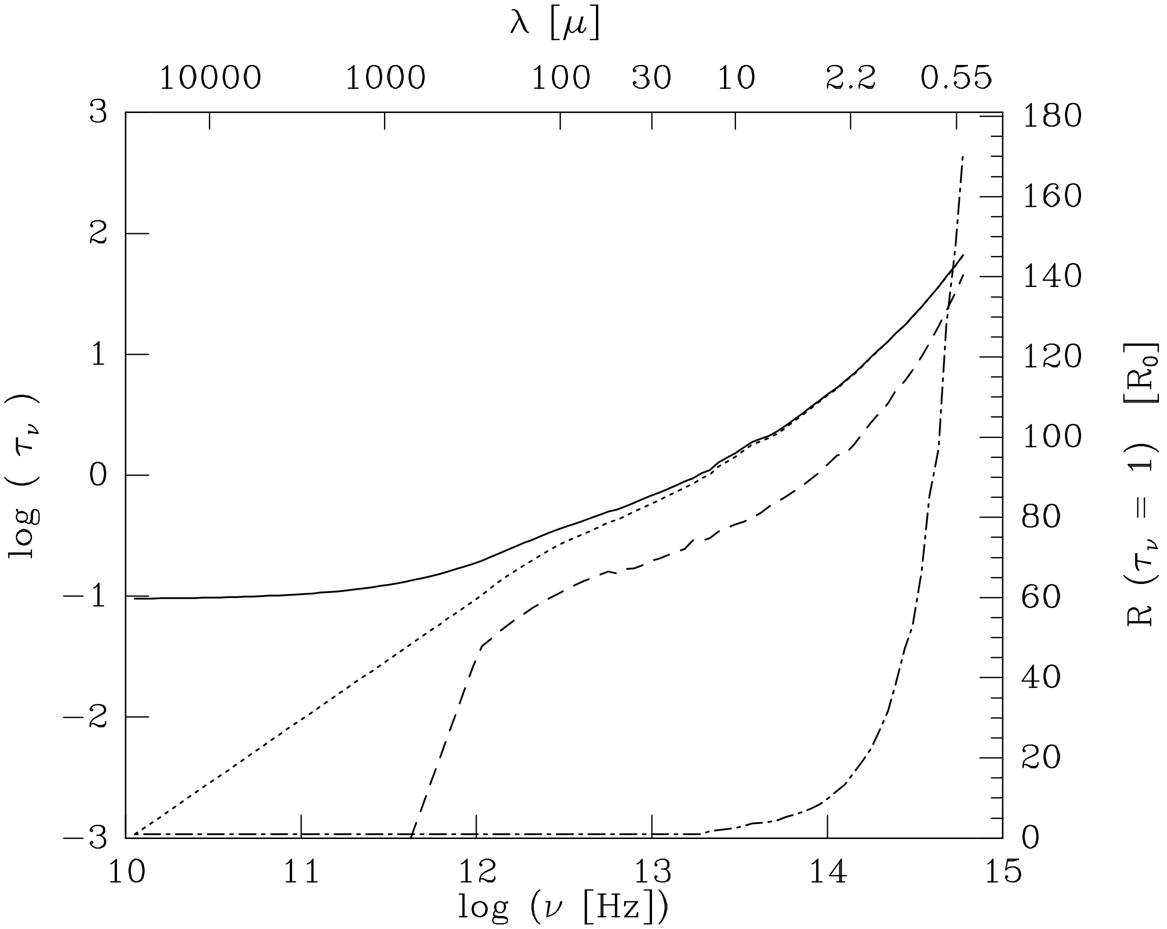

Figure 4.9: Wavelength dependence of the optical depth τ_ν of the dust shell (l.h.s. ordinate) and geometrical depth at which $\tau_\nu = 1$ is reached (r.h.s. ordinate). Solid line: total (gas and dust) optical depth, dotted line: dust optical depth, dashed line: scattering optical depth of dust; dash–dotted line: geometrical depth with $\tau \leq 1$ (r.h.s. ordinate).

corresponding geometrical radii r are given on the r.h.s. ordinate). For wavelengths longer than $\lambda \approx 10\mu$m, photospheric radiation can escape from the circumstellar shell and, thus, contributes to the emergent intensity. The abrupt change in the course of the scattering optical depth at $\lambda \approx 300\mu$m (dashed curve in Fig. 4.9) again reveals the existence of rather large particles in the inner dust shell region. Due to a lack of data for the complex refractive index at longer wavelengths, the scattering efficiency obtained by exact Mie calculations for the shorter wavelength region has simply been extrapolated to longer wavelengths. This extrapolation is based on the assumption, that the small particle limit is valid at least at these long wavelengths (i.e. a λ^{-4} dependence of $Q^{\mathrm{sca,d}}$ is assumed for $\lambda > 300\mu$m). Obviously, this is still not justified for the standard model.

4.4.5 Contribution of different sources to the radiation field

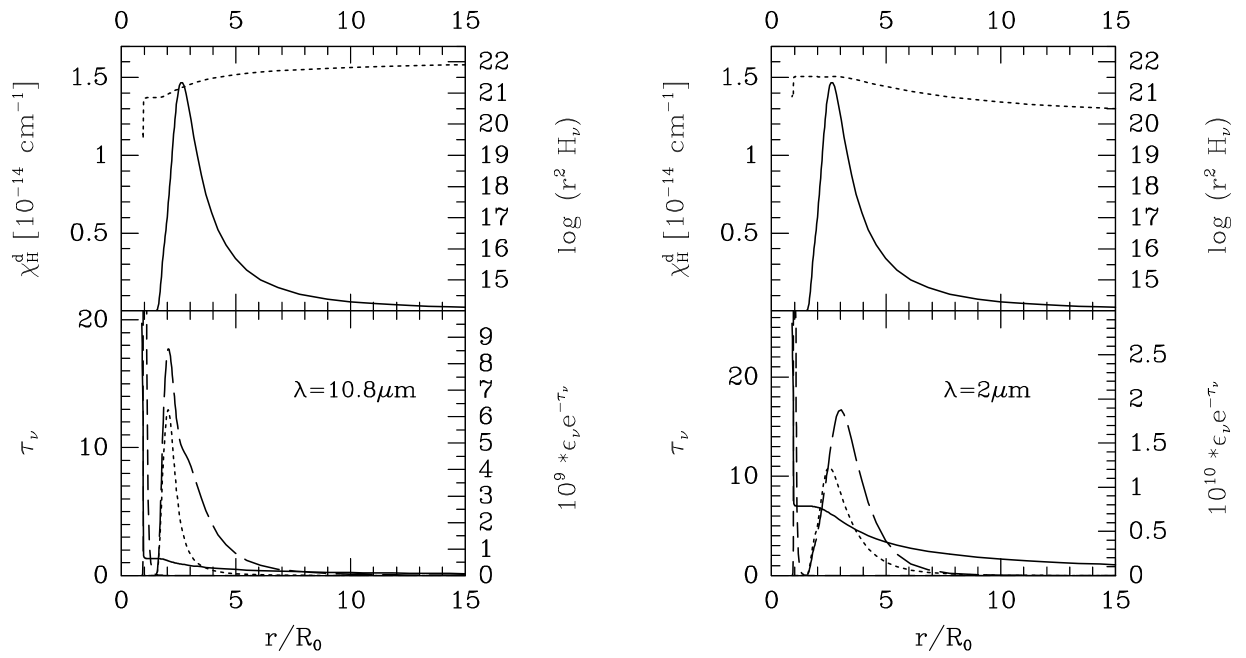

Figure 4.10: Radial variation of the different sources of radiation at $\lambda = 10.8\mu$m and $\lambda = 2\mu$m.
Upper panel: flux mean extinction coefficient of the dust component χ_H^d (solid line, l.h.s ordinate), and logarithm of the Eddington flux H_ν, multiplied by r^2 (dashed line). $r^2 H_\nu$ is given in [erg s^{-1}Hz^{-1}] (r.h.s. ordinate).
Lower panel: total (gas and dust) optical depth τ_ν in radial direction (solid line, l.h.s. ordinate), and local contribution of thermal dust emission (long–dashed line), thermal gas emission (short–dashed line) and dust scattering (dotted line). ϵ_ν e$^{-\tau_\nu}$ is given in [erg s^{-1}cm^{-3} sr^{-1} Hz^{-1}] around the radial direction (r.h.s. ordinate).

The monochromatic specific intensity emerging from the dust envelope in a fixed direction is given by the formal solution of the equation of radiative transfer along the respective ray of light propagation (characterized by its impact parameter p):

$$I_\nu(p, z(r_{\rm max})) = \int_{-\infty}^{\infty} dz \;\, \chi_\nu S_\nu(p, z) \mathrm{e}^{-\tau_\nu(p,z)} \tag{4.4}$$

Inserting the explicit expression for the source function S_ν in Eq. (4.4), we can split the emergent intensity into the individual contributions of the different radiative transfer processes:

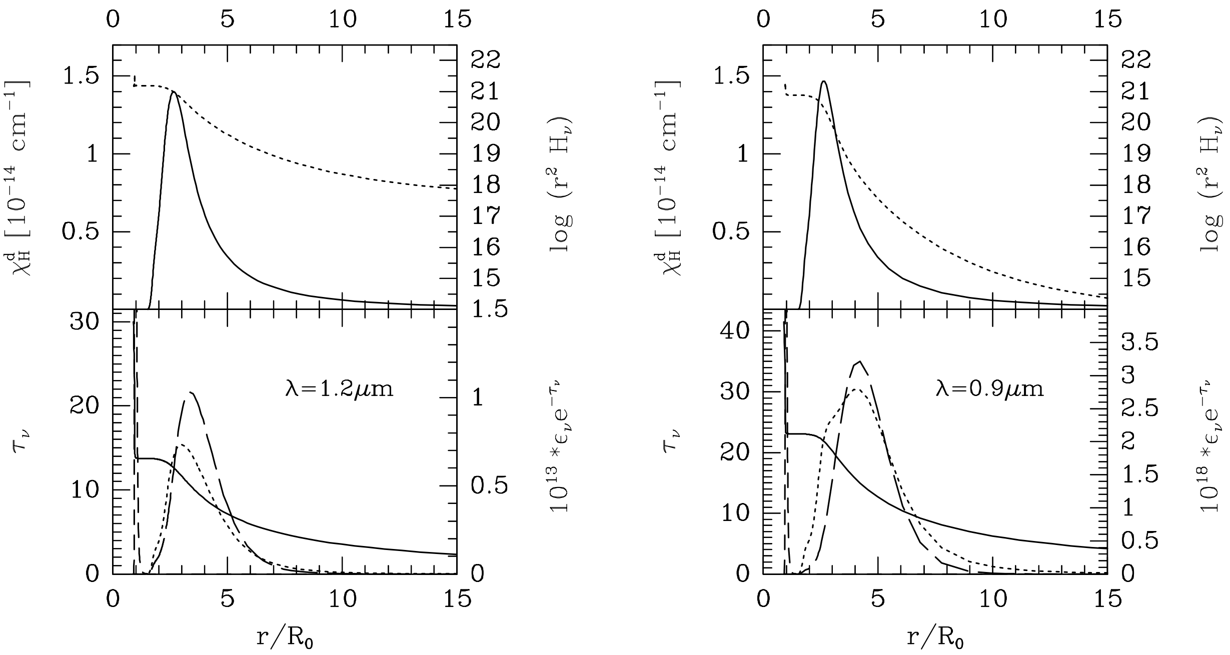

Figure 4.11: Same as Fig. 4.10 at $\lambda = 1.2\mu$m and $\lambda = 0.9\mu$m

$$
\begin{aligned}
I_\nu(p, z(r_{\max})) &= \int_{-\infty}^{\infty} dz\ \kappa_\nu^{\mathrm{abs,g}}(p,z) B_\nu(T^{\mathrm{g}}(p,z)) \mathrm{e}^{-\tau_\nu(p,z)} \\
&+ \int_{-\infty}^{\infty} dz\ \epsilon_\nu^{\mathrm{d}}(p,z) \mathrm{e}^{-\tau_\nu(p,z)} \\
&+ \int_{-\infty}^{\infty} dz\ \kappa_\nu^{\mathrm{sca,d}}(p,z) J_\nu(p,z) \mathrm{e}^{-\tau_\nu(p,z)} \quad . \qquad (4.5)
\end{aligned}
$$

Each term on the r.h.s. of Eq. (4.5) gives the net effect of the local gain processes for the radiation field caused by the respective source terms ($\kappa_\nu^{\mathrm{abs,g}} B_\nu(T^{\mathrm{g}})$, $\epsilon_\nu^{\mathrm{d}}$, $\kappa_\nu^{\mathrm{sca,d}} J_\nu$) and the loss processes due to extinction, which is described by the exponential attenuation due to the total optical depth τ_ν (measured in inward direction). As the radiation field at the outer shell boundary is strongly peaked in the radial direction (cf. Sect. 4.4.3), the value of the intensity strongly depends on the impact parameter p. In order to gain some insight into the radial distribution of the relevant sources of radiation, we consider only the central ray ($p = 0$, $z = r$) and discuss the integrands in Eq. (4.5) i.e. the respective local source contribution attenuated by extinction due to the material located outside the source.

Figs. 4.10 and 4.11 display the contribution of the different sources to the emergent intensity in radial direction at four different wavelengths. The upper panels show the flux–mean dust extinction coefficient χ_H^{d} (solid line), which, of course, is the same for all four wavelengths, and the logarithm of the monochromatic Eddington flux H_ν multipied by r^2 (in order to eliminate the pure geometrical dilution).

The lower row displays the total optical depth τ_ν (solid curve), the contribution by thermal gas emission to the emergent intensity $\kappa_\nu^{\mathrm{abs,g}}(r)B_\nu(T^{\mathrm{g}}(r))\mathrm{e}^{-\tau_\nu(r)}$ (short–dashed curve), the contribution of dust emission $\epsilon_\nu^{\mathrm{d}}(r)\mathrm{e}^{-\tau_\nu(r)}$ (long–dashed curve), and the contribution of dust scattering $\kappa_\nu^{\mathrm{sca,d}}(r)J_\nu(r)\mathrm{e}^{-\tau_\nu(r)}$ (dotted curve). At the r.h.s. ordinate, the pre–exponential factors are abbreviated by ϵ_ν.

From the upper panel it can be seen, that the monochromatic flux (dotted curve) at long wavelengths is increased due to thermal dust emission mainly within the inner shell region (left part of Fig. 4.10), while already at $\lambda = 2\mu$m dust absorption dominates and, consequently, the flux decreases. From the lower panel it is clear, that thermal gas emission (short–dashed lines around $r = 1R_0$) contributes at all wavelengths to the emergent intensity only from a very narrow layer of the stellar photosphere. The maximum contribution of thermal dust emission emerges at each wavelength from an extended zone located in the inner dust shell region. With increasing frequency, the location at which the attenuated source term reaches its maximum, is shifted outwards. This is caused by the dust optical depth (solid line), which increases proportional to the frequency and thus blocks the radiation emerging from the inner layers. Simultaneously, the contribution of dust scattering becomes more important and extends over a broader radial interval for decreasing wavelength. For $\lambda < 1.2\mu$m, the local contribution due to scattering even exceeds the thermal dust emission and, thus, also dominates the emergent intensity at these short wavelengths.

4.5 Dependence of the models on the stellar parameters

After the discussion of its internal structure, in this section the reaction of the standard dust shell model (cf. Tab. 4.1) to variations of each of the model parameters is described. As the considered dust driven wind represents the solution of a highly nonlinear physical problem (cf. Fig. 2.1), the variation of each of the model parameters affects the complete dust forming system in an rather intricate way. The main coupling among the different physical subsystems is provided by the dust opacity, which is roughly (in the small particle limit exactly) proportional to the amount of condensed material. It is therefore advantageous, to discuss the dependence of the model structure on the stellar parameters in terms of the *degree of condensation* f_c, i.e. the ratio of actually condensed material to the amount of condensable material, which in the case of pure carbon grains is given by

$$f_c = \frac{\mathrm{n}_{\mathrm{C,dust}}}{(\epsilon_{\mathrm{C}} - \epsilon_{\mathrm{O}}) n_{<\mathrm{H}>}} = \frac{K_3}{(\epsilon_{\mathrm{C}} - \epsilon_{\mathrm{O}}) n_{<\mathrm{H}>}} \ . \tag{4.6}$$

Thereby we have assumed that all oxygen is locked up in the CO molecule, which does not contribute to the formation of dust grains. The degree of condensation is closely connected to the dust–to–gas ratio by mass in the wind:

$$\frac{\rho^{\mathrm{d}}}{\rho^{\mathrm{g}}} = \frac{m_{\mathrm{C}} \int_{a_\ell}^{\infty} \left(\frac{a}{a_0}\right)^3 f(a)\, da}{1.4 m_{\mathrm{H}} n_{<\mathrm{H}>}} = \frac{12 m_{\mathrm{H}} K_3}{1.4 m_{\mathrm{H}} n_{<\mathrm{H}>}} = \frac{12}{1.4} \epsilon_{\mathrm{O}} \left(\frac{\epsilon_{\mathrm{C}}}{\epsilon_{\mathrm{O}}} - 1\right) f_c \tag{4.7}$$

This ratio cannot take arbitrary high values. The maximum value of f_c is of course unity and $\epsilon_{\mathrm{C}}/\epsilon_{\mathrm{O}}$ even in extreme cases seems to remain smaller than 10 (cf. [Gow 1977]). Assuming the oxygen abundance to be solar, we obtain an upper limit of

$$\frac{\rho^{\mathrm{d}}}{\rho^{\mathrm{g}}} = 5 \cdot 10^{-2} \ .$$

Typical values of the dust to gas ratio observed for carbon–rich CDS range from $2 \ldots 3 \cdot 10^{-3}$ ([Knapp 1985]) over a wide range of mass loss rates, i.e. this ratio is fairly constant for all carbon–rich circumstellar shells. Since the constancy of this ratio is a necessary condition if the outflow is caused by radiation pressure on dust with subsequent momentum transfer to the gas, the observed correlation strongly supports the hypothesis, that the winds of these objects are in fact dust driven.

To get some hints for the modelling of a special object, we concentrate on an exemplary investigation of the influence of the model parameters on the resulting spectra of the dust shell models and on the final outflow velocities. The basic model for this discussion is the standard model presented in Sect. 4.4. This model is always represented by the solid curves in Figs. 4.12, 4.14, 4.16, and 4.18. In the following discussion, one stellar parameter is varied at a time, while the three other parameters are held fixed.

- Dependence on the stellar mass $M_\star$:

  As was already mentioned in Sect. 3.6, the range of stellar masses, within which a purely dust driven wind is possible at all, is severely restricted for realistic values of the stellar luminosity. This is due to the existence of a lower limit luminosity $L_{\rm min} = L_{\rm Edd}$ (cf. Eq. (4.3)), which has to be exceeded in order to allow for a dust driven wind. With the values for luminosity and mass loss rate of the standard model, the stellar mass has to be smaller than $\approx 0.8 M_\odot$ in order to surmount the Eddington limit. Within the remaining narrow mass range ($0.5 M_\odot \leq M_\star \leq 0.8 M_\odot$), the spectra of the dust shells are almost independent of the stellar mass (cf. Fig. 4.12). As long as a stationary dust driven wind exists at all for a given set of stellar parameters, a variation of the stellar mass has also only minor influence on the internal structure of the model.

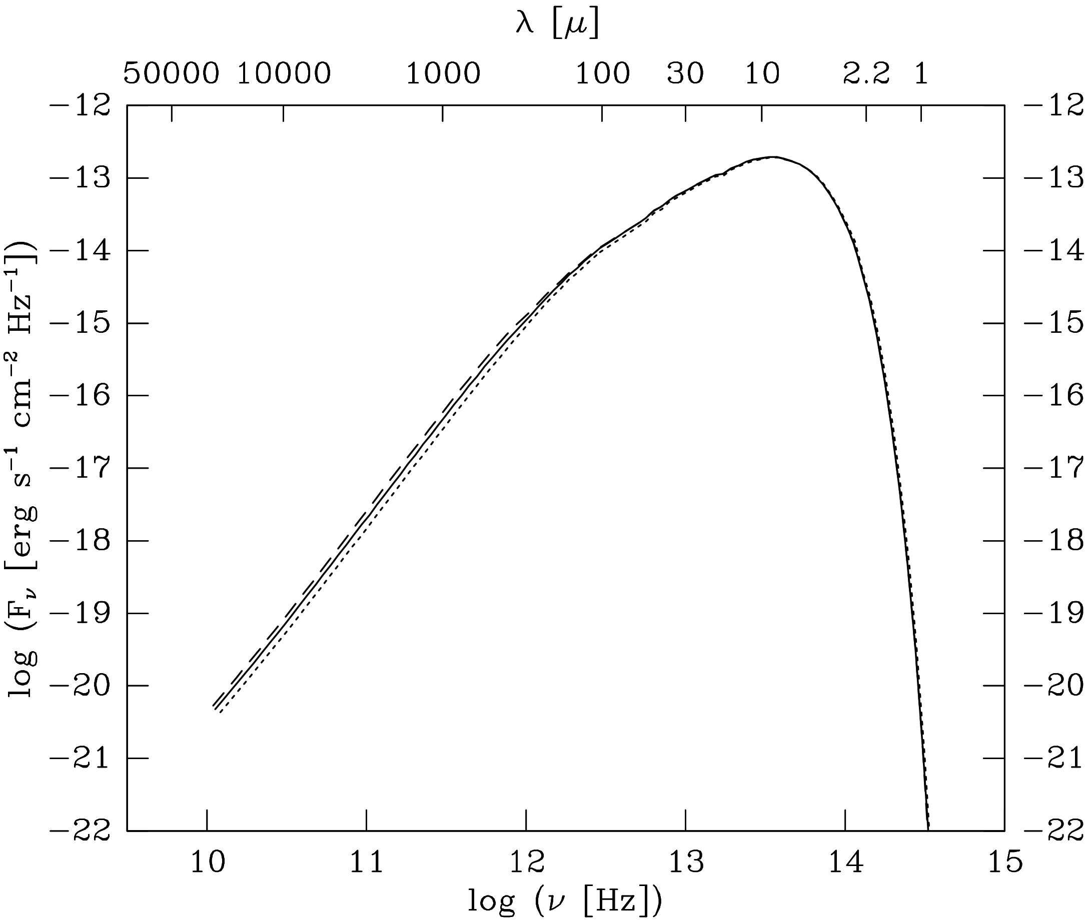

Figure 4.12: Comparison between the spectra produced by different stellar masses. Masses are $0.8 M_\odot$ (dashed curve), $0.7 M_\odot$ (solid curve), and $0.5 M_\odot$ (dotted curve). The remaining parameters are given in Tab. 4.1.

However, with $L_\star$ fixed, there exists an upper limit for the stellar mass above which pure dust driving is not sufficient to maintain the outflow (cf. Eq. (4.3)). Therefore, the range of stellar masses for which stationary dust driven winds exist is severely restricted for reasonable values of the stellar luminosity. An increase of the stellar mass results in slightly lower wind velocities (Fig. 4.13) due to the larger gravitation. This leads to a small increase of the degree of condensation, caused by a more effective growth of the dust particles due to the longer time interval spent by a co–moving gas element in the region of favourable growth conditions. The maximum value of α decreases almost linear with increasing mass of the central star (cf. Eq. (3.8)). Due to the larger degree of condensation the dust extinction reaches slightly higher values, an effect that results in slightly redder spectra in the FIR region, caused by the more efficient thermal dust emission. Simultaneously, the stellar temperature decreases ($\Delta T_\star \approx 200$K between $M_\star = 0.5 M_\odot$ and $M_\star = 0.8 M_\odot$, cf. Fig. 4.13). This variation of the photospheric temperature practically does not influence the emergent spectrum. Due to the large dust optical depth of the shell ($\tau_\nu >$ 10 for $\lambda < 2\mu$m), which increases with decreasing stellar mass, the central star is completely obscured by its own shell. Therefore, almost no information from the photosphere can escape from the dust shell at short wavelengths, where the variation of $T_\star$ causes the largest effects on the stellar radiation field.

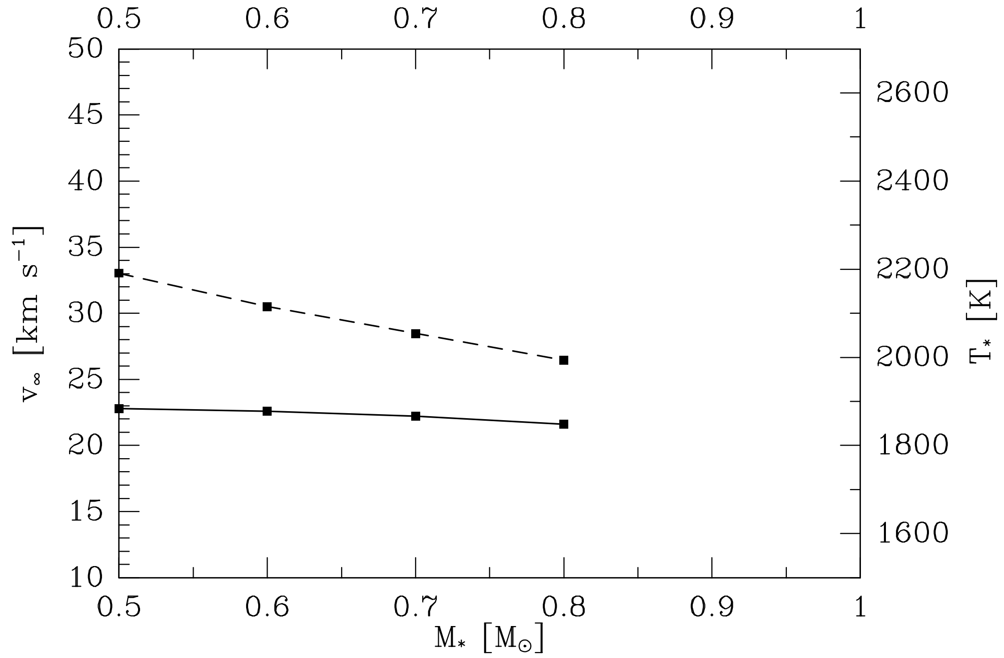

Figure 4.13: Dependence of final outflow velocity v_∞ (solid line) and stellar temperature $T_\star$ (dashed line) on the stellar mass $M_\star$. The remaining parameters are those of the standard model (see Tab. 4.1).

- Dependence on the stellar luminosity $L_\star$:

  With increasing stellar luminosity, the force acting on a *given* amount of dust increases. This leads to a steeper increase of the velocity in the region around the sonic point, where effective dust condensation and growth takes place. Due to the corresponding faster dilution of the particle density in a co-moving gas element, the collision rates between dust particles and gas molecules decrease accordingly and the dust grains grow less effectively. Hence, more carbon bearing molecules remain available in the gas phase, which are partly used up to increase the particle number of dust grains, i.e. the nucleation rate. Both effects together cause the dust grains to become smaller for increasing luminosity. The net result is a lower degree of condensation, which scales almost inversely with the logarithm of the luminosity.

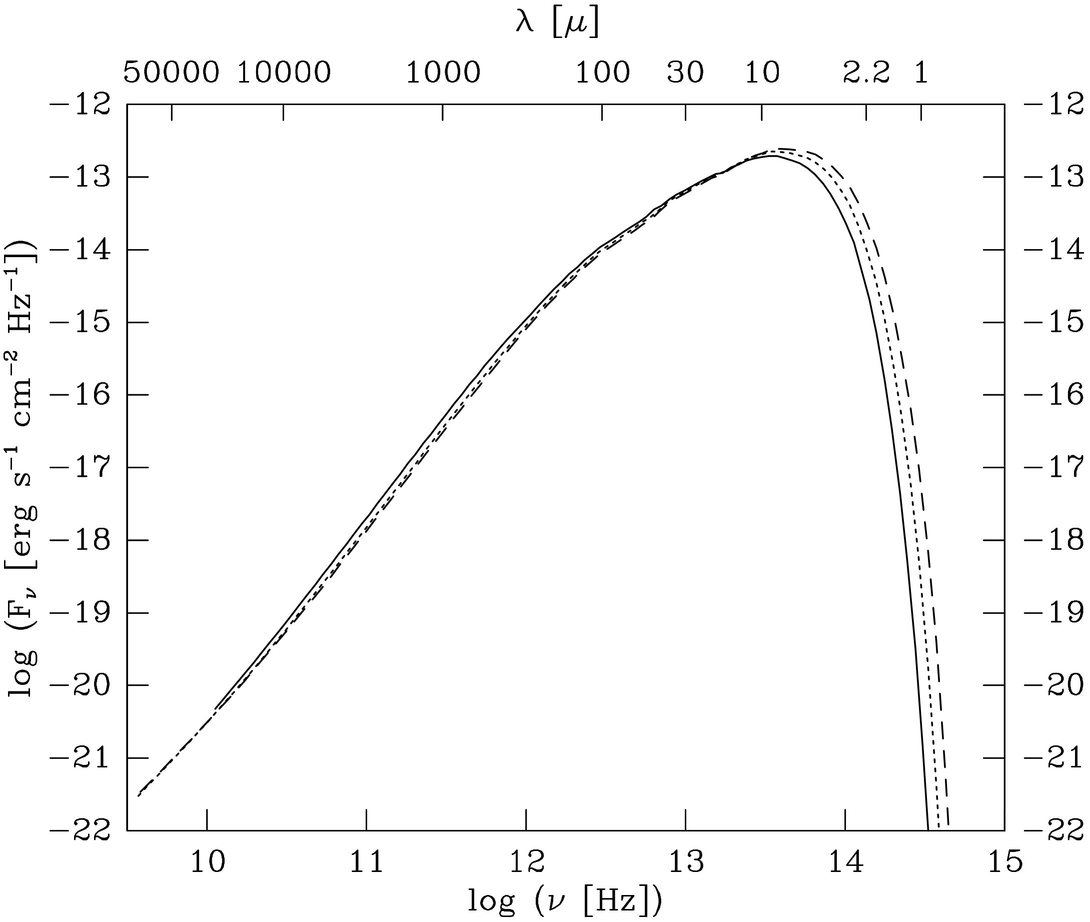

Figure 4.14: Comparison between the spectra produced by different stellar luminosities. Luminosities are $3 \cdot 10^4 L_\odot$ (solid curve), $4 \cdot 10^4 L_\odot$ (dotted curve), and $5 \cdot 10^4 L_\odot$ (dashed curve). The remaining parameters are given in Tab. 4.1.

As the smaller particles absorb the stellar radiation more effectively than large particles, the extinction coefficient decreases more smoothly than does the degree of condensation. Consequently, the radiative acceleration (which is proportional to the product $L_\star \cdot \chi_{\mathrm{H}}/\rho$) increases with increasing luminosity, which results in a moderate increase of the terminal wind velocity (cf. Fig. 4.15).

Due to the smaller dust opacity, the shell remains more transparent which, together with the simultaneously increased stellar temperature ($\Delta T_\star \approx 220$K between $L_\star = 2.4 \cdot 10^4 L_\odot$ and $L_\star = 6 \cdot 10^4 L_\odot$) leads to "hotter" spectra. The largest effects occur at short wavelengths, where the flux drops by about 4 orders of magnitude (Fig. 4.14). Thus, the enhanced spectral flux at short wavelengths is caused by the combined effects of the higher stellar temperature and the lower optical depth. At FIR wavelengths, the emergent flux is smaller for higher luminosities (and, hence, for higher stellar temperatures) which is due to the less effective thermal dust emission resulting from the smaller dust opacity.

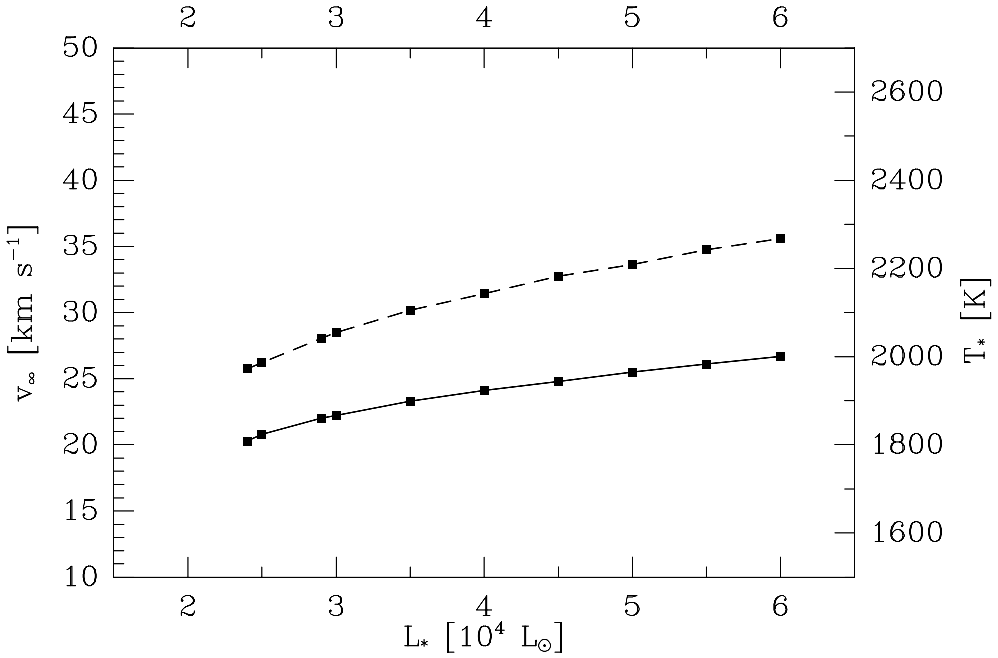

Figure 4.15: Dependence of final outflow velocity v_∞ (solid line) and stellar temperature $T_\star$ (dashed line) on the stellar luminosity $L_\star$. The remaining parameters are those of the standard model (see Tab. 4.1).

- Dependence on the mass loss rate $\dot{M}$:

  The main effect of increasing the mass loss rate is, due to mass conservation, a corresponding increase of the local mass– and, thus, the local particle–density throughout the atmosphere. Therefore, the collision rates between dust particles and gas molecules increase with increasing $\dot{M}$, leading to a more efficient growth of the dust particles. Hence, the grains become larger and the degree of condensation increases. This results in higher values of the radiative acceleration, in particular outside the sonic point. Therefore, more energy is supplied to the material in the supersonic wind region, which increases the terminal velocity for the smaller mass loss rates ($\dot{M} < 3 \cdot 10^{-5} M_{\odot}\mathrm{yr}^{-1}$, cf. Fig. 4.17). A further increase of the mass loss rate above this value does not affect the terminal velocity any more.

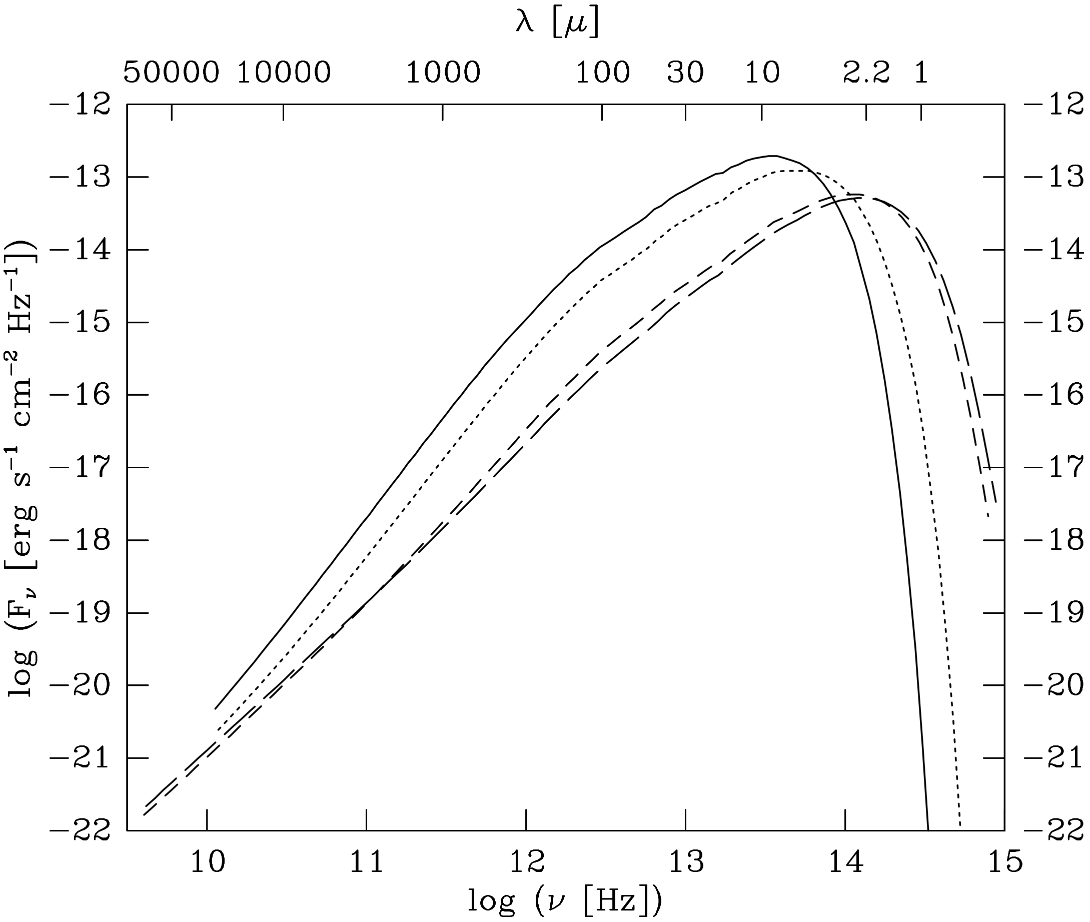

Figure 4.16: Comparison between the spectra produced by different mass loss rates. Mass loss rates are $1 \cdot 10^{-4} M_{\odot}\mathrm{yr}^{-1}$ (solid curve), $5 \cdot 10^{-5} M_{\odot}\mathrm{yr}^{-1}$ (dotted curve), $1 \cdot 10^{-5} M_{\odot}\mathrm{yr}^{-1}$ (short–dashed curve) and $5 \cdot 10^{-6} M_{\odot}\mathrm{yr}^{-1}$ (long–dashed curve). The remaining parameters are given in Tab. 4.1.

This saturation is an effect of the optical depth, which for the higher mass loss rates becomes so large, that the short wavelength stellar radiation field is completely blocked already in the innermost shell region and the accelerating photons cannot reach the outer wind regime. Due to the increased dust opacity the shell spectrum becomes "cooler" as can be seen from Fig. 4.16. Simultaneously the stellar temperature decreases by about 300K between $\dot{M} = 5 \cdot 10^{-6} M_{\odot}\mathrm{yr}^{-1}$ and $\dot{M} = 1 \cdot 10^{-4} M_{\odot}\mathrm{yr}^{-1}$ (Fig. 4.17), which additionally supports the significant reddening of the spectra.

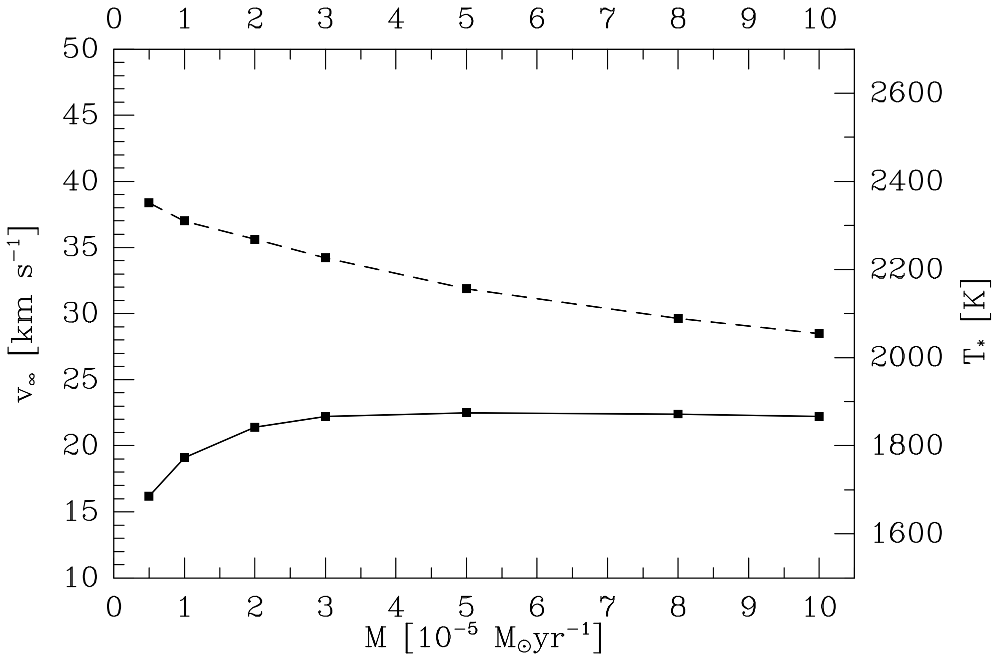

Figure 4.17: Dependence of final outflow velocity v_∞ (solid line) and stellar temperature $T_\star$ (dashed line) on the mass loss rate $\dot{M}$. The remaining parameters are those of the standard model (see Tab. 4.1).

- Dependence on the carbon abundance ϵ_C:

  An increase of the carbon abundance directly increases the amount of condensable material $(\epsilon_C - \epsilon_O)n_{<H>}$. This results mainly in an increase of the maximum value of the nucleation rate, i.e. more critical clusters are formed per second and unit volume. Therefore, a larger number of dust grains is formed, which increase the degree of condensation. The maximum value of α increases accordingly, and leads to a considerably increased terminal wind velocity (cf. Fig. 4.19). Thus, the collision rates decrease in a co-moving gas element, which results in a less effective growth of the particles. Consequently, the dust grains remain smaller at the end of the growth process.

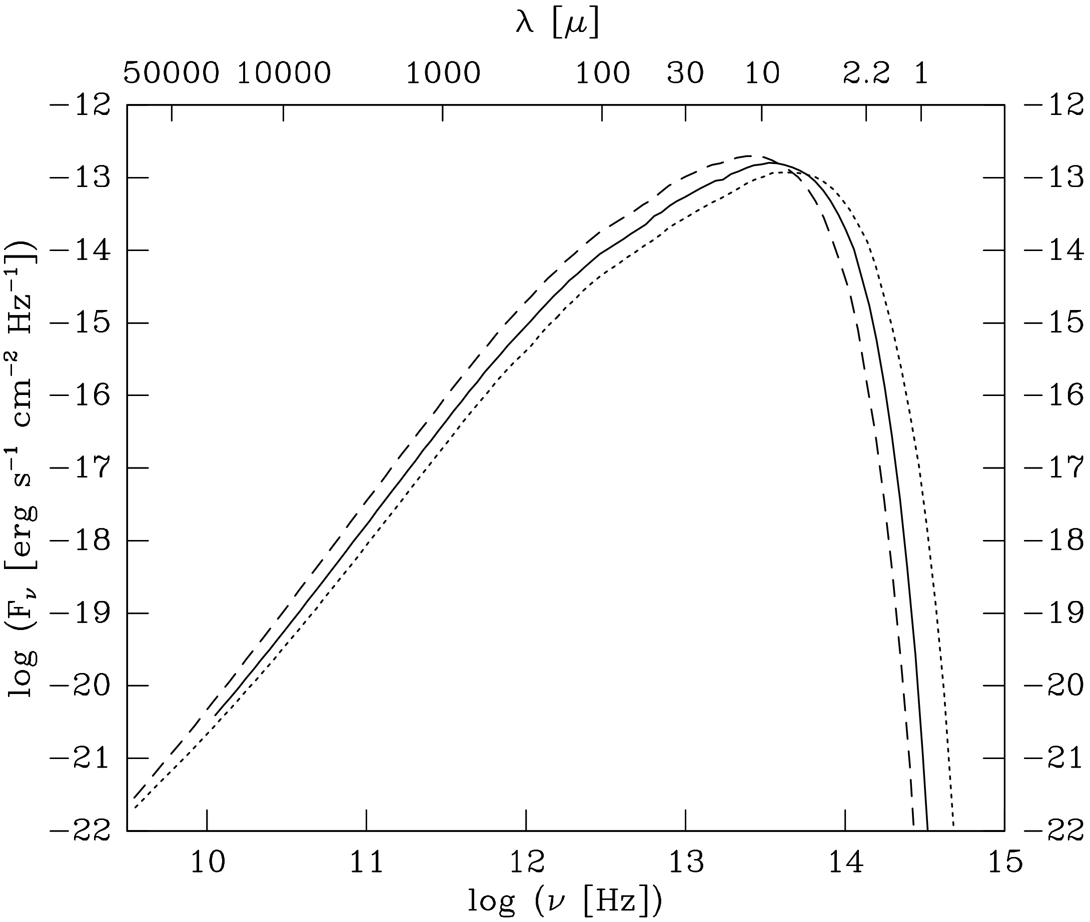

Figure 4.18: Comparison between the spectra produced by different carbon abundances. Overabundance of carbon to oxygen is $\epsilon_C/\epsilon_O = 2.00$ (dashed curve), $\epsilon_C/\epsilon_O = 1.40$ (solid curve), and $\epsilon_C/\epsilon_O = 1.20$ (dotted curve). The remaining parameters are given in Tab. 4.1.

Due to the larger amount of dust (caused by the larger number of grains), the absorption of the short wavelength stellar radiation field becomes more efficient and, at the same time, more energy is thermally re-radiated by the dust grains in the FIR region. Thus, the spectra exhibit considerably less flux in the visible and near infrared region and more flux in the FIR (Fig. 4.18). The variations seen in the emergent spectra and in the terminal outflow velocity are only due to the increased degree of condensation, which causes a corresponding increase of the dust optical depth with increasing C/O ratio. The stellar temperature is completely unaffected by variations of the carbon abundance (cf. Fig. 4.19).

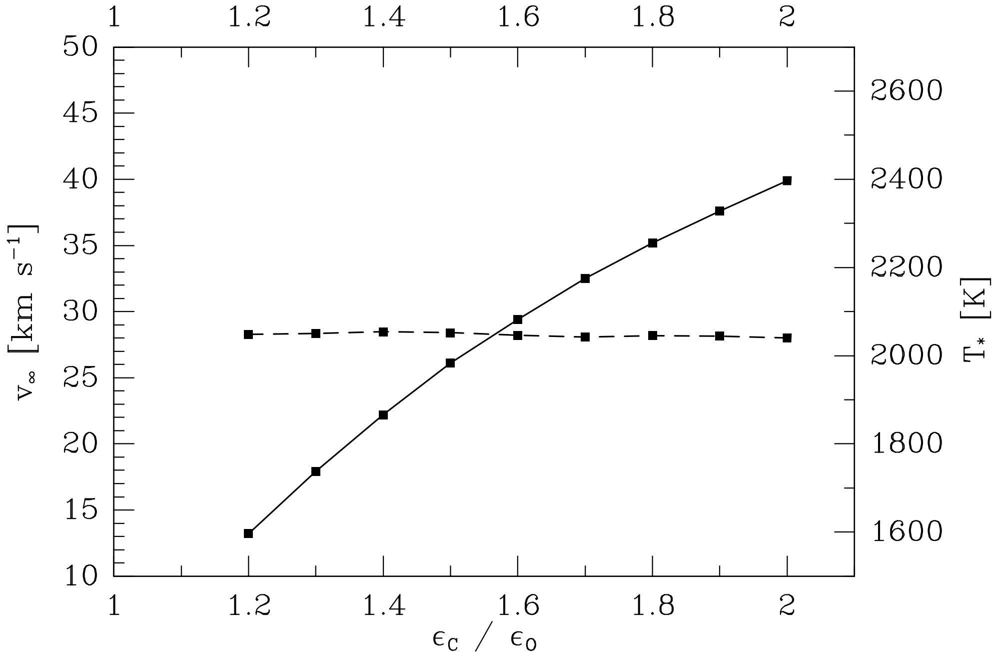

Figure 4.19: Dependence of final outflow velocity v_∞ (solid line) and stellar temperature $T_\star$ (dashed line) on the carbon–to–oxygen ratio ϵ_C/ϵ_O. The remaining parameters are those of the standard model (see Tab. 4.1).

From the preceding discussion one concludes, that the observable properties of the stationary dust shells are decisively influenced by the amount of dust formed in the outflowing circumstellar material, i.e. by the final degree of condensation. The final degree of condensation reached in the CDS, after the process of dust formation and growth has ceased, is fixed by the model parameters and can be expressed as

$$\begin{aligned} f_c \; &= \; \left(\frac{\dot{M}}{10^{-5} M_\odot \mathrm{yr}^{-1}}\right)^{0.78} \\ &\cdot \; \left(12.7\,(\epsilon_\mathrm{C}/\epsilon_\mathrm{O}) \; - 10.2\,\log(\frac{L_\star}{L_\odot}) + 34.9\right) \quad , \end{aligned} \tag{4.8}$$

which is obtained from a fit to the results of the numerical calculations. Equation (4.8) is correct within 20 % for the range of parameters given in Tab. 4.2. Within the range of stellar masses considered here ($0.5M_\odot < M_\star < 1M_\odot$) the degree of condensation is almost independent of $M_\star$.

Very interesting from an observational point of view is the correlation between the final outflow velocity v_∞ and the C/O ratio. In Fig. 4.20, the respective values resulting from a larger grid of model calculations (cf. Tab. 4.2) are shown.

We clearly find an almost linear correlation between v_∞ and $\epsilon_\mathrm{C}/\epsilon_\mathrm{O}$. The scattering of v_∞ at fixed C/O ratio is due to the different luminosities and mass loss rates of the models, which also affect the outflow velocity (cf. the preceding discussion).

Table 4.2: Range of model parameters

$M_\star/M_\odot$	$L_\star/10^4 L_\odot$	$\dot{M}/10^{-4} M_\odot\mathrm{yr}^{-1}$	$\epsilon_\mathrm{C}/\epsilon_\mathrm{O}$
0.5	3.0	1.0	1.4
0.6	2.0 – 5.0	0.1 – 1.0	1.4
0.7	2.0 – 6.0	0.05 – 1.0	1.2 – 3.0
0.8	3.0 – 6.0	0.1 – 1.0	1.4
0.9	4.0 – 6.0	0.1 – 1.0	1.4
1.0	3.5 – 6.0	0.01 – 1.0	1.3 – 3.0
1.1	5.0	0.1	1.4

As the terminal velocities observed for dusty AGB stars are generally less than 40 kms^{-1} (e.g. [Zuckerman *et al.* 1986], [Olofsson *et al.* 1993a]) we would conclude from Fig. 4.20 that the photospheric C/O ratios of late–type C–stars in general are less than about $\epsilon_\mathrm{C}/\epsilon_\mathrm{O} = 2$. This result is consistent with the values found from photospheric molecular line observations, which range from $1 \leq \epsilon_\mathrm{C}/\epsilon_\mathrm{O} \leq 10$ (cf. [Lambert *et al.* 1986] and [Gow 1977]) and most objects have $\epsilon_\mathrm{C}/\epsilon_\mathrm{O} \leq 4$. Such

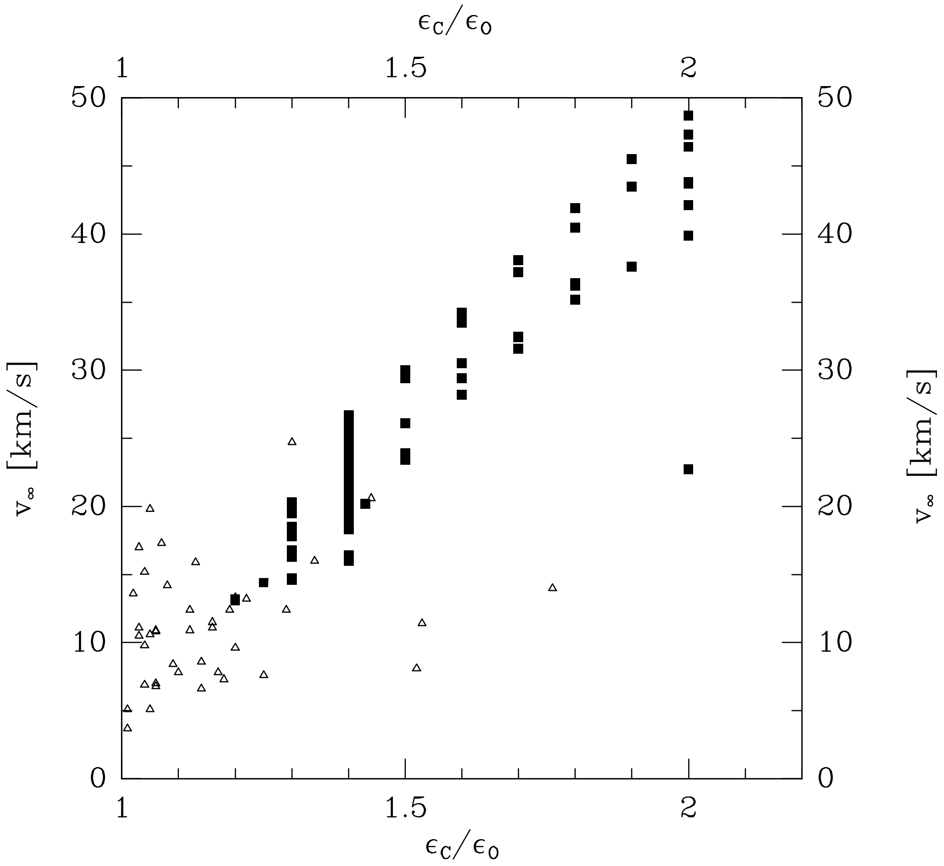

Figure 4.20: Correlation between v_∞ and carbon abundance. Filled squares represent the model calculation. Observed values ($\triangle$) are taken from [Olofsson *et al.* 1993a] and [Olofsson *et al.* 1993b].

observations, however, are only possible for objects with relatively thin dust shells, which allow the photosphere to be seen at those wavelengths, where the respective molecular lines are located. As the stellar photospheres are comparably hot ($T_\star \geq 2000\,\mathrm{K}$), only small molecules (mainly diatomic species) can survive. The absorption lines of these molecules, which can be used as diagnostic tool for probing the photospheric conditions (e.g. the element composition) result from electronic transitions (occuring in the UV– and optical spectral region) or, at best, from fundamental mode vibration bands, which have typical energies in the near infrared region ($\lambda \leq 5\mu$m). Since the more massive dust shells are optically thick at these "short" wavelengths, only little information from these photospheric lines can escape from the dust shell, because the photospheric molecular bands are increasingly blurred by thermal dust emission with increasing optical depth of the dust shell. As the optical depth in our models becomes larger for higher C/O ratios, it may be difficult to observe this correlation, simply because high photospheric C/O ratios would prevent the determination of this ratio from observations.

On the other hand, those objects for which the photospheric element composition can be determined, are surrounded by comparably thin circumstellar shells and, therefore, tend to have comparably low mass loss rates. As there exists a minimum mass loss rate for dust driven winds (cf. [Gail and Sedlmayr 1987c] and [Dominik *et al.* 1990]), mass loss from these optically thin shells may not be dust driven at all, but rather produced by different mechanisms (e.g. dissipation of acoustic wave energy and –momentum), which are not connected to the chemical composition of the photospheric gas.

Thus, the theoretically determined linear correlation between v_∞ and ϵ_C/ϵ_O does not necessarily contradict the observed large scatter of v_∞. On the contrary, this theoretical result in principle may be used to derive the photospheric carbon abundance in particular for those objects, which are surrounded by massive dust shells.

At this point it seems to be noteworthy that a corresponding correlation is also found from dynamic models of circumstellar dust shells around LPVs (see [Fleischer 1994]). In these models, the terminal velocities resulting for the same values of the carbon abundance are systematically lower than in the stationary models presented here. This effect is due to a levitation of the atmosphere by shock wave dissipation, which provides an additional energy supply for driving the outflow (beyond radiation pressure) in particular inside the dust formation region (cf. also Sect. 4.8.4).

The fact that a linear correlation between carbon abundance and the outflow velocity is also found in these time–dependent models, strongly supports the universal validity of such a relation in those cases, where the mass loss mechanism is intimately connected to radiation pressure on dust.

4.6 Infrared two colour diagrams for stationary dust driven wind models: A comparison between theory and observations

In order to investigate the dependence of the spectral appearance of the dust shell models on the stellar parameters, a grid of about 100 models has been calculated for the range of parameters compiled in Tab. 4.2. The results are presented in terms of the colour indices obtained from the FIR IRAS bands at 12μm, 25μm and 60μm (Fig. 4.21) and from the near infrared (NIR) standard photometric bands H ($\lambda_{\text{eff}} = 1.65\mu$m), K ($\lambda_{\text{eff}} = 2.2\mu$m) and L ($\lambda_{\text{eff}} = 3.6\mu$m) (Fig. 4.22 on p. 83).

The crosses in Figs. 4.21 and 4.22 represent observed photometric fluxes of about 200 carbon-rich AGB-stars which are taken from [Epchtein *et al.* 1990]. In both figures, the observed colours of two particular objects are indicated by large open hexagons: in the (lower) left part of the diagrams the carbon Mira R For and in the (upper) right part the dust enshrouded C-star IRC +10216. The small filled symbols connected by lines of different type represent the model calculations. Along each line, one of the model parameters is varied while all other parameters are held constant.

The model which is chosen as basis for the parameter variation (indicated by a filled triangle in both figures) is fixed by $M_\star = 0.7 M_\odot$, $L_\star = 3 \cdot 10^4 L_\odot$, $\dot{M} = 1 \cdot 10^{-4} M_\odot \mathrm{yr}^{-1}$ and $\epsilon_\mathrm{C}/\epsilon_\mathrm{O} = 1.40$ (this is the standard model, cf. Tab. 4.1).

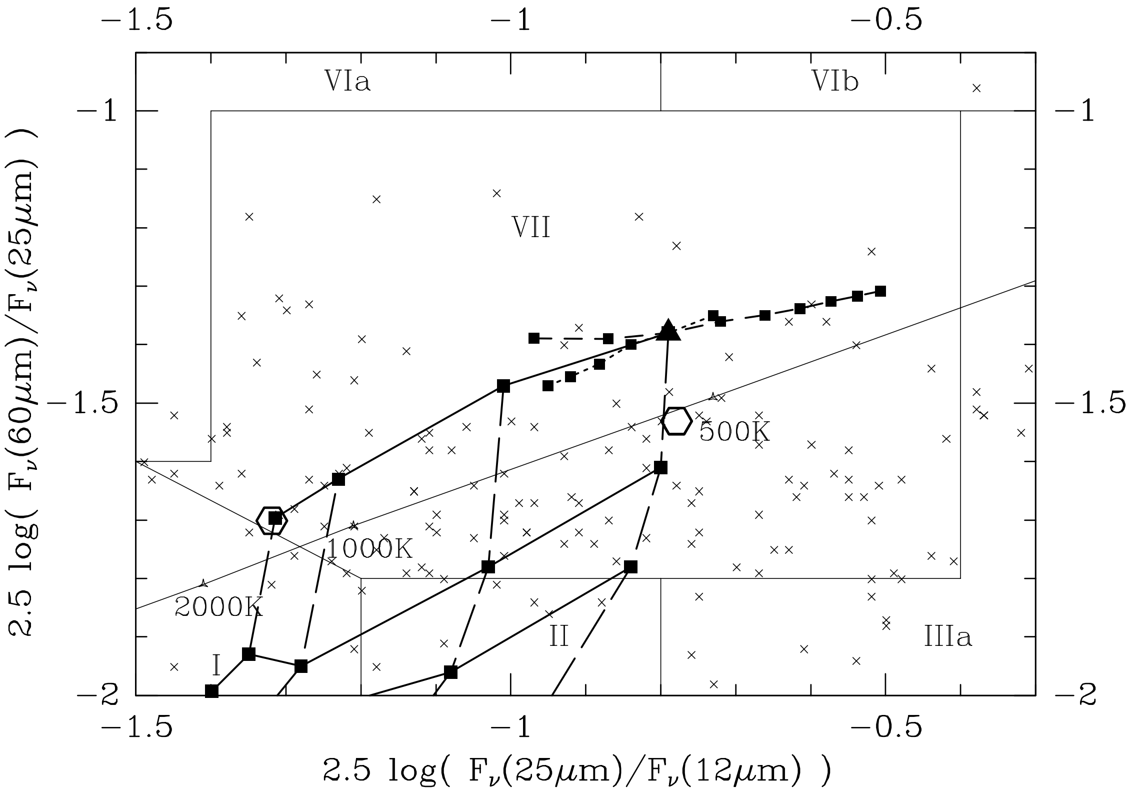

Figure 4.21: IRAS two colour diagram. The roman numbered regions refer to the classification of [Veen and Habing 1988]. Crosses are observed values taken from [Epchtein *et al.* 1990]. The thin diagonal line connects blackbody spectra at the indicated temperatures. The large open hexagons indicate the locations of IRC +10216 (right hexagon) and R For (left hexagon), the other symbols represent the model calculations (see text).

In case of the FIR colour indices (Fig. 4.21) the geometrical shell extension has a strong additional influence in particular on the ([25]-[60]) colour index in the sense, that an increasing shell extension shifts this colour index to larger values. This well known fact is indicated in Fig. 4.21 by the almost vertical dashed lines, each of which corresponds (from bottom to top) to an increasing value of R_max, the location of the outer shell boundary. Thermal emission of cool dust, located at large distances from the central star, contributes significantly to the emergent flux at FIR wavelengths. The amount of thermally emitted radiation of course depends on the density in the outer shell region and, thus, on the mass loss rate.

Along the solid lines the mass loss rate increases from left to right ($5 \cdot 10^{-6} M_\odot \mathrm{yr}^{-1}$, $1 \cdot 10^{-5} M_\odot \mathrm{yr}^{-1}$, $5 \cdot 10^{-5} M_\odot \mathrm{yr}^{-1}$, $1 \cdot 10^{-4} M_\odot \mathrm{yr}^{-1}$). The upper solid line refers to a location of the outer shell boundary at $R_{\max} = 1 \cdot 10^4 R_0$, the middle solid line to $R_{\max} = 1 \cdot 10^3 R_0$ and the lowest to $R_{\max} = 5 \cdot 10^2 R_0$. It can be seen, that with increasing mass loss rate the location of the outer boundary $R_{\max}$ has to be reduced accordingly in order to match the observed IRAS fluxes. This is due to the fact that the complete shell in the models is produced by a mass loss rate, which is constant with time. The phase of constant mass loss rate, however cannot last for an arbitrary long time interval, the star would eventually completely evaporate. In the real objects the mass loss rate is believed to increase with time (cf. [Dominik *et al.* 1990]) and, therefore, the most extended parts of the shell have been produced in an evolutionary phase of the star when it had a smaller mass loss rate. The mass density in the outer parts of the real shell, therefore, is expected to be lower than the density produced by the stationary wind models. Of course, if the mass loss rate of the star changes over a timescale of say 10^4yrs, then also the mass of the central star changes accordingly, which cannot be accounted for in our stationary models. As the mass loss timescale in the case of an highly evolved AGB object is of the order of the nuclear evolutionary timescale of the star itself, the evolution of the central star will be affected by its mass loss. To investigate the implications of the resulting effects on the emergent spectra of the dust shells in more detail, the calculation of an evolutionary sequence is required, taking into account the varying mass loss. Such calculations would provide the mass loss history of the star and, thus, a consistently calculated density structure of the circumstellar shell. Such evolutionary calculations are currently being performed by our group (in cooperation with Dr. A. Weiss and J. Wagenhuber (MPIA Garching)). First results from this investigation are expected to be obtained in the near future.

The dotted line in Fig. 4.21 indicates the effect of decreasing the stellar luminosity in steps of $5 \cdot 10^3 L_\odot$ from $5 \cdot 10^4 L_\odot$ (on the left) to $2.5 \cdot 10^4 L_\odot$ (on the right). Lower luminosities produce “cooler” shell spectra which is of course partly due to the corresponding reduction of the stellar temperature but is also due to a larger amount of dust produced in the models with lower luminosities (cf. Sect. 4.5).

Along the short-dashed line the overabundance of carbon to oxygen ϵ_C/ϵ_O is increased in steps of 0.1 from a value of 1.2 at the left to $\epsilon_C/\epsilon_O = 2$ at the right. The reddening of the spectra by the increased carbon abundance is a pure effect of the increased amount of dust, the stellar temperature remains almost constant (between 2054K and 2040K) along this line.

All models shown in Figs. 4.21 and 4.22 refer to a stellar mass of $M_\star = 0.7 M_\odot$. Within the range of masses considered (cf. Tab. 4.2), the model spectra are almost independent of mass.

From Fig. 4.21 it can be seen that selfconsistent models of stationary, dust driven winds are capable of reproducing the observed FIR fluxes of evolved carbon-rich circumstellar dust shells, which are believed to mainly populate region VII of the IRAS two colour diagram (cf. [Veen and Habing 1988]).

In the NIR region (Fig. 4.22) the theoretical colour indices resulting from the selfconsistent stationary wind models deviate in a systematic way from the cor-

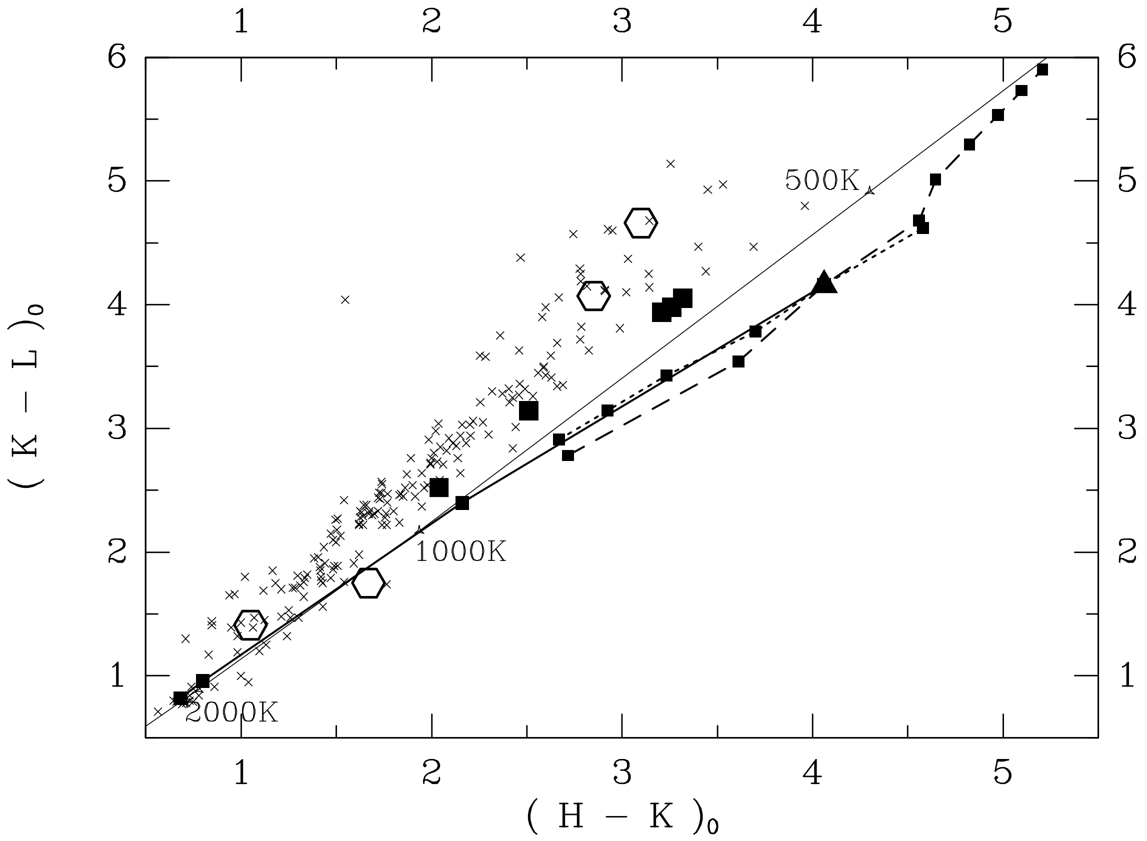

Figure 4.22: Near infrared two colour diagram. Crosses represent observed colours taken from [Epchtein *et al.* 1990], the thin diagonal line connects blackbody spectra at the indicated temperatures. The large open hexagons represent the locations of IRC +10216 (upper right) and R For (lower left) at different phases of the light curve. Right and left symbol in each case correspond to light minimum and light maximum, respectively. The other symbols represent the model calculations (see text).

responding observed values. Both, the observations and the calculations show an almost linear correlation between the $(\mathrm{H}\text{-}\mathrm{K})_0$ and $(\mathrm{K}\text{-}\mathrm{L})_0$ colour index, but with different gradients. The filled squares connected by lines of different type, which represent the calculations, again are obtained from varying the model parameters in the same way as described above. Solid line: mass loss rate increases from left $(5 \cdot 10^{-6} M_{\odot}\mathrm{yr}^{-1})$ to right $(1 \cdot 10^{-4} M_{\odot}\mathrm{yr}^{-1})$; dashed line: carbon to oxygen ratio increases from left $(\epsilon_{\mathrm{C}}/\epsilon_{\mathrm{O}} = 1.2)$ to right $(\epsilon_{\mathrm{C}}/\epsilon_{\mathrm{O}} = 2)$; dotted line: luminosity decreases from left $(L_{\star} = 5 \cdot 10^4 L_{\odot})$ to right $(L_{\star} = 2.5 \cdot 10^4 L_{\odot})$. Obviously, none of them affects the gradient of the theoretical colour index correlation. In all models located below the blackbody line, the transport coefficients of the dust grains are calculated from Eqs. (3.20) and (3.21), taking into account the particle size distribution function. Above the blackbody line, five filled squares are shown at the lower border of the observed colours. These theoretical colour indices are obtained from model calculations, where the *small particle limit* has been assumed for calculating the dust opacity, although this assumption is not justified in a stationary dust driven wind (cf. Sect. 4.4.2). A possible reason for this discrepancy between calculated and observed NIR colours might be the fact, that almost all objects which possess circumstellar dust shells are pulsating variables (Miras or LPVs) ([Habing 1990]). Due to the periodic passage of shocks through the atmosphere, the time available for the dust grains to grow under favourable thermodynamic conditions is at least limited by the pulsation period of the star which is typically of the order of one year. Time–dependent model calculations of dust forming circumstellar shells around LPVs ([Fleischer *et al.* 1992], [Fleischer 1994]) in fact yield narrow grain-size distribution functions with a mean particle radius of $r_{\rm m} \leq 0.1\mu$m throughout the circumstellar shell. These particles are small compared to the NIR wavelengths considered in Fig. 4.22. The theoretical near infrared colours of these time–dependent models are discussed in Sect. 5.6.

4.7 IRC+10216 – The prototype of an extreme carbon star

IRC+10216 is an extended object located out of the galactic plane in an unreddened region. At 5μ it is the brightest source observed outside the solar system; at 2.2μ it varies by as much as 2 mag, with a time scale on the order of 600 days. Its energy distribution resembles that of a 650° K blackbody, and no spectral features have been observed in the wavelength range from 1.5 to 14μ. The object is interpreted as being consistent with a galactic source surrounded by an optically thick dust shell.

Abstract of the letter
"The unusual infrared object IRC+10216"
by [Becklin *et al.* 1969],
which is the first paper devoted to this object.

Since its discovery in 1965 by the *Two Micron Sky Survey* ([Neugebauer and Leighton 1969]), IRC +10216 has attracted considerable attention by astronomers and astrophysicists.

Though it is extremely bright at 5, 10, and 20μm, IRC +10216 (also designated CW Leo) is visually fainter than eighteenth magnitude. In the terrestrial atmospheric transmission windows between 1.5 and 14μm, its spectrum shows a featureless continuum, and in the $5000 - 7000\text{Å}$ region IRC +10216 is observed to be elliptically extended with a lower limit size of $2'' \times 4''$ in this wavelength region and, thus, is definitely a non–stellar object ([Becklin *et al.* 1969]). Due to these unusual properties, until 1970 it was still a matter of debate whether IRC +10216 is extragalactic or galactic. However, already in 1969 [Becklin *et al.* 1969] estimated a lower limit for the distance of $d \approx 100\,\mathrm{pc}$ from the lack of proper motion. They even speculated already in this first paper on IRC +10216, that the object may be a highly evolved star in a state immediately preceding that of a planetary nebula. They also discuss the possibility of IRC +10216 being a protostar. However, its location outside the galactic plane, in a region devoid of gas, dust, and young stars is not typical for such objects. Additionally, the observed light variations with a ≈ 600d period make the protostar hypothesis very unlikely.

One year later [Miller 1970] discovered three stellar absorption features in the $7000 - 11000\text{Å}$ spectral region, which he identified as CN absorption bands. From this result he suggested, that IRC +10216 is a carbon star, surrounded by an optically thick dust cloud of its own making. In the same year, [Herbig and Zappala 1970] confirmed the carbon star nature by a detailed analysis of near infrared spectra obtained in the $7500 - 8700\text{Å}$ region. Assuming an absolute bolometric magnitude of $M_{\mathrm{bol}} = -7$, they also derived for the first time a distance to IRC +10216. Their value of $d = 290\,\mathrm{pc}$ served as a standard value during the next 16 years.

High resolution spectra in the 10μm region obtained by [Treffers and Cohen 1974] revealed the presence of a broad emission feature extending from 10.3 to 12.7μm. The authors suggested, that this feature is produced by solid SiC particles which might condense in a cool, carbon–rich atmosphere (as was demonstrated by [Gilman 1969], who came to this conclusion by chemical equilibrium calculations). Nearly one decade later, a second broad emission feature was detected, which extends from 24μm ([Forrest *et al.* 1981]) to at least 37μm ([Herter *et al.* 1982]). This feature also was attributed to a solid state resonance of some sort of dust grains ([Forrest *et al.* 1981]), possibly condensed MgS ([Goebel and Moseley 1985]).

With the increasing data base it became possible during the years to investigate the long term temporal behaviour of IRC +10216. By analyzing the photometric data obtained between 1965 and 1978, [Witteborn *et al.* 1980] first noted, that the variability of IRC +10216 is irregular, and that the minima of the 2.2 μm lightcurve have become fainter by about one magnitude over a timescale of 10 yrs.

Recent interferometric observations at 11μm, combined with earlier measurements clearly indicate, that the inner radius of the dust shell varies with the phase of the star's luminosity ([Danchi *et al.* 1990]). These authors found, that the inner edge of the dust shell is located at $\approx 2.5R_\star$ during light minimum and at $\approx 3R_\star$ during light maximum. They interpret this variation by means of periodic dust formation near the phase of minimum light at a temperature of $\approx 1300 - 1500$K.

An extensive compilation of photometric and interferometric data, covering the time interval between 1965 and 1990 confirmed, that long term structural changes definitely occur in the circumstellar shell around IRC +10216 ([Dyck *et al.* 1991]). They found, that the decrease of the mean K magnitude by 1.2 mag between 1969 and 1978 (already noted by [Witteborn *et al.* 1980]) was followed by an increase of the mean magnitude at 2.2 μm by 0.2 mag until 1990, when the latest data of their compilation were obtained. Also the visibility curves at 2.2 μm obtained from north–south scans across the object indicate systematic changes in the spatial shell structure between 1979 and 1990. [Dyck *et al.* 1991] discuss several models, which could account for these structural changes, e.g. an orbiting mass element, which has moved into the line of sight, or simply an outwards moving mass element, that has left the field of view, or enhanced dust formation concentrated north–northeast of the central star (possibly due to an asymmetry in the mass loss mechanism). As the first spatial observations used for this investigation stem from 1979, which almost coincides with the long term minimum in the lightcurve in 1978, the latter suggestion would be consistent with the finding of [Danchi *et al.* 1990], that new dust preferentially forms during the phases of low luminosity. The dust formation event suggested by [Dyck *et al.* 1991] would then correspond to an exceptionally deep minimum of the long term light variation.

Apart from these interesting dynamic features, the shell of IRC +10216 has also proven to represent a giant chemistry factory. Until 1990, 36 circumstellar molecules (plus numerous isotopic species) have safely been identified in this object ([Lucas and Guélin 1990]). More than 20 of these molecules are organic compounds (cf. [Lucas and Guélin 1990]) and several of the molecules found in the IRC +10216 shell were first detections outside the solar system (the latest now being MgNC, cf.

[Guélin *et al.* 1993]).

Since the shell of IRC +10216 is expanding with a velocity of $v_\infty \approx 14\,\mathrm{kms^{-1}}$ (e.g. [Olofsson *et al.* 1993a]), these chemical species together with the dust grains, which have formed in the circumstellar shell, are injected into the interstellar medium, presently at a rate of about $5 \cdot 10^{-5} M_\odot \mathrm{yr}^{-1}$ ([Knapp and Morris 1985]). Thus, the material from which this star once has formed, is now being recycled and may serve as a source of processed matter from which the formation of new stars or planets can be fed.

Due to its unusual properties and its exceptional brightness in the long wavelength spectral region, which makes it an easy target for astronomers, IRC +10216 probably is one of the best observed stellar objects in the sky besides our sun. At the present time (end of 1993) the SIMBAD database (a compilation of the complete astrophysical literature) contains 637 references to investigations, which are concerned with this astonishing C–rich AGB star.

4.8 A model for IRC+10216

In the following sections we discuss the structure and infrared appearance of a self-consistent stationary dust driven wind model characterized by the stellar parameters $M_\star = 0.7 M_\odot$, $L_\star = 2.4 \cdot 10^4 L_\odot$, $\dot{M} = 8 \cdot 10^{-5} M_\odot \mathrm{yr}^{-1}$ and a carbon to oxygen ratio of $\epsilon_\mathrm{C}/\epsilon_\mathrm{O} = 1.40$.

This model yields a synthetic spectrum and spatial intensity distributions, that closely approximate the observed spectrum and visibilities of the carbon star IRC +10216 at maximum light. However, the terminal outflow velocity of $20.7\,\mathrm{kms^{-1}}$ resulting from this model calculation is significantly higher (about $6\,\mathrm{kms^{-1}}$) than the respective value presently observed for IRC +10216 ($13.7\,\mathrm{kms^{-1}}$ – $14.8\,\mathrm{kms^{-1}}$, e.g. [Olofsson *et al.* 1993a]). This discrepancy is discussed in Sect. 4.8.4 and possible reasons for this failure are given.

4.8.1 Radial structure

In Fig. 4.23 (p. 89) the radial structure of this dust shell model is shown. The formation of dust grains starts around $1.4 R_0$ ($R_0 = 9.25 \cdot 10^{13}$cm), which leads to a steep increase of the dust extinction χ_H and, therefore, of the radiative force accelerating the dust grains. By momentum coupling of the grains to the surrounding gas, the momentum gained by the dust particles is transferred to the gas. This process results in an outward directed net acceleration ($\alpha > 1$ for $r > 2.25 R_0$) of the grain-gas mixture and, therefore, in an increasing outflow velocity v of the material. The transition from subsonic to supersonic motion occurs at $r = r_\mathrm{c} = 2.2 R_0$ where α reaches a value of 0.75. Around $3 R_0$ the wind velocity exceeds the local escape velocity v_esc. The atmospheric material, therefore, is lifted out of the stellar gravitational field within the first two stellar radii above the photosphere. The final outflow velocity of $20.7\,\mathrm{kms^{-1}}$ (cf. Sect. 4.8.4) is nearly reached at $20R_0$.

The essential acceleration of the material occurs in the region between $2R_0$ and $5\,R_0$. In the region of effective dust formation and growth (around $r = 2.5R_0$) the gas temperature is $T^{\mathrm{g}} \approx 1300\mathrm{K}$, while the mass density in this region is about $10^{-14}\mathrm{gcm^{-3}}$. Thermal dust emission from the inner edge of the circumstellar shell heats the gas inside the dust formation zone. The dust opacity, thus, leads to a substantial backwarming which results in an almost constant temperature throughout the region of effective dust formation. The size–independent dust temperature T^{d} (cf. Eq. (3.67)) exceeds the (grey) gas temperature. The temperature difference produced by this greenhouse effect increases with increasing distance from the photosphere. The temperature difference between gas and dust reaches a maximum value of about 50K in this model.

The final degree of condensation reached in this calculation is $f_{\mathrm{c}} = 42\%$. Thus, Eq. 4.7 (inserting $\epsilon_{\mathrm{C}}/\epsilon_{\mathrm{O}} = 1.40$ and the solar value of $\epsilon_O = 6.6 \cdot 10^{-4}$) yields a dust–to–gas ratio by mass of $\rho^{\mathrm{d}}/\rho^{\mathrm{g}} = 9.56 \cdot 10^{-4}$. With the total mass loss rate of the model, $\dot{M} = 8 \cdot 10^{-5} M_{\odot}\mathrm{yr}^{-1}$, this ratio is equivalent to a dust mass loss rate of $\dot{M}^{\mathrm{d}} = 7.65 \cdot 10^{-8} M_{\odot}\mathrm{yr}^{-1}$. A more vivid idea of this number may be gained by scaling it in units of earth masses per year: $\dot{M}^{\mathrm{d}} = 2.55 \cdot 10^{-2} M_{\mathrm{earth}}\,\mathrm{yr}^{-1}$. In other words, if the model presented here is in fact appropriate to describe IRC +10216, then this object looses material in form of solid carbon particles at a rate which amounts to the mass of one earth every 39.3yrs !

Values for the mass loss rate and the dust–to–gas ratio for IRC +10216 have also been derived from CO (1–0) rotational line observations and from spectral fits to the infrared continuum, respectively e.g. by [Knapp 1985]. She finds a total mass loss rate of $\dot{M} = 4.4 \cdot 10^{-5} M_{\odot}\mathrm{yr}^{-1}$ (assuming a model for the CO line emission, see [Knapp and Morris 1985]) and a dust–to–gas ratio of $\rho^{\mathrm{d}}/\rho^{\mathrm{g}} = 1.3 \cdot 10^{-3}$ (applying the simple parameterized dust shell model of [Rowan-Robinson and Harris 1983]). The estimated uncertainty of both values is about a factor of 2 (apart from the uncertainty of the distance to IRC +10216, cf. [Knapp 1985] and [Veen and Rugers 1989]). From these observed values, one gets a dust mass loss rate of $\dot{M}^{\mathrm{d}} = 5.7 \cdot 10^{-8} M_{\odot}\mathrm{yr}^{-1}$, or equivalently one earth mass lost every 52.6yrs in form of solid particles. Thus, the theoretical values of mass loss rate and dust–to–gas ratio are consistent with the respective observed values within the estimated errors quoted above.

These numbers further underline, that the total galactic mass injection rate is essentially brought up by late–type stars during the short time ($\approx 10^4$yr) of heavy mass loss at the very end of their AGB evolution (e.g. [Jura 1991]).

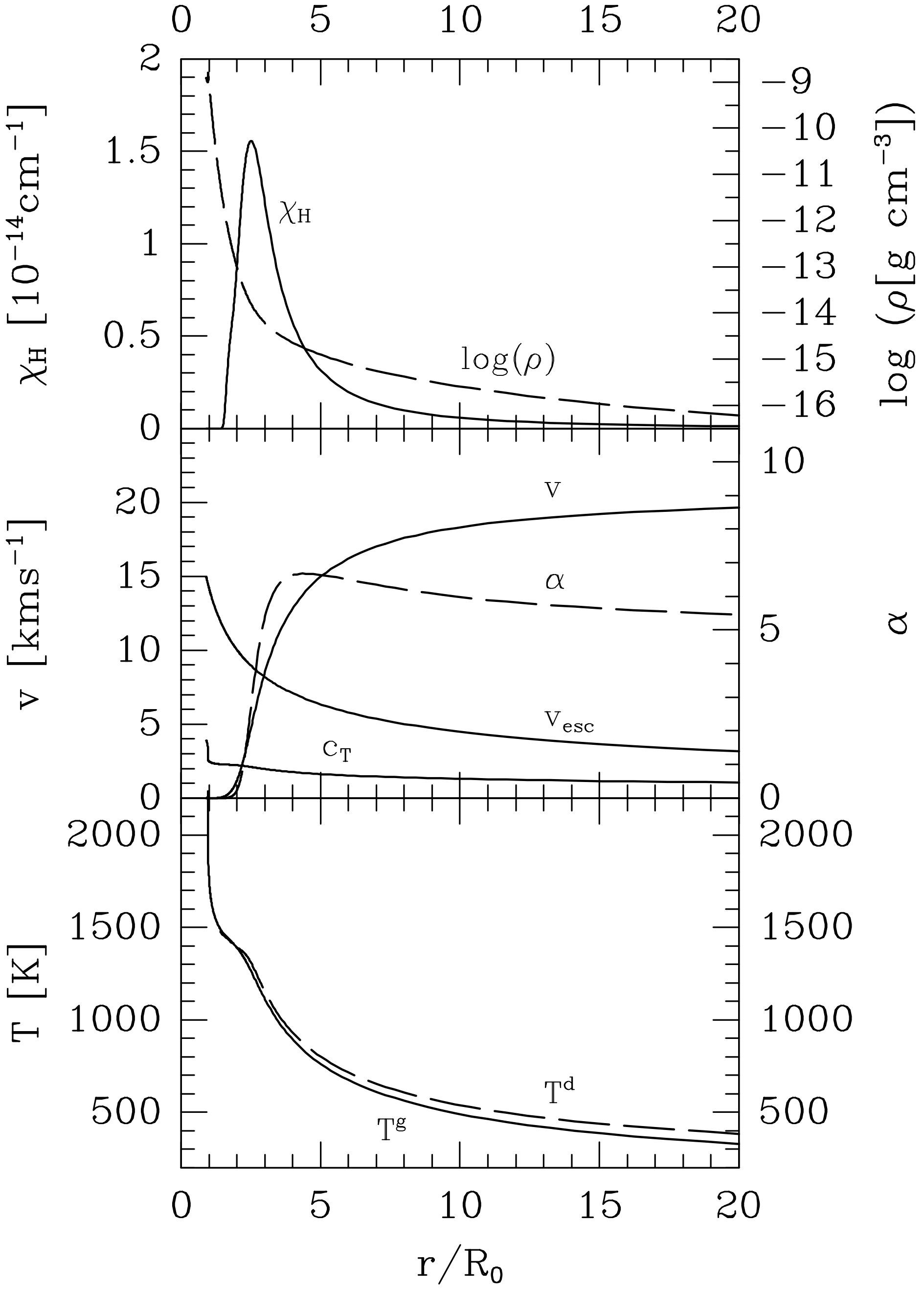

Figure 4.23: Radial structure of the dust shell.
Upper diagram: flux-mean extinction coefficient χ_H of the dust component (solid line, l.h.s. ordinate) and logarithm of the density ρ (dashed line, r.h.s. ordinate);
middle diagram: hydrodynamic velocity v and velocity of sound c_T (l.h.s. ordinate) and radiative acceleration in units of the local gravitational deceleration α (r.h.s. ordinate);
lower diagram: temperature of the gas (solid line) and the dust component (dashed line).

4.8.2 Spatial intensity distribution

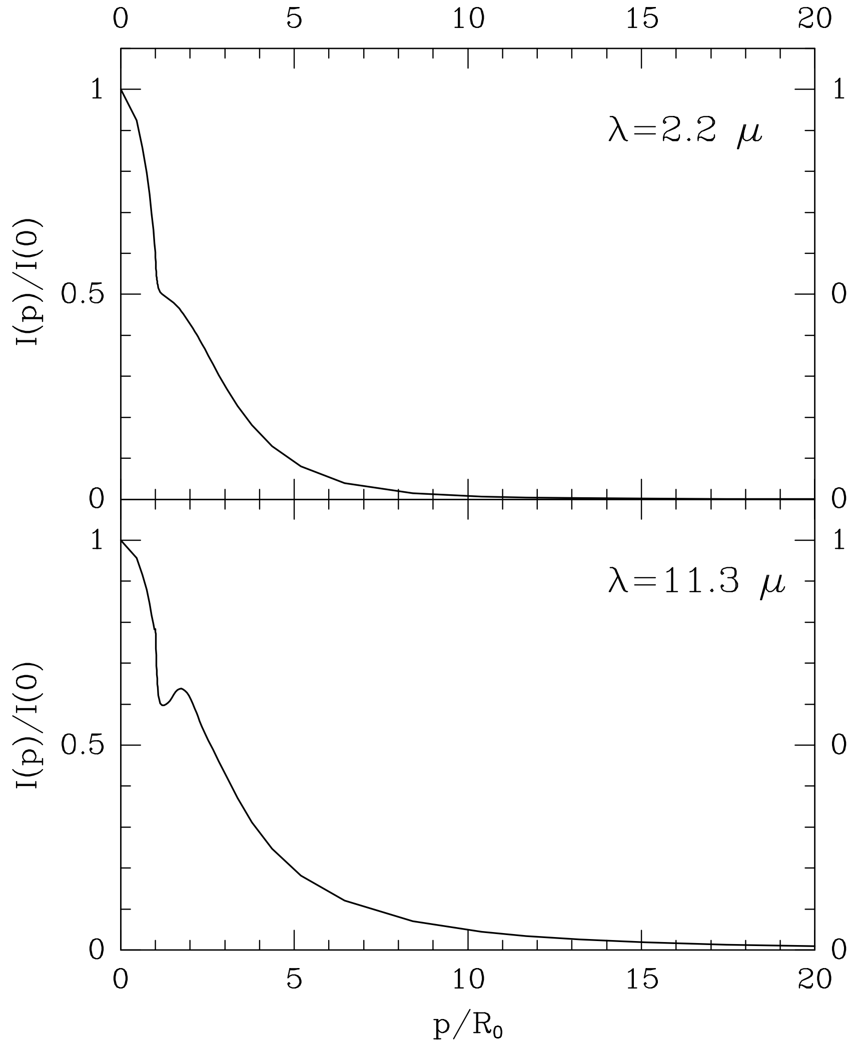

Figure 4.24: Calculated spatial brightness distribution at the outer shell boundary. Upper diagram: $\lambda = 2.2\mu$m, lower diagram: $\lambda = 11.3\mu$m. The abscissa gives the normalized impact parameter p of the line of sight with respect to the center of the star.

The spatial structure of the CDS may be accessible to observations either by direct mapping, which requires very high direct angular resolution of the telescope, or by interferometric techniques. In Fig. 4.24 the calculated center-to-limb variation of the specific intensity is shown at the outer boundary of the dust shell for two different wavelengths. Besides the main maximum at the center, a pronounced secondary maximum of the emergent 11μm intensity is seen at an impact parameter $p \approx 2R_0$, which is caused by thermal dust emission from the dense inner region of the dust shell.

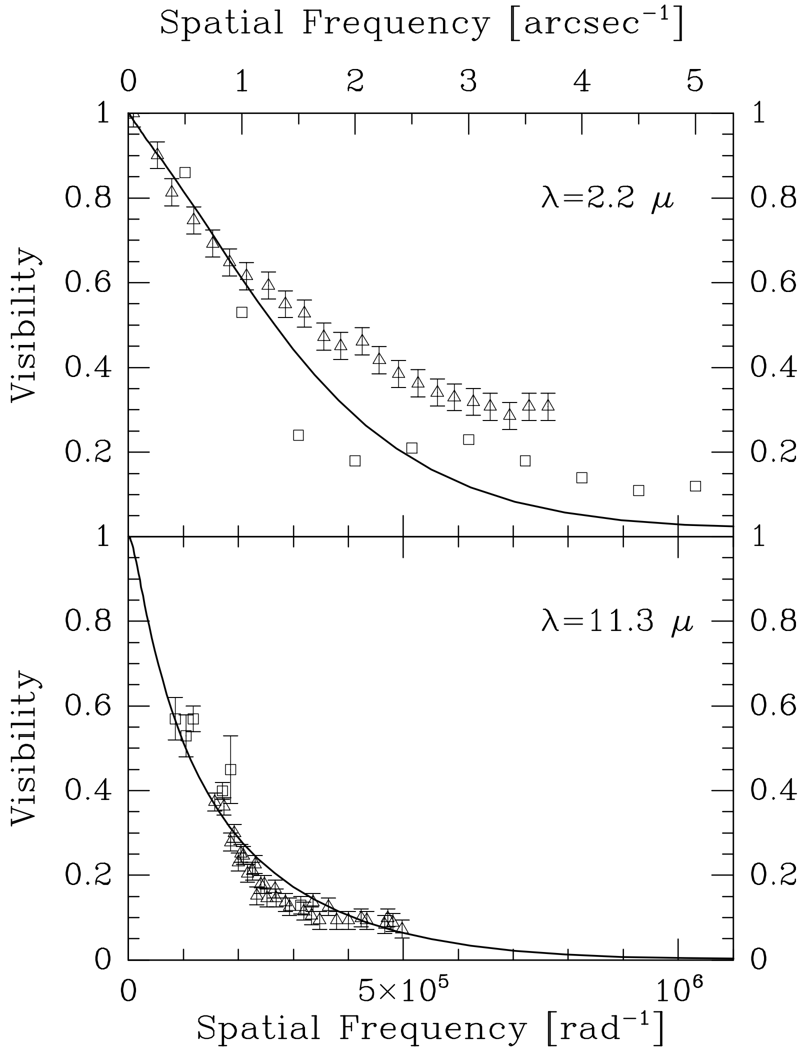

Figure 4.25: Calculated visibility (solid lines) at 2.2μm (upper diagram) and 11.3μm (lower diagram) compared with the interferometric observations of: [Ridgway and Keady 1988] ($\square$, N-S scan) and [Dyck *et al.* 1984] ($\triangle$, E-W scan) at 2.2μm (upper diagram) and of [McCarthy *et al.* 1980] ($\square$, at 10.2μm, 11.1μm and 12.5μm) and of [Sutton *et al.* 1979] ($\triangle$) at 11.1μm (lower diagram). All observed values are obtained near maximum light.

Due to the larger optical depth at 2.2μm ($\tau_{2.2\mu} = 6.05$, $\tau_{11.3\mu} = 1.31$), the spatial intensity distribution at this shorter wavelength merely exhibits a plateau–like structure around $2R_0$. At an assumed distance of 170 pc (cf. Sect. 4.8.3), this striking intensity structure would subtend an angular region of $\approx 0.15''$ diameter, which is too small to be directly resolved with current IR telescopes. Interferometric observations of IRC +10216 have been performed by several authors at different wavelengths (e.g. $1.6-4.8\mu$m ([Dyck *et al.* 1984]); $1.6-5\mu$m ([Ridgway and Keady 1988]); $2.2-20\mu$m ([McCarthy *et al.* 1980]); 2μm and 11μm ([Dyck *et al.* 1987]);

11μm ([Sutton *et al.* 1979]; [Danchi *et al.* 1990]; [Danchi *et al.* 1994]). These observations reveal an asymmetric spatial structure of the source at wavelengths shorter than 5μm ([Dyck *et al.* 1984]; [Dyck *et al.* 1987]; [McCarthy *et al.* 1980]; [Ridgway and Keady 1988]) while in the 10μm region no major asymmetries are found ([Dyck *et al.* 1987]; [Sutton *et al.* 1979]). A temporal variation of the visibility data with the phase of the light curve is also seen at 2.2μm ([Dyck *et al.* 1984]), 5μm ([McCarthy *et al.* 1980]) and at 11μm ([Danchi *et al.* 1990]; [Danchi *et al.* 1994]).

In Fig. 4.25 the calculated visibility of the dust shell model is shown at $\lambda = 2.2\mu$m (upper diagram) and $\lambda = 11.3\mu$m (lower diagram) together with the corresponding visibility data observed near the maximum of the 2.2μm light curve. In the 10μm region we find a rather satisfactory agreement between the calculated and the observed visibility. The agreement between calculated and observed visibilities at 2.2μm, however, is less satisfactory. This may be due to the fact, that our model is spherically symmetric, whereas the observations indicate an asymmetric shape of the IRC +10216 shell at this wavelength (cf. upper diagram of Fig. 4.25, where two perpendicular scans across the source are shown). However, it should be noted that our result is much closer to the observed 2.2μm visibility than the parameterized, also spherical model of [Martin and Rogers 1987]. In their model, the emergent intensity at 2.2μm drops by a factor of ≈ 30 at the outer edge of the central star which produces high values of the visibility at high spatial frequencies. They obtain a considerable improvement between observed and calculated values by a "flat interpolation through the central region" of the emergent 2.2μm intensity resulting from their model.

In order to calculate the theoretical fringe visibilities from the spatial intensity distribution, the radial coordinate has to be converted to an angular separation from the center of the star. For the results shown in Fig. 4.25 we had to assume a distance of 140pc to IRC +10216, which is about 20% less than the value derived from the spectrum (cf. next section). Although both values are in reasonable agreement, this difference in the derived distance values may point at a problem of our treatment of grain condensation by classical nucleation theory. In our models the nucleation of dust grains starts at rather high temperatures of ≈ 1400K i.e. relatively close to the photosphere. Theoretical investigations of the more realistic microscopic treatment of grain formation by calculating the chemical pathway indicate, that carbon grains should form at a lower temperature around ≈ 1000K ([Keller 1987]; [Gail and Sedlmayr 1987a]; [Cherchneff *et al.* 1992]) and, thus, at a larger distance from the star. This would lead to a more extended intensity distribution and thus to visibility curves, which are more strongly peaked towards small spatial frequencies. In other words: if the onset of grain nucleation would take place at a larger separation from the star, we had to assume a larger distance to the star in order to obtain the same fit to the observed values as shown in Fig. 4.25. In order to retain the distance of 170pc, the onset of dust formation has to be shifted outwards by a factor of 1.2 to a location at around $1.7R_0$.

4.8.3 Emergent spectrum

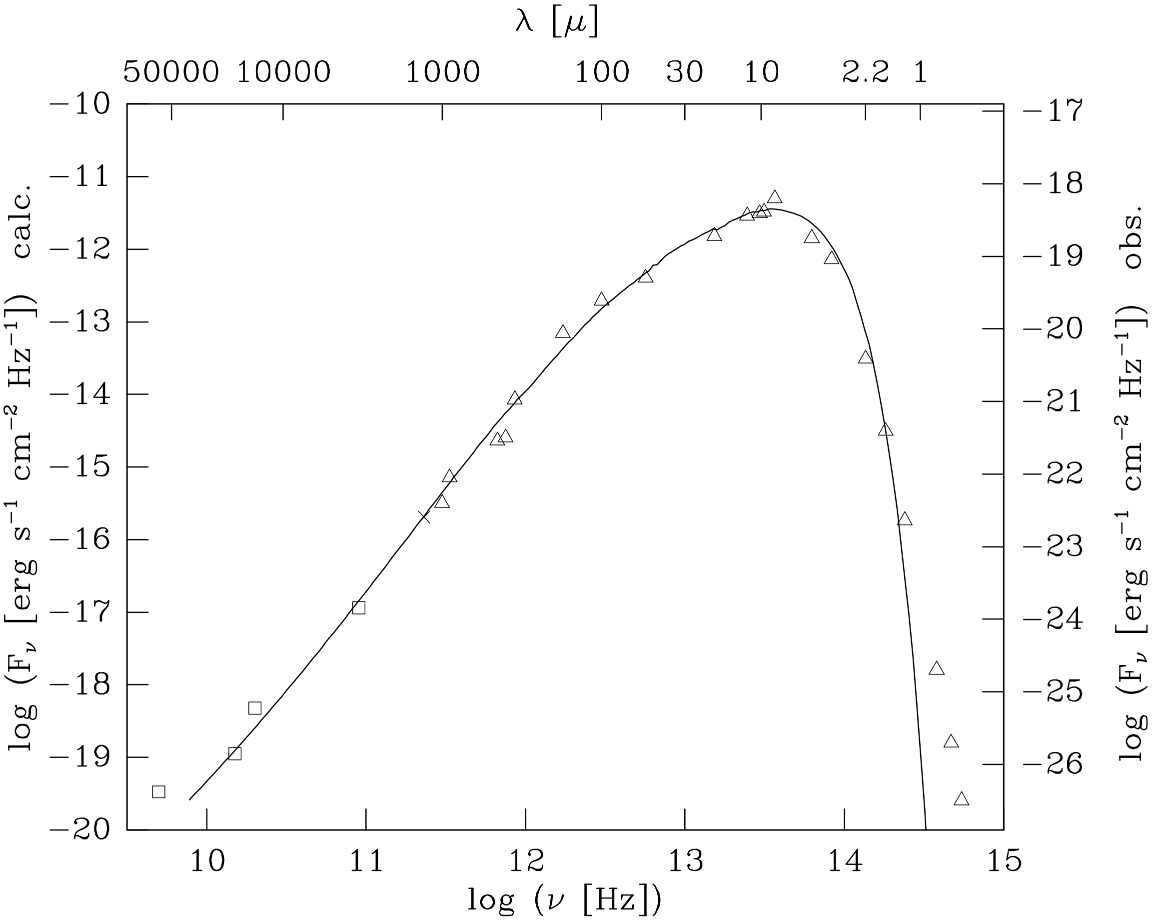

Figure 4.26: Emergent spectrum of the dust shell model described in the text (solid line). The observed data for IRC +10216 are taken from [LeBertre 1987] and references therein (△), [Sahai *et al.* 1989] (□) and [Walmsley *et al.* 1991] (×).

In Fig. 4.26 the energy distribution produced by the dust shell model is shown together with observed photometric data of IRC +10216. This source is known to be variable with a period of $\sim$ 640d ([Witteborn *et al.* 1980]; [Ridgway and Keady 1988]). The symbols shown in Figs. 4.26 and 4.27 represent fluxes measured near the maximum of the 2.2μm light curve. The calculated spectrum shown in Fig. 4.26 results from assuming amorphous carbon described by the complex refractive index tabulated in [Maron 1990]. The outer boundary of the dust shell model is located at $2 \cdot 10^3 R_0$ which corresponds to a distance from the center of the star of $1.85 \cdot 10^{17}$cm. The synthetic spectrum of this model is in close agreement with the observed spectrum of IRC +10216 in the wavelength region between 2μm and 5cm. In the near infrared region shortward of $\lambda \approx 2\mu$m the calculated spectrum decreases much too steeply as compared to the observed fluxes. As discussed in Sect. 4.6, this behaviour may be due to the existence of unrealistically large dust particles in the inner part of the dust shell model, which is a result of the assumption of stationarity. A second, probably more important reason could be our assumption of spherical geometry, which cannot account for possible 'holes' in the dust shell, which would produce smaller optical depths along certain lines of sight in direction to the central object. In consequence, short wavelength radiation originating from the photosphere could escape through such holes and thus could lead to an emergent short wavelength flux which is possibly considerably enhanced compared to the flux resulting from a spherically symmetric model.

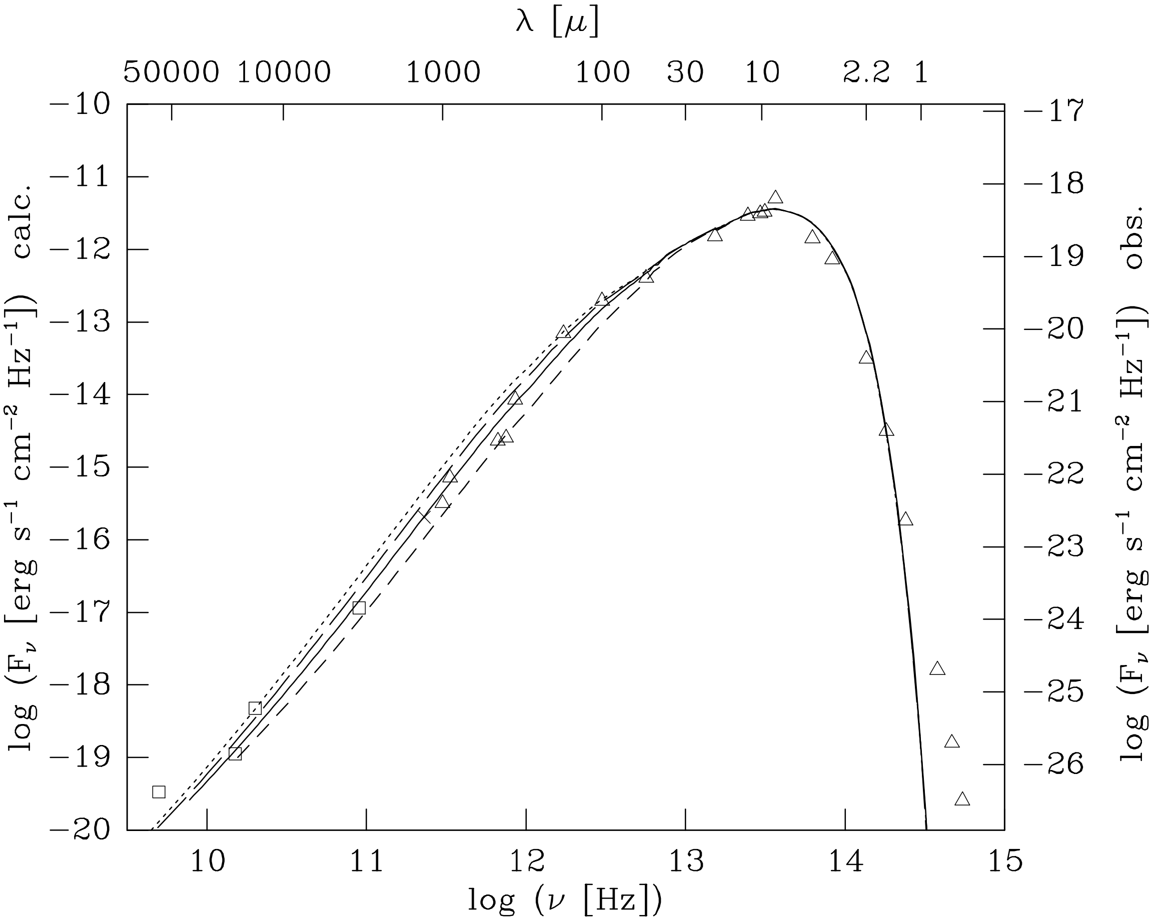

Figure 4.27: The effect of varying the location of the outer boundary. Observed data are the same as in Fig. 4.26. The outer boundary is located at: $5 \cdot 10^2 R_0$ (short-dashed curve, calculated values multiplied by 1/16); $2 \cdot 10^3 R_0$ as in Fig. 4.26 (solid curve); $5 \cdot 10^3 R_0$ (long–dashed curve, calculated values multiplied by 6.25) and $1 \cdot 10^4 R_0$ (dotted curve, calculated values multiplied by 25). The observed spectrum is best represented for an outer shell boundary located at $2 \cdot 10^3 R_0$ (solid curve).

The dependence of the FIR flux on the location of the outer boundary is shown in Fig. 4.27. The solid line is the same as in Fig. 4.26 with $R_{\max} = 2{\cdot}10^3 R_0$. A reduction of the shell extension to $5 \cdot 10^2 R_0$ leads to a reduction of the FIR flux of the calculated spectrum as indicated by the short-dashed curve (the calculated flux values are multiplied by a factor of 1/16 in order to eliminate the pure geometrical effect). The dotted curve results from a location of the outer boundary at $10^4 R_0$ (the calculated values are increased by a factor of 25), which produces too much flux at wavelengths larger than $\approx 200\mu$m. Thus, the observed mid– and FIR spectrum of IRC +10216 is best reproduced by our model for an outer shell radius of $R_{\rm max} = 2 \cdot 10^3 R_0$ (cf. Fig. 4.26).

From CO (2–1) line observations [Knapp *et al.* 1982] and [Huggins *et al.* 1988] find that the CO molecular envelope around IRC +10216 extends out to ~ 3 arcmin. Outside this radius the CO molecule is presumably destroyed via photodissociation by the interstellar radiation field. If the dust shell is even more extended, it is, thus, at least optically thin for the CO dissociating UV photons. Since the dust extinction decreases with increasing wavelength, there should also be no relevant contribution to the emergent flux by thermal dust emission at FIR wavelengths from this outer region. Therefore, we consider the measured outer radius of the CO envelope also as an upper limit for the relevant extension of the dust shell.

As the stellar luminosity is a physical parameter of our models, we can estimate the distance to IRC +10216. If we assume that there is no interstellar extinction in direction to the object, then the distance d is given by

$$d = R_{\rm max} \left(\frac{F_{\nu,\rm calc}(R_{\rm max})}{F_{\nu,\rm obs}(d)} \right)^{\frac{1}{2}} \quad . \tag{4.9}$$

With $R_{\rm max} = 2 \cdot 10^3 R_0 = 1.85 \cdot 10^{17}$cm, Eq. (4.9) yields $d \approx 170$pc. Given this distance the measured angular shell extension of $3'$ yields an outer radius of the IRC +10216 envelope of $4.58 \cdot 10^{17}$cm. In our model this corresponds to $R_{\rm max} = 4.95 \cdot 10^3 R_0$. With this value for the outer boundary (long–dashed curve in Fig. 4.27), the calculated flux is slightly higher than the observed spectrum at wavelengths longward of $\lambda = 200\mu$m. As the stationary models are likely to overestimate the thermal emission in the outer parts of the shell (Sect. 4.6), this flux deviation should not be attached too much importance to.

The total mass contained in the circumstellar shell results to $M_{\rm CS} = 0.60 M_\odot$ for $R_{\rm max} = 2 \cdot 10^3 R_0$ and $M_{\rm CS} = 0.95 M_\odot$ for $R_{\rm max} = 5 \cdot 10^3 R_0$, respectively from our calculations. These values imply a mass of the main sequence progenitor of IRC +10216 of $M_{\rm ZAMS} > 1.30 M_\odot$.

The distance of 170pc to IRC +10216 is about 60 per cent smaller than the often quoted value of 290pc suggested by [Herbig and Zappala 1970]. They assume an absolute bolometric magnitude of $M_{\rm bol} = -7$ ($L_\star = 4.88 \cdot 10^4 L_\odot$) for IRC +10216 and a value for the measured bolometric flux of $2 \cdot 10^{-12}$Wcm^{-2}. However, it is not clear at which phase of the light curve this value is obtained. The distance to IRC +10216 of 170pc as derived from our synthetic spectrum, on the other hand, is in rather good agreement with the value of ≈ 150pc which was first suggested by

[Zuckerman *et al.* 1986] and has recently been supported by [Kastner 1992].

4.8.4 The final outflow velocity

As already mentioned above, the terminal velocity $v_\infty = 20.7\,\mathrm{kms}^{-1}$ resulting from the model calculation presented here is significantly higher than the value of ≈ 14 – $15\,\mathrm{kms}^{-1}$ observed for IRC +10216 (e.g. [Olofsson *et al.* 1993a]).

The terminal outflow velocity resulting from the model calculations can effectively be reduced by reducing the carbon abundance ϵ_C (cf. Sect. 4.5). A model fixed by the same mass loss rate $\dot{M} = 8 \cdot 10^{-5} M_\odot \mathrm{yr}^{-1}$, luminosity $L_\star = 2.4 \cdot 10^4 L_\odot$, and stellar mass $M_\star = 0.7 M_\odot$ as the IRC +10216 model, but with a reduced carbon–to–oxygen ratio of e.g. $\epsilon_\mathrm{C}/\epsilon_\mathrm{O} = 1.25$ yields a terminal velocity of $v_\infty = 14.4\,\mathrm{kms}^{-1}$. A reduction of ϵ_C however, simultaneously leads to a significant "blue shift" of the emergent spectrum (cf. Sect. 4.5), which would no longer match the observed energy distribution of IRC +10216. Thus, in order to compensate for this effect, we additionally have to reduce the stellar luminosity $L_\star$ and/or to increase the mass loss rate $\dot{M}$, which both would lead to a "red shift" of the spectrum (cf. Sect. 4.5). An alternative model, which also would fit the individual observations of IRC +10216 reasonably well is fixed by the set of parameters $M_\star = 0.7 M_\odot$, $L_\star = 2.3 \cdot 10^4 L_\odot$, $\dot{M} = 8 \cdot 10^{-5} M_\odot \mathrm{yr}^{-1}$, and $\epsilon_\mathrm{C}/\epsilon_\mathrm{O} = 1.30$. This model yields a terminal velocity of $16.6\,\mathrm{kms}^{-1}$, a spectrum very similar to the one presented in Fig. 4.26 and also visibilities very similar to those depicted in Fig. 4.25. For the alternative model we derive a distance to IRC +10216 from the measured flux again of $d \approx 170$pc but a value of $d \approx 120$pc from the measured visibilities and, thus, obtain an inconsistency of about 40% between both distances derived for the same object. Therefore, and for the reason given below, we have chosen to put up with the too high value of the terminal velocity.

The main problem of the approach presented here, is of course the application of a stationary model for the interpretation of a pulsating object. As discussed in Sects. 4.4.2 and 4.6, this assumption leads to the formation of unrealistically large particles in the region around the sonic point, which absorb radiative momentum less effectively than the same amount of dust contained in small particles would do. In order to surmount the Eddington limit (Eq. (4.3)), i.e. in order to provide the energy, necessary to lift the material out of the star's gravitational field, therefore, a larger amount of condensed material is needed if the grains are large compared to the typical wavelength of the radiation field. In the models, this larger degree of condensation can be achieved by increasing the carbon abundance over the value needed for small particles to drive the wind. The higher degree of condensation, however, also leads to a more effective acceleration of the wind in the region outside the sonic point and, thus, to higher terminal velocities (cf. Sect. 4.5).

In the real pulsating objects two effects are present, which are in favour for smaller outflow velocities:

i) the particles remain smaller (cf. Sect. 4.6) and

ii) the dissipation of shock wave momentum supports the levitation of the material out of the gravitational field, i.e. a smaller contribution of radiative acceleration is needed in the inner shell region to separate the material from the star.

In fact, the dynamic calculations of [Fleischer *et al.* 1992] and [Fleischer 1994] for dust forming shells around long–period variable stars yield lower terminal wind velocities as do the stationary models presented here. Detailed radiative transfer calculations in these time–dependent models are presently being performed. The first results are presented in Chapter 5.

4.9 Conclusions

Selfconsistent models of spherically symmetric, stationary dust driven winds around cool carbon stars have been discussed. These models include a detailed treatment of hydrodynamics, thermodynamics, chemistry, dust formation and growth and of the radiative transfer problem. In this approach, the structure of the dust shell is completely fixed by four parameters: stellar mass M_*, stellar luminosity L_*, mass loss rate $\dot{M}$ and the initial element composition of the gas ϵ_i. The transport coefficients of the dust grains are calculated by means of Mie theory for homogeneous spherical particles of arbitrary size, taking explicitly into account the resulting local size distribution function of the dust grains.

The results discussed in this chapter imply, that in a stationary dust driven wind the common assumption of the small particle approximation for calculating the transport coefficients of the dust component is not justified. Especially in the inner region of the dust envelope, where the mass outflow is generated by radiation pressure on dust grains, the dust opacity and, thus, the radiative force acting on the grains, is strongly reduced by the presence of the large particles. This effect considerably increases the value of the Eddington limit, which has to be exceeded in order to drive the outflow by radiation pressure on dust alone. Furthermore, these large particles in the inner shell region give rise to a considerably increased final outflow velocity of the wind.

The theoretical spectra produced by the dust shell models are in agreement with the FIR observations of cool carbon-rich AGB objects. The calculated spectra are sensitive to variations of the mass loss rate, the stellar luminosity and the initial carbon abundance. Within the range of stellar masses, for which purely dust driven winds exist for reasonable values of the stellar luminosity, the calculated spectra are almost independent of the stellar mass. In the NIR spectral region the response of the calculated colour indices to changes of the stellar parameters is only in qualitative agreement with the observed colour indices. The absolute values of the theoretical colour indices deviate in a systematic way from the observations. This deviation is most probably a consequence of the stationary approach. The assumption of stationarity results in the formation of rather large dust grains in the circumstellar shell. As the real dust forming objects are mostly pulsating variables, the formation of very large grains is prevented by the limitation of the time available for grain growth due to significant periodic changes of the hydrodynamic and thermodynamic conditions in the dust forming region. Thus, for a quantitative reliable calculation of the NIR spectra the effects of pulsation have to be taken into account.

Investigations with regard to a dynamic modelling are currently under way. Based on the time–dependent model calculations of [Fleischer *et al.* 1992] and [Fleischer 1994] for circumstellar dust shells around long–period variable stars, we already have calculated the synthetic lightcurves and colour indices of these models (see Chap. 5). A detailed discussion of the complete resulting spectra will be performed in the near future.

Applying the stationary model calculations to IRC +10216, we find a satisfactory agreement with the observed energy distribution and the observed interferometric data obtained at light maximum for a model, which is fixed by a stellar mass $M_\star = 0.7 M_\odot$, a stellar luminosity $L_\star = 2.4 \cdot 10^4 L_\odot$, a mass loss rate $\dot{M} = 8 \cdot 10^{-5} M_\odot \mathrm{yr}^{-1}$ and a carbon to oxygen ratio $\epsilon_\mathrm{C}/\epsilon_\mathrm{O} = 1.40$. From the spectral energy distribution of this model we obtain a distance to IRC +10216 of $d = 170\,\mathrm{pc}$ and a mass contained in the circumstellar shell of $0.6 M_\odot \leq M_\mathrm{CS} \leq 0.95 M_\odot$. The comparison between observed and calculated visibilities yields a distance of $d = 140\,\mathrm{pc}$. This difference may result from our treatment of carbon grain condensation by classical nucleation theory, which leads to the formation of grains already at relatively high temperatures and, thus, close to the stellar photosphere. A larger separation of the grain formation zone from the photosphere, as is expected if carbon grain condensation proceeds via the formation of PAHs, possibly could resolve this problem.

Despite of the shortcomings mentioned above, which are largely due to the application of stationary theoretical models to in reality pulsating objects, we achieve satisfactory agreement with important observed quantities by applying a selfconsistent model which involves only the four fundamental parameters.

Zu jeder Zeit t wird der Theoretiker besonders daran interessiert sein, die am besten prüfbare der konkurrierenden Theorien zu finden und zu prüfen. Ich habe gezeigt, daß dies gleichzeitig die Theorie mit dem größten Informationsgehalt und der größten Erklärungskraft ist. [...] Besteht sie die Prüfungen, so ist sie auch die am besten geprüfte der bisher betrachteten Theorien einschließlich aller ihrer Vorgänger.

Diese Aussagen über „die beste“ Theorie gehen davon aus, daß eine gute Theorie nicht ad–hoc ist. Die Idee des ad–hoc–Charakters und ihr Gegenteil, das man „Kühnheit“ nennen könnte, sind sehr wichtig. Ad–hoc–Erklärungen sind solche, die nicht unabhängig prüfbar sind, unabhängig von dem zu erklärenden Effekt. Sie sind billig zu haben und sind deshalb von geringem theoretischem Interesse.

Karl R. Popper: Objektive Erkenntnis

Chapter 5

Optical appearance of dynamic models of LPV atmospheres

Based on the dynamic models of circumstellar dust shells (CDS) of [Fleischer *et al.* 1992, Fleischer 1994], which include time–dependent hydrodynamics and a detailed treatment of the processes of formation, growth and evaporation of carbon grains, frequency–dependent radiative transfer calculations have been carried out.

In this chapter, the resulting lightcurves, the near infrared (NIR) colour indices and the synthetic radial brightness distributions for three models are discussed and compared to observations of individual long–period variable stars (LPVs).

5.1 Introduction

LPVs are intrinsically cool AGB objects ($T_\star < 3500$K) many of which are surrounded by large amounts of dust. These dust particles are effective absorbers of radiative energy which they reradiate at longer wavelengths after an internal relaxation process. Therefore, most LPVs are primarily infrared sources.

Improved instrumental capabilities in this spectral range and in the millimeter range have led to an increased interest in observations of late–type giants in the last years and produced a vast amount of observed data. This provided an extensive basis for a more thorough understanding of these objects. Based on this material e.g. [Sopka *et al.* 1985], [Claussen *et al.* 1987], [Thronson *et al.* 1987], [Willems and deJong 1988], [Jura *et al.* 1989]), [Jura and Kleinmann 1989], [Groenewegen *et al.* 1992] were able to derive e.g. mass loss rates, gas–to–dust ratios, distances, luminosities or final outflow velocities for various large samples of objects.

Compared to this kind of investigations relatively little attention was drawn to a systematic photometric monitoring of LPVs in the infrared range. The up–to–date most complete set of observations was published recently by [LeBertre 1992], [LeBertre 1993]). His monitoring of C–stars [LeBertre 1992] covered observations of 23 objects in the $1 - 20\mu$m range during a period of ≈ 6 years. He is perhaps the first to note that the usual interpretation of lightcurves to be sinusoidal should be taken with care. The lightcurves of a large fraction of his sample of C–stars show "irregularities", i.e. some lightcurves exhibit a plateau on their ascending branches or even intermediate extrema, especially at short wavelengths. Since these "irregularities" are reproducible from cycle to cycle, they have to be considered as real features of the lightcurves. In addition he notes that some lightcurves show a drift in time either of the average magnitude or of the amplitude. Similar behaviour with "bumps" and secondary maxima on the rising as well as on the declining branch is reported for visual lightcurves by [Mattei *et al.* 1990].

Other authors, e.g. [Lockwood and Wing 1971], [Celis 1977], [Werner *et al.* 1980], [Feast *et al.* 1984], or [Jones *et al.* 1990] presented photometric observations either for a more restricted time interval, for only one object or only at one wavelength, or with a less continuous coverage of the observed time interval.

Regarding the spatial structure of the dust shells, rather detailed information e.g. on the location of the dust formation zone is gained from interferometric observations in the NIR spectral region. It was found, that the spatial extension of the dust shells varies with the phase of the star's lightcurve ([McCarthy *et al.* 1980, Dyck *et al.* 1991, Danchi *et al.* 1990, Danchi *et al.* 1994]), being interpreted by means of periodic dust formation close to the photosphere near the phase of minimum luminosity (e.g. [Danchi *et al.* 1990, Danchi *et al.* 1994]). The obtained visibility curves often show a rippled structure (e.g. [Dyck *et al.* 1984, Ridgway and Keady 1988, Dyck *et al.* 1991, Danchi *et al.* 1990, Danchi *et al.* 1994]), which, by image reconstruction leads to a step–like course of the one–dimensional radial brightness profiles (cf. [Ridgway and Keady 1988]). The physical mechanisms leading to these striking profiles, however, are not yet fully understood. The spatial spectra also reveal an increasing angular size of the dust shells proportional to a power of the wavelength and also an increase of the angular size proportional to the star's mass loss rate (e.g. [Dyck *et al.* 1984]). These findings may be used to constrain the optical properties of the dust material and the dust density.

Parallel to the advances on the part of observations, also the dynamic modelling of CDS around Miras and LPVs achieved fundamental improvements in the last years. Based on the pioneering papers of [Willson and Hill 1979] and [Wood 1979], [Bowen 1988]) and [Bowen and Willson 1991] improved this modelling approach by an inclusion of parameterized cooling laws which yield a more realistic modelling of the post–shock relaxation of the gas in the atmosphere. Very recently [Feuchtinger *et al.* 1993]) have formally overcome the problem of parameterized cooling laws by solving the complete set of equations of radiation hydrodynamics.

Nevertheless, all these models severely lack a detailed treatment of dust formation, growth and destruction. Instead, only a simple formula, first introduced by [Wood 1979], is assumed to simulate the acceleration by radiation pressure on dust.

This approach was shown to be insufficient to reveal the key role of the solid particles in determining the structure of the CDS [Fleischer *et al.* 1991] and [Fleischer *et al.* 1992, Fleischer 1994]).

In [Fleischer *et al.* 1992] and [Fleischer 1994] dynamic models of CDS around LPVs are presented, which include time–dependent hydrodynamics and a detailed treatment of the processes of formation, growth and evaporation of carbon grains. The models are calculated in the limit case of isothermal shocks, which, nevertheless, yield a realistic picture of the dynamic interactions which determine the internal structure of the CDS. In these calculations the radiative transfer problem is solved using the semi–analytical method of Lucy ([Lucy 1971], [Lucy 1976]) in grey approximation which yields a radiative equilibrium temperature structure at every instant of time but neither a spectrum nor a lightcurve or the brightness profiles of the model.

For the investigation presented here, we have coupled the hydro–code of [Fleischer *et al.* 1992, Fleischer 1994] with the frequency and angle–dependent radiative transfer code described in Sect. 3.2.4 to study the optical appearance of the time–dependent dust shell models.

This chapter starts with a short description of the modelling method. In Sect. 5.2.1 the approach to calculate the dynamic structure of the shell is summarized. Section 5.2.2 comprises a brief description of the radiative transfer code and the coupling to the hydro–code. During the rest of this chapter, three demonstrative shell models of carbon–rich LPVs are considered, which are specified by the parameters given in Sect. 5.3. In Sect. 5.4 some basic results of the hydrodynamic calculations are presented. Since the time–dependent dust shell models are discussed in detail in [Fleischer 1994], Sect. 5.4 contains only a summary of the main features of these results, which are relevant for the subsequent discussion of the optical appearance of these models. In Sect. 5.5 theoretical lightcurves in the wavelength range $0.5-200\mu$m are presented for these three models. A detailed analysis of the lightcurves resulting from one of the models is given in Sect. 5.5.1. This analysis demonstrates, how the shape of the lightcurves is influenced or even produced by the discrete structure of the CDS. In the subsequent section 5.5.2 the lightcurves of the three dust shell models are considered with respect to their long–term behaviour. These results are followed by a discussion in Sect. 5.5.3 where a comparison of the exemplary calculations with results from observations is drawn. The temporal behaviour of the NIR flux ratios resulting from the models is presented in the frame of a two colour diagram in Sect. 5.6, where also a discussion with respect to the observed facts is given. Subsequently, the radial brightness profiles and the synthetic visibilities produced by the dust shell models are discussed and qualitatively compared to the respective observations in Sect. 5.7. A direct comparison with the observed brightness profile of IRC +10216 finishes this section. The chapter ends with some conclusions concerning the time–dependent approach, given in Sect. 5.8.

5.2 The modelling method

Since the details of the modelling method and the basic equations solved with both codes have been discussed elsewhere ([Fleischer *et al.* 1992, Fleischer 1994], and Chap. 3 of this thesis), only a brief summary of the main ingredients is given here.

5.2.1 Hydrodynamic model calculation

A spherically symmetric dust forming circumstellar shell around a pulsating red giant with stellar mass $M_\star$, stellar temperature $T_\star$, luminosity $L_\star$ and pulsation period P is considered.

The time–dependent hydrodynamic equations are discretized on a Lagrangian mesh and solved by explicit integration according to the difference scheme given in ([Richtmyer and Morton 1967]). Cooling of the gas behind the shock fronts is assumed to take place instantaneously, i.e. the shocks are treated in the isothermal limit case as in the calculations presented in [Fleischer *et al.* 1992] and [Fleischer 1994]. If cooling of the post–shock gas is taken into account, the interaction processes among the physical subsystems become even more complicated but the discrete structure of the CDS is conserved (cf. [Gauger *et al.* 1993] and [Gauger *et al.* 1994]). Since a main cause for the behaviour of the observable results presented here is the periodic formation of dust, it is expected that the basic characteristics of the optical appearance discussed below, will also appear in models where time–dependent post–shock cooling of the gas is taken into account.

The set of moment equations describing dust formation, growth and dust destruction due to thermal evaporation developed by [Gail and Sedlmayr 1988]) and [Gauger *et al.* 1990]) is solved simultaneously. For the calculation of the dust complex it is essential to know the chemical composition of the gas phase. We use the same set of hydrocarbons (H, H_2, C, C_2, C_2H, C_2H_2) in chemical equilibrium as in [Fleischer *et al.* 1992] to calculate the particle densities of the species contributing to the growth of carbon grains. Solar abundances [Allen 1973]) are assumed for all elements except for the abundance of carbon ϵ_C which is considered as a free model parameter in order to account for a carbon–rich element composition.

For the calculation of the dynamic structure of the circumstellar shell the radiative transfer problem is treated by the semi–analytical method of ([Lucy 1971], [Lucy 1976]) which yields the local equilibrium temperature T_{eq} at every instant of time. Due to the assumption of isothermal shocks, the gas temperature T^g equals T_{eq} throughout the atmosphere at every instant of time.

At the inner boundary of the model a sinusoidal variation of the velocity with amplitude Δu and period P, the piston, is applied to simulate the interior pulsation of the star.

The models, therefore, are defined by the prescription of the 4 fundamental stellar parameters ($T_\star$, $L_\star$, $M_\star$, ϵ_i) and of (P, Δu) to describe the interior pulsation. To start the calculation an initial hydrostatic model with a selected number of grid points (here 1024) and the desired values of $T_\star$, $L_\star$ and $M_\star$ is constructed. Subsequently, the velocity amplitude of the piston is increased slowly until the maximum value is reached and the calculation of the dust complex is started simultaneously. The development of the model is followed until a cyclic pattern of the radial structure is reached.

5.2.2 Radiative transfer calculation

For a given radial structure of the dust shell model, i.e. at a fixed instant of time (every $0.05P$), the angle and frequency–dependent stationary radiative transfer equation is solved in spherical geometry. The radiation field is calculated by an iteration between the monochromatic moment equations (the system is closed by the variable Eddington factor) and the formal solution for the monochromatic specific intensity along the characteristic paths of the partial differential equation. At the inner boundary we apply the diffusion approximation in a form that provides a total flux of $L_\star/16\pi^2$ entering the atmosphere. The outer boundary condition is given by the assumption that no inward flowing radiation exists at $r = R_{\rm max}(= 60R_\star$ for the models presented in this chapter). For details of this method we refer to Sect. 3.2.4.

The radiative transfer processes considered are grey absorption and thermal emission of the gas and frequency–dependent absorption and thermal emission of the dust component. In order to keep consistency with the hydrodynamic model, the transport coefficients of the gas are replaced by an average absorption coefficient $\kappa^{\rm g}$ which gives a gas opacity of $\kappa^{\rm g}/\rho = 2 \cdot 10^{-4}{\rm cm}^2{\rm g}^{-1}$ (ρ: mass density) (cf. [Bowen 1988], [Fleischer *et al.* 1992]). This value roughly represents the Rosseland mean gas opacity in the relevant temperature and density range.

For calculating the dust opacity the dust particles are assumed to be spherical and small compared to the relevant wavelength of the radiation field. The assumption of the *small particle limit* is approximately justified for the time–dependent models considered here, since the mean particle radius remains smaller than 0.1μm throughout the circumstellar shell (cf. [Fleischer *et al.* 1992] and [Fleischer 1994]). With these assumptions the absorption coefficient of the dust component $\kappa_\nu^{\rm d}$ can be expressed as (cf. [Gail *et al.* 1984])

$$\kappa_\nu^{\rm d}(r) = \frac{8\pi^2 a_0^3}{\lambda} {\rm Im}\left\{\frac{m(\nu)^2 - 1}{m(\nu)^2 + 2}\right\} K_3(r) = \chi_\nu^{\rm d}(r)\,, \tag{5.1}$$

and equals the extinction coefficient of the dust component $\chi_\nu^{\rm d}$. Eq. (5.1) is obtained by inserting the small particle efficiency Eq. (3.24) into the definition of the extinction coefficient Eq. (3.15) and integrating over the particle size. For all calculations presented here, the complex refractive index $m(\nu)$ of the grain material is taken from [Maron 1990] which is appropriate for pure amorphous carbon grains. The quantity $K_3(r)$ is the third moment of the size distribution function $f(a, r)$ of the dust particles. It is defined by

$$a_0^3 K_3 = \int_{a_\ell}^{\infty} a^3 f(a,r) da \,, \tag{5.2}$$

where a is the radius of the dust grain, a_0 denotes the hypothetical radius of a monomer contained in a dust grain, and a_ℓ is a lower limit size of the dust particles. Since the dust particles are assumed to be small compared to the wavelength, the contribution of light scattering by the grains is neglected here. Thus, the emissivity ϵ_ν is given by thermal emission of gas and dust:

$$\epsilon_\nu(r) = \epsilon_\nu^{\mathrm{g}}(r) + \epsilon_\nu^{\mathrm{d}}(r) = \kappa^{\mathrm{g}} B_\nu(T(r)) + \kappa_\nu^{\mathrm{d}} B_\nu(T(r)) \,, \tag{5.3}$$

where B_ν is the Kirchhoff–Planck function and the superscripts $^{\mathrm{g}}$ and $^{\mathrm{d}}$ denote the gas and the dust component, respectively.

By definition, K_3 equals the number of monomers condensed into grains per cm^3 and, therefore, is related to the degree of condensation f_c, i.e. the fraction of condensable material actually condensed into grains. In the case of pure carbon grains, which is considered here, the degree of condensation is given by

$$f_c = \frac{K_3}{(\epsilon_{\mathrm{C}} - \epsilon_{\mathrm{O}}) n_{<\mathrm{H}>}} \,, \tag{5.4}$$

where we have assumed that all oxygen is locked up in the CO–molecule ($n_{<\mathrm{H}>}$: total density of hydrogen atoms). Thus, the radiative acceleration in units of the local gravitational deceleration

$$\alpha = \frac{\chi_H}{\rho} \frac{L_\star}{4\pi c G M_\star} \tag{5.5}$$

is directly proportional to the degree of condensation in the small particle approximation (χ_H: flux–mean extinction coefficient, c: speed of light, G: gravitational constant).

5.3 Parameters of three LPV models

Table 5.1 shows the parameters of the three initial hydrostatic models. Additionally given are the time averaged values of the mass loss rate and the final outflow velocity of the evolved models. Since there are few, if any, real objects for which all of these parameters are determined by observations, we have chosen the model parameters to represent prototypes of cool, dust–enshrouded carbon giants. For this kind of objects, e.g. [Claussen *et al.* 1987] find typical values of the luminosity of the order of $10^4 L_\odot$, irrespective of the pulsation period. The investigations of [Lambert *et al.* 1986] and [Olofsson *et al.* 1993a], [Olofsson *et al.* 1993b] confirm, that the objects under consideration are in fact rather cool with effective temperatures well below or approximately 3000 K. [Lambert *et al.* 1986] find e.g. for R Scl an overabundance of carbon to oxygen of 1.34 and an effective temperature of 2550 K. [Olofsson *et al.* 1993a] quote a period of R Scl of 370 d, cf. Model B. IRC +10216, for instance, is known to be a highly evolved luminous source with a period exceeding 600 d, cf. [Witteborn *et al.* 1980] and [Ridgway and Keady 1988].

Since the model parameters inevitably had to be chosen following different observational investigations, one cannot expect that the sets of parameters satisfy the various fit–formulae obtained from the results of certain evolutionary calculations (e.g. core mass–luminosity relations (cf. [Boothroyd and Sackmann 1988a] and [Boothroyd and Sackman 1992]), or the radius–mass–luminosity relation ([Iben 1984])). Furthermore, our sets of model parameters do not fit to the well known period–mass–radius relations of [Ostlie and Cox 1986], which were derived from linear, nonadiabatic pulsation analysis calculations for oxygen–rich, less luminous ($L_\star \leq 7000\,L_\odot$) models with stellar temperatures between 2700 K and 3400 K.

Table 5.1: Parameters of the initial hydrostatic models. Also given are the time averaged mass loss rates and final outflow velocities of the evolved models.

	Model A	Model B	Model C
$M_\star$ $[M_\odot]$	1.0	1.0	1.0
$L_\star$ $[10^4\,L_\odot]$	1.0	1.0	3.0
$T_\star$ [K]	2600	2500	2450
(R_0 $[10^{13}\,\mathrm{cm}]$	3.43	3.70	6.68)
ϵ_C/ϵ_O	1.8	1.34	1.25
P [d]	650	370	621
Δu [km s^{-1}]	2.0	6.0	3.0
$<\dot{M}>$ $[M_\odot\ \mathrm{yr}^{-1}]$	1.0 10^{-5}	3.0 10^{-5}	2.9 10^{-4}
$<u_\infty>$ [km s^{-1}]	28.5	12.8	14.7

5.4 Typical radial structure of the dust shell models

Figure 5.1 depicts a typical radial structure of the CDS at the beginning of the hydrodynamic cycle shown for Model A, cf. Table 5.1.

The following quantities are plotted:

upper diagram: the velocity v (solid line), velocity of sound c_T (dotted line) and the temperature T (dashed line),

middle diagram: the logarithm of the density ρ (solid line) and the degree of condensation f_c, i.e. the fraction of condensable material actually condensed into grains (dashed line) (cf. Eq. (5.4)),

lower diagram: the logarithm of the nucleation rate per H–atom $J_\star/n_{<\mathrm{H}>}$, i.e. the number of dust grains formed per second and H–atom (solid line) and the logarithm of the number of dust grains per H–atom $n_\mathrm{d}/n_{<\mathrm{H}>}$ (dashed line).

Radii are always given in units of the stellar radius R_0 of the initial hydrostatic model.

The consistent calculation of dust formation and grain growth and destruction shows up to have significant influence on the resulting dynamic structure of the CDS, which is rather different from the stationary models presented in Chap. 4.

As the degree of condensation and the number of dust grains per H–atom in Fig. 5.1 show, the dust is distributed inhomogeneously across the shell. The dust grains are concentrated in distinct layers, equidistant for each model, and exhibit a shell or onion–like structure which is closely related to the hydrodynamic structure, e.g. the velocity profile of the CDS.

Fig. 5.1 also shows the determining influence of the dust on the thermodynamic structure of the CDS. There are several steps in the course of the temperature which coincide with spikes in the degree of condensation.

These interactions are investigated in detail in [Fleischer *et al.* 1992] and [Fleischer 1994] and, therefore, are only briefly summarized here.

The discrete structure of the atmosphere is not produced solely by the shock waves caused by the interior pulsation of the star, but is a very product of the process of dust formation. In a first step the interior pulsation defines the onset of dust *formation* by providing appropriate low temperatures in the region between 3 and $4R_0$. In a second step pulsation triggers grain *growth* by a compression of the material in this radius interval and, thus, provides the high densities favourable for the growth process. In a short time interval values of f_c as high as 1 are reached, i.e. all of the condensable material is actually condensed into grains. The radiative acceleration α is directly proportional to the degree of condensation f_c (cf. Eqs. (5.1), (5.4), (5.5)).

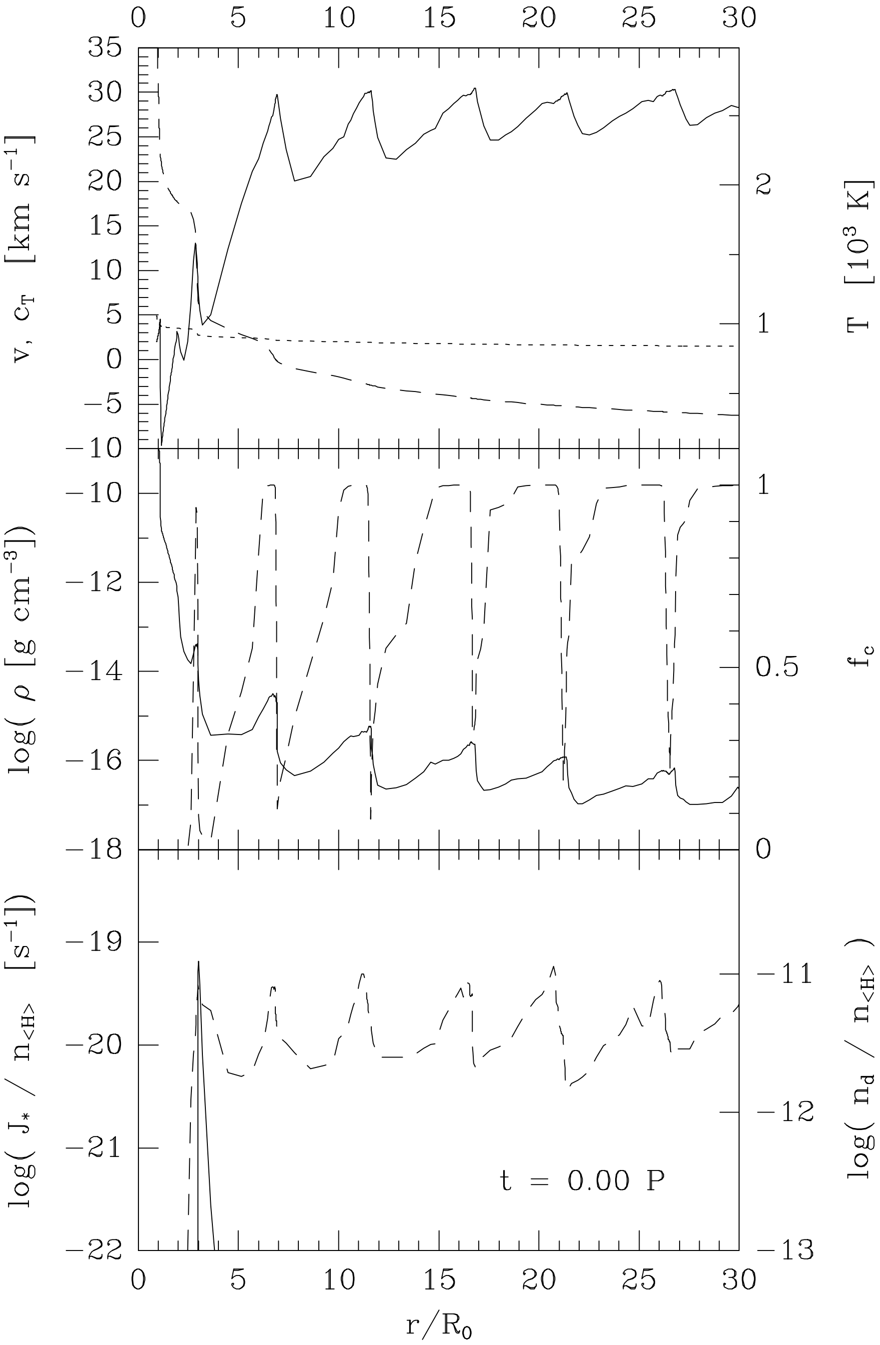

Figure 5.1: Radial structure of Model A at $t = 0.00P$.

Since the grains are closely momentum coupled to the gas, the sudden increase of the radiative acceleration causes a perturbation in the velocity field which steepens to become a shock wave, thereby compresses the material and, in turn, accelerates dust growth. Thus, the prominent shock waves which propagate through the atmosphere (cf. upper diagram of Fig. 5.1) are produced by a self–accelerating mechanism caused by the interaction between dust formation and hydrodynamics.

Furthermore, the newly formed dust in the inner shells, due to its opacity, effectively blocks the outgoing radiation and heats the material located closer to the star. This backwarming, seen as steps in the temperature structure in the upper diagram of Fig. 5.1, also influences the formation of new dust particles. Caused by the enhanced temperature inside the innermost dust layer, the formation of new particles is confined to a rather narrow spatial region as can be seen from the course of the nucleation rate $J_\star$ (lower diagram of Fig. 5.1).

Due to pulsation and backwarming, dust formation and growth is only possible in a small radius range and during a limited time interval. This results in the discrete structure of the CDS. The complex interplay among the processes of dust formation and growth, hydrodynamics and thermodynamics shows that the dust particles play the key role in determining the atmospheric structure of LPVs and Miras.

The influence of periodic dust formation on the lightcurves of these objects is discussed in detail for Model A in the next section.

5.5 Synthetic lightcurves of the LPV models

5.5.1 The lightcurves of Model A, detailed analysis

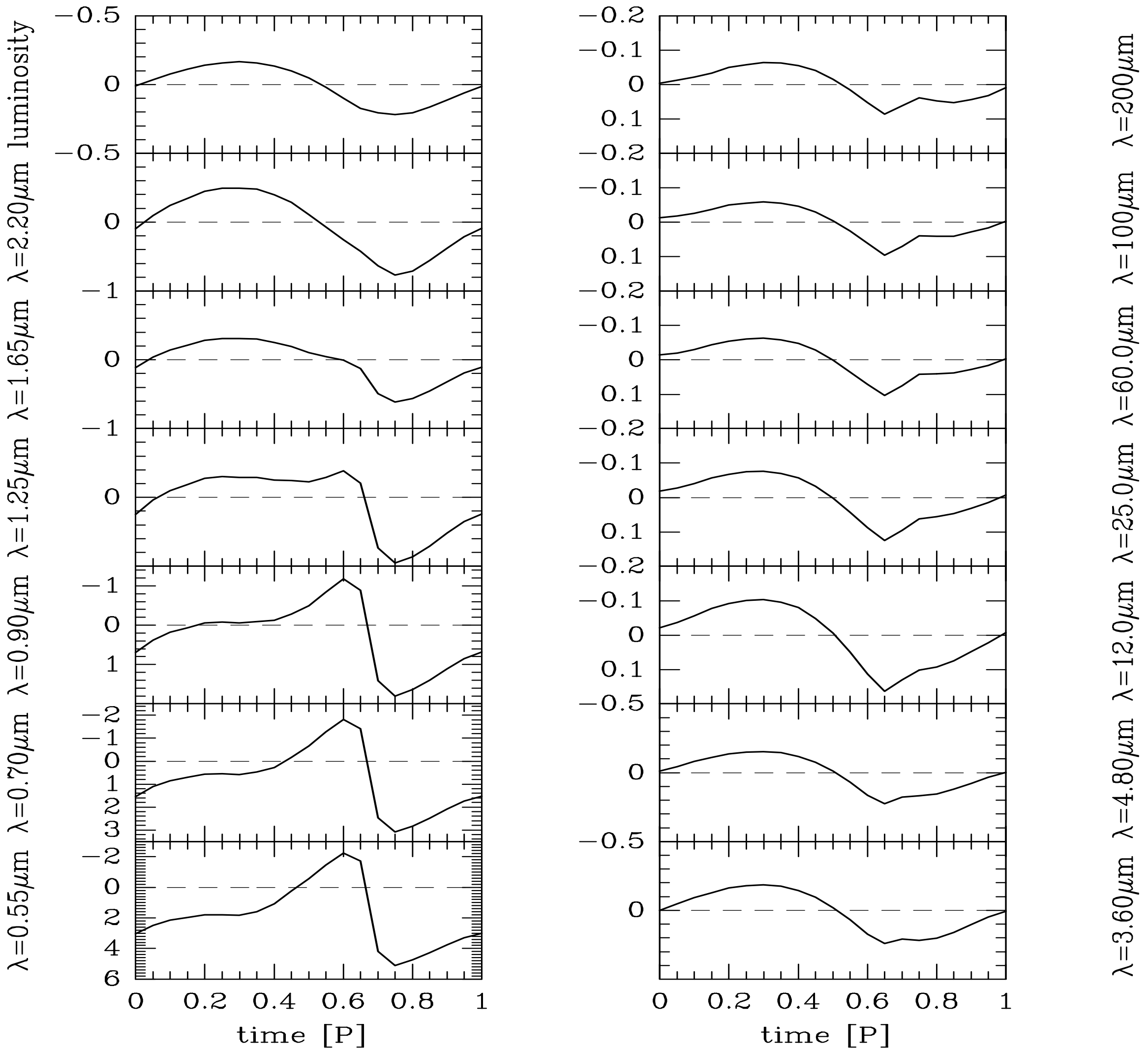

Figure 5.2: Synthetic lightcurves (in magnitudes, relative to the mean magnitude) of Model A at different wavelengths over a time interval of one pulsational period. Note the different scaling of the ordinate at different wavelengths.

The synthetic lightcurves of Model A are displayed in Fig. 5.2 for several wavelengths between 0.55μm and 200μm during a time interval of one hydrodynamic period P. The sinusoidal variation of the inner boundary (cf. Sect. 5.2.1) is reflected by the temporal variation of the stellar luminosity, shown in the upper left panel of Fig. 5.2. Apart from the smooth temporal variation of the flux, which is caused by this luminosity variation, the long wavelength lightcurves ($\lambda > 3.6\mu$m, right hand column) additionally exhibit pronounced narrow secondary maxima which occur periodically within the third quarter of the pulsational cycle around $t = 0.70P$ (cf. also Fig. 5.4). In the short wavelength lightcurves ($\lambda < 2.2\mu$m, left hand column), the variation due to the luminosity is almost completely concealed by strong features occuring periodically around $t = 0.60P$. The maximum value of these peaks decreases towards longer wavelengths until the pronounced structure eventually disappears at $\lambda = 2.2\mu$m. The flux minimum seen at $t = 0.70$P in the short wavelength lightcurves exactly corresponds to the intermediate maximum in the long wavelength lightcurves.

The occurrence of these striking features in the lightcurves is an immediate consequence of the dynamic behaviour of the discrete dust layers.

In Fig. 5.3 the radial course of several quantities which are of interest for the following discussion of the lightcurves are shown at four selected instants during the pulsational cycle. The quantities shown in these figures are:

upper row: the degree of condensation f_c (solid line) and the logarithm of the particle density of dust grains $n_{\rm d}$ normalized to the total hydrogen particle density $n_{<{\rm H}>}$ (dashed line),

middle row: the flux mean absorption coefficient of the dust component κ_H^d (solid line) and the logarithm of the Eddington flux H_ν at $\lambda = 0.90\mu$m passing through the spherical surface at radius r, multiplied by r^2 to eliminate the pure geometrical dilution (dashed line),

lower row: the total (gas and dust) optical depth τ_ν at $\lambda = 0.90\mu$m (solid line), the local contribution of dust emission to the 0.90μm *intensity* reaching the outer shell boundary in radial direction $\epsilon_\nu^d e^{-\tau_\nu}$ (short–dashed line) and the respective contribution due to gas emission $\epsilon_\nu^g e^{-\tau_\nu}$ (long–dashed line).

We start the discussion of the lightcurves at time $t = 0.60P$ shortly after the beginning of a new dust formation cycle (cf. Fig. 5.3 a)). At this instant, all dust layers present in the circumstellar shell are fully developed, i.e. the degree of condensation within these layers has reached its maximum value of 1 and the layers are moving outwards. At $t = 0.60P$ the total dust optical depth has reached its minimum value during the cycle, the dust optical depth at $\lambda = 0.90\mu$m is $\tau_{0.90\mu} = 7.23$. Simultaneously the short wavelength lightcurves reach their peak value (cf. Fig. 5.2). Due to the relatively small optical depth, the dominant contribution to the short wavelength radiation that escapes from the shell is produced by photospheric gas emission (cf. lower diagram of Fig. 5.3 a)). Between $t = 0.60P$ and $t = 0.70P$ a new dust layer starts to form as indicated by the enhanced particle density of dust grains already at $t = 0.60P$ seen in the upper diagram of Fig. 5.3 a) around $3R_0$. At this instant new dust particles condense from the gas phase, but these particles are still too small to produce a relevant degree of condensation. Although the nuclei already show up in the flux mean absorption coefficient $\kappa_H^{\rm d}$, they still do not influence the optical depth at this time.

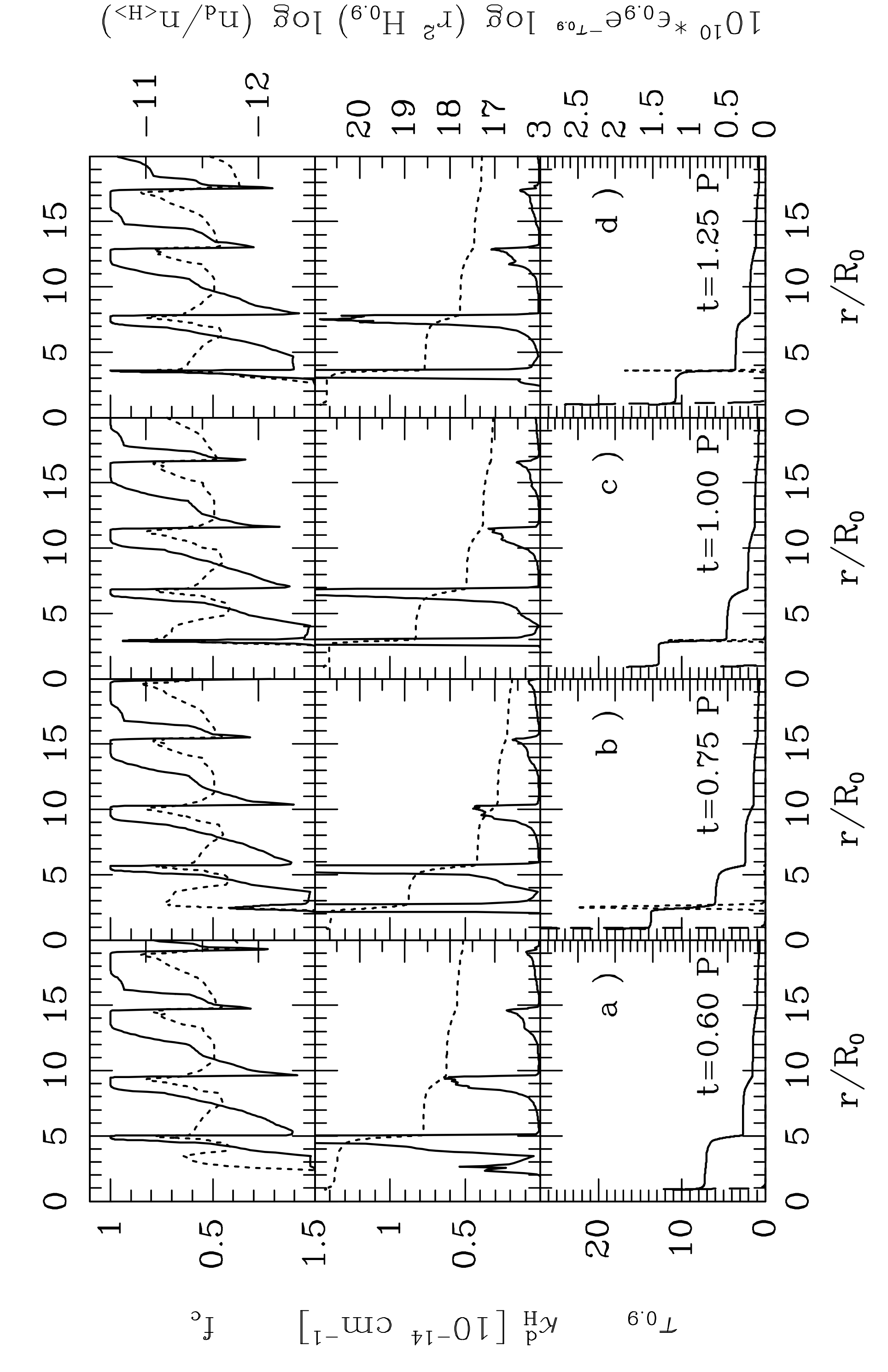

Figure 5.3: Radial structure of Model A at
a) the beginning of the *dust formation cycle* at $t = 0.60P$,
b) at $t = 0.75P$,
c) $t = 1.00P$ and
d) at $t = 1.25P$.
The quantities shown are explained in the text. $r^2 H_\nu$ is given in [erg s^{-1}Hz^{-1}] and $\epsilon_\nu e^{-\tau_\nu}$ in [erg s^{-1}cm^{-3}sr^{-1}Hz^{-1}]. Frequency–dependent quantities refer to a corresponding wavelength of $\lambda = 0.90\mu$m.

The newly formed dust particles subsequently grow very effectively and, thereby, increase the optical depth of the new dust layer. From $t = 0.70P$ on, the short wavelength photospheric radiation is already effectively blocked by the new layer (cf. the radial variation of the Eddington flux in the middle diagrams of Figs. 5.3 a) and b)). At the same time, $t = 0.70P$, the minimum value of the short wavelength lightcurves is reached, whereas in the long wavelength lightcurves a shallow intermediate maximum occurs. The main contribution to the short wavelength flux is now provided by thermal dust emission, emanating from the front of the new, innermost dust shell. (Note that the emergent *flux* is given by an angle integration of $\epsilon_\nu e^{-\tau_\nu}$ and, thus, the respective source contribution is weighted by the radiating surface.) At longer wavelengths, absorption of the stellar radiation field is less effective, and thermal dust emission from the newly formed layer contributes a significant fraction to the emergent flux and produces the (with respect to the peak at short wavelengths) retarded intermediate structure in the long wavelength lightcurves. At $t = 0.75P$ the degree of condensation in the newly formed dust layer has reached a value of $f_c = 0.41$ (cf. Fig. 5.3 b)), the optical depth of the new layer alone has increased to $\Delta\tau_{0.90\mu} = 7.75$ and, thus, produces the innermost step of the τ–structure displayed in the lower diagram of Fig. 5.3 b) (the optical depth of the new layer at 25μm is $\Delta\tau_{25\mu} = 0.21$ at this instant). During the following time interval until $t = 1.00P$ the optical depth of the new dust layer increases up to its maximum value of $\Delta\tau_{0.90\mu} = 8.40$ due to growth of the dust grains. The degree of condensation reaches the maximum possible value of $f_c = 1$ not until $t = 1.25P$ (cf. the sequence of Figs. 5.3 b), c), d)). Obviously, there are two competing processes at work during this phase: Between $t = 0.75P$ and $t = 1.00P$, the effects of dust formation and growth exceed the dilution of the material due to expansion, whereas between $t = 1.00P$ and $t = 1.25P$ expansion predominates. Simultaneously, the outer layers merely expand and, due to geometrical dilution of the material, the optical depth in front of the newly formed layer decreases. Within this time interval, the short wavelength radiation which escapes from the dust envelope is predominantly produced by thermal emission of dust located in the outer part of the new layer. This situation changes at $t = 1.35P$, when the total optical depth has reached a value of $\tau_{0.90\mu} = 9.70$. Due to expansion, caused by radiation pressure on the new dust shell, the innermost layer has become increasingly transparent ($\Delta\tau_{0.90\mu} = 6.50$ at $t = 1.35P$) and increasingly cooler. At this time, the contribution of photospheric gas emission again exceeds the contribution emerging from the radiating dust layer. Simultaneously, the short wavelength lightcurves start to rise steeply until $t = 1.60P$, when the total optical depth of the shell has again reached its minimum value of $\tau_{0.90\mu} \approx 7$, with the innermost dust layer at this instant contributing $\Delta\tau_{0.90\mu} = 4.37$ to this value.

Thus, in the case of Model A discussed here, we can clearly distinguish two different phases within one hydrodynamic period which are essentially characterized i) by effective dust formation and growth (between $t = 0.60P$ and $t \approx 1.00P$) and ii) by expansion of the dust layers (between $t \approx 1.20P$ and $t = 1.60P$). During the relatively short first part of phase i), where very effective dust formation and growth takes place, the optical depth of the newly formed innermost dust layer increases from almost zero at $t = 0.60P$ to $\Delta\tau_{0.90\mu} = 7.75$ at $t = 0.75P$ and, thus, leads to the steep decline of the short wavelength lightcurves. Due to expansion of the dust layers during phase ii), the optical depth decreases, which results in the increase of the short wavelength lightcurves. In the long wavelength lightcurves, the formation of the new dust layer between $t = 0.60P$ and $t = 0.75P$ leads to the intermediate maxima seen in Figs. 5.2 and 5.4, which are caused by thermal dust emission originating from this new layer.

A necessary condition for the strong features in the lightcurves to occur, produced by the mechanism of dust formation, is the existence of distinct phases, during which the respective competing processes (dust formation and expansion) are subject to very different time scales. For Model A this is the case in the interval between $t = 0.60P$ and $t = 0.75P$ where the time scale of grain growth $\tau_{\rm gr}$ is considerably shorter than the expansion time scale $\tau_{\rm exp}$, and between $t = 1.25P$ and $t = 1.60P$, where expansion, caused by radiative acceleration of the new layer predominates. For Models B and C these distinct phases are multiple times longer, cf. the discussion in the next section.

Summarizing the preceding discussion, we state:

- The occurrence of the intermediate structures in the lightcurves critically depends on the temporal evolution of the optical depth of the innermost dust layer.
- The short wavelength radiation seen during the peak of the lightcurves of Model A (between $t = 0.35P$ and $t = 0.70P$, cf. Fig. 5.2) is mainly produced by photospheric gas emission. In principle, this effect might offer the possibility, to directly observe the short wavelength photospheric radiation during this short time interval. Hence, e.g. the photospheric element composition might be accessible during this phase.

5.5.2 The lightcurves of Models A – C, long–term analysis

Figs. 5.4, 5.5 and 5.6 show the lightcurves of Models A – C for 10 representative wavelengths in the spectral range from 1.25μm to 200μm.

Fig. 5.4 shows the long–term behaviour of the lightcurves of Model A which has been discussed in detail in the previous section. From the periodic occurrence of the different intermediate structures at short wavelengths $\lambda < 2.2\mu$m and at long wavelengths $\lambda > 2.2\mu$m it can be inferred that the formation of a new dust layer periodically takes place during every second half of the hydrodynamic cycle. The lightcurves at wavelengths $\lambda > 2.2\mu$m show a slightly asymmetric shape and exhibit an internal structure on the rising branch which regularly occurs and is even more pronounced towards longer wavelengths.

All curves are characterized by a periodic re–occurrence of all features at the same phase during the sequence of hydrodynamic pulsation cycles.

In contrast to Model A, Models B and C exhibit a different behaviour. These models (cf. Figs. 5.5 and 5.6 on p. 118 and 119) show alternating high maxima at all wavelengths. Models B and C show a quasi–sinusodial behaviour on the scale of one pulsational period which is superposed by a long–scale oscillation. To get an idea how these surprising finding could be explained we have to go back to the results of the hydrodynamic calculations.

In [Fleischer *et al.* 1992] it is mentioned that, depending on the carbon abundance ϵ_C, the formation of a new dust shell can take place *every* hydrodynamic period, as is the case for Model A, but also every second, third ... pulsational period, i.e. the radial structure of the CDS at a certain instant of time $t = \beta P$ equals the structure at $t = (\beta + n_P)P$, where β is an arbitrary dimensionless time parameter and $n_P = 1, 2, \ldots$ is the *multiperiodicity* number. A detailed analysis of the occurrence of multiperiodicity is beyond the scope of this thesis but is given in [Fleischer 1994]. Here we just state that for Model B $n_P = 4$, for Model C $n_P = 5$ whereas for Model A $n_P = 1$. In principle, the process of the formation of a new dust layer is the same in Models B and C as described in detail for Model A. The difference is the timescale: The formation of a fully evolved new dust layer takes a time interval of four pulsational cycles in Model B and five pulsational cycles in Model C, compared to one pulsational cycle for Model A.

Obviously, the course of the lightcurves at longer wavelengths, $\lambda > 3.6\mu$m reflects the global dynamic behaviour of the dust shell model. A new dust layer is formed at each of the deep minima at $t \approx 0.5, 4.5, 8.5 \ldots$ P in Model B (cf. Fig. 5.5), and at $t \approx 4.5, 9.5, 14.5, 19.5 \ldots$ P in Model C (cf. Fig. 5.6), respectively. The newly formed layers subsequently move outwards and reach their maximum degree of condensation just before the next layer is formed, i.e. at $t \approx 4.0, 8.0, \ldots$ P in Model B, and at $t \approx 4.0, 9.0, 14.0, \ldots$ P in Model C, respectively.

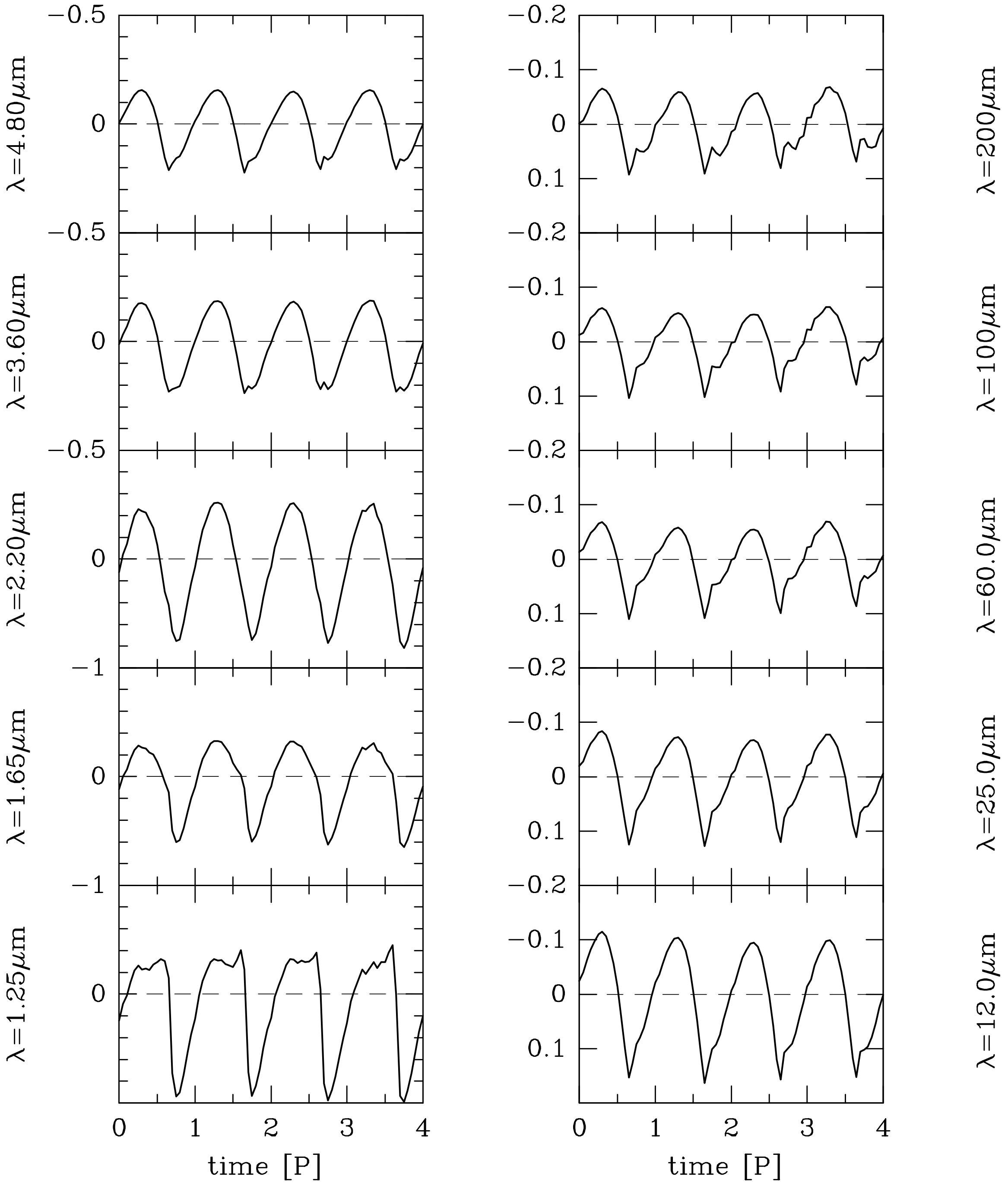

Figure 5.4: Theoretical lightcurves (in magnitudes, relative to the mean magnitude) of Model A at different wavelengths. Note the different scaling of the ordinate at different wavelengths.

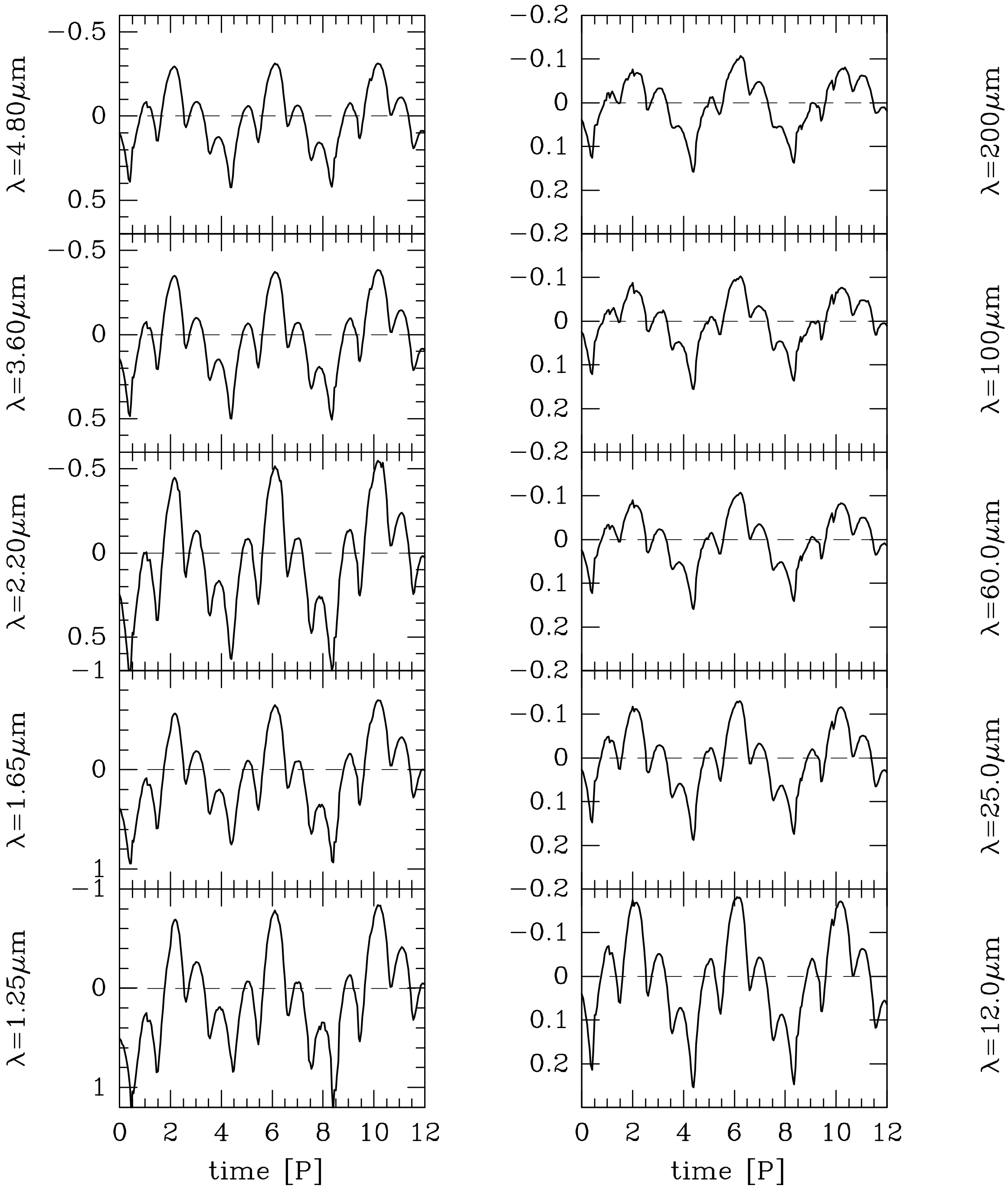

Figure 5.5: Theoretical lightcurves (in magnitudes, relative to the mean magnitude) of Model B at different wavelengths. Note the different scaling of the ordinate at different wavelengths.

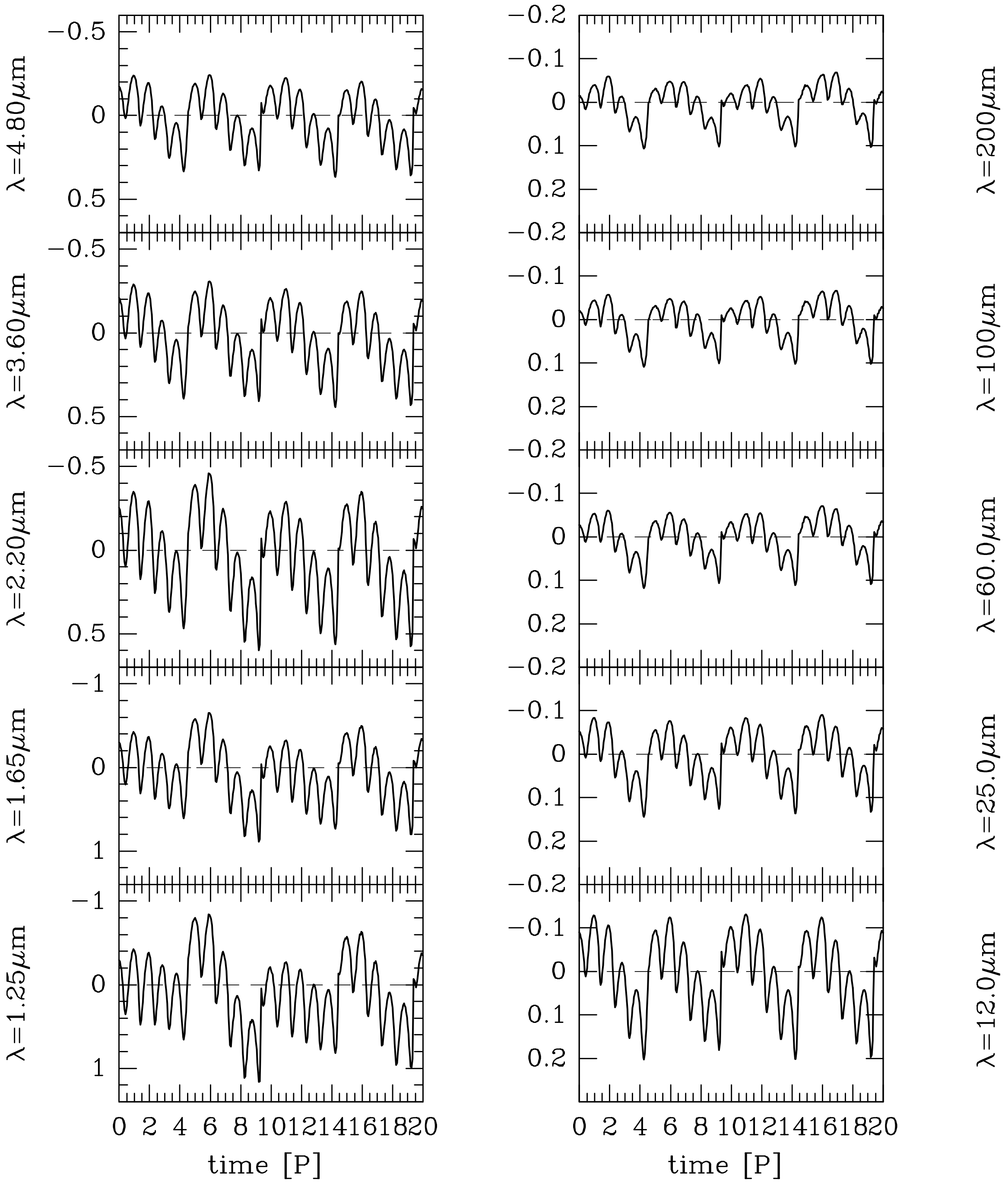

Figure 5.6: Theoretical lightcurves (in magnitudes, relative to the mean magnitude) of Model C at different wavelengths. Note the different scaling of the ordinate at different wavelengths.

The minima at $t \approx 0.5, 4.5, 8.5 \ldots$ P (cf. Fig. 5.5) and at $t \approx 4.5, 9.5, 14.5, 19.5 \ldots$ P (cf. Fig. 5.6) have an alternating depth at shorter wavelengths. This is due to a slight variation of approximately 0.5 R_0 of the exact radial location where the new dust layer is formed. Caused by the local hydrodynamic conditions at $t \approx 0.5, 8.5, \ldots$ P in Model B and at $t \approx 9.5, 19.5, \ldots$ P in Model C, respectively, dust formation already starts at slightly smaller radii and, therefore at higher densities which leads to a larger optical depth of the newly formed layer. Thus, the course of the short wavelength lightcurves sensitively probes the physical conditions in the innermost region of the dust shell.

Concluding this section, we want to point to a general property, which is common to all three models presented in this chapter. Irrespective of the different long–term behaviour of the lightcurves resulting from the three individual models and also independent of the different shape-variations with wavelength of the lightcurves of each individual model, the light amplitude decreases with increasing wavelength (cf. Figs. 5.4, 5.5 and 5.6). This behaviour also seems to be a general property of the real LPVs and has been noticed for many objects. From the observed lightcurves presented in the next section for AFGL 1085 and R For (Figs. 5.7 and 5.8), a decrease of the amplitude with wavelength is clearly seen. [LeBertre 1988a] found this trend also for IRC +10216 and for the carbon–rich objects AFGL 971 and AFGL 1235, which are in the sense of their *redness* (cf. Sect. 5.6) intermediate between the classical carbon-rich Miras (as R For) and the very red extreme carbon stars (like IRC +10216). In our synthetic lightcurves this wavelength dependence of the amplitude is largely due to the redistribution of radiative energy from short wavelengths to long wavelengths caused by the dust grains: The energy absorbed in the rather narrow short wavelength portion of the stellar radiation field is redistributed by thermal dust emission over the broad infrared spectral range. Therefore, a comparison between observed and calculated wavelength dependence of the light amplitude may provide some constraints on the optical properties of the dust actually formed in the real objects.

5.5.3 Discussion

At the present state it is not intended to model a special object but to present results of a theoretical investigation, which is devoted to the principle physical mechanisms, and reveals an important influence of the dynamic structure on the optical appearance of LPVs and Miras. Thus, we cannot expect a quantitative agreement between our model calculations and the observations but at most a qualitative agreement of certain characteristic features.

To draw this comparison, the measured lightcurves of two objects from the sample of [LeBertre 1992] are chosen, these are AFGL 1085 and the carbon–rich Mira R Fornacis (cf. Figs. 5.7, 5.8). For R For it is possible to combine the data of Le Bertre with those of [Feast *et al.* 1984], except for a slight disagreement of the L

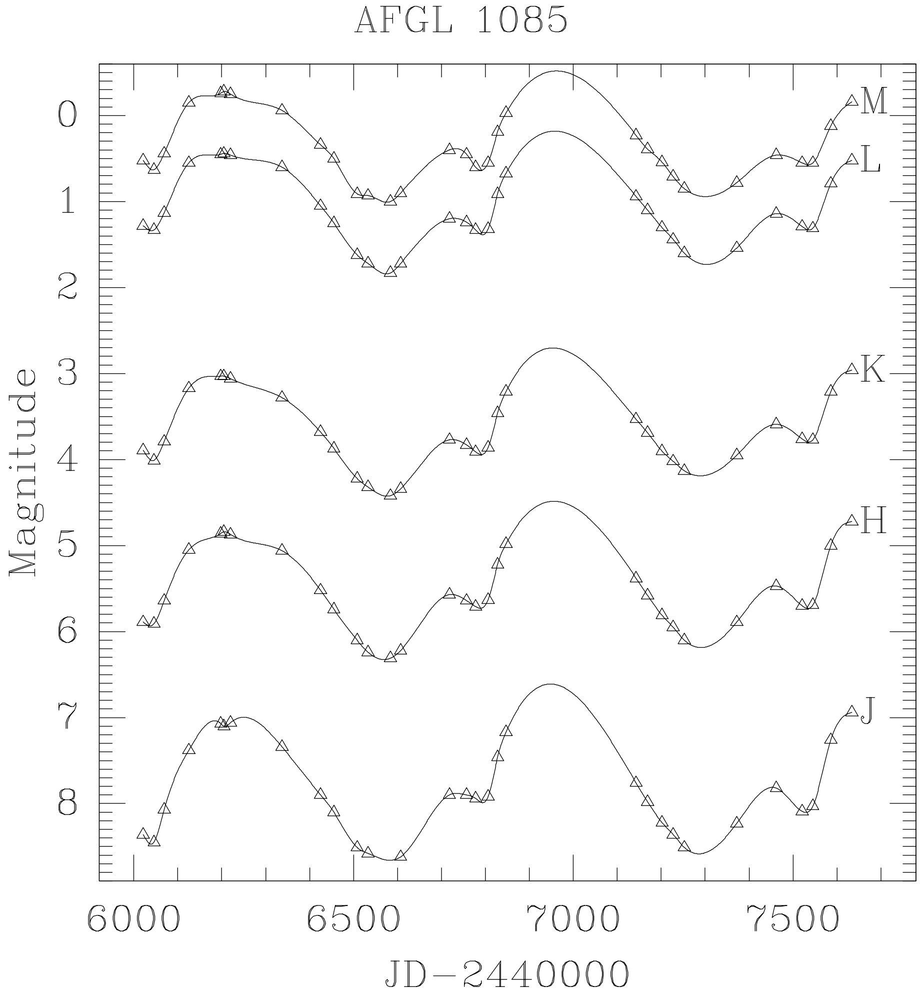

Figure 5.7: Observed lightcurves of AFGL 1085, data are taken from [LeBertre 1992]. The effective wavelengths $\lambda_{\rm eff}$ of the filter bands J, H, K, L, M are: $\lambda_{\rm eff}(J) = 1.25\mu$m, $\lambda_{\rm eff}(H) = 1.65\mu$m, $\lambda_{\rm eff}(K) = 2.2\mu$m, $\lambda_{\rm eff}(L) = 3.8\mu$m, and $\lambda_{\rm eff}(M) = 4.65\mu$m.

photometric fluxes. Therefore, these data were omitted, when we connected the measured points of R For and AFGL 1085 by a cubic spline interpolation (the M fluxes were not measured by [Feast *et al.* 1984]).

The characteristic features of the AFGL 1085 lightcurves (cf. Fig. 5.7) are the intermediate extrema, already noted by [LeBertre 1992]. With respect to the model calculations, these intermediate structures could be caused by the sudden formation of a new dust layer similar to Model A.

In the short wavelength lightcurves ($\lambda < 2.2\mu$m) of Model A, the dynamic behaviour of the discrete dust layers causes rather narrow, additional maxima, which are steeply decreasing in time due to the rapid increase of the dust optical depth. These additional maxima follow the broad, plateau–like maxima produced by the

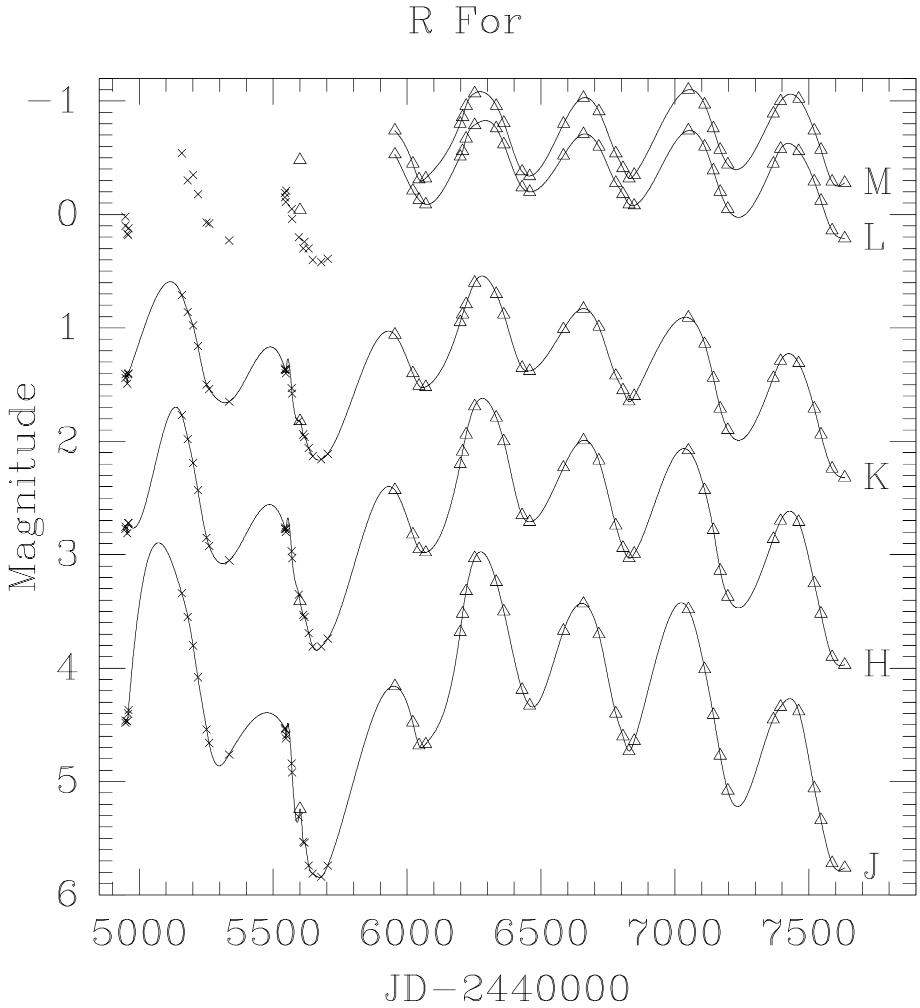

Figure 5.8: Observed lightcurves of R For. Data are taken from [LeBertre 1992] ($\triangle$) and from [Feast *et al.* 1984] ($\times$). Wavelengths are the same as in Fig. 5.7.

varying luminosity (cf. Figs. 5.2 and 5.4). At longer wavelengths ($\lambda > 2.2\mu$m) on the other hand, the periodic formation of new dust layers leads to shallow intermediate maxima on the ascending branches of the lightcurves, which are produced by thermal dust emission originating mainly from these new layers. Due to the wavelength dependence of the dust opacity, the features in the synthetic lightcurves, which are produced by absorption of photospheric radiation at shorter wavelengths and by dust emission at longer wavelengths, accordingly depend on the wavelength.

However, the intermediate structures present in the observed lightcurves (e.g. AFGL 1085) could also be caused by different mechanisms, e.g. by the dissipation of shock wave energy in the inner parts of the atmosphere (cf. [Feuchtinger *et al.* 1993] which is transferred to the radiation field. Furthermore, the formation of secondary shocks in the innermost dust–free region (the occurrence of which has thoroughly been investigated by [Bowen 1990] and [Willson *et al.* 1994]) could also lead to such intermediate structures in the lightcurves. If this is the case, the *strength* of the secondary maxima might also depend on the wavelength, but we do not expect that this mechanism could produce minima at shorter wavelengths and simultaneously maxima at longer wavelengths. To decide, whether dust formation is responsible for the occurrence of the observed intermediate maxima, the promising objects (e.g. AFGL 1085, R Lep, ...(see [LeBertre 1992])) should be simultaneously monitored with a sufficient temporal resolution during the phases of interest in a wide spectral regime (e.g. between 0.90μm and 100μm). A first step in this direction is intended to be performed using the **I**nfrared **S**pace **O**bservatory (ISO) satellite to be launched in autumn 1995. During this mission, periodic observations of suitable objects will be performed at 25, 60 and 100μm. These ISO observations will be complemented by a simultaneous ground based monitoring in the NIR spectral range between $0.9\mu m$ and 5μm.

The presence of discrete dust layers in our models also causes rippled or even step–like structures in the radial brightness profiles as well as in the theoretical visibilities, which result from these calculations (cf. Sect. 5.7). Similar structures have been observed e.g. for IRC +10216 by [Ridgway and Keady 1988] and A. Richichi (1993, private communication). Since the discrete structure of the dust shell may provide an explanation for both, the occurrence of intermediate structures in the lightcurves as well as the pronounced structures in observed brightness distributions, from a theoretical point of view, we would favour the dust mechanism described in this chapter to be responsible for the bumps in the lightcurves.

The lightcurves of R For (cf. Fig. 5.8) show a systematic drift in magnitude very similar to the multiperiodic Model B. [Feast *et al.* 1984] found R For to exhibit an "anomalously" deep minimum in 1983. A similar deep minimum has been observed in 1990 by [LeBertre 1992]. Secondary variations with periods multiple times longer than the main period have also been found in the lightcurves of several other objects by [Alksnis 1990].

In terms of our model calculations we could explain this behaviour by the interplay of two distinct processes with different time scales: The regular pulsation of the star, which provides the "short" hydrodynamic time scale, and the process of dust formation and growth, which, under the conditions of Models B and C, has a time scale of four times and five times longer, respectively. Thus, the CDS can be conceived as a dynamic system under the influence of an external excitation mechanism, or, to use a simple analogy from classical mechanics, the CDS behaves similar to a pendulum, which is subject to a periodic external force.

We expect from our model calculations that observations of R For continuing the monitoring of [LeBertre 1992] would again reveal a long–term increase of the lightcurves.

5.6 Near infrared colours of the dynamic models

As already demonstrated in Sect. 4.6 for the stationary models, the spectra of the dust shells can be ordered according to their redness by means of two colour diagrams. In order to give an impression of this sequence in the case of pulsating atmospheres, in Fig. 5.9 the locations of Models A, B, and C are displayed in a NIR two colour diagram together with the observed colours of 4 different objects.

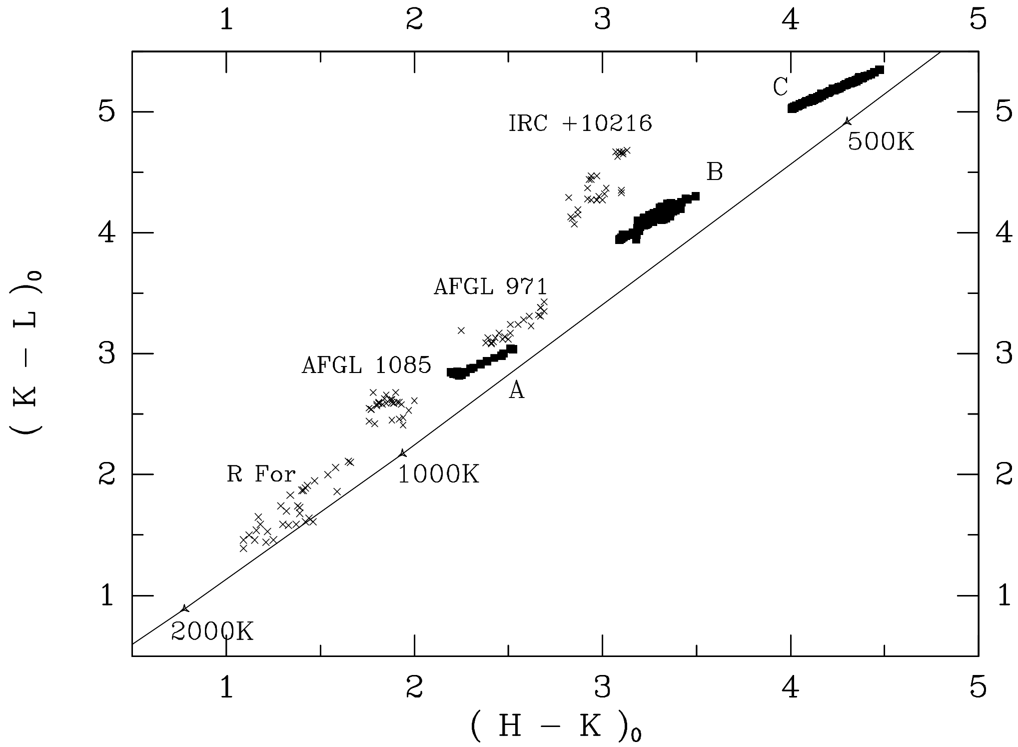

Figure 5.9: Near infrared two colour diagram. Crosses represent observed colours for R For, AFGL 1085, AFGL 971 and IRC +10216, taken from [LeBertre 1992]. The diagonal line connects blackbody spectra at the indicated temperatures. The filled squares represent the calculations for Model A over one pulsational period, Model B over four pulsational periods, and Model C over five pulsational periods.

The objects as well as the models are plotted for a time interval of several pulsation periods, each single symbol indicating the colour index at one instant of time. During the phase of light minimum, the real objects as well as the models appear to be redder than at maximum light, i.e. the data points corresponding to light minimum are located in the upper right corner of the region populated by each object and each model, respectively. For the multiperiodic Models B and C, these points correspond to the deep minima of the lightcurves (cf. Figs. 5.5 and 5.6), as is also the case for R For (cf. Fig. 5.8).

From Fig. 5.9 one clearly sees that the data points representing the temporal colour variations of observed and calculated spectra are strongly correlated and almost fall along a straight line in this diagram. This fact is in excellent agreement with the general behaviour of carbon stars. It was found by [Epchtein *et al.* 1990] from an analysis of the near infrared colours of a sample of about 200 carbon–rich AGB stars, that this class of objects defines a rather narrow strip in the NIR colour diagrams (cf. also Fig. 4.22 on page 83, where their sample is plotted). In that investigation, only one data point is considered for each object, which is obtained at an arbitrary phase of the lightcurve. The fact, that the same correlation between the colour indices holds for the carbon stars in general (spanning the range from the optical carbon Miras like R For up to the extreme carbon stars like IRC +10216), as well as for the individual objects during their light variation, suggests a common physical reason which is responsible for this colour correlation. As the near infrared colours are largely determined by the optical properties of the dust grains, this correlation may indicate that the same kind of dust forms in the shells of all these objects.

By simple dust shell modelling as a function of phase [LeBertre 1988a] noted, that the aforementioned observed correlation is well reproduced assuming a unique opacity law in $\lambda^{-1.3}$ for the dust component. (This opacity law was first proposed by [Jura 1983a] for describing the grains around IRC +10216). The synthetic colours presented here result from the optical properties for amorphous carbon as tabulated in [Maron 1990], which give roughly a $\lambda^{-1.0}$ dependence of the dust opacity. Since the calculated colours slightly deviate from the observed ones for large values of the colour index (cf. Fig. 5.9), it may be concluded, that the dust grains formed under the circumstellar conditions are characterized by a steeper wavelength dependence of the opacity, than is assumed here. This is further supported by the results of the stationary calculations: In Sect. 4.6 it was shown, that the colour indices of the spectra produced by the stationary models are also linearly correlated, but that the gradient of the theoretical correlation in this case systematically deviates from the observed colours. The reason for this deviation was argued to be the presence of unrealistically large particles produced in the stationary outflow, which lead to an even less steep wavelength dependence of the dust opacity (λ^{-p}, $p < 1$) in the NIR region. For the time–dependent models shown in Fig. 5.9, the deviation is considerably smaller than in the stationary calculations. This improved agreement between the observed colours and the colours resulting from the time–dependent models strongly supports the conclusion, that the NIR colours could be used as a diagnostic tool to obtain information about the internal structure of the dust grains actually formed in the real circumstellar shells (cf. Sect. 3.2.2).

Applying a parameterized dust shell model for fitting the observed shell spectra, [LeBertre 1988a] also found, that the sequence of increasing redness in the near infrared colour diagrams can be described as a sequence of increasing optical depth of the dust shells (see also [Epchtein *et al.* 1990]). He further points out, that the correlation between the colour indices can be understood in terms of a linear

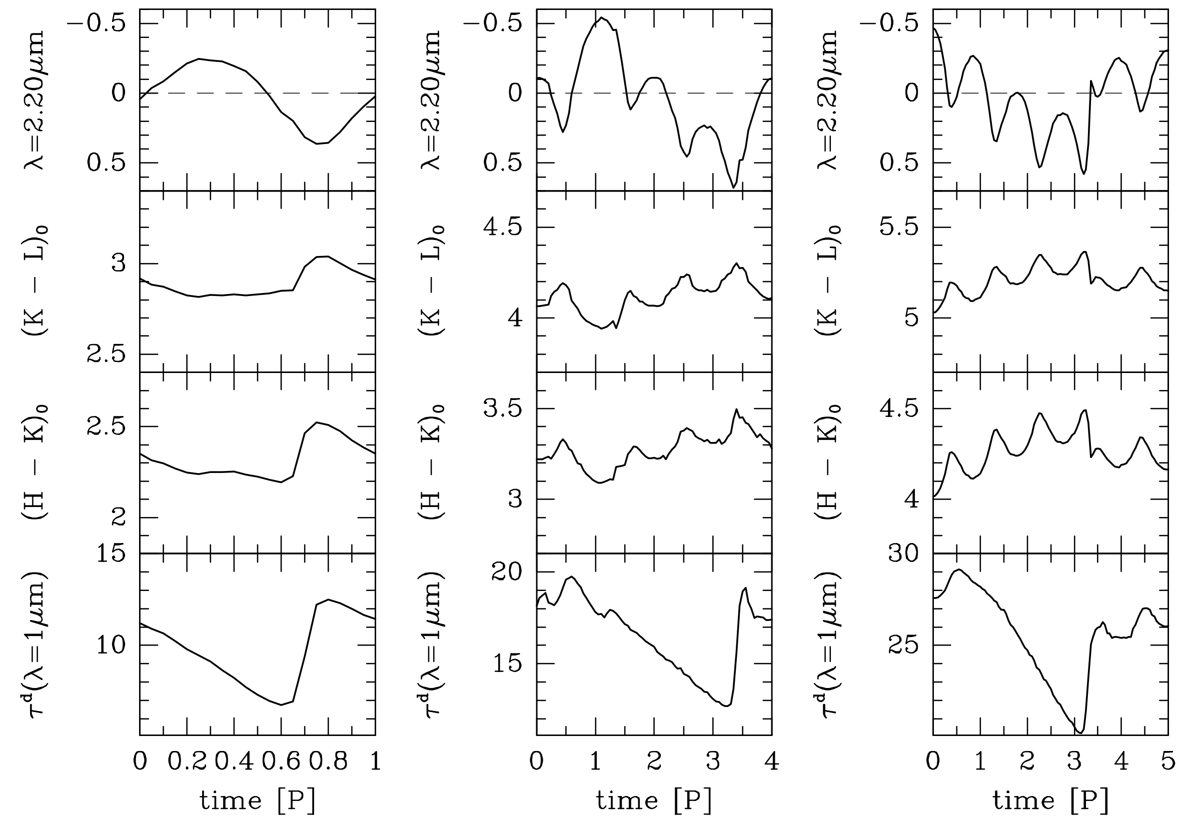

Figure 5.10: Temporal variation of several quantities for Model A over one pulsational period (left hand column), for Model B over four pulsational periods (middle column), and for Model C over five pulsational periods (right hand column). For each Model, the following quantities are plotted:
1st row: lightcurve at 2.2μm in magnitudes, normalized to the mean value
2nd row: colour index (K-L)$_0$
3rd row: colour index (H-K)$_0$
4th row: dust optical depth $\tau^{\rm d}$ at $\lambda = 1\mu$m.

dependence of each of both colour indices on the dust optical depth of the shell at a fixed wavelength, e.g. at $\lambda = 1\mu$m.

This finding is supported on a large scale by the results of the detailed models presented here. The sequence of increasing redness of the different models reflects a sequence of increasing *time averaged* optical depth ($< \tau_{1\mu{\rm m}} > \approx 10$, 16, and 25 for Models A, B, and C, respectively, which can be seen by averaging the values given in the lower row of Fig. 5.10). However, the linear correlation between optical depth and colour index does not hold for the individual models during the cycle of the light variation (cf. 2nd and 3rd row of Fig. 5.10 in comparison to the 4th row).

From the lower row of Fig. 5.10 it can be seen, that the formation of a new dust layer in the inner shell region leads to a steep increase of the optical depth within an interval of $\approx 10\%$ of the pulsation period. The formation of a new dust layer takes place around $t = 0.70P$ for Model A, around $t = 3.5P$ for Model B, and around $t = 3.2P$ for Model C. In all three models, the phase of dust formation coincides with the phase of light minimum (for Models B and C these are the deep minima), cf. the lightcurves shown in the upper row of Fig. 5.10. That dust formation takes place near the phase of light minimum is also inferred from rather different kinds of observations:

- By modelling the shell spectrum of R For at different phases of the light curve, [LeBertre 1988b] explained the increased obscuration of the central star around light minimum by the condensation of dust grains in the inner part of the CDS.
- From fitting the visibility curve of IRC +10216 obtained by an interferometric measurement at 10μm, [Danchi *et al.* 1990] also found, that dust appears to form near minimum luminosity.
- The latter work has recently been extended to interferometric observations of 13 late–type stars, indicating that dust formation takes place near light minimum at least in some of these objects (including Mira (= o Ceti) itself).

In the multiperiodic Models B and C, also at intermediate phases of the dust formation cycle a moderate increase of the optical depth occurs close to the intermediate light minima. These phases are immediately followed by a time interval of decreasing optical depth (see lower row of Fig. 5.10). This alternating behaviour of $\tau^{\rm d}$ is due to the periodically enhanced density caused by the shock waves: The formation of a new dust layer causes the steep increase of the optical depth (cf. also the discussion in Sect. 5.5.1, in particular Figs. 5.3 a) and b)), which occurs every pulsation cycle in Model A, but only every 4^{th} and every 5^{th} pulsation cycle in the multiperiodic Models B and C. In the latter two models, the passage of subsequent shocks almost periodically enhances the gas density at the position of the newly formed dust layer, which leads to an effective *growth* of the already existing dust particles and, therefore, to a successive increase of the degree of condensation and, thus, also of the optical depth. The following phase of decreasing optical depth is caused by the geometrical dilution of the innermost dust layer after the passage of the shock. Once the degree of condensation in the innermost layer has reached a value close to unity, the passage of further shocks merely drives the dust layer outwards. Continuous expansion of the layer now causes the comparably long phase of decreasing optical depth (between $t = 1.5P$ and $t = 3.5P$ for Model B and between $t = 0.5P$ and $t = 3.2P$ for Model C).

During this phase of expansion, the colour indices (2^{nd} and 3^{rd} row of Fig. 5.10) mainly indicate the varying temperature of the innermost dust layer, rather than their optical depth. During the light variation of one single model, the temporal variation of the colour index, therefore, is not correlated to the variation of the optical depth.

Another obvious correlation, however may be more important for diagnostic purposes, namely that the increasing redness of the different model spectra simultaneously reflects an increasing value of the time averaged mass loss rate (cf. Tab. 5.1 on page 107). This interpretation could also explain the fact, that the three model spectra presented here tend to be redder than the respective observed objects.

In the preceding section it was demonstrated, that the lightcurve of Model B looks very similar to the observed lightcurve of R For, and Model A was compared to AFGL 1085. However, Model B produces an average mass loss rate of $< \dot{M} > = 3 \cdot 10^{-5} M_{\odot} \mathrm{yr}^{-1}$ (which compares to the mass loss rate of IRC +10216 within a factor of 3, cf. the locations of Model B and IRC +10216 in Fig. 5.9), whereas a value of only $\dot{M} = 2 \cdot 10^{-6} M_{\odot} \mathrm{yr}^{-1}$ is derived from CO line observations for R For ([Loup *et al.* 1993]). Model C has an extremely high mass loss rate ($< \dot{M} > = 3 \cdot 10^{-4} M_{\odot} \mathrm{yr}^{-1}$) and, thus, is located in the upper right corner of the NIR two colour diagram, while Model A with $< \dot{M} > = 1 \cdot 10^{-5} M_{\odot} \mathrm{yr}^{-1}$ exhibits NIR colours intermediate between that of AFGL 1085 and AFGL 971. For these objects, mass loss rates of $\dot{M} = 6.2 \cdot 10^{-6} M_{\odot} \mathrm{yr}^{-1}$ for AFGL 1085 and $\dot{M} = 2.6 \cdot 10^{-6} M_{\odot} \mathrm{yr}^{-1}$ for AFGL 971 are found from the literature (cf. the compilation in [Loup *et al.* 1993]). These values, however, are rather uncertain as is discussed in [Loup *et al.* 1993]. Although it is premature to draw a definite conclusion, it may be speculated on the basis of the three models presented here, that AFGL 971 actually has a higher mass loss rate than AFGL 1085. In order to confirm this hypothesis, a larger grid of models should be analyzed to get comprehensive information about the dependence of mass loss rate and spectra on the basic model parameters. Such an investigation is of course also a necessary prerequisite to obtain the information required for the detailed modelling of individual objects, which yet has to be done.

5.7 Spatial intensity profiles and spatial spectra

The typical radial structure of the dynamic dust shell models is characterized by the presence of discrete dust layers (cf. Fig. 5.1 on p. 109, where the radial structure of Model A is shown). This onion–like dust distribution is an immediate consequence of the interaction among time–dependent hydrodynamics, thermodynamics and dust formation. Since these interactions are discussed in detail in [Fleischer *et al.* 1992] and [Fleischer 1994], only the result, which is of particular importance in the present context, is mentioned here.

In the case of Model A, every hydrodynamic period a new dust layer is formed in the region between $2R_0$ and $3R_0$, whereas the same occurs in Model B only every 4^{th} and in Model C every 5^{th} pulsation cycle. Each newly formed layer subsequently moves outwards, thereby producing the rather regular pattern of the shell–like distribution of dust across the CDS. As was demonstrated in Sect. 5.5, this periodic formation of new dust leads to pronounced effects in the synthetic lightcurves, which compare well to similar structures already observed in the lightcurves of real LPVs. However, there exist other mechanisms currently discussed in the literature, which in principle may also explain e.g. the intermediate maxima present in the observed lightcurves of many carbon–rich LPVs (cf. the discussion in Sect. 5.5.3). To decide, whether the mechanism of the periodic formation of new dust layers proposed here is actually at work in the shells of the real objects, a further test of the models is highly desirable. An independent check of the theoretical results presented here can in fact be based directly on the striking spatial structure produced by the dust shell models: Due to thermal dust emission emanating from the discrete layers, the discontinuous dust distribution is reflected in the spatial intensity profiles across the dust shell, projected onto the plane perpendicular to the line of sight. These synthetic spatial intensity profiles are shown for the Models A, B, and C in the following figures 5.11, 5.13, and 5.15 for different wavelengths and different phases of the lightcurves. In each of these figures the time increases from left to right and each row refers to one wavelength. The instants of time given in each column correspond to the phases displayed in Fig. 5.10.

Caused by the different optical depths of the dust shell at different wavelengths, the emergent intensity exhibits either a step–like structure (at shorter wavelengths) or even local intermediate maxima (at longer wavelengths), which are located at the current position of the discrete dust shells. The radial distance between successive layers of course depends on the period of the dust formation cycle and on the hydrodynamic velocity at the position of the dust shells. In the models presented here, the typical distance between the dust shells is of the order of a few R_0, i.e. some 10^{14} cm. Viewed from a distance of 100 pc (only a few real late–type stars are that close to the sun), this separation between the dust layers already corresponds to an angular separation of the order of some 0.01 arcsec, which is not easily directly resolved by current ground–based infrared telescopes.

On the other hand, highly resolved spatial spectra have been obtained in the

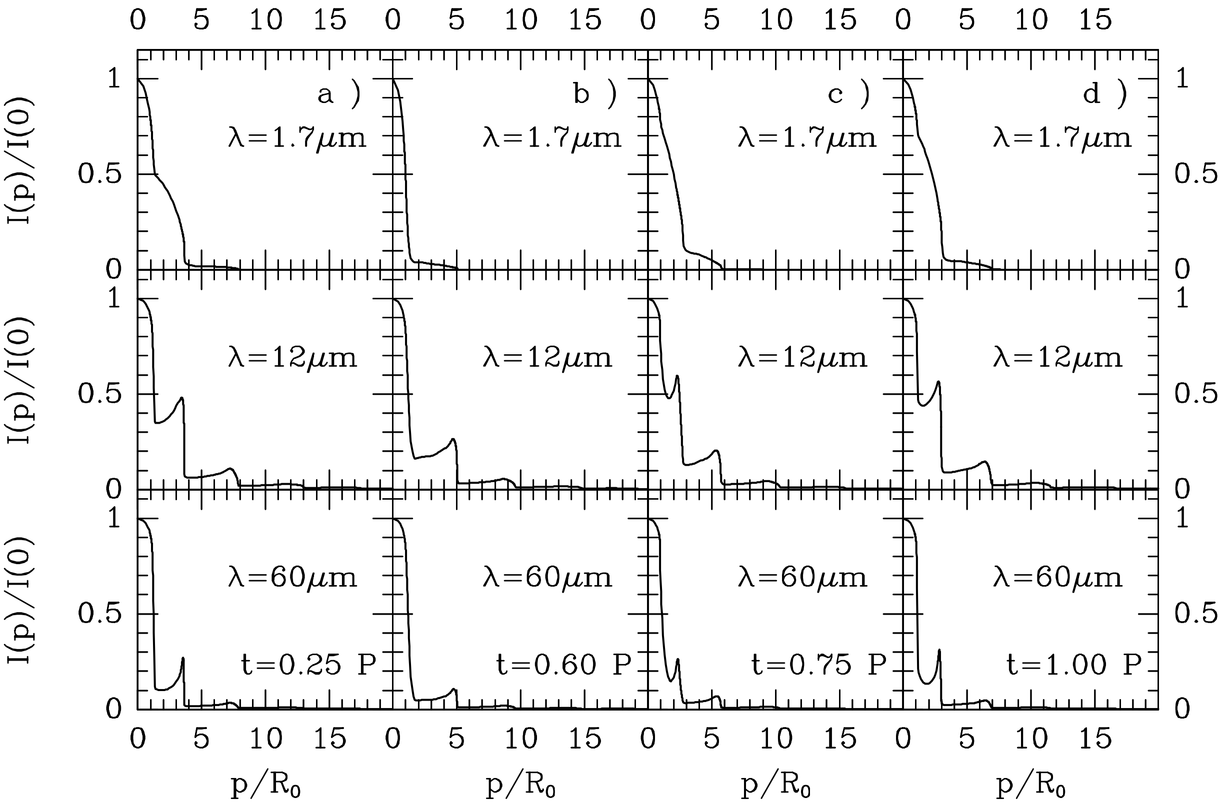

Figure 5.11: Spatial brightness distribution of Model A for different wavelengths and at different instants of time.

near infrared region by interferometric techniques during the last decade. To allow for at least a qualitative comparison with such observations, in Figs. 5.12, 5.14, and 5.16 the synthetic spatial spectra (i.e. the visibilities) of the three dust shell models are additionally shown at the same wavelengths and for the same instants of time as the radial intensity profiles. For calculating the spatial spectra, a unique distance of 100 pc has been assumed for all three models.

The instants of time at which the radial intensity distributions and the spatial spectra of Model A are plotted in Figs. 5.11 and 5.12 are:
a) $t = 0.25P$ (left hand column): all dust layers are completely developed and merely are moving outwards;
b) $t = 0.60P$ (second column): just prior to the formation of a new dust layer, this is the instant of minimum shell optical depth (cf. Fig. 5.10);
c) $t = 0.75P$ (third column): a new dust layer has formed and the shell optical depth has almost reached its maximum value (cf. Fig. 5.10), and
d) $t = 1.00P$ (right hand column): the newly formed dust grains are still growing but the optical depth is already decreasing due to geometrical dilution of the expanding material.

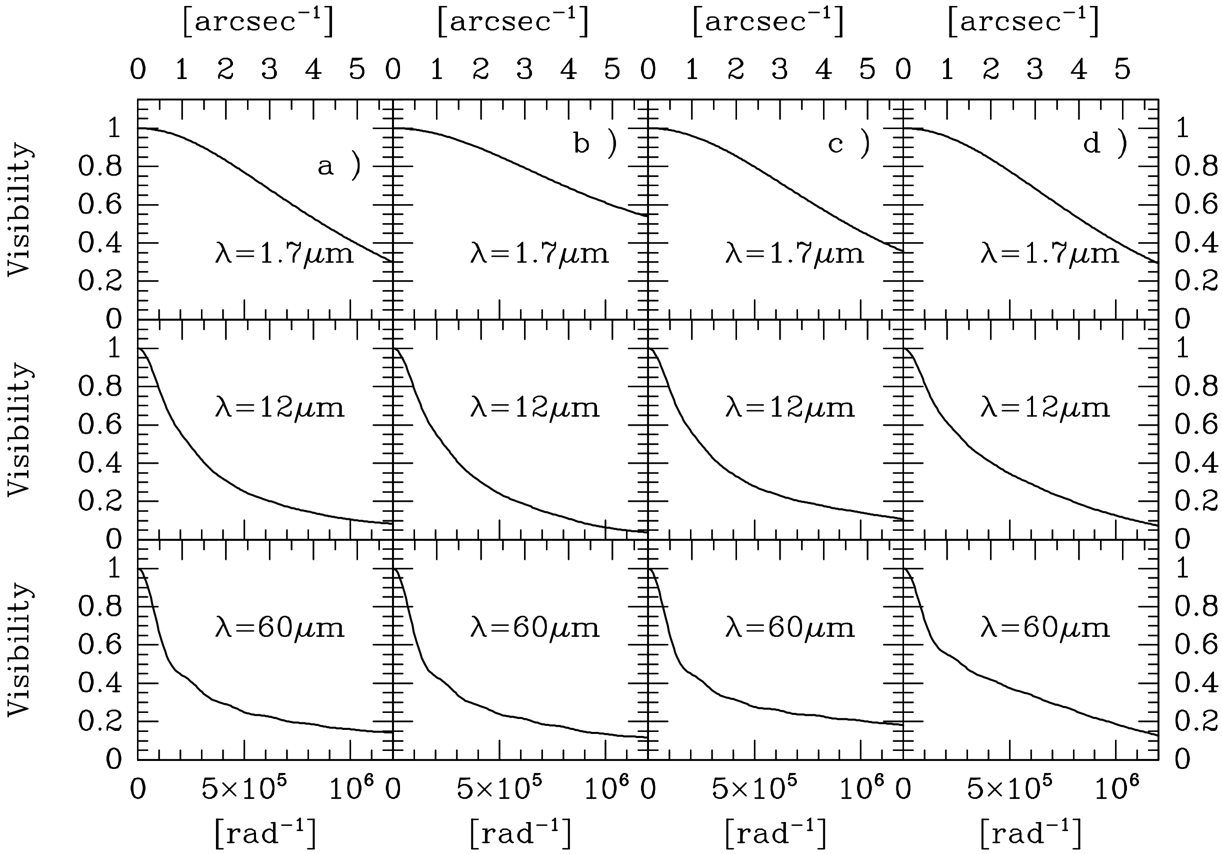

Figure 5.12: Visibilities of Model A for different wavelengths at **a)** $t = 0.25P$, **b)** at $t = 0.60P$, **c)** at $t = 0.75P$ and **d)** at $t = 1.00P$ as in Fig. 5.11.

The 1.7μm intensity reflects almost only the temporal behaviour of the innermost dust layer, while the outer layers are nearly invisible in the linear scaling of the intensity profile. A temporal variation of the compact emitting region is evident from the upper rows of Figs. 5.11 and 5.12, which is largely caused by the dynamic behaviour of the innermost dust layer.

At the longer wavelengths, some of the outer dust layers are also visible. These layers produce the step–like intensity profiles which, in a two–dimensional image, would be seen as concentric bright rings surrounding the central star. The temporal evolution of the intensity distributions of course leads to a temporal variation also of the synthetic visibility functions, indicating a varying geometrical extension of the light emitting region. Such temporal variations are also present in observed visibility functions and have frequently been reported in the literature (e.g. [McCarthy *et al.* 1980, Ridgway and Keady 1988, Dyck *et al.* 1991, Danchi *et al.* 1990, Danchi *et al.* 1994]). These temporal changes are usually interpreted by means of a periodic variation of the inner dust shell boundary. From such observations the conclusion was drawn, that dust formation periodically takes place close to the phase of light minimum at a radial distance of less than $2.4R_{\star}$ from the photosphere (cf. [Danchi

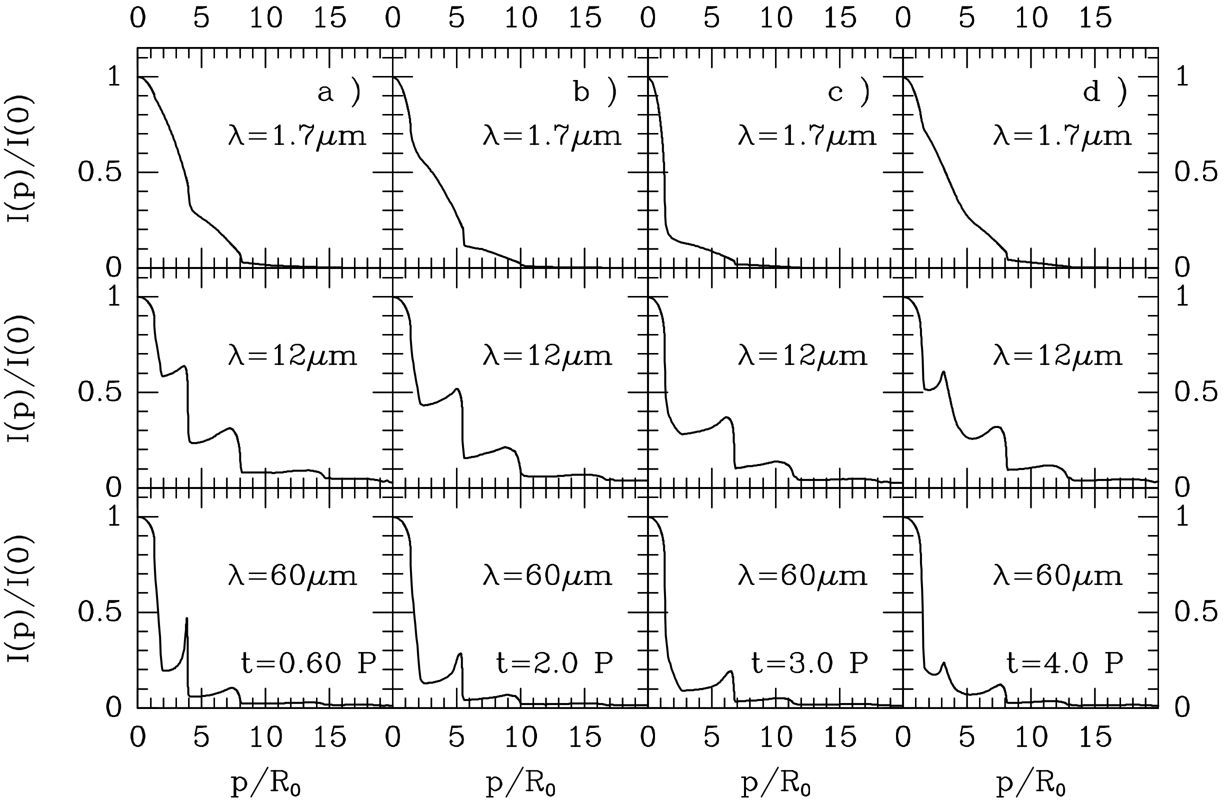

Figure 5.13: Spatial brightness distribution of Model B for different wavelengths and at different instants of time.

et al. 1990, Danchi *et al.* 1994]).

These observations, however, are analyzed using rather simple dust shell models, assuming power laws for representing the radial density distribution of the dust.

At the longer wavelengths, the visibility functions clearly exhibit a rippled structure, which cannot be accounted for by a continuous intensity profile. At these longer wavelengths, the pronounced step–like intensity distribution, which is a natural result of the models discussed here, leads to small scale structures in the synthetic visibility functions. Such structures already have been observed in several objects (e.g. CIT5, CIT6, VY CMa [Dyck *et al.* 1984]; IRC +10216 [Sutton *et al.* 1979, Ridgway and Keady 1988, Danchi *et al.* 1994]; *o* Ceti, α Ori [Danchi *et al.* 1994]), and usually are interpreted in terms of rather ad–hoc multicomponent models for the radial dust distribution (e.g. [Toombs *et al.* 1972, Dyck *et al.* 1984]).

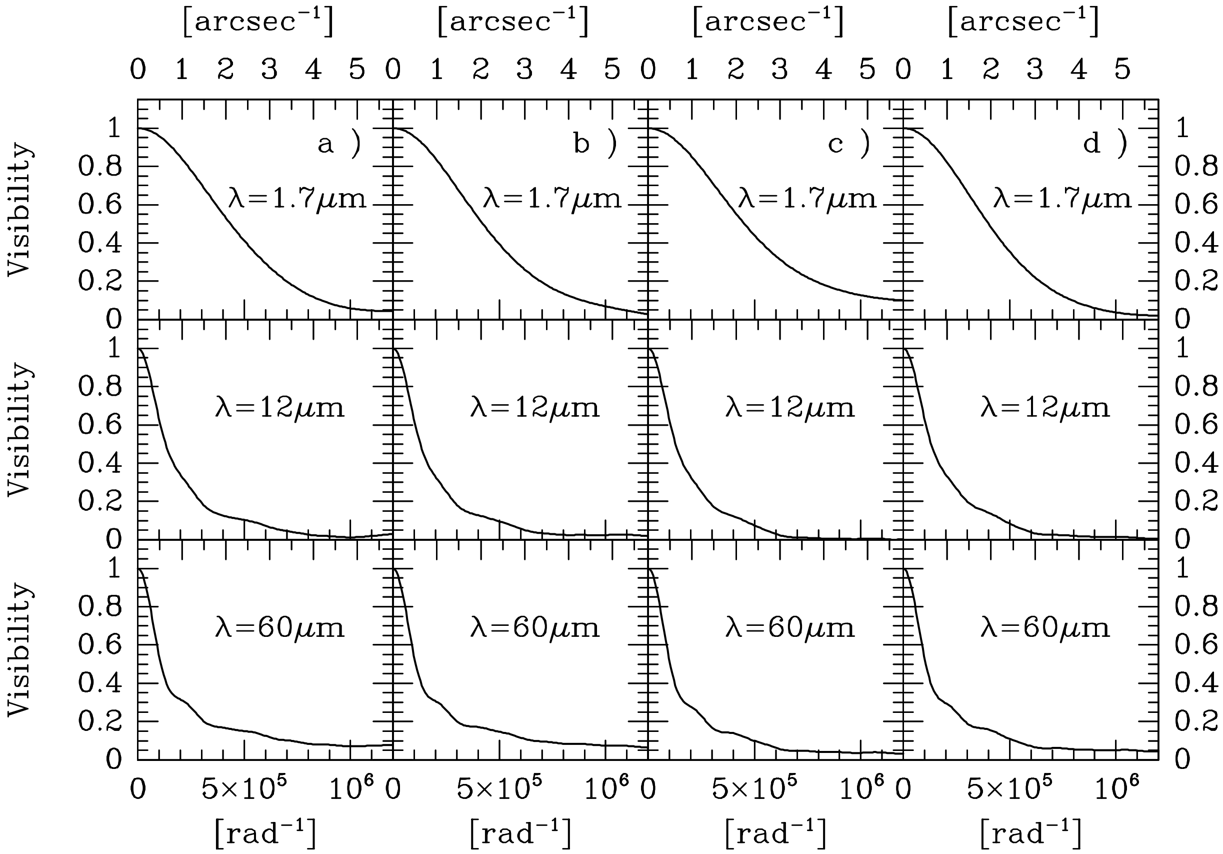

Figure 5.14: Visibilities of Model B for different wavelengths at **a)** $t = 0.60P$, **b)** at $t = 2.00P$, **c)** $t = 3.00P$ and **d)** at $t = 4.00P$. as in Fig. 5.13

The instants of time at which the radial intensity distributions and the spatial spectra of the multiperiodic Model B are plotted in Figs. 5.13 and 5.14 are:
a) $t = 0.60P$ (left hand column) close to maximum shell optical depth, caused by periodic growth of the innermost dust layer (cf. Fig. 5.10);
b) $t = 2.00P$ (second column): all dust layers are completely developed and are moving outwards, thereby causing the phase of continuously decreasing optical depth (cf. Fig. 5.10);
c) $t = 3.00P$ (third column): just prior to the formation of a new dust layer near the deep minimum of the lightcurve, and
d) $t = 4.00P$ (right hand column): new dust has condensed and the shell optical depth has already passed its first intermediate maximum (cf. Fig. 5.10).

In this multiperiodic model the emitting region is considerably more extended than in Model A due to the large contribution of the outer dust layers to the emergent intensity (cf. Fig. 5.13). The enhanced contribution of the outer layers leads to more pronounced small–scale structures present in the spatial spectra of Model B (cf. Fig. 5.14).

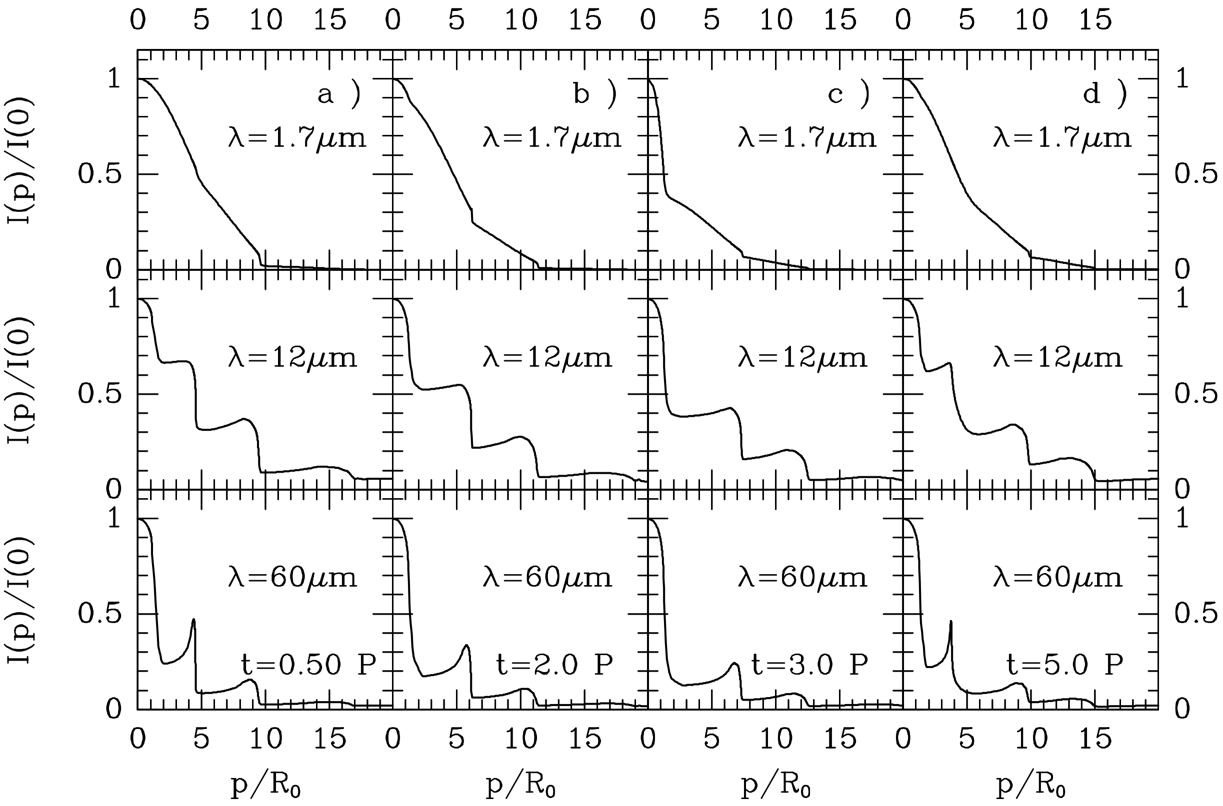

Figure 5.15: Spatial brightness distribution of Model C for different wavelengths and at different instants of time.

The instants of time at which the radial intensity distributions and the spatial spectra of the multiperiodic Model C are plotted in Figs. 5.15 and 5.16 are:
a) $t = 0.50P$ (left hand column): instant of maximum shell optical depth (cf. Fig. 5.10);
b) $t = 2.00P$ (second column): all dust layers are completely developed and are moving outwards, causing the phase of continuously decreasing optical depth;
c) $t = 3.00P$ (third column): just prior to the formation of a new dust layer near the deep minimum of the lightcurve, and
d) $t = 5.00P$ (right hand column): new dust has condensed and already has experienced two subsequent growth phases; the shell optical depth has reached its last intermediate minimum value (cf. Fig. 5.10).

In Model C, the intensity distribution is even more extended, now producing zeroes in the synthetic spatial spectra, which clearly indicate temporal variations caused by the dynamics of the discrete dust layers.

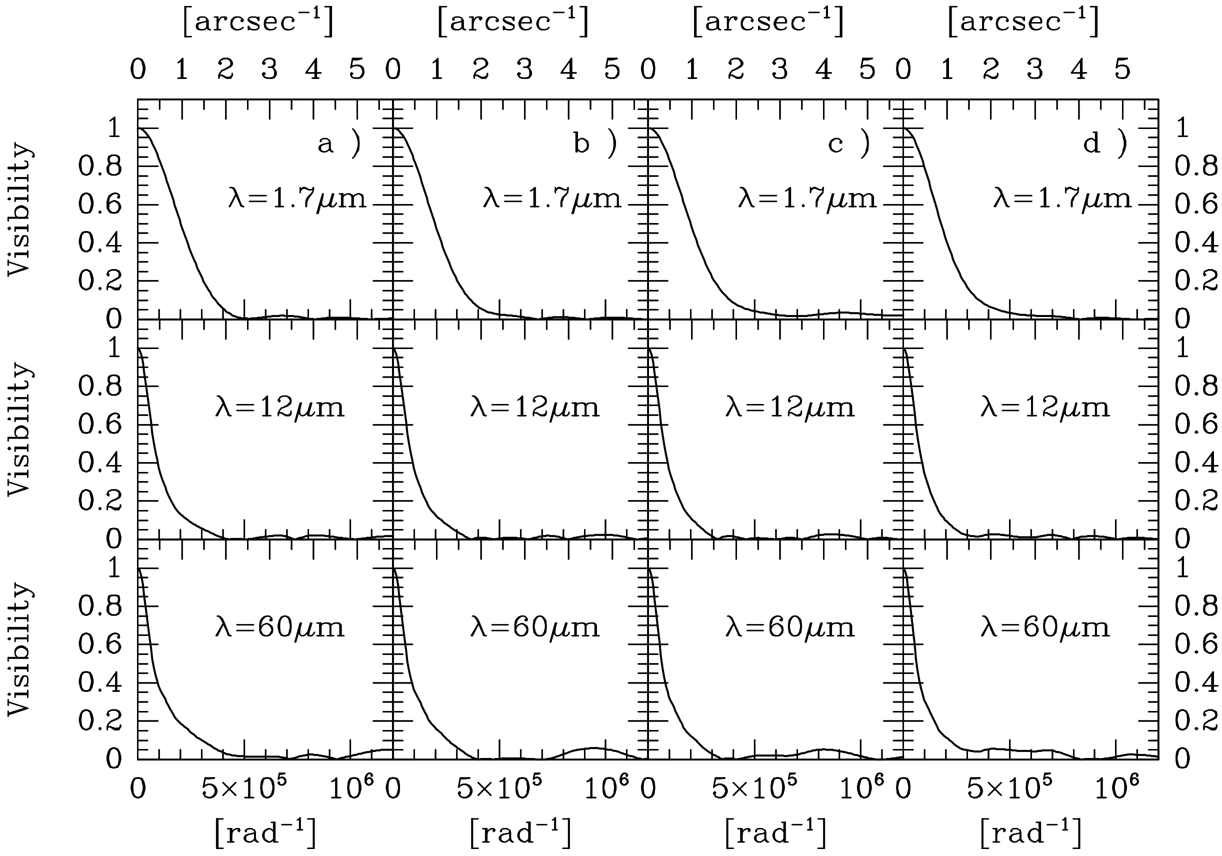

Figure 5.16: Visibilities of Model C for different wavelengths at **a)** $t = 0.50P$, **b)** at $t = 2.00P$, **c)** $t = 3.00P$ and **d)** at $t = 5.00P$ as in Fig. 5.15.

From the general course of the visibility functions of all three models a clear trend between the two shorter wavelengths is apparent, in the sense of increasing angular size of the shells with increasing wavelength (indicated by the steeper decay of the visibility functions at 12μm than at 1.7μm). This trend reverses towards even longer wavelengths, as can be seen from the slope of the 60μm spatial spectra. The short wavelength behaviour has also been found from observations, e.g. by [Dyck *et al.* 1984]. They performed speckle interferometry in the NIR spectral region between 1.65μm and 4.8μm for 16 late–type stars and bipolar nebulae. To interpret the observations, these authors assumed the visibility functions to be Gaussian distributions and fitted the FWHM (full width at half maximum) θ for the different objects. They found, that θ varies as λ^α in the observed wavelength range, with $\alpha \approx 0.2$ in the case of C–stars and $0.7 < \alpha < 1.3$ in the case of M–stars, indicating different dust opacities for both types of objects.

They also noted as a further general trend, that the objects with higher mass loss rates have significantly larger angular diameters than those with smaller rates. This trend is also evident from the calculations presented here and can be seen from Figs. 5.12, 5.14, and 5.16 which give the results for the model calculations in an ordered sequence of increasing mass loss rate.

The smallest angular extension at short wavelengths occurs for all three models just before the formation of a new dust layer, at the instant when mainly the intensity peak of the central star contributes to the spatial spectra (cf. Figs. 5.11 b) and 5.12 b) for Model A, Figs. 5.13 c) and 5.14 c) for Model B, Figs. 5.15 c) and 5.16 c) for Model C). In all three models, these instants of time correspond to phases of the lightcurve shortly before the (deep) light minimum, this is also the instant of minimum shell optical depth.

Temporal changes in the observed visibilities have been found e.g. for IRC +10216. [McCarthy *et al.* 1980] noted a systematic increase of the 5μm visibility between maximum and minimum light by about 30%. Structural changes of this source on a time scale of one year were also noted by [Ridgway and Keady 1988], who interpreted this fact by means of dust destruction near maximum light. At $\lambda = 11\mu$m, [Danchi *et al.* 1990] found large variations of the IRC +10216 visibility and interpreted this result by the formation of new dust near minimum luminosity. In a very recent investigation, [Danchi *et al.* 1994] present visibility measurements for 13 late–type stars in the 11μm region obtained over a time interval of five years. They find substantial variations of the visibilities with time for many of these stars, which they interpret by periodic dust formation near the phase of light minimum. For the oxygen–rich star Mira (*o* Ceti) they find in particular, that the visibilities vary from cycle to cycle enough to give notable differences at the same phase but in different cycles, i.e. the visibility (and thus the spatial structure) is not repeating from cycle to cycle. Such a behaviour results as a natural consequence from the multiperiodic Models B and C presented here (cf. Figs. 5.14 and 5.16).

A clear rippled structure in the visibilities of IRC +10216 is evident in the 11μm observations of [Sutton *et al.* 1979] (cf. the lower diagram of Fig. 4.25 on p. 91, where these data are plotted) and also at 1.65μm, 2.2μm, 3.15μm and in the 10μm region (cf. [Ridgway and Keady 1988]). The latter authors perform a one–dimensional image reconstruction of their measured visibilities and of a lunar occultation measurement at 4.65μm, which all yield obvious step–like structures in the images (i.e. the intensity profiles) on a scale of ≈ 0.1 arcsec. A rippled structure in the measured 11μm visibilities is also seen in the results presented by [Danchi *et al.* 1994] for IRC +10216, *o* Ceti, VY CMa and NML Tau. However, no physical model has been proposed so far which could explain these observed structures.

Very recently, Richichi et al. 1993 (private communication) obtained lunar occultation data of IRC +10216 at $\lambda = 1.65\mu$m, which give a one–dimensional radial brightness profile with an angular resolution of 0.002 arcsec. The algorithm used for the image reconstruction from the occultation lightcurve is described in [Richichi 1989b] and already has been successfully applied to several late–type stars ([Richichi 1989a, Richichi 1989b, Richichi *et al.* 1991]).

The image obtained for IRC +10216 is shown in Fig. 5.17. It should be noted, that this brightness profile is still rather preliminary and is not too reliable on "the

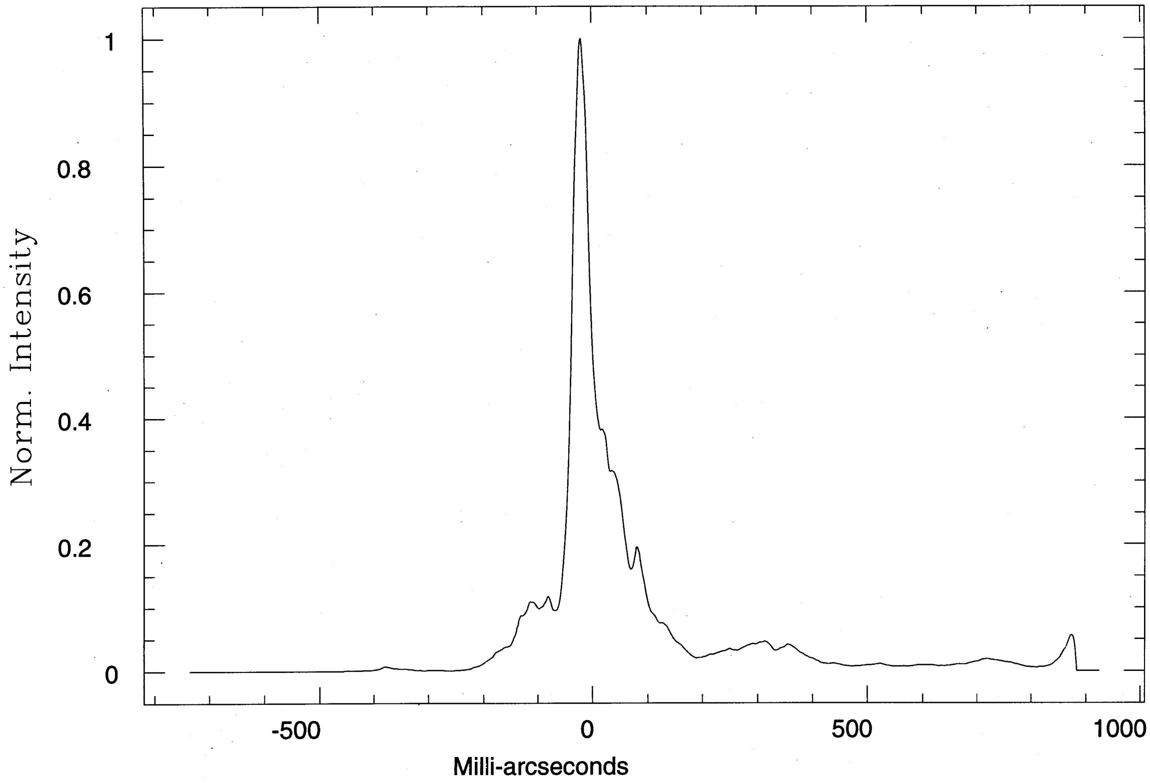

Figure 5.17: Observed radial brightness profile of IRC +10216 at 1.65μm. This figure was kindly made available to me by Dr. A. Richichi prior to publication.

left side" of the central peak, while it is much more accurate on the "right side" (Richichi 1994, private communication). This one–dimensional image represents the radial monochromatic specific intensity function (as shown for Models A–C in the preceding figures 5.11, 5.13, and 5.15) integrated over one spatial dimension. At the present state it is not yet intended to describe any real object by one of the Models A–C discussed here. Nevertheless, in order to allow for at least a qualitative comparison with the observations, in Fig. 5.18 the theoretical one–dimensional image of Model A (i.e. the radial intensity profile integrated over one coordinate) is plotted for the same three wavelengths and the same four instants of time as in Figs. 5.11 and 5.12.

In the observed image (Fig. 5.17), a step–like structure on an angular scale of about 0.03 arcsec is evident to the right of the central peak. If the FWHM of the central peak ($\Phi \approx 45$ milli–arcsec (mas)) is conceived as the stellar diameter, then the separation of the first three steps from the center of the peak ($\approx$ 31.4 mas, 57 mas, and 86 mas) correspond to a radial distance of $1.4R_\star$, $2.5R_\star$, and $3.8R_\star$ from the center of the star.

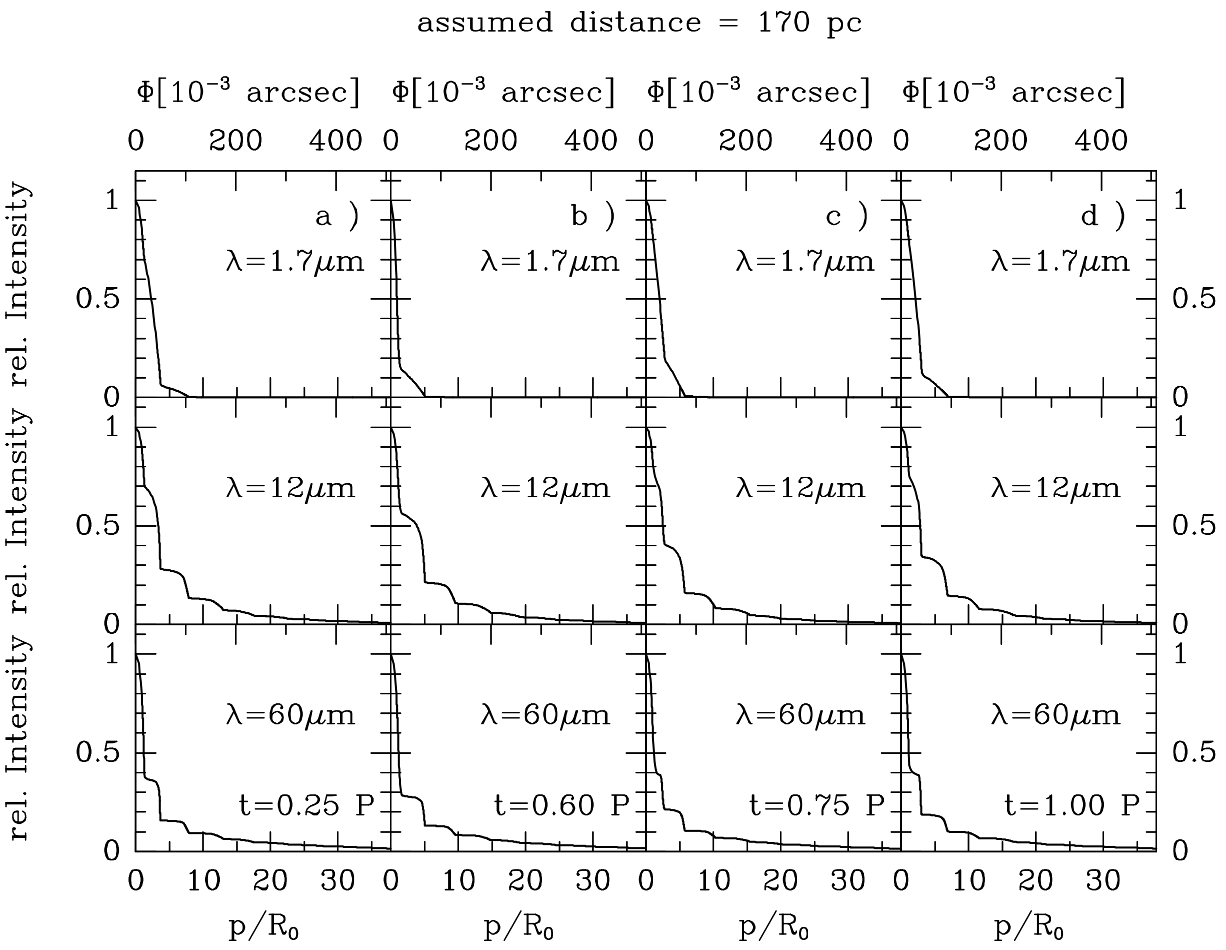

Figure 5.18: One–dimensional image of Model A for different wavelengths (upper row: $\lambda = 1.7\mu$m, middle row: $\lambda = 12\mu$m, lower row: $\lambda = 60\mu$m) at **a)** $t = 0.25P$, **b)** at $t = 0.60P$, **c)** $t = 0.75P$ and **d)** at $t = 1.00P$.

The angular scale given at the upper abscissa in Fig. 5.18 corresponds to the linear separation (given at the lower abscissa), if the model would be seen from the distance to IRC +10216 of 170 pc derived in Sect. 4.8.3. The first three steps (corresponding to the three innermost dust layers) in the synthetic images are located at

$t = 0.25P$: $1.4R_0$, $3.6R_0$, $7.9R_0$
$t = 0.60P$: $1.6R_0$, $5.1R_0$, $9.6R_0$
$t = 0.75P$: $1.5R_0$, $2.7R_0$, $5.7R_0$
$t = 1.00P$: $1.2R_0$, $3.0R_0$, $6.8R_0$

These numbers show, that the separation between the steps in the synthetic images is somewhat larger than it is the case for IRC +10216. The deviation increases with increasing distance of the dust layers from the center of the star. However, this behaviour can easily be understood since the velocity in Model A has already reached a value around $25 - 30\,\mathrm{kms}^{-1}$ at $5R_0$ (cf. Fig. 5.1 on p. 109), whereas the *terminal* outflow velocity of IRC +10216 is about a factor of two smaller ($v_\infty \approx 15\,\mathrm{kms}^{-1}$, e.g. [Olofsson *et al.* 1993a] and is reached only around $20R_\star$, cf. [Keady and Ridgway 1993]). The dust layers produced in the model calculation, therefore, move much faster outwards than does the material in the inner shell region of IRC +10216. The steep increase of the calculated velocity field causes a rapidly increasing separation between successive layers with increasing distance from the star.

Nevertheless, the location of the steps resulting from the model calculation agrees within a factor of 2–3 with the location of the structures in the observed intensity profile, which is of the same order as is the velocity difference between model and object. This satisfactory agreement between the results of the model calculation and the observed structure of IRC +10216 strongly suggests that the formation of discrete dust layers is not only a theoretical result, but also a real phenomenon, actually occuring in the circumstellar shells of pulsating late–type stars.

One major difference between synthetic and observed image however, remains to be resolved: The observed image exhibits the pronounced step–like structure already at a wavelength of $\lambda = 1.65\mu$m, whereas the model calculation produces this significant intensity distribution only at wavelengths $\lambda > 3\mu$m.

The strength of the structures in the synthetic brightness profiles depends on the wavelength via the transport coefficients of the dust grains. As was already mentioned in Sects. 5.5.3 and 5.6, the wavelength–dependence of the dust opacity is crucial for a quantitative modelling of the real objects. A first problem was already encountered in the lightcurves of Model A, which show the shallow intermediate maxima on the ascending branch only at longer wavelengths than is observed. Secondly, from the NIR colours of all three models a small, but systematic deviation with respect to the observations was found and attributed to the smooth wavelength–dependence of the dust absorption efficiency used in the present model calculations.

These three shortcomings might be resolved simultaneously, if the dust grains formed in the shells of the real objects are characterized by an internal structure intermediate between the pure amorphous and the pure crystalline modification. This would produce a steeper opacity law and, thus, would lead to smaller optical depths at the shorter wavelengths. Since a different opacity law however, would also influence the details of the dynamic model structure, which is the result of a strongly nonlinear problem, the definite answer has to await a further detailed investigation.

5.8 Conclusions

Based on dynamic models of circumstellar dust shells, which include time–dependent hydrodynamics and a detailed treatment of the processes of formation, growth and evaporation of carbon grains (discussed in detail in [Fleischer *et al.* 1992] and [Fleischer 1994]), frequency–dependent radiative transfer calculations have been carried out which yield the synthetic lightcurves, the near infrared colours and the brightness profiles of these dust shell models.

It is demonstrated how the complex interplay among the processes of dust formation and growth, hydrodynamics and thermodynamics decisively influences the short–scale behaviour as well as the long–term course of the lightcurves. The dust component plays the key role in producing features, such as intermediate extrema and secondary periods, which similarly occur in observed lightcurves.

The discrete shell–like distribution of dust also causes significant structures in the surface brightness distributions and in the synthetic visibility functions, which are at least in qualitative agreement with the respective observations.

The comparison between our theoretical results and the observations shows that our simple coupling of the dynamic dust shell calculations and the radiative transfer calculations is a promising approach to understand the optical appearance of LPVs and Miras. Thus, although the models presented here are still preliminary, theoretical modelling has been improved to reduce the gap between theory and observation. The calculations discussed in this chapter are not designed to describe any individual object but to investigate the basic physical mechanisms occuring in a pulsating dust forming atmosphere. Nevertheless, the results can account for rather different specific features observed in several late–type stars, which are hitherto not really understood.

On the observer's part a simultaneous monitoring of LPVs and Miras in a wide spectral region with an appropriate temporal resolution is desirable to improve the observational data base and to allow a detailed comparison with improved theoretical model calculations in the near future.

Der Nebel wurde stellenweise so dicht, daß wir die anderen aus dem Blickfeld verloren und uns nur noch durch Rufen verständigen konnten. Aber gleichzeitig wurde es über uns heller. [...] und nach weiteren zehn Minuten scharfen Anstiegs standen wir auf einer Sattelhöhe über dem Nebelmeer in der Sonne. Im Süden waren die Spitzen des Sonnwendgebirgs und dahinter die Schneegipfel der Zentralalpen in voller Klarheit zu erkennen, und über unseren weiteren Aufstiegsweg gab es keinerlei Zweifel.

Werner Heisenberg in: Der Teil und das Ganze

Chapter 6

Summary of results and outlook

Late–type AGB stars represent important stages in the evolution of low and intermediate mass stars. These objects generally are surrounded by extended circumstellar shells accompanied by considerable mass loss. In fact, these shells are the main sources for the enrichment of the interstellar medium in a variety of chemical species and in small solid particles, called dust grains. A reliable quantitative diagnostic and interpretation of these objects can only be based on rather sophisticated physical models. Since the dust forming stellar atmosphere is a nonlinear dynamic system, the description of its local physics and its global structure requires an appropriate treatment of the fundamental processes involved and of the interactions among these processes.

In this thesis, detailed physical models of the dust forming circumstellar shells around carbon–rich AGB stars are presented. These models include a consistent simultaneous treatment of hydrodynamics, thermodynamics, chemistry, and dust formation and of the radiative transfer problem. The complete atmospheric structure as well as the infrared appearance of the models is a result of the calculations. The main emphasis is placed on a comparison between the results of the theoretical models and the observations of individual objects.

This work is divided into two major parts.

In the first part (Chapter 4), a stationary approach to describe the dust forming circumstellar envelopes is discussed and selfconsistent models of purely dust driven winds are presented. These models include a simultaneous treatment of hydrodynamics, thermodynamics, chemistry, dust formation and growth and of the frequency and angle–dependent radiative transfer problem. The transport coefficients of the dust grains are calculated by means of Mie theory for homogeneous spherical particles of arbitrary size, taking explicitly into account the resulting local size distribution function of the dust grains. For calculating the temperature stratification, the equation of radiative equilibrium is solved separately for the gas and the dust component. In this approach, the structure of the dust shell is completely determined by the four stellar parameters: stellar mass $M_\star$, stellar luminosity $L_\star$, mass loss rate $\dot{M}$ and the initial element composition of the gas $\epsilon_{\rm i}$.

The results imply, that in a stationary dust driven wind the common assumption of the small particle approximation for calculating the transport coefficients of the dust component is not justified. Especially in the inner region of the dust envelope, where the mass outflow is generated by radiation pressure on dust grains, the dust opacity and, thus, the radiative force acting on the grains, is essentially reduced by the presence of the large particles.

The calculated energy distributions are sensitive to variations of the mass loss rate, the stellar luminosity and the initial carbon abundance. Within the range of stellar masses, for which purely dust driven winds exist for reasonable values of the stellar luminosity, the spectra are almost independent of the stellar mass.

It is demonstrated that the synthetic spectra produced by the stationary dust shell models are in agreement with the FIR observations of cool carbon-rich AGB objects. In the NIR spectral region the response of the calculated colour indices to changes of the stellar parameters is in qualitative agreement with the observed colour indices. The absolute values of the theoretical colour indices however, deviate in a systematic way from the observations. This deviation is found to be a consequence of the stationary approach. The assumption of stationarity results in the formation of rather large dust grains in the circumstellar shell. As the real dust forming objects are mainly pulsating variables, the formation of very large grains is prevented by the limitation of the time available for grain growth due to significant periodic changes of the hydrodynamic and thermodynamic conditions in the dust forming region. Thus, for a quantitative reliable calculation of the NIR spectra the effects of pulsation have to be taken into account.

Applying the stationary model calculations to IRC +10216, a satisfactory agreement with the observed energy distribution and the observed interferometric data obtained at light maximum is found for a model defined by a stellar mass $M_\star = 0.7 M_\odot$, a stellar luminosity $L_\star = 2.4 \cdot 10^4 L_\odot$, a mass loss rate $\dot{M} = 8 \cdot 10^{-5} M_\odot {\rm yr}^{-1}$ and a carbon to oxygen ratio $\epsilon_{\rm C}/\epsilon_{\rm O} = 1.40$. From the energy distribution of this model a distance to IRC +10216 of $d = 170$pc is derived. The mass contained in the circumstellar shell is $0.6 M_\odot \le M_{\rm CS} \le 0.95 M_\odot$, which implies a main–sequence mass of the progenitor star of $M_{\rm ZAMS} > 1.3 M_\odot$.

The comparison between observed and calculated visibilities yields a distance of $d = 140$pc. This difference is probably caused by our treatment of carbon grain condensation in the framework of classical nucleation theory, which leads to the formation of carbon grains already at relatively high temperatures and, thus, close to the stellar photosphere. A larger separation of the grain formation zone from the photosphere, as is expected if carbon grain condensation proceeds via the formation of PAHs, possibly could resolve this problem.

Despite the obvious limitations of the stationary approach, a selfconsistent solution of the dust driven wind problem, which involves only the four fundamental stellar parameters is capable of reproducing important observed properties of dusty

AGB stars.

In the second part (Chapter 5) the results of detailed frequency and angle–dependent radiative transfer calculations are presented. These calculations are based on the time–dependent models of [Fleischer 1994], which describe the pulsating atmospheres around Long–period variable stars. In order to specify a particular model, the fundamental parameters of the central star – stellar mass $M_\star$, stellar luminosity $L_\star$, stellar temperature $T_\star$ and the element composition $\epsilon_{\rm i}$ – are prescribed. To simulate the interior pulsation of the star, two additional quantities, the pulsation period P and the velocity amplitude at the inner boundary Δu_P are added to the set of fundamental parameters. The internal structure of these models is calculated in the limit case of isothermal shocks which, nevertheless, yield a realistic picture of the dynamic interactions among hydrodynamics, thermodynamics, chemistry, and dust formation, growth and evaporation. In the calculations for the atmospheric structure, the radiative transfer problem is solved using the semi–analytical method of Lucy ([Lucy 1971, Lucy 1976]) in grey approximation. This treatment yields a radiative equilibrium temperature stratification throughout the circumstellar shell at every instant of time but neither a spectrum nor a lightcurve or the brightness profiles of the model.

For the investigation presented here, we have coupled the hydro–code with a frequency and angle–dependent radiative transfer calculation to study the optical appearance of the time–dependent dust shell models. In these calculations, the transport coefficients of the dust component are described in the small particle limit of Mie theory, which is justified in the case of a pulsating atmosphere.

It turns out that the discrete structure of the CDS due to the periodic formation of new dust layers decisively influences the optical appearance of these models.

In a first step it is shown how the complex interplay among the processes of dust formation and growth, hydrodynamics and thermodynamics decisively influences the short–scale behaviour as well as the long–term course of the synthetic lightcurves resulting from these models. The dust component plays the key role in producing significant features in the shape of the lightcurves. This is demonstrated in detail for one model, which exhibits pronounced intermediate maxima in its lightcurves. Furthermore, two dust shell models are presented whose lightcurves are characterized by the superposition of two different oscillations: The oscillation with the period of the interior pulsation is superposed by an oscillation with a longer period which is caused by the dynamic structure of the CDS. It is shown that both, intermediate extrema and secondary periods similarly occur in the observed lightcurves of real LPVs.

In a second step the dynamic models are compared with observations in the frame of a near infrared two colour diagram. This comparison demonstrates that the near infrared spectra produced by the dynamic models are in considerably better agreement with the short wavelength observations than are the stationary calculations. For a physically consistent modelling of the near infrared spectra, it is therefore necessary to take the effects caused by the pulsation of the star into account. The results also suggest, that the dust grains formed in the shells of the real objects are characterized by an internal structure intermediate between the pure amorphous and the pure crystalline modification.

It is further shown, that the discrete shell–like distribution of dust causes significant structures also in the surface brightness distributions and in the synthetic visibility functions produced by these models, which are at least in qualitative agreement with the respective observations.

The discrete structure of the circumstellar dust shell provides for the first time a physical explanation for both, the significant characteristics present in the observed lightcurves of carbon–rich LPVs and for the small–scale structures present in the observed spatial spectra and in the brightness profiles of these objects.

The calculations discussed in Chapter 5 are not designed to describe any individual object but to investigate the basic physical mechanisms occuring in a pulsating dust forming atmosphere. Nevertheless, the results can account for rather different specific features observed in several late–type stars, which are hitherto not really understood. The comparison between our theoretical results and the observations demonstrates that already our simple coupling of the dynamic dust shell models and the radiative transfer calculations is a promising approach to understand the optical appearance of LPVs and Miras.

By the work presented in this thesis, a physically reliable basis for the description of dust forming circumstellar environments is provided, on which more advanced subsequent investigations can be built. Although the current models already include a rather detailed treatment of the most important physical processes and of their mutual interactions, several improvements and extensions of the present theoretical description are obvious:

All the models discussed here are calculated for carbon–rich element mixtures and include the formation of pure carbon grains only. There is however strong evidence from the observations (e.g. [Treffers and Cohen 1974, Herter *et al.* 1982, Goebel and Moseley 1985]), that also heteromolecular grains are formed in the circumstellar shells around C–stars. This is inferred from the presence of characteristic spectral features at typical wavelengths around 11μm and 30μm in the shell spectra. These features currently are attributed to solid SiC and MgS particles. Up to now, there exists no reliable treatment describing the formation of these particles under the circumstellar conditions. In order to explain these features physically, an appropriate treatment of heterogeneous grain formation (e.g. the approach of [Dominik *et al.* 1993]) should be considered in the model calculations.

From the observations of interstellar clouds, where molecular gas and UV photons are simultaneously present, diffuse emission bands are found, which indicate that polyaromatic hydrocarbon molecules (PAHs) exist in the interstellar medium (e.g. [Léger and Puget 1984, Léger *et al.* 1989]). These molecules have already been predicted from theoretical arguments to form in the circumstellar shells of carbon–

rich stars by [Keller and Sedlmayr 1983, Keller 1987, Gail and Sedlmayr 1987a]. First calculations of PAH formation in a circumstellar environment are presented in [Cherchneff and Barker 1992] and [Cherchneff *et al.* 1992]. These calculations are currently being refined in another thesis of our group (T. Allain), and will be incorporated in our model calculations in the near future.

In order to calculate the chemical pathway through the regime of PAH molecules quantitatively reliable, the abundance ratio H/H_2 is of particular importance and should be provided by a non–equilibrium description of the circumstellar chemistry. Chemical non–equilibrium effects are expected to occur in the shocked gas in a pulsating atmosphere, but also in the outer regions of the circumstellar shells, where the velocity field and the interstellar radiation field cause significant deviations of the molecular concentrations from their equilibrium values. These effects are also of considerable importance for the interpretation of molecular line observations, from which e.g. the mass loss rates are derived. For a quantitatively correct determination of the mass loss rates from these observations, the abundance ratio of the respective molecule to the H_2 concentration needs to be known. For both purposes, the calculation of PAH formation and the reliable molecular line diagnostics, it is therefore necessary to include an appropriate non–equilibrium chemistry in the model calculations, which is numerically tractable.

An important step towards a reliable quantitative diagnostic of the CDS would be provided by a non–LTE treatment of the radiative transfer in those molecular lines (e.g. the rotational lines of the CO molecule), which are useful as diagnostic tools e.g. for probing the radial velocity structure or deriving molecular concentrations and/or mass loss rates. These calculations will be performed in collaboration with Drs. J. Keady and A. Gauger (Los Alamos).

In order to describe the circumstellar shells around late–type M–stars, the present models have to be applied to oxygen–rich element compositions as well. A thermodynamic description of the involved grain formation processes (leading to heterogeneous silicate grains) is at hand by now ([Gail and Sedlmayr 1986, Dominik *et al.* 1993]) and is presently being incorporated into the model calculations (K.S. Jeong, thesis, in preparation).

A further important improvement can be achieved by a more realistic description of the molecular opacities. Up to now, only the Rosseland–mean values of the gas opacity have been used in our calculations. This treatment is appropriate for calculating the equilibrium temperature structure in an optically thick situation (e.g. in the stellar interior), but is not adequate for describing the optically thin outer regions above the stellar photosphere. Detailed tables, containing the cross sections of millions of molecular lines for the most important species are now available to us and will soon be used in the model calculations. Besides a more reliable temperature structure, this will also provide an inclusion of the broad molecular absorption bands present in the photospheric spectra.

The model calculations demonstrate, that dust formation may induce mass loss rates as high as $10^{-4} M_{\odot}\mathrm{yr}^{-1}$. Since the AGB stars, which experience such an enormous mass loss have themselves typical masses of only about $1 M_\odot$, the phase of copious mass loss cannot last for a long time. Mass loss therefore strongly affects the evolutionary timescale during the AGB phase. However, no consistent treatment of the mass loss process has been incorporated so far in stellar evolution calculations. It is therefore intended, to replace the hydrostatic atmospheres usually used in evolutionary calculations by the stationary wind models and to construct for the first time consistent evolutionary tracks along the asymptotic giant branch.

Regarding the time–dependent models discussed in this thesis, several improvements are evident. The coupling between radiative transfer and hydrodynamic calculation is still rather incomplete and will be improved in several respects: In a first step the grain size distribution function will be used together with improved values of the complex refractive index of the dust material to calculate the radiative acceleration and the grain temperature consistently from the exact solution for the radiation field. For calculating a reliable gas temperature, the assumption of isothermal shocks has to be dropped. Instead, the energy equation will be solved with appropriate cooling functions describing the relaxation of the shocked gas.

These calculations will be used to model individual objects. In order to obtain reliable far infrared spectra of the models (which are largely influenced by the emission of cold dust located in the outer shell regions), it is necessary to extend the shell models outwards to the appropriate outer radii, which are of the order of at least some $10^3 R_*$. Due to the numerical scheme used for calculating the hydrodynamic shell structure (Lagrangian scheme, explicit integration in time), this cannot be achieved by a straight–forward numerical integration. Instead, a suitable analytical continuation of the shell structure should be invoked, which could be based on the increasing smoothness of the velocity profile in the outer parts of the shell.

In order to get the information about the dependence of the observable model characteristics (e.g. the colour indices, mass loss rates, terminal velocities, ...) on the stellar parameters, a larger grid of models has to be calculated.

Application of these improved time–dependent models to well observed individual LPVs should provide important information about these objects and in particular will allow the determination of those stellar parameters (e.g. the stellar mass), which are not directly accessible to the observations. In the case that the detailed models fail to reproduce the observed characteristics, the detailed comparison will at least reveal the major shortcomings of the current modelling approach and will provide specific implications for further improving the theoretical description. Thereby, the results of the model calculations will also yield rather specific hints for further qualified observations to be performed in order to gain a thorough understanding of the important class of dust forming late–type stars.

Such improvements of course are necessary to reach the ultimate aim: the self-consistent description of the complete pulsating star, including the inner nuclear active zone, the pulsation driving layers as well as the circumstellar dust shell.

We are still a long way from reaching this ambitious goal, but the work presented here provides an important step along this way.

Appendix A

Determination of stellar temperature and stellar radius

In this Appendix the problem of determining the classical parameters $T_\star$ and $R_\star$ for an extended stellar atmosphere is exemplarily discussed for the stationary model of IRC +10216 presented in Sect. 4.8.

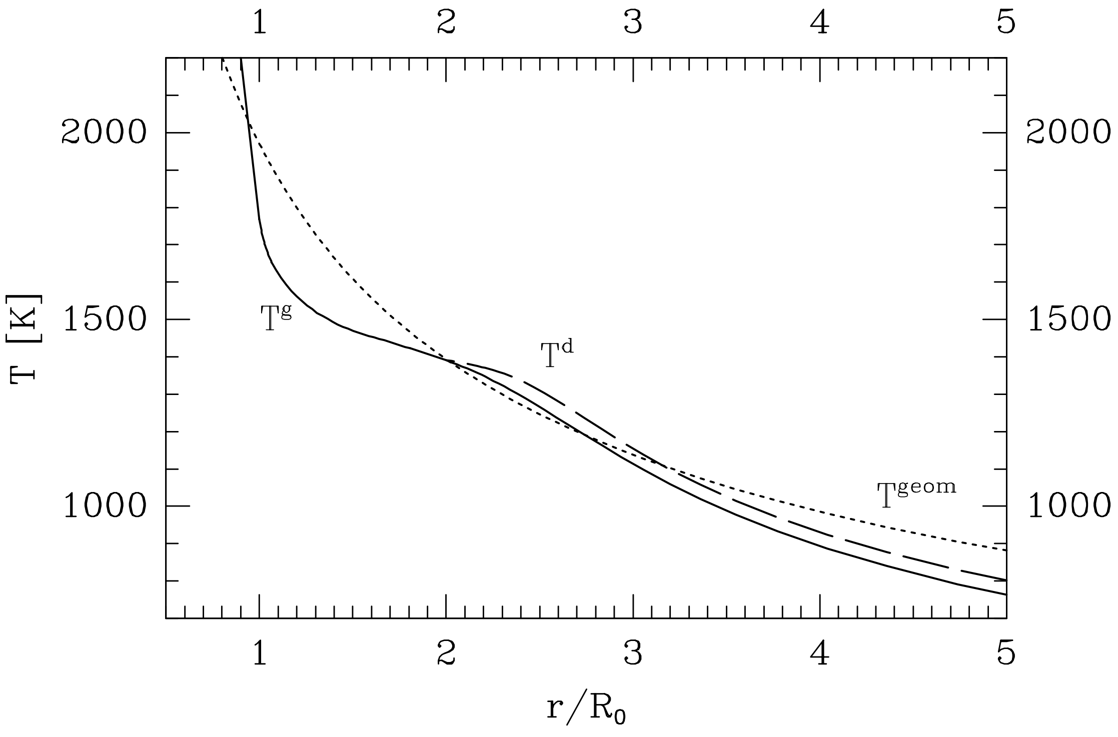

Figure A.1: Radial variation of gas temperature $T^{\rm g}$ (solid line), size–independent dust temperature $T^{\rm d}$ (dashed line) and the temperature resulting from a geometrically diluted radiation field $T^{\rm geom}$ (dotted line).

Table A.1: Possible values for stellar temperature and stellar radius in the converged model

$R_\star/R_0$	$T_\star$/K	$\tau_{\rm L}$	$\tau_{1\mu}$	$\tau_{10\mu}$	$\tau_{\rm R}$
0.96	2008	4.23	23.1	5.27	4.13
2.02	1387	1.29	19.1	1.20	0.14
2.75	1189	1.12	17.0	0.85	0.08
3.16	1108*	0.83	15.5	0.75	0.07
128	175*	0.01	0.35	0.02	0.001
1.00	1971	2/3	—	—	2.94

* refers to the dust temperature

starting model: $R_{\star,0} = 9.25 \cdot 10^{13}cm= R_0$

In the case of a spherically extended stellar atmosphere, composed of the "stellar photosphere" and a circumstellar shell, it is not a priori obvious how to define the so called "basic stellar parameters" *effective (or stellar) temperature* and *photospheric (or stellar) radius* (cf. Baschek et al. 1991). The virtual relevant physical quantity in this context is the energy released in the stellar interior and subsequently transported through the outer layers of the star. A physically meaningful determination of the stellar temperature and the stellar radius is then based on the Stefan–Boltzmann law from the requirement that the local temperature equals $(L_\star/4\pi\sigma r^2)^{1/4}$ at a certain radial distance $r = R_\star$. However, this is only possible if the temperature stratification of the atmosphere is already known, e.g. from a model calculation. In order to calculate the model atmosphere, on the other hand, one has to prescribe four parameters which characterize the star. The classical choice for this parameter set is of course the quadruple ($M_\star$, $L_\star$, $T_\star$, $\epsilon_{\rm i}$). But then the problem arises, how to force the resulting local temperature to match the stellar temperature at the radius $R_\star$ which, for given $L_\star$ and $T_\star$ is uniquely determined from Stefan–Boltzmann's law. This problem is usually solved by prescribing additionally (and somewhat arbitrary in the case of a non-grey atmosphere) a certain value of some optical depth to be reached at $R_\star$.

Based on a two stream approximation for the specific intensity, Lucy (1971) obtains a closure relation for the moment equations of the radiation field. In the case of radiative equilibrium this approximation leads to a semi-analytical expression for the temperature structure (Lucy 1976):

$$T^4(r) = \frac{1}{2}T_\star^4\left[1 - \sqrt{1 - \left(\frac{R_\star}{r}\right)^2} + \frac{3}{2}\tau_{\rm L}(r)\right]\frac{\kappa_{\rm J}}{\kappa_{\rm P}} \tag{A.1}$$

with the geometrically diluted optical depth $\tau_{\rm L}$ defined by the differential equation

$$\frac{d\tau_{\rm L}}{dr} = -(\frac{R_\star}{r})^2 \chi_{\rm H}(r) \tag{A.2}$$

with the boundary condition

$$\tau_{\rm L}(r \to \infty) = 0 \ . \tag{A.3}$$

The value of the stellar radius $R_\star$ then follows from the consistency condition $T(R_\star) = T_\star$ which in terms of Eq. (A.1) requires

$$\tau_{\rm L}(R_\star) = \frac{2}{3}\left[2\frac{\kappa_{\rm P}}{\kappa_{\rm J}} - 1\right] \ . \tag{A.4}$$

As Eq. (A.4) is a second boundary condition to the first order differential equation (A.2), the stellar radius becomes an Eigenvalue of Eq. (A.2). Since the stellar radius on the other hand is uniquely determined by the Stefan–Boltzmann law for given stellar temperature and stellar luminosity, Eq. (A.4) can be used to calculate another unknown quantity as an Eigenvalue of the equation system which describes the CDS. This method is used in grey approximation to fix the mass loss rate as the Eigenvalue in our initial models. The stellar radius of the initial model subsequently serves as the normalization constant R_0. The two-stream approximation, however, is only justified in an optically thin atmosphere. In the case of an optically thick atmosphere, therefore, the temperature has to be calculated from a detailed treatment of the radiative transfer problem. From the given starting model, we consider the mass loss rate as a parameter of the equation system instead of $T_\star$. Stellar temperature and stellar radius are then no longer needed in order to fix the solution. If a value of $T_\star$ is required for some purpose (e.g. for the location of the model in the HR diagram) it can be obtained from the converged model via the Stefan–Boltzmann law. In Fig. A.1 the kinetic gas temperature $T^{\rm g}$, the size–independent dust temperature $T^{\rm d}$ and the temperature which results from a geometrically diluted radiation field $T^{\rm geom} = (L_\star/4\pi\sigma r^2)^{1/4}$ are shown for the model of IRC +10216 discussed in Sect. 4.8. The possible determinations of $R_\star$ and $T_\star$ are summarized in Tab. A.1 together with the values of different optical depths at the respective radii.

Bibliography

[Adams and MacCormack 1935] Adams, W. S. and MacCormack, E., 1935. Systematic displacements of lines in the spectra of certain bright stars. *ApJ*, **81**, 119–131.

[Alksnis 1990] Alksnis, A., 1990. Variability of carbon stars. In Mennessier, M. and Omont, A., editors, *From Miras to Planetary Nebulae: Which Path for Stellar Evolution?*, pages 279–285, Editions Frontières, Gif sur Yvette Cedex.

[Allen 1973] Allen, C. W., 1973. *Astrophysical Quantities*. The Athlone Press, London.

[Bak *et al.* 1988] Bak, P., Tang, C., and Wiesenfeld, K., 1988. Self-organized criticality. *Phys. Rev. A*, **38**(1), 364–374.

[Balick 1989] Balick, B., 1989. The shapes and shaping of planetary nebulae. In Torres-Peimbert, S., editor, *Planetary Nebulae*, pages 83–92, Kluwer Academic Publishers, Dordrecht.

[Barnbaum *et al.* 1991] Barnbaum, C., Kastner, J. H., and Zuckerman, B., 1991. The mass range of carbon stars. *AJ*, **102**, 289–294.

[Baschek *et al.* 1991] Baschek, B., Scholz, M., and Wehrse, R., 1991. The parameter R and T_{eff} in stellar models and observations. *A&A*, **246**, 374–382.

[Beck *et al.* 1992] Beck, H. K. B., Gail, H.-P., Henkel, R., and Sedlmayr, E., 1992. Chemistry in circumstellar shells. I. Chromospheric radiation fields and dust formation in optically thin shells of M-giants. *A&A*, **265**, 626–642.

[Becklin *et al.* 1969] Becklin, E. E., Frogel, J. A., Hyland, A. R., Kristian, J., and Neugebauer, G., 1969. The unusual infrared object IRC+10216. *ApJ*, **158**, L133–L137.

[Berruyer and Frisch 1983] Berruyer, N. and Frisch, H., 1983. Dust-driven winds. I. A two-fluid model and its numerical solution. *A&A*, **126**, 269–277.

[Beyer 1965] Beyer, M., 1965. *Variable stars*, volume VI/I of *Landolt–Börnstein*, chapter 6.2, pages 532–537. Springer–Verlag, Berlin, Heidelberg, New York.

[Bohren and Huffman 1983] Bohren, C. F. and Huffman, D. R., 1983. *Absorption and Scattering of Light by Small Particles*. John Wiley & Sons, New York.

[Boothroyd and Sackman 1992] Boothroyd, A. I. and Sackman, I.-J., 1992. Breakdown of the core mass-luminosity relation at high luminosities on the asymptotic giant branch. *ApJ*, **393**, L21–L24.

[Boothroyd and Sackmann 1988a] Boothroyd, A. I. and Sackmann, I.-J., 1988. Low–mass stars. II. The core mass–luminosity relations. *ApJ*, **328**, 641–652.

[Boothroyd and Sackmann 1988b] Boothroyd, A. I. and Sackmann, I.-J., 1988. Low–mass stars. III. Low–mass stars with steady mass loss: Up to the asymptotic giant branch and through the final thermal pulses. *ApJ*, **328**, 653–670.

[Boothroyd and Sackmann 1988c] Boothroyd, A. I. and Sackmann, I.-J., 1988. The production of low–mass stars. IV. Carbon stars. *ApJ*, **328**, 671–679.

[Bowen 1988] Bowen, G. H., 1988. Dynamical modelling of long-period variable star atmospheres. *ApJ*, **329**, 299–317.

[Bowen 1990] Bowen, G. H., 1990. Dynamical phenomena in pulsating star atmospheres. In Buchler, J. R., editor, *The Numerical Modelling of Nonlinear Stellar Pulsations*, pages 155–171. Kluwer Academic Publishers.

[Bowen and Willson 1991] Bowen, G. H. and Willson, L. A., 1991. From wind to superwind: The evolution of mass-loss rates for Mira models. *ApJ*, **375**, L53 – L56.

[Bussoletti *et al.* 1987] Bussoletti, E., Colangeli, L., Borghesi, A., and Orofino, V., 1987. Tabulated extinction efficiencies for various types of submicron amorphous carbon grains in the wavelength range 1000 $\AA - 300\mu$m. *A&AS*, **70**, 257–268.

[Castor *et al.* 1975] Castor, J. I., Abbott, C., and Klein, R. I., 1975. Radiation–driven winds in Of stars. *ApJ*, **195**, 157–174.

[Celis 1977] Celis, L., 1977. Light and colour variation of the Mira stars. *A&AS*, **29**, 15–30.

[CRC Handbook] CRC Handbook, 1988. *CRC Handbook of Chemistry and Physics*. CRC Press, Inc., Boca Raton, Florida, 69^{th} edition.

[Cherchneff and Barker 1992] Cherchneff, I. and Barker, J. R., 1992. Polycyclic Aromatic Hydrocarbons and Molecular Equilibria in Carbon-Rich Stars. *ApJ*, **394**, 703–716.

[Cherchneff *et al.* 1992] Cherchneff, I., Barker, J. R., and Tielens, A. G. G. M., 1992. Polycyclic Aromatic Hydrocarbon formation in carbon-rich stellar envelopes. *ApJ*, **401**, 269–287.

[Claussen *et al.* 1987] Claussen, M. J., Kleinmann, S. G., Joyce, R. R., and Jura, M., 1987. A flux-limited sample of galactic carbon stars. *ApJS*, **65**, 385–404.

[Cohen 1990] Cohen, R. J., 1990. High resolution radio observations of circumstellar envelopes. In Mennessier, M. O. and Omont, A., editors, *From Miras to Planetary Nebulae: Which path for stellar evolution?*, pages 239–249, Editions Frontières, Gif sur Yvette Cedex - France.

[Danchi *et al.* 1990] Danchi, W. C., Bester, M., Degiacomi, C. G., McCullogh, P. R., and Townes, C. H., 1990. Location and phase of dust formation in IRC +10216 indicated by 11 micron spatial interferometry. *ApJ*, **359**, L59–L63.

[Danchi *et al.* 1994] Danchi, W. C., Bester, M., Degiacomi, C. G., Greenhill, L. J., and Townes, C. H., 1994. Characteristics of dust shells around thirteen late–type stars. *AJ*, **in press**.

[Deutsch 1956] Deutsch, A. J., 1956. The circumstellar envelope of alpha Herculis. *ApJ*, **123**, 210–227.

[Dominik 1992] Dominik, C., 1992. *Formation of dust grains in the winds of cool giants*. PhD thesis, Technische Universität, Berlin, FRG.

[Dominik *et al.* 1989] Dominik, C., Gail, H.-P., and Sedlmayr, E., 1989. The size distribution of dust particles in a dust-driven wind. *A&A*, **223**, 227–236.

[Dominik *et al.* 1990] Dominik, C., Gail, H.-P., Sedlmayr, E., and Winters, J. M., 1990. HR diagrams for dust driven winds around C-stars. *A&A*, **240**, 365–375.

[Dominik *et al.* 1993] Dominik, C., Sedlmayr, E., and Gail, H.-P., 1993. Dust formation in stellar winds. VI. Moment equations for the formation of heterogeneous and core-mantle grains. *A&A*, **277**, 578–594.

[Dyck *et al.* 1984] Dyck, H. M., Zuckerman, B., Leinert, C., and Beckwith, S., 1984. Near-infrared speckle interferometry of evolved stars and bipolar nebulae. *ApJ*, **287**, 801–813.

[Dyck *et al.* 1987] Dyck, H. M., Zuckerman, B., Howell, R. R., and Beckwith, S., 1987. Measurements of the circumstellar shell geometry in IRC +10216. *PASP*, **99**, 99–106.

[Dyck *et al.* 1991] Dyck, H. M., Benson, J. A., Howell, R. R., Joyce, R. R., and Leinert, C., 1991. The light curve and changes in the circumstellar envelope around IRC+10216. *AJ*, **102**, 200–207.

[Efstathiou and Rowan-Robinson 1990] Efstathiou, A. and Rowan-Robinson, M., 1990. Radiative transfer in axisymmetric dust clouds. *MNRAS*, **245**, 275–288.

[Epchtein *et al.* 1990] Epchtein, N., LeBertre, T., and Lépine, J. R. D., 1990. Carbon star envelopes: Near-IR photometry, mass loss and evolutionary status of a sample of IRAS stars. *A&A*, **227**, 83–104.

[Feast *et al.* 1984] Feast, M. W., Whitelock, P. A., Catchpole, R. M., Roberts, G., and Overbeek, M. D., 1984. Variable circumstellar obscuration of the carbon star R Fornacis. *MNRAS*, **211**, 331–337.

[Feuchtinger *et al.* 1993] Feuchtinger, M. U., Dorfi, E. A., and Höfner, S., 1993. Radiation hydrodynamics in atmospheres of long–period variables. *A&A*, **273**, 513–523.

[Fleischer 1994] Fleischer, A. J., 1994. *Hydrodynamics and Dust Formation in the Circumstellar Shells of Miras and Long–Period Variables*. PhD thesis, Technische Universität, Berlin, FRG.

[Fleischer *et al.* 1991] Fleischer, A. J., Gauger, A., and Sedlmayr, E., 1991. Generation of shocks by radiation pressure on newly formed circumstellar dust. *A&A*, **242**, L1–L4.

[Fleischer *et al.* 1992] Fleischer, A. J., Gauger, A., and Sedlmayr, E., 1992. Circumstellar Dust shells around Long-period Variables. I. Dynamical models of C-stars including dust formation, growth and evaporation. *A&A*, **266**, 321–339.

[Forrest *et al.* 1981] Forrest, W. J., Houck, J. R., and McCarthy, J. F., 1981. A far–infrared emission feature in carbon–rich stars and planetary nebulae. *ApJ*, **248**, 195–200.

[Frantsman and Eglitis 1988] Frantsman, Y. L. and Eglitis, I. E., 1988. The C / O – ratio in N stars: observations and theory. *SvA*, **14**, L109 – L111.

[Gail 1990] Gail, H.-P., 1990. Winds of late type stars. *Rev. Mod. Astron.*, **3**, 156–173.

[Gail and Sedlmayr 1984] Gail, H.-P. and Sedlmayr, E., 1984. Formation of crystalline and amorphous carbon grains. *A&A*, **132**, 163–167.

[Gail and Sedlmayr 1985] Gail, H.-P. and Sedlmayr, E., 1985. Dust formation in stellar winds. II. Carbon condensation in stationary, spherically expanding winds. *A&A*, **148**, 183–190.

[Gail and Sedlmayr 1986] Gail, H.-P. and Sedlmayr, E., 1986. The primary condensation process for dust around late M-type stars. *A&A*, **166**, 225–236.

[Gail and Sedlmayr 1987a] Gail, H.-P. and Sedlmayr, E., 1987. Dust formation in stellar winds. In Morfill, G. E. and Scholer, M., editors, *Physical Processes in Interstellar Clouds*, pages 275–303. D. Reidel Publ. Comp.

[Gail and Sedlmayr 1987b] Gail, H.-P. and Sedlmayr, E., 1987. Dust formation in stellar winds. III. Self-consistent models for dust-driven winds around C-stars. *A&A*, **171**, 197–204.

[Gail and Sedlmayr 1987c] Gail, H.-P. and Sedlmayr, E., 1987. Dust formation in stellar winds. V. The minimum mass loss rate for dust-driven winds. *A&A*, **177**, 186–192.

[Gail and Sedlmayr 1988] Gail, H.-P. and Sedlmayr, E., 1988. Dust formation in stellar winds. IV. Heteromolecular carbon grain formation and growth. *A&A*, **206**, 153–168.

[Gail *et al.* 1984] Gail, H.-P., Keller, R., and Sedlmayr, E., 1984. Dust formation in stellar winds. I. A rapid computational method and application to graphite condensation. *A&A*, **133**, 320–332.

[Gauger *et al.* 1990] Gauger, A., Gail, H.-P., and Sedlmayr, E., 1990. Dust formation, growth and evaporation in a cool pulsating circumstellar shell. *A&A*, **235**, 345–361.

[Gauger *et al.* 1993] Gauger, A., Fleischer, A. J., Winters, J. M., and Sedlmayr, E., 1993. Dynamical models of dust shells around LPVs: Effects of time–dependent postshock cooling. *AG Abstract Series*, **9**, 127.

[Gauger *et al.* 1994] Gauger, A., Fleischer, A. J., Winters, J. M., and Sedlmayr, E., 1994. Circumstellar shells of long–period variables: Dust formation and optical appearance. In Clegg, R. E. S., Meikle, P., and Stevens, I., editors, *Circumstellar Media in the late stages of Stellar evolution*, page in press, Cambridge University Press, Cambridge.

[Gehrz 1989] Gehrz, R. D., 1989. Sources of stardust in the galaxy. In Allamandola, L. J. and Tielens, A. G. G. M., editors, *Interstellar Dust*, pages 445–453, Kluver Academic Publishers, Dordrecht.

[Gehrz and Woolf 1971] Gehrz, R. D. and Woolf, N. J., 1971. Mass loss from M stars. *ApJ*, **165**, 285–294.

[Gillett *et al.* 1971] Gillett, F. C., Merrill, K. M., and Stein, W. A., 1971. Observations of infrared radiation from cool stars. *ApJ*, **164**, 83–90.

[Gilman 1969] Gilman, R. C., 1969. On the composition of circumstellar grains. *ApJ*, **155**, L185–187.

[Goebel and Moseley 1985] Goebel, J. H. and Moseley, S. H., 1985. MgS grain component in circumstellar shells. *ApJ*, **290**, L35–L39.

[Gow 1977] Gow, C., 1977. Spectrophotometry of cool carbon stars. *PASP*, **89**, 510–518.

[Griffin 1990] Griffin, I. P., 1990. A model for the infrared and radio spectral energy distribution of IRC +10216 . *MNRAS*, **247**, 591–605.

[Groenewegen *et al.* 1992] Groenewegen, M. A. T., deJong, T., van der Bliek, N. S., Slijkhuis, S., and Willems, F. J., 1992. A flux-limited sample of galactic carbon stars. *A&A*, **253**, 150–172.

[Guélin *et al.* 1993] Guélin, M., Lucas, R., and Cernicharo, J., 1993. MgNC and the carbon–chain radicals in IRC +10216. *A&A*, **280**, L19–L22.

[Gustafsson 1989] Gustafsson, B., 1989. Chemical analyses of cool stars. *ARA&A.*, **27**, 701–756.

[Gustafsson and Plez 1992] Gustafsson, B. and Plez, B., 1992. Can classical model atmospheres be of any use for the study of hypergiants? In de Jager, C. and Nieuwenhuijzen, A., editors, *Instabilities in evolved super– and hypergiants*, pages 86–97, North Holland, Amsterdam.

[Habing 1990] Habing, H. J., 1990. The evolution of Red Giants to White Dwarfs, a review of the observational evidence. In Mennessier, M. O. and Omont, A., editors, *From Miras to Planetary Nebulae: Which path for stellar evolution?*, pages 16–40, Editions Frontières, Gif sur Yvette Cedex - France.

[Habing *et al.* 1989] Habing, H. J., te Lintel Hekkert, P., and van der Veen, W. E. C. J., 1989. OH/IR stars and other IRAS point sources as progenitors of planetary nebulae. In Torres-Peimbert, S., editor, *Planetary Nebulae*, pages 359–380, Kluwer Academic Publishers, Dordrecht.

[Hearn 1990] Hearn, A. G., 1990. The physics of mass loss from AGB stars. In Mennessier, M. O. and Omont, A., editors, *From Miras to Planetary Nebulae: Which path for stellar evolution?*, pages 121–130, Editions Frontières, Gif sur Yvette Cedex - France.

[Herbig and Zappala 1970] Herbig, G. H. and Zappala, R. R., 1970. Near-infrared spectra of NML Cygni and IRC+10216. *ApJ*, **162**, L15–L18.

[Herter *et al.* 1982] Herter, T., Briotta, D. A., Jr., Gull, G. E., and Houck, J. R., 1982. Observations of the 30 micron feature in IRC +10216. *ApJ*, **259**, L25–L27.

[Holzer and MacGregor 1985] Holzer, T. E. and MacGregor, K. B., 1985. Mass loss mechanisms for cool, low-gravity stars. In Morris, M. and Zuckerman, B., editors, *Mass Loss from red giants*, pages 229–255. D. Reidel Pub. Com.

[Holzer *et al.* 1983] Holzer, T. E., Flå, T., and Leer, E., 1983. Alfvén waves in stellar winds. *ApJ*, **275**, 808–835.

[Huggins *et al.* 1988] Huggins, P. J., Olofsson, H., and Johansson, L. E. B., 1988. The CO envelope of IRC +10216. *ApJ*, **332**, 1009–1018.

[Iben 1984] Iben, I. J., 1984. On the frequency of planetary nebula nuclei powered by Helium burning and on the frequency of white dwarfs with hydrogen–deficient atmospheres. *ApJ*, **277**, 333–354.

[Iben 1991] Iben, I., 1991. Single and binary star evolution. *ApJS*, **76**, 55–114.

[Jones *et al.* 1981] Jones, T. W., Ney, E. P., and Stein, W. A., 1981. Pulsations, grain condensation, and mass loss in long-period variable stars. *ApJ*, **250**, 324–326.

[Jones *et al.* 1990] Jones, T. J., Bryja, C. O., Gehrz, R. D., Harrison, T. E., Johnson, J. J., Klebe, D. I., and Lawrence, G. F., 1990. Photometry of variable AFGL sources. *ApJS*, **74**, 785–817.

[Jørgensen and Johnson 1992] Jørgensen, U. G. and Johnson, H. R., 1992. Radiative force on molecules and its possible role for mass loss in evolved AGB stars. *A&A*, **265**, 168–176.

[Jura 1983a] Jura, M., 1983. The dust around the carbon star IRC +10216. *ApJ*, **267**, 647–652.

[Jura 1983b] Jura, M., 1983. Mass loss rates and anisotropies in the outflows from late-type stars. *ApJ*, **275**, 683–690.

[Jura 1986a] Jura, M., 1986. Mass loss from carbon stars. *ApJ*, **303**, 327–332.

[Jura 1986b] Jura, M., 1986. The Role of dust in mass loss from late-type stars. *Irish astr. J.*, **17**, 322–330.

[Jura 1991] Jura, M., 1991. High–luminosity single carbon stars in stellar and galactic evolution. *A&AR*, **2**, 227–247.

[Jura and Kleinmann 1989] Jura, M. and Kleinmann, S. G., 1989. Dust–enshrouded asymptotic giant branch stars in the solar neighborhood. *ApJ*, **341**, 359–366.

[Jura *et al.* 1989] Jura, M., Joyce, R. R., and Kleinmann, S. G., 1989. High–luminosity carbon stars in the galactic anticenter. *ApJ*, **336**, 924–936.

[Kastner 1992] Kastner, J. H., 1992. Mass-Loss Rates for IRAS-bright Red Giants: A revised model of circumstellar CO emission. *ApJ*, **401**, 337–352.

[Keady and Ridgway 1993] Keady, J. J. and Ridgway, S. T., 1993. The IRC+10216 circumstellar envelope III: Infrared molecular line profiles. *ApJ*, **406**, 199–214.

[Keller 1987] Keller, R., 1987. Polyaromatic hydrocarbons and the condensation of carbon in stellar winds. In Léger, A., d'Hendecourt, L., and Boccara, N., editors, *Polycyclic Aromatic Hydrocarbons and Astrophysics*, pages 387–397. Reidel Publ. Comp.

[Keller and Sedlmayr 1983] Keller, R. and Sedlmayr, E., 1983. Entstehung von Kohlestaub in Sternhüllen. *Mitt. Astron. Ges.*, **60**, 312.

[Kippenhahn and Weigert 1990] Kippenhahn, R. and Weigert, A., 1990. *Stellar Structure and Evolution*. Astronomy and Astrophysics Library. Springer Verlag, Berlin, Heidelberg, New York.

[Knapp 1985] Knapp, G. R., 1985. Mass Loss from evolved stars. IV. The dust-to-gas ratio in the envelopes of Mira variables and carbon stars. *ApJ*, **293**, 273–280.

[Knapp 1986] Knapp, G. R., 1986. Mass loss from evolved stars. VI. Mass-loss mechanisms and luminosity evolution. *ApJ*, **311**, 731–741.

[Knapp and Morris 1985] Knapp, G. R. and Morris, M., 1985. Mass loss from evolved stars. III. Mass loss rates for 50 Stars from CO $J = 1 - 0$ observations. *ApJ*, **292**, 640–669.

[Knapp *et al.* 1982] Knapp, G. R., Phillips, T. G., Leighton, R. B., Lo, K. Y., Wannier, P. G., Wooten, H. A., and Huggins, P., 1982. Mass Loss from evolved stars. I. Observations of 17 stars in the CO $(2-1)$ line. *ApJ*, **252**, 616–634.

[Kozasa *et al.* 1984] Kozasa, T., Hasegawa, H., and Seki, J., 1984. Grain formation in the expanding gas flow around cool luminous stars. *Ap&SS*, **98**, 61–79.

[Krüger *et al.* 1994] Krüger, D., Gauger, A., and Sedlmayr, E., 1994. Two–fluid models for stationary dust driven winds. I. Momentum and energy balance. *A&A*, **submitted**.

[Lafon and Berruyer 1991] Lafon, J.-P. and Berruyer, N., 1991. Mass loss mechanisms in evolved stars. *A&AR*, **2**, 249–289.

[Lambert *et al.* 1986] Lambert, D., Gustafsson, B., Eriksson, K., and Hinkle, K. H., 1986. The chemical composition of carbon stars. I. Carbon, Nitrogen, and Oxygen in 30 cool carbon stars in the galactic disk. *ApJS*, **62**, 373–425.

[LeBertre 1987] LeBertre, T., 1987. The opacity of the dust around the carbon star IRC + 10216. *A&A*, **176**, 107–113.

[LeBertre 1988a] LeBertre, T., 1988. Optical and infrared observations of IRC+10216 and related objects. Dust shells modelling. *A&A*, **203**, 85–98.

[LeBertre 1988b] LeBertre, T., 1988. Optical and infrared observations of the carbon Mira R For. Dust shell modelling as a function of phase. *A&A*, **190**, 79–86.

[LeBertre 1992] LeBertre, T., 1992. Carbon-star lightcurves in the 1-20 μm range. *A&AS*, **94**, 377–398.

[LeBertre 1993] LeBertre, T., 1993. Oxygen-rich late-type star lightcurves in the 1-20 μm range. *A&AS*, **97**, 729–753.

[Lefèvre *et al.* 1983] Lefèvre, J., Daniel, J.-Y., and Bergeat, J., 1983. Numerical simulation of radiative transfer in circumstellar dust shells II. Ellipsoidal shells. *A&A*, **121**, 51–58.

[Léger and Puget 1984] Léger, A. and Puget, J. L., 1984. Identification of the unidentified IR emission features of interstellar dust? *A&A*, **137**, L5–L8.

[Léger *et al.* 1989] Léger, A., d'Hendecourt, L., and Défourneau, D., 1989. Physics of IR emission by interstellar PAH molecules. *A&A*, **216**, 148–164.

[Little *et al.* 1987] Little, S. J., Little-Marenin, I. R., and Bauer, W. H., 1987. Additional late–type stars with technetium. *AJ*, **94**, 981–995.

[Lockwood and Wing 1971] Lockwood, G. and Wing, R., 1971. Light curves of Mira variables at 1.04 microns. *ApJ*, **169**, 63–86.

[Loup *et al.* 1993] Loup, C., Forveille, T., Omont, A., and Paul, J. F., 1993. CO and HCN observations of circumstellar envelopes. A catalogue – mass loss rates and distributions. *A&AS*, **99**, 291–377.

[Lucas and Guélin 1990] Lucas, R. and Guélin, M., 1990. Spectroscopy of circumstellar envelopes with the IRAM 30-m telescope. In Watt, G. D. and Webster, A. S., editors, *Submillimetre Astronomy*, pages 97–102. Kluwer Academic Publishers.

[Lucy 1971] Lucy, L. B., 1971. The formation of resonance lines in extended atmospheres. *ApJ*, **163**, 95–110.

[Lucy 1976] Lucy, L. B., 1976. Mass loss by cool carbon stars. *ApJ*, **205**, 482–491.

[Mamon *et al.* 1988] Mamon, G. A., Glassgold, A. E., and Huggins, P. J., 1988. The photodissociation of CO in circumstellar envelopes. *ApJ*, **328**, 797–808.

[Maron 1990] Maron, M., 1990. Optical properties of fine amorphous carbon grains in the infrared region. *Ap&SS*, **172**, 21–28.

[Martin and Rogers 1987] Martin, P. G. and Rogers, C., 1987. Carbon grains in the envelope of IRC +10216. *ApJ*, **322**, 374–392.

[Mattei *et al.* 1990] Mattei, J. A., Cannizzo, J. K., and Goodings, D. A., 1990. AAVSO data files on pulsating stars and chaos studies on three long period variables. In Cacciari, C. and Clementini, G., editors, *Confrontation between stellar pulsation and evolution*, pages 461–463. ASP Conf. Ser. 11.

[McCarthy *et al.* 1980] McCarthy, D. W., Howell, R., and Low, F. J., 1980. Spatial spectra of IRC +10216 from 2.2 to 20 microns. Deviations from spherical symmetry. *ApJ*, **235**, L27–L31.

[Menietti and Fix 1978] Menietti, J. D. and Fix, J. D., 1978. Models of mass flows from cool, luminous stars. *ApJ*, **224**, 961–968.

[Mihalas and Hummer 1974] Mihalas, D. and Hummer, D. G., 1974. Theory of extended stellar atmospheres. I. Computational method and first results for static spherical models. *ApJS*, **28**, 343–372.

[Miller 1970] Miller, J. S., 1970. Scanner observations of the Leo infrared object IRC+10216. *ApJ*, **161**, L95–L99.

[Miller and Scalo 1979] Miller, G. E. and Scalo, J. M., 1979. The initial mass function and stellar birthrate in the solar neighborhood. *ApJS*, **41**, 513–547.

[Neugebauer and Leighton 1969] Neugebauer, G. and Leighton, R. B., 1969. *Two–Micron Sky Survey – a Preliminary Catalog.* NASA SP–3047. Government Printing Office, Washington, D.C.

[Olofsson 1988] Olofsson, H., 1988. Radio and infrared observations of circumstellar envelopes. *Space Sci. Rev.*, **47**, 145–174.

[Olofsson *et al.* 1992] Olofsson, H., Carlström, U., Eriksson, K., and Gustafsson, B., 1992. The circumstellar envelope of the carbon star S Scuti. *A&A*, **253**, L17–L20.

[Olofsson *et al.* 1993a] Olofsson, H., Eriksson, K., Gustafsson, B., and Carlström, U., 1993. A study of circumstellar envelopes around bright carbon stars. I. Structure, kinematics, and mass loss rate. *ApJS*, **87**, 267–304.

[Olofsson *et al.* 1993b] Olofsson, H., Eriksson, K., Gustafsson, B., and Carlström, U., 1993. A study of circumstellar envelopes around bright carbon stars. II. Molecular abundances. *ApJS*, **87**, 305–330.

[Orofino *et al.* 1990] Orofino, V., Colangeli, L., Bussoletti, E., Blanco, A., and Fonti, S., 1990. Amorphous carbon grains and emission spectra of IRC+10216. *A&A*, **231**, 105–110.

[Ostlie and Cox 1986] Ostlie, D. A. and Cox, A. N., 1986. A linear survey of the mira variable star instability region of the hertzsprung–russell diagram. *ApJ*, **311**, 864–872.

[Pauldrach and Puls 1990] Pauldrach, A. W. A. and Puls, J., 1990. Radiation driven winds of hot luminous stars. Applications of stationary wind models. *Rev. Mod. Astron.*, **3**, 124–139.

[Pauldrach *et al.* 1986] Pauldrach, A. W. A., Puls, J., and Kudritzki, R. P., 1986. Radiation–driven winds of hot luminous stars. Improvements of the theory and first results. *A&A*, **164**, 86–100.

[Peery 1971] Peery, J. B. F., 1971. Technetium stars. *ApJ*, **163**, L1–L3.

[Pijpers and Habing 1989] Pijpers, F. P. and Habing, H. J., 1989. Driving the stellar wind of AGB stars by acoustic waves; exploration of a simple model. *A&A*, **215**, 334–346.

[Pijpers and Hearn 1989] Pijpers, F. P. and Hearn, A. G., 1989. A model for the stellar wind driven by linear acoustic waves. *A&A*, **209**, 198–210.

[Puls and Pauldrach 1990] Puls, J. and Pauldrach, A. W. A., 1990. Theory of radiatively driven winds of hot stars: II. Some aspects of radiative transfer. *Rev. Mod. Astron.*, **3**, 140–155.

[Reimers 1975] Reimers, D., 1975. Circumstellar envelopes and mass loss of red giants. In Baschek, B., Kegel, W. H., and Traving, G., editors, *Problems in stellar atmospheres and envelopes*, pages 229–256, Springer Verlag, Berlin–Heidelberg.

[Renzini 1981] Renzini, A., 1981. Red giants as precursors of planetary nebulae. In Iben Jr., I. and Renzini, A., editors, *Physical Processes in Red Giants*, pages 431–446, D. Reidel Publishing Company, Dordrecht: Holland.

[Richichi 1989a] Richichi, A., 1989. Lunar occultations for milliarcsecond resolution and their relation to interferometric techniques at present and in future. In Alloin, D. M. and Mariotti, J.-M., editors, *Diffraction–Limited Imaging with Very Large Telescopes*, pages 414–424, Kluwer Academic Publishers, Dordrecht.

[Richichi 1989b] Richichi, A., 1989. Model–independent retrieval of brightness profiles from lunar occultation lightcurves in the near infrared domain. *A&A*, **226**, 366–372.

[Richichi *et al.* 1991] Richichi, A., Lisi, F., and Calamai, G., 1991. Observational constraints on the cool carbon star T Cancri and its circumstellar shell. *A&A*, **241**, 131–136.

[Richtmyer and Morton 1967] Richtmyer, R. D. and Morton, K. W., 1967. *Difference methods for initial-value problems.* John Wiley & Sons, New York, 2^{nd} edition.

[Ridgway and Keady 1988] Ridgway, S. T. and Keady, J. J., 1988. The IRC +10216 circumstellar envelope. II. Spatial measurements of the dust. *ApJ*, **326**, 843–858.

[Rose 1987] Rose, W. K., 1987. Infrared continuum radiation from red giants. *ApJ*, **312**, 284–289.

[Rowan-Robinson and Harris 1983] Rowan-Robinson, M. and Harris, S., 1983. Radiative transfer in dust clouds. IV. Circumstellar dust shells around carbon stars . *MNRAS*, **202**, 797–811.

[Rowan-Robinson 1980] Rowan-Robinson, M., 1980. Radiative transfer in dust clouds. I. Hot-centered clouds associated with regions of massive star formation. *ApJS*, **44**, 403–426.

[Sahai *et al.* 1989] Sahai, R., Claussen, M. J., and Masson, C. R., 1989. The centimeter radio continuum from IRC+10216 and other late-type stars with massloss envelopes. *A&A*, **220**, 92–98.

[Salpeter 1974] Salpeter, E. E., 1974. Formation and flow of dust grains in cool stellar atmospheres. *ApJ*, **193**, 585–592.

[Scholz and Tsuji 1984] Scholz, M. and Tsuji, T., 1984. The effects of spherical extension upon the photospheric structure and spectrum of red giants: comparison of M and C stars. *A&A*, **130**, 11–18.

[Schönberner 1983] Schönberner, D., 1983. Late stages of stellar evolution. II. Mass loss and the transition of Asymptotic Giant Branch stars into hot remnants. *ApJ*, **272**, 708–714.

[Schönberner 1990] Schönberner, D., 1990. Mass loss and evolution of Planetary Nebulae. In Mennessier, M. O. and Omont, A., editors, *From Miras to Planetary Nebulae: Which path for stellar evolution?*, pages 355–367, Editions Frontières, Gif sur Yvette Cedex - France.

[Schutte and Tielens 1989] Schutte, W. A. and Tielens, A. G. G. M., 1989. Theoretical studies of the infrared emission from circumstellar dust shells: The infrared characteristics of circumstellar silicates and the mass-loss rate of oxygen-rich late-type giants. *ApJ*, **343**, 369–392.

[Sedlmayr 1994] Sedlmayr, E., 1994. From molecules to grains. In Jørgensen, U. G., editor, *IAU Colloquium 146: Molecules in the Stellar Environment*, pages 163–185, Springer–Verlag, Berlin.

[Sedlmayr and Winters 1991] Sedlmayr, E. and Winters, J. M., 1991. Dust in the shells of cool giants and supergiants. In Crivellari, L., Hubeny, I., and Hummer, D. G., editors, *Stellar Atmospheres: Beyond Classical Models*, pages 397–408. Kluwer Academic Publishers.

[Shu *et al.* 1987] Shu, F. H., Adams, F. C., and Lizano, S., 1987. Star formation in molecular clouds: Observation and theory. *ARA&A*, **25**, 23–81.

[Sopka *et al.* 1985] Sopka, R. J., Hildebrand, R., Jaffe, D. T., Gatley, I., Roelling, T., Werner, M., Jura, M., and Zuckerman, B., 1985. Submillimeter observations of evolved stars. *ApJ*, **294**, 242–255.

[Sutton *et al.* 1979] Sutton, E. C., Betz, A. L., Storey, J. W. V., and Spears, D. L., 1979. The brightness distribution of IRC +10216 at 11 microns. *ApJ*, **230**, L105–L108.

[Thronson *et al.* 1987] Thronson, H. A., Latter, W. B., Black, J. H., Bally, J., and Hacking, P., 1987. Properties of evolved mass–losing stars in the Milky Way and variations in the interstellar dust composition. *ApJ*, **322**, 770–786.

[Tielens 1983] Tielens, A., 1983. Stationary flows in the circumstellar envelopes of M giants. *ApJ*, **271**, 702–716.

[Toombs *et al.* 1972] Toombs, R. I., Becklin, E. E., Frogel, J. A., Law, S. K., Porter, F. C., and Westphal, J. A., 1972. Infrared diameter of IRC+10216 determined from lunar occultations. *ApJ*, **173**, L71–L74.

[Treffers and Cohen 1974] Treffers, R. and Cohen, M., 1974. High-resolution spectra of cool stars in the 10- and 20-micron regions. *ApJ*, **188**, 545–552.

[Tsuji 1981] Tsuji, T., 1981. Intrinsic properties of Carbon stars. I. Effective temperature scale of N-type Carbon stars. *J. Astrophys. Astr.*, **2**, 95–113.

[Vassiliadis and Wood 1993] Vassiliadis, E. and Wood, P. R., 1993. Evolution of low- and intermediate– mass stars to the end of the asymptotic giant branch with mass loss. *ApJ*, **413**, 641–657.

[Veen and Habing 1988] van der Veen, W. E. C. J. and Habing, H. J., 1988. The IRAS two-colour diagram as a tool for studying late stages of stellar evolution. *A&A*, **194**, 125–134.

[Veen and Rugers 1989] van der Veen, W. E. C. J. and Rugers, M., 1989. A comparison between CO-, OH- and IR-mass-loss rates of evolved stars. *A&A*, **226**, 183–202.

[Wagenhuber and Weiss 1994] Wagenhuber, J. and Weiss, A., 1994. Numerical methods for AGB evolution. *A&A*, **A&A**, submitted.

[Walmsley *et al.* 1991] Walmsley, C. M., Chini, R., Kreysa, E., Steppe, H., Forveille, T., and Omont, A., 1991. 1.3 mm continuum emission from circumstellar envelopes. *A&A*, **248**, 555–562.

[Weidemann and Koester 1983] Weidemann, V. and Koester, D., 1983. The upper mass limit for white dwarf progenitors and the initial–final mass relation for low and intermediate mass stars. *A&A*, **121**, 77–84.

[Weidemann and Schönberner 1990] Weidemann, V. and Schönberner, D., 1990. Stellar evolution theory: Up to and on the AGB. In Mennessier, M. O. and Omont, A., editors, *From Miras to Planetary Nebulae: Which path for stellar evolution?*, pages 3–15, Editions Frontières, Gif sur Yvette Cedex - France.

[Werner *et al.* 1980] Werner, M. W., Beckwith, S., Gatley, I., Sellgren, K., and Berriman, G., 1980. Simultaeous far–infrared, near–infrared, and radio observations of OH/IR stars. *ApJ*, **239**, 540–548.

[Wickramasinghe *et al.* 1966]
Wickramasinghe, N. C., Donn, B. D., and Stecher, T. P., 1966. A mechanism for mass ejection in red giants. *ApJ*, **146**, 590–593.

[Willems and deJong 1988] Willems, F. J. and de Jong, T., 1988. IRAS low resolution spectra of cool carbon stars. IV. A scenario for carbon star evolution. *A&A*, **196**, 173–184.

[Willson and Hill 1979] Willson, L. A. and Hill, S. J., 1979. Shock wave interpretation of emission lines in long period variable stars. II. Periodicity and mass loss. *ApJ*, **228**, 854–869.

[Willson *et al.* 1994] Willson, L. A., Struck-Marcell, C., and Bowen, G., 1994. Winds from pulsating stars. In Jokipii, J. R., Sonett, C. P., and Giampapa, M. S., editors, *Cosmic Winds and the Heliosphere*, page in press, University of Arizona Press, Tucson.

[Winters *et al.* 1993] Winters, J. M., Fleischer, A. J., Gauger, A., and Sedlmayr, E., 1993. Circumstellar Dust shells around Long-period Variables. II. Theoretical lightcurves of C–stars. *A&A*, **submitted**.

[Wirsich 1987] Wirsich, J., 1987. Extinction coefficients of carbon grains in far-infrared. *Infrared Phys.*, **27**(6), 399–405.

[Witteborn *et al.* 1980] Witteborn, F. C., Strecker, D. W., Erickson, E. F., Smith, S. M., Goebel, J. H., and Taylor, B. J., 1980. The spectrum of IRC+10216 from 2.0 to 8.5 microns. *ApJ*, **238**, 577–584.

[Wolfire and Cassinelli 1986] Wolfire, M. G. and Cassinelli, J. P., 1986. The temperature structure in accretion flows onto massive protostars. *ApJ*, **310**, 207–221.

[Wood 1979] Wood, P. R., 1979. Pulsation and mass loss in Mira variables. *ApJ*, **227**, 220–231.

[Woolf and Ney 1969] Woolf, N. J. and Ney, E. P., 1969. Circumstellar infrared emission from cool stars. *ApJ*, **155**, L181–L184.

[Zuckerman *et al.* 1986] Zuckerman, B., Dyck, H. M., and Claussen, M. J., 1986. Carbon Monoxide Emission from Stars in the IRAS and Revised AFGL Catalogs. II. Massive Carbon stars. *ApJ*, **304**, 401–408.

Danksagung–Acknowledgements

Ich danke meinem Lehrer Prof. Dr. E. Sedlmayr nicht nur für seine Anteilnahme, die er dieser Arbeit entgegengebracht hat, sondern insbesondere auch dafür, daß er das ausgezeichnete Arbeitsklima an unserem Institut ermöglicht hat.

Priv.–Doz. Dr. J. P. Kaufmann bin ich sehr dankbar für seine nützlichen Hinweise zur Verbesserung des Textes und für die Erstellung des Zweitgutachtens.

Prof. Dr. H. Niedrig danke ich dafür, daß er sich sofort und mit offensichtlichem Interesse bereiterklärt hat, den Vorsitz der Prüfungskommission zu übernehmen.

Ich danke meinem Freund Axel Fleischer, der entscheidend die Stimmung in "801" mitbestimmt hat. Unzählige Unterhaltungen wissenschaftlicher, wie auch privater Natur haben viel zu meiner Motivation zu dieser Arbeit beigetragen. Du bist durch einen seltsamen, aber glücklichen Zufall (Schicksal?) zu unserer "U–Boot Crew" gestoßen, der mich auch heute noch nachdenklich stimmt.

Immer wichtig waren mir die wissenschaftlichen Diskussionen mit Andreas Gauger, die oft Licht in das Dunkel verwickelter physikalischer Zusammenhänge gebracht haben. Und Du konntest einen wieder aufbauen: Als ich mich über meine Stümperei ärgerte, war Deine Antwort: "Stimmt. Aber es ist Stümperei auf hohem Niveau" …

Uwe Bolick, "Thor" der erreichbaren Rechenanlagen und aller darauf verfügbaren Software, hat mit einer unglaublichen Geduld alle meine diesbezüglichen Probleme umgehend gelöst (auch außerhalb der Sprechstunde!) und damit die technischen Voraussetzungen zu dieser Arbeit geschaffen. Nur wenn's "klemmt" dauert's manchmal etwas länger … Daran wirst Du wohl noch arbeiten müssen! Aber vielleicht klären wir das lieber mal am Klobichsee (falls wir dann nicht gerade anderweitig beschäftigt sind!).

Carsten Dominik hat wesentlich bei der Kopplung zwischen stationärem Windmodell und Strahlungstransport mitgewirkt und mitgelitten: "Erste Testrechnungen mit dem neuen Verfahren liegen vor und zeigen ein stabiles Konvergenzverhalten … Die Programmierer werden in wenigen Tagen wieder feste Nahrung zu sich nehmen können". Außerdem hattest Du die Idee mit Lanzarote. Danke Carsten !

Ganz besonders danke ich auch Dir, Winfried für Deinen Einsatz wenn's mal wieder eng wurde. Hoffentlich kann "Folie 6" im Ordner bleiben, wenn Du diese Arbeit liest !

Allen Mitarbeitern des Instituts, besonders den Teilnehmerinnen und Teilnehmern der Bierrunde, danke ich dafür, daß sie eine abwechslungsreiche und interessante Atmosphäre in unserer Arbeitsgruppe geschaffen haben, in der ich mich sehr wohl gefühlt habe; ohne Eure menschliche Unterstützung hätte ich diese Arbeit nie zuende bringen können.

I am grateful to Dr. Andrea Richichi for making available to me his plot of the intensity profile of IRC +10216 prior to publication.

Anne und Oliver Hemmers haben dankenswerterweise die Einleitung zu dieser Arbeit gelesen und sich sehr darum verdient gemacht, an meinen englischen Formulierungsversuchen zu retten, was noch zu retten war.

Meine Lebensgefährtin Beatrice Wenk hat mir den menschlichen Rückhalt gegeben, den eine solche Arbeit auch braucht. Du hattest es oft nicht leicht mit mir, außer in den letzten Monaten ... da hattest Du fast gar nichts von mir. Aber das ist jetzt auch geschafft. Danke, daß Du durchgehalten hast !

Schließlich bedanke ich mich bei meinen Eltern, die mir das Studium ermöglicht haben, und die mich immer dort unterstützt haben, wo es nötig war und in ihrer Macht stand.

Most of the calculations were performed on the CRAY computers operated by the Konrad–Zuse–Zentrum für Informationstechnik Berlin. Some calculations and further processing of the results made extensive use of the IRIS Indigo R4000 workstations of the WAP Cluster at the Fachbereich Physik der Technischen Universität Berlin. This work has partly been supported by the Deutsche Forschungsgemeinschaft, DFG-Schwerpunkt: “Theorie kosmischer Plasmen” (grant Se 420/4-3).

Lebenslauf

Persönliche Daten

geboren am	4. August 1961 in Stuttgart
Eltern	Dr. Peter Jochen Winters (Redakteur) Ehefrau Rosemarie, geb. Trenkel (Hausfrau)
Familienstand	ledig
Staatsangehörigkeit	deutsch
Konfession	evangelisch

Ausbildungsdaten

1968-1969	Grundschule in 7031 Breitenstein
1969-1972	Grundschule in 6380 Bad Homburg
1972-1980	Ev. Schule in Berlin-Frohnau Grundschule und Gymnasium
Dezember 1980	Abschluß: Abitur
April 1981	Beginn des Physikstudiums am Fachbereich 4 der Technischen Universität Berlin
Okt. 1986 - Sept. 1988	Studentische Hilfskraft mit Lehraufgaben am Institut für Astronomie und Astrophysik
14. 9. 1988	Abschluß des Physikstudiums: Diplom Thema der Diplomarbeit: *Sphärischer Strahlungstransport in Staubhüllen*

Beruflicher Werdegang

Okt. 1988 - Sept. 1991	Wissenschaftlicher Mitarbeiter in einem Projekt des DFG-Schwerpunktes "Theorie kosmischer Plasmen" mit dem Thema "Entwicklung von Staubhüllen" bei Prof. Dr. E. Sedlmayr (Institut für Astronomie und Astrophysik, TU Berlin)
Okt. 1991 - März 1992	Wissenschaftlicher Mitarbeiter im DFG Projekt "Staubhüllenchemie" am selben Institut
seit April 1992	Wissenschaftlicher Mitarbeiter am Institut für Astronomie und Astrophysik, TU Berlin
Forschungsschwerpunkt	Selbstkonsistente Beschreibung und Modellierung kühler, zirkumstellarer Staubhüllen

Berlin, den 19. April 1994